# Analysis of Three Phase Carbon/(CNT+Epoxy) Composites with Flaws

*A Thesis submitted to*

*Indian Institute of Technology Guwahati*

*in partial fulfilment of the requirements for the award of the degree*

*of*

**Doctor of Philosophy**

*by*

**Chukka Atchuta Rao**

**(Roll No: 166103110)**

*Under the supervision of*

**Dr Debabrata Chakraborty** **Dr K. S. R. Krishna Murthy**

**DEPARTMENT OF MECHANICAL ENGINEERING**

**INDIAN INSTITUTE OF TECHNOLOGY GUWAHATI**

**GUWAHATI-781039, ASSAM, INDIA**

**September 2023**


भारतीय प्रौद्योगिकी संस्थान गुवाहाटी
Indian Institute of Technology Guwahati

**Department of Mechanical Engineering**
**Indian Institute of Technology Guwahati**
**Guwahati, Assam, India, 781039**

# CERTIFICATE

This is to certify that the thesis entitled "**Analysis of three phase carbon/(CNT+epoxy) composites with flaws**", submitted by **Chukka Atchuta Rao** (166103110) to the Department of Mechanical Engineering, Indian Institute of Technology Guwahati, for the award of the degree of **Doctor of Philosophy** is a record of an original research work carried out under our supervision and guidance. The work in this thesis has not been submitted elsewhere for the award of any other degree or diploma.

**(Debabrata Chakraborty)**
Professor
Department of Mechanical Engineering
Indian Institute of Technology Guwahati
Guwahati-781039, Assam, India

**(K. S. R. Krishna Murthy)**
Professor
Department of Mechanical Engineering
Indian Institute of Technology Guwahati
Guwahati-781039, Assam, India

# DECLARATION

I declare that,

a. The work contained in this thesis is original and has been done by me under the guidance of my supervisor.
b. The work has not been submitted to any other Institute for any degree or diploma.
c. I have followed the guidelines provided by the Institute in preparing the thesis.
d. I have conformed to the norms and guidelines given in the Ethical Code of Conduct of the Institute.
e. Wherever I have used materials (data, theoretical analysis, figures, and text) from other sources, I have given due credit to them by citing them in the text of the thesis and giving their details in the references. Further, I have taken permission from the copyright owners of the sources, wherever necessary.

**Chukka Atchuta Rao**


भारतीय प्रौद्योगिकी संस्थान गुवाहाटी
Indian Institute of Technology Guwahati

*Dedicated to….*

*Sri Girija Rama Lingeswara Swamy,*

*My Parents and Family Members*

# Acknowledgments

The research presented in this thesis entitled *Analysis of three phase carbon/(CNT+epoxy) composites with flaws*, was undertaken at Department of Mechanical Engineering in Indian Institute of Technology Guwahati, India. Herein, I would like to start by thanking the Almighty and continuous blessings from spiritual gurus Kanchi Swamy and hierarchy specifically for keeping me physically and mentally fit. I would like to extend my sincere thanks to everyone, including parents, professors, family, and friends whose contributions and support throughout have made this thesis possible.

First and foremost, I would like to express my sincere gratitude to my supervisors, Prof. Debabrata Chakraborty and Prof. K. S. R. Krishna Murthy for guiding me and mentoring me throughout the entire period of my research work. I am extremely grateful to my supervisors for their valuable advice, providing critical insight based on their knowledge and experience in this field which has benefitted me immensely in carrying out my research work.

I also take this opportunity to express my sincere gratitude to Doctoral Committee members Prof. Atanu Banerjee and Prof. Pankaj Biswas from the Department of Mechanical Engineering and Prof. Souptick Chanda from the Department of Biosciences and Bioengineering for their valuable suggestions at various stages of my research work. I am also grateful to the former and present Heads of the Department of Mechanical Engineering for providing a congenial academic and research environment for research work.

I sincerely acknowledge the financial support provided by the Ministry of Education (MoE) during the entire period of the doctoral research work. I sincerely acknowledge the computational facility provided by the Department of Mechanical Engineering to carry out my research work smoothly.

I would like to thank my lab members Sasanka, Pran Jyoti, Rajdeep, Mirzaul Bhayya, and Shiv Shukla for their valuable inputs and also to Sai Kumar, Sukanya, Ankan, Avneesh, Lalit Kumar, Krishna Murthy, Rakesh including all my lab members who are present and passed out from the institute for their support and maintaining a friendly working environment. I am also grateful to Durga Rao, Dheeraj, Sibananda, Mukesh, Pankaj Pardeep, Utpal Kiran, Ramesh Anna and many more who encouraged me through their unabated support throughout my work.

I would like to thank the security of the institute especially those who worked in the Umiam Hostel. I also thank the people who worked in Umiam Hostel for providing good services such as catering, sanitary, canteen, stationery, and fruit shop.

I would like to thank Dr. B. Sateesh, Prof. R. Rudrabhi Ram, and other faculty members of the Department of Mechanical Engineering, Vignan's Institute of Information Technology, Visakhapatnam for encouraging me to complete my research.

I would like to thank Mr. Lakshmana Rao Nadiminti (Late), Mr. Kolli Dhananjaya Rao and other friends from my village for their understanding, and constant support in accomplishing my goal.

Last but by no means least, I express my sincere gratitude and heartfelt love to my mother Mrs. Radha Chukka, father Mr. Narayana Chukka, younger brother Mr. Hareesh Chukka, grandmother Seethamma Reddi, maternal uncle Mr. Ramu Naidu Reddi, brother-in-law Mr. Srinivasa Rao Pudi, other family members for their patience, understanding, love and constant support in accomplishing my goal.

There are many more persons who helped me in many ways and whose names elude me at this moment of time. I extend my gratitude to them.

Indian Institute of Technology Guwahati **Chukka Atchuta Rao**

Date: 22/09/2023

# Abstract

Three phase FRP composites like carbon/(CNT+epoxy) are developed where the matrix dominated properties of FRP composites are enhanced to improve the performance. FRP composites though possess a very high specific strength and stiffness sometimes show poor performance when their interlaminar strengths are challenged. Especially when defects like ply break and embedded delaminations occur due to events like low velocity impact, delaminations usually grows at the interface of the broken and intact plies leading to the final fracture. These defects are sub-surface in nature many a time go unnoticed and results in catastrophic failure. It is therefore extremely important to strengthen the laminates against such failure. Resistance against such failures are decided predominantly by matrix dominated properties like interlaminar strengths. Therefore, three phase composites such as carbon/(CNT+epoxy) with modified matrix properties is expected to provide improved resistance against such failure. The present thesis thus aimed at investigating the performance of three phase carbon/(CNT+epoxy) laminates having internal flaws like ply break and impact induced embedded delamination subjected to loading with the specific objective of understanding qualitatively and quantitatively how adding CNTs to the epoxy enhances the resistance delamination growing from such defects. To study this, full 3D finite element analyses (FEA) have been carried out for carbon/(CNT+epoxy) laminates having two types of flaws viz. ply break and embedded delamination. Delamination at the interface has been modelled using a very thin resin rich layer and the interlaminar stresses around the ply break and embedded delaminations are obtained from the 3D FEA. Using the stresses and displacements from FEA, Virtual Crack Closure Integral (VCCI) has been used to determine strain energy release rate (SERR) components as measures of propensity of delamination. FE results show that delamination from such defects is a mixed mode phenomenon and in the case of embedded delamination the mode mix ratio also varies along the delamination front making the estimation of delamination growth difficult. Delamination at the interface arising from such flaws are observed to be influenced by many factors such as size, shape, relative fiber orientation, loading condition. Critical SERR as a measure of resistance to such delamination has been evaluated in the present work using stress based criteria and virtual crack closure integral from LEFM. From the results, it is clear that in the case of three phase carbon/(CNT+epoxy), addition of CNTs to epoxy leads to significant improvement in resistance to delamination at the interface from ply bear as well as from embedded delamination in all the cases studied. In addition, it was also observed that tendency of two neighbouring delamination to grow as a large delamination is also reduced by adding CNTs to the epoxy. However, results from the FE simulations also show that there is a limit till which CNTs could be added to the epoxy for best performance and beyond this the performance further reduces and it is important to know the limit to the adding CNTs will enhance the resistance to such delamination.

# Table of contents

# List of Figures

# List of Tables

# List of Symbols

| | |
|---|---|
| $a$ | Crack length |
| $\Delta a$ | Crack extension length |
| $a_1$, $a_2$ | Major axes of delamination 1 and 2 |
| $b_1$, $b_2$ | Minor axes of delamination 1 and 2 |
| $c$ | Width of the delamination front |
| $[C]$ | Global material matrix |
| $d$ | Separating distance between delaminations |
| $d_{CNT}$, $d_m$ | Diameter of carbon nanotube and matrix |
| $e$ | Aspect ratio of embedded delamination |
| $E_c$, $E_{CNT}$, $E_m$ | Elastic modulus of CNT+epoxy composite, carbon nanotube, and matrix |
| $E_1$ | Longitudinal tensile modulus in the direction 1 |
| $E_2$, $E_3$ | Transverse tensile modulus in directions 2 and 3 |
| $F_n$ | Normal contact force |
| $G$ | Strain energy release rate |
| $G_I$, $G_{II}$, $G_{III}$ | Mode I, Mode II, and Mode III strain energy release rates |
| $G_c$ | Critical strain energy release rate or fracture toughness |
| $G_{Ic}$, $G_{IIc}$, $G_{IIIc}$ | Mode I, Mode II, and Mode III critical strain energy release rates |
| $G_{12}$, $G_{23}$, $G_{31}$ | Shear modulus in 1-2, 2-3 and 3-1 planes |
| $h$ | Thickness of each lamina |
| $K_n$ | Contact normal stiffness |
| $L$ | Length of the specimen |
| $l_{CNT}$ | Length of the CNT |
| $[l]$ | Direction cosines matrix |
| $M_m$, $M_{CNT}$ | Mass fraction of matrix and CNTs |
| $N_i$ | Shape function |
| $P$ | A point on the delamination front |
| $Q$ | Condition for Quadratic Stress Criterion |
| $t$ | Thickness of the laminate |
| $t_r$ | Thickness of the resin layer |
| $[T]$ | Transformation matrix |
| $u_b$, $v_b$, $w_b$ | Bottom surface nodal displacements in $x$, $y$, and $z$ directions |
| $u_t$, $v_t$, $w_t$ | Top surface nodal displacements in $x$, $y$, and $z$ directions |
| $u_n$ | Contact gap size |

| | |
|---|---|
| $V_{CNT}$ | Volume fraction of CNTs |
| $W$ | Width of the specimen |
| $x\,,y\,,z$ | Global coordinates |
| $X\,,\,Y$ | Interlaminar shear strengths |
| $Z$ | Interlaminar normal strength |
| $1\,,2\,,3$ | Material or reference coordinates |
| $\phi$ | Angle measured from the x-axis to the point *P* |
| $\sigma_{ij}$ | Stress tensor |
| $\varepsilon_{kl}$ | Strain tensor |
| $C_{ijkl}$ | Stiffness matrix |
| $S_{ijkl}$ | Compliance matrix |
| $\bar{\sigma}_z$ | Average interlaminar normal stress |
| $\sigma_z$ | interlaminar normal stress |
| $\bar{\tau}_{xz}\,,\,\bar{\tau}_{yz}$ | Average interlaminar shear stresses |
| $\tau_{xz}\,,\,\tau_{yz}$ | Interlaminar shear stresses |
| $\tau_{zn}\,,\,\tau_{zt}$ | Interlaminar shear stresses in normal and tangential directions |
| $\rho_{CNT}\,,\,\rho_m$ | Density of CNTs and epoxy matrix |
| $\alpha\,,\beta\,,\gamma$ | Angles made by *1*, *2*, and *3* axes with respect to the x, y, and z axes |
| $\eta\,,\zeta\,,\xi$ | Natural coordinates |
| $\nu_{12},\ \nu_{23},\ \nu_{31}$ | Poisson's ratio in 1-2, 2-3 and 3-1 planes |

# Abbreviations

| | |
|---|---|
| BP | Buckypaper |
| CB | Carbon black |
| CF | Carbon fiber |
| CFRP | Carbon fiber reinforced polymer |
| CMCs | Ceramic matrix composites |
| CNTs | Carbon nanotubes |
| CNFs | Carbon nanofibers |
| CTOD | Crack tip open displacement |
| CVD | Chemical vapor deposition |
| CZM | Cohesive zone modeling |
| 2D | Two dimensional |
| 3D | Three dimensional |
| DC | Direct current |
| DCB | Double cantilever beam |
| DMA | Dynamic mechanical analysis |
| DWCNTs | Double-walled carbon nanotubes |
| EP | Epoxy |
| ELS | End-loaded split |
| ENF | End notch flexure |
| EPD | Electrophoretic deposition |
| EPFM | Elastic-plastic fracture mechanics |
| FEA | Finite element analysis |
| FRCs | Fiber reinforced composites |
| FRP | Fiber reinforced polymer |
| GFRP | Glass fiber reinforced polymer |
| HDPE | High-density polyethylene |
| ILSS | Interlaminar shear strength |
| i-MBP | In situ deposition of a multiwalled carbon nanotube bukcypaper |
| LEFM | Linear elastic fracture mechanics |
| LSB | Large-scale bridging |
| LVI | Low-velocity impact |
| MMCs | Metal matrix composites |
| MPC | Multi-point constraints |

| | |
|---|---|
| MWCNTs | Multi-walled carbon nanotubes |
| PCF | Functionalized CF fabric |
| PMCs | Polymer matrix composites |
| PSF | Polysulfone nanofiber |
| PZT | Piezoelectric |
| P(St-co-GMA) | Polystyrene-co-glycidyl methacrylate |
| QSC | Quadratic stress criterion |
| SBS | Short beam shear |
| SEM | Scanning electron microscopy |
| SERR | Strain energy release rate |
| SiC | Silicon carbide |
| SIF | Stress intensity factor |
| SSY | Small scale yielding |
| SWCNTs | Single-walled carbon nanotubes |
| S-MWCNT-COOH | Carboxyl functionalized short multi-walled carbon nanotubes |
| VCCI | Virtual crack closure integral |
| VCCT | Virtual crack closure technique |
| VGCF | Vapor-grown carbon fiber |
| VARIM | Vacuum-assisted resin infusion molding |
| VARTM | Vacuum-assisted resin transfer molding |

## CHAPTER 1

# Introduction

This chapter provides a brief overview of the work presented in this thesis, by presenting the background and the technical relevance of the problems undertaken, starting with the brief introduction of fiber reinforced polymer matrix (FRP) composites. Starting with the advantages and applications, commonly used defects in such FRP composites are presented. The need for improving the strength of FRP composites in the presence of such defects by adding carbon nanotubes (CNTs) to the matrix leading to the development of three phase FRP composites has been discussed leading to the motivation of undertaking the present work.

## 1.1 Composite materials: Overview

Monolithic metals and their alloys have been the most commonly used materials for different applications over the past few decades. They have properties like low specific strength, low specific stiffness, low corrosion resistance, more weight, etc. Due to poor properties, they were not meeting the demands of present day technology. Hence, there has been a considerable demand for new materials with improved desired properties. Though it is difficult to achieve all these properties in a single material, however, many of the desired properties could be attained in composite materials.

The word 'composite' is derived from the Latin word compositus, which means "placed together". Egyptians first made composites by reinforcing mud walls with bamboo sticks to build houses (1500 B.C.). Composite materials are made by one or more constituents combined macroscopically and do not dissolve in each other. They exhibit better properties than constituent materials such as reinforcement and matrix. The basic idea of the composite is to improve the properties of the matrix by incorporating reinforcement such as fiber, particles, or flakes. Generally, fibers are the principal load carrying constituents, while the surrounding matrix helps to keep them in their preferred location and orientation and acts as a load transfer medium between them.

### 1.1.1 Classification of composites

Composites are classified based on the geometry of the reinforcement used or based on the type of matrix used. Based on the geometry of the composites, they are classified into three types such as particulate composites, flake composites, and fiber composites [1].

In particulate composites, particulates such as alloys and ceramics are immersed in matrices randomly. The advantages of such composites are enhancement in strength, increased operating temperature, and oxidation resistance. Common examples include using aluminum particles in rubber; silicon particles in aluminum; and sand, gravel, and cement to make concrete. In flake composites, flake materials such as glass, mica, aluminum, and silver are used as reinforcements dipped in matrices. Flake composites offer advantages such as high out-of-plane flexural modulus, low cost, and high strength.

In fiber reinforced composites (FRCs), fibers are reinforced in matrices. Fibers are the main cause of strength and their function is to carry the load along the longitudinal direction. The matrix keeps all the fibers together and its function is to transfer the stress among the reinforcing fibers. The fibers in long fiber composites are continuous and are discontinuous in short fiber composites. The continuous fibers may be unidirectional or bidirectional and the discontinuous fibers may be aligned or present in random orientations as shown in **Fig. 1.1**.

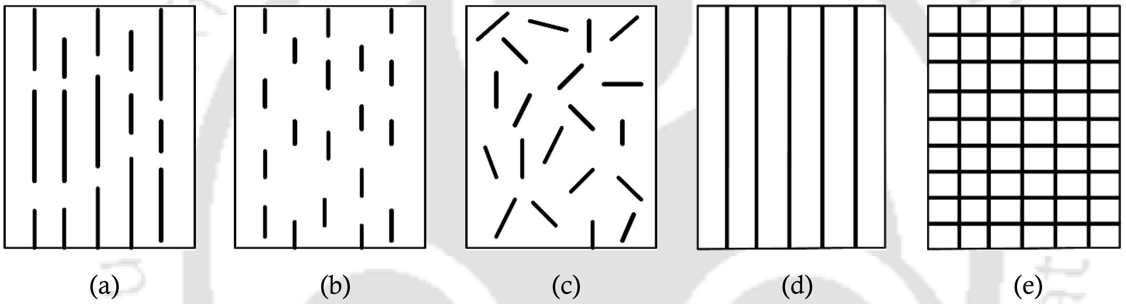

**Figure 1.1:** Different types of fibers in composites (a) long fibers (b) short aligned fibers (c) random fibers (d) unidirectional continuous fibers (e) bi-directional continuous fibers

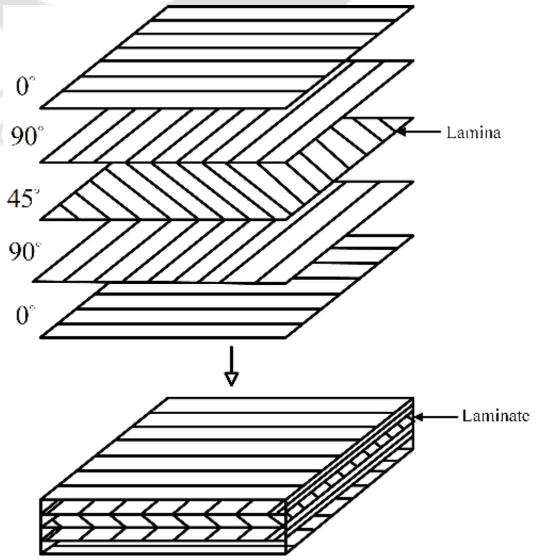

**Figure 1.2:** Development of laminate from different lamina orientation

Lamina or ply is a thin layer, the basic building block of the composite material. A lamina may have fibers, matrix, fillers, and coupling agents. In lamina, fibers may be aligned, random, or woven. A unidirectional fiber reinforced lamina is shown in **Fig. 1.1(d)**. A laminate is made by adding lamina in different stacking sequences to get the desired properties. The sequence of different orientations of fiber reinforced composite layer or lamina in a laminate is called the lamination scheme or stacking sequence. The stacked laminae are added together using the same matrix as that in a lamina. **Figure 1.2** shows a laminate made from different lamination scheme of the lamina.

Composites are also classified based on type of the matrix used as polymer matrix composites (PMCs), metal matrix composites (MMCs), ceramic matrix composites (CMCs), and carbon-carbon composites (CCCs). Polymer matrix composites consist of a polymer (e.g., epoxy, urethane, polyester) reinforced with thin diameter fibers (e.g., carbon, glass, graphite). The most common examples are carbon/epoxy, glass/epoxy, etc. Due to the low cost, high strength, and manufacturing ease of PMCs, they are widely used in most applications. The major limitations of PMCs include a high coefficient of thermal and moisture expansion, low operating temperatures, and low elastic properties in certain directions. Metal matrix composites consist of a metal matrix (e.g., aluminum, magnesium, titanium) reinforced with fibers such as carbon and silicon carbide. The advantages of PMCs include high elastic properties, high specific strength, high operating temperatures, and good wear resistance. Hence, they are used in space, military, and transportation applications. The major limitations of MMCs over PMCs are higher densities and processing temperatures.

Ceramic matrix composites consist of a ceramic matrix (e.g., alumina, calcium, alumino silicate) reinforced with fibers such as carbon and silicon carbide. Ceramic composites have high service temperature limits, high melting points, and good corrosion resistance. Therefore, they are used in high-temperature areas where PMCs and MMCs cannot be used. The major drawback of the CMCs is low fracture toughness. Carbon-carbon composites use carbon for both fiber and matrix. CCCs offer many advantages like high operating temperatures, high coefficient of friction, high fatigue resistance, and high thermal conductivity. Hence, they are used in space shuttle nose cones, aircraft brakes, and mechanical fasteners. The major drawbacks include low shear strength, high cost, and susceptibility to oxidation at high temperatures.

### 1.1.2 Fiber reinforced polymer (FRP) composites

Fiber reinforced polymer (FRP) composites are made of a polymer matrix reinforced with fibers. Glass, graphite, carbon, and aramid are the commonly used fibers and epoxy, vinyl ester, and polyester are the commonly used polymers in FRP composites. Laminates are made by stacking laminae in different orientations to get the desired properties. FRP composites have high strength in the direction of the fiber and low strength in the transverse direction [1].

### *1.1.2.1 Advantages of FRP composites*

FRP composites have many advantages over monolithic materials. A few of the major advantages are listed as follows

- Light in weight or low density
- High strength to weight ratio as compared to traditional materials
- High specific stiffness
- High corrosion resistance
- Dimensional stability (can be designed for zero coefficient of thermal expansion)
- High internal damping
- FRPs can be recycled

### *1.1.2.2 Applications of FRP composites*

FRPs are used in most applications due to their high specific strength and specific stiffness and some of the important applications are listed below.

- Aircrafts such as – aircraft panels and floorings, doors of landing gears, and the skin of aircraft. engines, airplanes with fuselage, wing spars, helicopters, and tilt rotors.
- Spacecraft such as – space shuttle bay doors, antenna ribs in satellite systems, and spaceships.
- Sporting goods such as – golf stick shafts, bicycle frames, tennis rackets, ice hockey sticks, and ski poles.
- Medical devices such as – lightweight face masks, artificial lungs, and X-ray tables.
- Marine applications such as – boats, housings of oceanographic research instruments, and bridges.
- Automotive parts such as – composite leaf springs, bumpers, doors, body panels, brake shoes, drive shafts, and fan blades.
- Military applications such as – bulletproof vests, helmets, and impact-resistant vehicles.
- Commercial applications – brooms in pharmaceutical factories, pressure vessels in chemical plants, and garden tools.

### 1.1.3 Defects in FRP composites

A component made of FRP composite can be different from the ideal one in many ways, both during manufacturing and while it is in service. A defect can be defined as an extent of any of these deviations from the ideal. It is well known that every sort of defect has some negative impact on the expected performance of the component. Most of the defects in FRP composites can be induced either during the manufacturing process or during the service of a component [2].

The chances of defect formation are very high in FRP composites during the manufacturing process. Different methods used for the preparation of composites will produce various types of internal defects. Different types of defects during manufacturing are given below

*Resin matrix defects – Void:* Voids may be formed due to volatile resin or improper control of air during curing stage, and resin-rich areas can be formed due to the staggered fiber bundles and localized fiber breakage.

*Fiber reinforcement defects – Fiber breakage*: Fiber breakage may occur due to differential contraction of the fibers after cure, wrinkling and waviness can be formed due to the misalignment of fibers.

*Interface defects:* Weak bonding strength between fiber and matrix, and delamination due to uneven curing and uneven wetting.

Numerous mechanisms can cause composites to degrade while they are in service, and the most significant ones will rely on the exposed environment and the susceptibility of the specific materials used. Degradation occurs due to static overload, fatigue, impact, overheating, hygrothermal effects, and creep. Even though there are different mechanisms by which defects initiate and grow, there are relatively fewer types of defects that can occur. These defects are delaminations, bond failures, fracture or buckling of fibers, cracks, and interface failure between the fiber and matrix. Often fiber fracture or weak interfacial bond leads to delamination in composites.

With the technological advancement in manufacturing processes, many of these defects could be eliminated or minimized. However, in-service defects may still be present. Such defects many a time go unnoticed and cause degradation leading to the final fracture of the component. Some of the defects arising during service are fiber or ply breakage due to low velocity impact (LVI) as shown in **Fig. 1.3(a)**. In addition, there may be edge delamination from the free edge or hole edge.

In many cases, the delamination initiates at the interface of the ply break which leads to the final fracture of the components. In some cases, LVI induces interfacial delamination as shown in **Fig. 1.3(b)** which is sub-surface in nature and not visible. Moreover, the size of the delamination being small does not lead to a significant change in the strength of the components. However, this delamination grows under loading leading to catastrophic failure of the laminate [3]. Hence, it is important to improve the resistance to the growth of such delamination which is mostly dominated by the properties of the polymer matrix in FRP composites. Therefore, to improve the properties of the matrix, three phase CNT composites were developed in which fibers were reinforced in a matrix modified with nanofillers such as carbon nanotubes (CNTs), carbon nanofibers (CNFs), carbon black (CB), and nano clay, etc. [4].

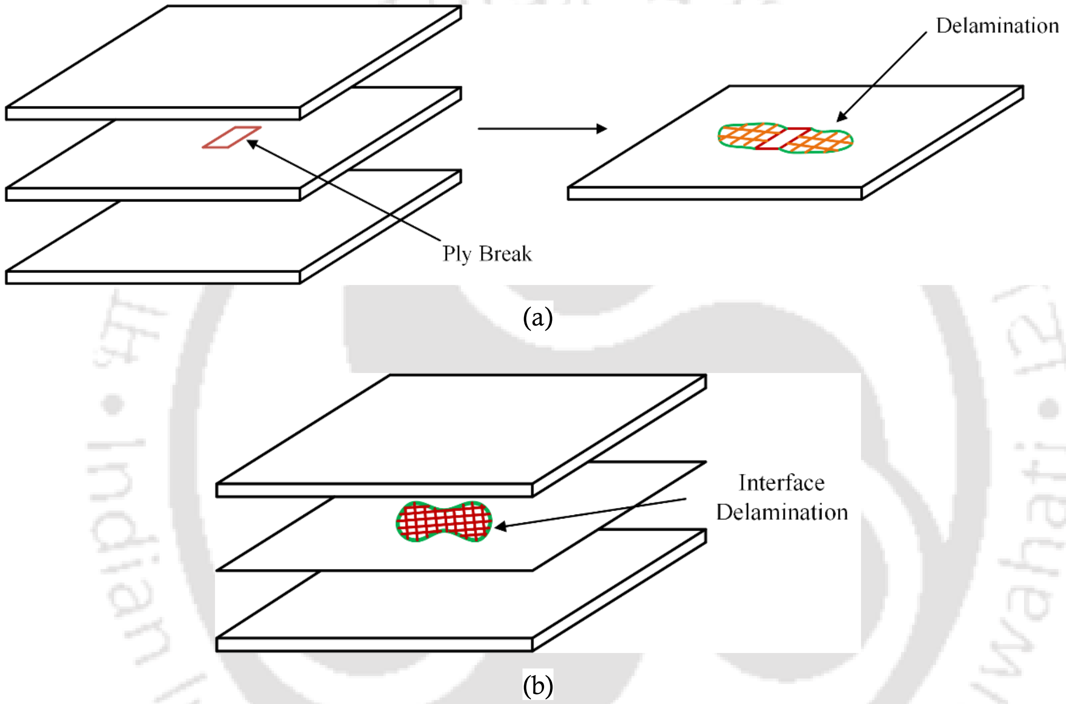

**Figure 1.3:** Defects in FRP laminated composites (a) ply break (b) delamination

## 1.2 Three phase CNT composites

Three phase composites refer to advanced composites that consist of three distinct phases: a polymer matrix, reinforcing fibers, and a third phase, which can be another type of fiber, nanofillers, or additives. Especially, due to their improved properties, carbon nanotubes (CNTs) have been finding more applications every day since their discovery. CNTs can be introduced to overcome the drawbacks of structural composites by mixing in a polymer matrix or by reinforcing onto the fibers, or by using as a layer at the interface. CNTs are the main constituents in the three phase CNT composites. Hence, it is essential to study some of the characteristics of CNT.

### 1.2.1 Carbon nanotubes (CNTs)

Carbon nanotubes (CNTs) are allotropes of carbon, a cylindrical nanostructure discovered by Iijima in 1991 [5]. Due to the unique properties of CNTs, they are used in a wide range of applications [6–7]. Experimental results and theoretical calculations revealed that CNTs are as stiff as a diamond, with the highest Young's modulus and tensile strength [8]. CNTs display remarkable properties, having diameters of 1 to 2 nm, a tensile strength of 200 GPa, an approximate elastic modulus of 1TPa, and a strain of 10-30% without breakage [9]. They have a thermal conductivity of approximately two times that of diamond and are also thermally invariable up to 2800 °C in a vacuum. Additionally, they have 1000 times higher electrical-current-carrying capacity than copper wires. Due to their high aspect ratio, they are widely used in advanced composites, small scale electronics, and as biological molecules in different biotechnological applications. As a result of these superior properties, they attracted industrial and academic interest with potential structural applications.

#### *1.2.1.1 Classification of CNTs*

CNTs are classified into two types based on the direction of hexagons in the graphene sheet and the processes used for the fabrication of carbon nanotubes (CNTs). Based on the direction of hexagons in the graphene sheet, CNTs again can be classified into an armchair, zigzag, and chiral types. **Figure 1.4** represents the different types of CNTs made from a hexagonal graphene sheet. CNTs are defined in terms of tube diameter, chiral angle, and chiral vector. The chiral angle finds the amount of twist in the tube. If the chiral angle is $0^{\circ}$ and $30^{\circ}$, the graphene sheet form a zigzag and armchair CNTs, respectively. When the chiral angle varies between $0^{\circ}$ to $30^{\circ}$, the graphene sheet form a chiral CNT [10].

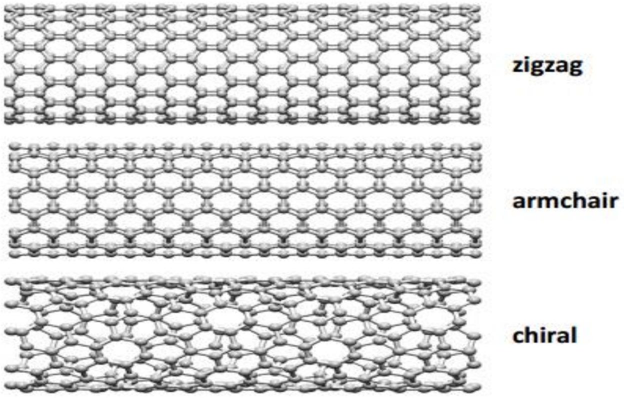

**Figure 1.4:** Different types of CNTs based on the chiral angle [10]

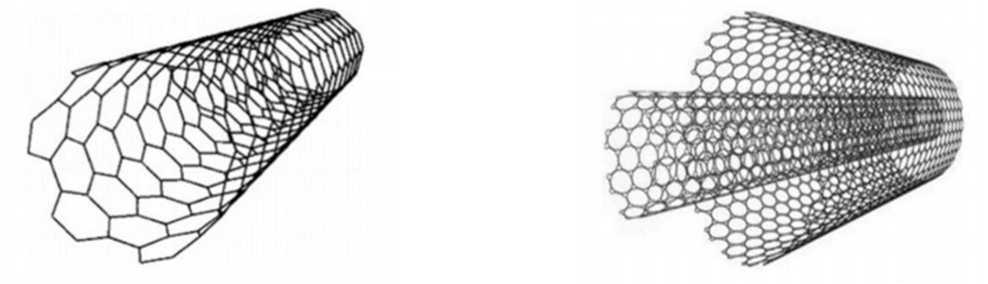
(a) (b)

**Figure 1.5:** Illustrations of the atomic structure of (a) SWCNT (b) MWCNT [11]

Based on the processes used for the fabrication of carbon nanotubes (CNTs), they are classified into two types such as single-walled carbon nanotubes (SWCNTs) and multi-walled carbon nanotubes (MWCNTs) as shown in **Fig. 1.5**. In the case of SWCNTs, a single graphene layer rolled up into a seamless cylinder whereas in MWCNTs two or more concentric cylindrical shells of graphene sheets are coaxially arranged around a central hollow core with van der Waals force between the adjacent layers.

### *1.2.1.2 Advantages of CNTs*

Some of the major advantages of CNTs are as follows:

- CNTs have a modulus of elasticity of approximately 1 TPa, which is 10 times higher than that of steel.
- CNTs have high tensile strength, which is nearly 100 times higher than that of steel of the same diameter.
- CNTs are extremely small and light in weight.
- CNTs behave as good thermal conductors in the longitudinal direction of the tube, but good insulators in the transverse direction of the tube.
- CNTs have a very high aspect ratio of greater than 1000.
- CNTs have a low coefficient of thermal expansion. CNTs have a high specific surface area

### *1.2.1.3 Application of CNTs*

The excellent properties of CNTs make them a feasible candidate for use in different fields. Some of the major applications of CNTs are as follows:

- CNTs are used as reinforcements in composites and structural applications due to their excellent load-bearing capacity and mechanical properties.

- CNTs are also dispersed in polymers and resins to enhance the stiffness and fracture toughness without affecting other mechanical properties.
- CNTs are widely used in marine current turbine coatings and other coating applications such as thin film heaters, flame retardant coating, and transparent conductors which were used in industries.
- Energy storage and environment (solar cells, hydrogen fuel cells, mobile phones, and supercapacitors).
- CNTs are widely used in biomedical applications such as artificial implants, tissue regeneration, drug delivery systems, and cancer therapy.
- CNTs are widely used in the development of sensors and actuators.
- CNTs are widely used in electromagnetics applications as electrical conductors, semiconductors, and insulators.
- Acoustic and electro-acoustics (nano-transceivers, tunable filters, acoustic speakers, acoustic microphones, and nano-speakers).

### 1.2.2 Fiber reinforced CNT/polymer composites

Polymer composites, made of additives and polymer matrices comprising thermosets, thermoplastics, and elastomers, are regarded to be an important group of reasonably low cost materials for various useful applications. Constituents with different material properties are chosen to make composites to improve one or more properties. Although there are some constraints in optimizing the properties by using conventional microscale fillers, the traditional filler content is in the range of 10 to 70% in polymer composites leading, to a higher density than that of the polymer matrix. Microscopic defects and voids are formed due to the high volume fraction of filler which often leads to premature failure of the composites. Carbon nanotubes (CNTs) are nanoscale fillers incorporated as an additive in a polymer resin and fibers are reinforced into the modified polymer matrix three phase fiber reinforced CNT/polymer composites. The excellent physical and mechanical properties combined with many desirable functional properties of CNTs are finding huge potential applications of such composites. In the future, three phase composites will play an important role in building space vehicles and could be used to make different goods that are being used in our daily life.

#### *1.2.2.1 Fabrication of three phase composites*

Three phase composite fabrication includes the preparation of CNT-modified epoxy composite and the preparation of three phase composite by infusing the modified epoxy onto fibers. A predetermined amount of CNTs can be mixed together with epoxy and subjected to sonication to reduce the tendency of CNTs to agglomerate in the form of stable bundles due to van der Waals attractive forces. The mixture can be stirred using wet ball milling or a magnetic stirring process to increase the homogeneity of the modified epoxy CNT mixture. Then, the hardener can be added to the mixture for fast curing of the composite. The modified epoxy nanocomposite part can be used with fiber to fabricate the composite laminates. Further, a three phase composite can be fabricated using the hand layup process with vacuum bagging or vacuum assisted resin transfer molding (VARTM). The fabrication process of the three phase composite is shown in **Fig. 1.6**.

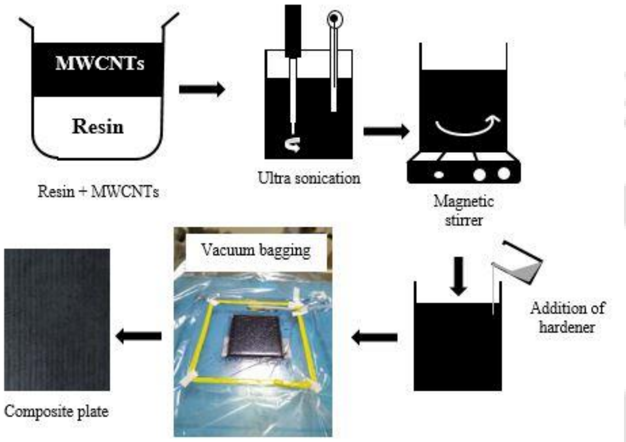

**Figure 1.6:** Schematic representation of three phase composite fabrication

### *1.2.2.2 Advantages of three phase composites*

Three phase composites in which nanofillers are added to the epoxy matrix and fibers are reinforced into a modified matrix have several advantages compared to FRP composites. A few of the major advantages are listed as follows:

- Improved mechanical properties such as strength, stiffness, and toughness
- Improved durability
- Improved fatigue resistance
- Enhanced thermal conductivity and stability
- Increased electrical conductivity

### *1.2.2.3 Applications of three phase composites*

Three phase composites are used in most applications due to their improved properties [12–13]. A few applications based on various fields are listed below

- Structural applications – aerospace, automobile, and marine industries.

- Electronic and electrical applications – printed circuit boards, electronic enclosures, and antennas.
- Energy storage and conversion – solar cells and fuel cells to improve their performance.
- Biomedical and healthcare – biosensors, implantable devices, tissue engineering scaffolds, and drug delivery systems.
- Sports equipment – tennis rackets, golf clubs, bicycle frames.

#### *1.2.2.4 Limitations of three phase composites*

Three phase composites offer several advantages but have some limitations, and are listed below [14–15]:

- Manufacturing of these composites requires special techniques
- Increased cost of manufacturing compared to FRP composites
- Agglomeration of nanofillers leads to uneven dispersion within the polymer matrix, which results in a reduction of mechanical properties
- The mishandling of nanoparticles while manufacturing may lead to health and safety issues
- Disposal and recycling of these composites are difficult

### 1.2.3 Failure analysis of three phase composites with defects

Among the defects discussed, impact induced fiber breakage and interfacial delamination are extremely important from the view point of the failure of laminate since both these defects are sub-surface in nature and many a time go unnoticed but are the causes of final fracture of the laminate. Generally, under low velocity impact one of the weakest fiber breaks leading to the ply break. Near the ply break and at the interface of the broken and intact plies delamination initiates leading to the failure. Sometimes due to impact of a small embedded delamination occurs at a specific interface which grows during the post impact loading leading to the final fracture of the laminate. In both cases, the defects are sub-surface, small without appreciable degradation in stiffness and hence go unnoticed but they grow and cause the final fracture. Therefore, it is important that such defects are analyzed and resistance to such defects growing to be enhanced. Failure of three phase composites with defects such as ply break and embedded delamination could be approached in two ways viz. the stress based approach and the fracture mechanics based approach. In stress based approach, based on the magnitudes of the interlaminar stresses and the corresponding strengths, appropriate failure theories could be applied to assess whether delamination would initiate at the interface or not. Many stress based criteria have been proposed over the years for predicting delamination initiation and quadratic stress criteria is one of those which has been extensively used by earlier researchers. Many a times such defects like ply break or embedded delamination are considered as cracks and concepts of fracture mechanics are advantageously used to analyze the laminates with such defects.

The phenomenon of fracture is clearly explained by three fundamental modes of fracture shown in **Fig. 1.7** (first observed by Irwin (1957)) such as opening mode (mode I), sliding mode (mode II), and tearing mode (mode III).

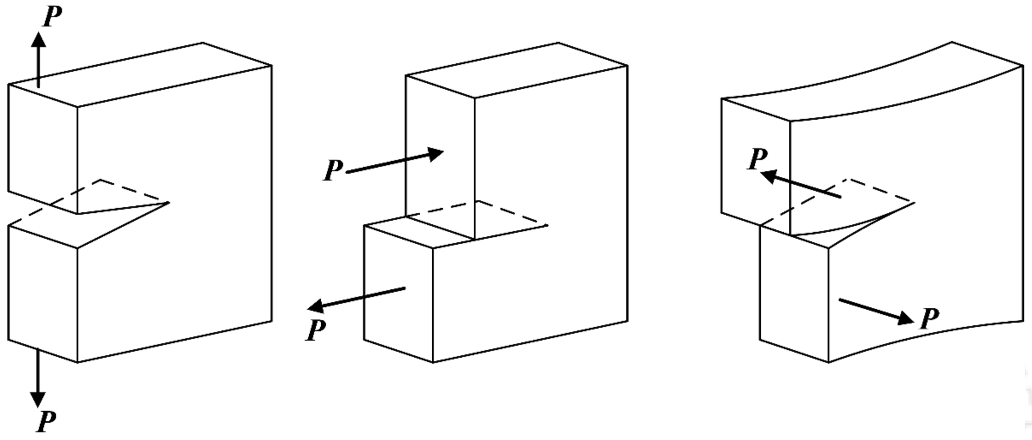

(a) opening mode (b) sliding mode (c) tearing mode

**Figure 1.7:** Different modes of fracture

- Opening mode or mode I – tensile stress normally acts to the plane of the crack and corresponding displacements are also normal to the plane of the crack.
- Sliding mode or mode II – In-pane shear stress acting parallel to the plane of the crack and perpendicular to the crack front. The relative displacement is normal to the crack front.
- Tearing or mode III – Out-of-plane shear stress acting parallel to the plane of the crack and perpendicular to the crack front. The displacements are parallel to the crack front.

A combination of any two or all three modes results in a mixed mode of fracture. *Linear elastic fracture mechanics* (LEFM) is based on the concept of small-scale yielding (SSY). In SSY, the plastic zone size ahead of the crack tip is very small compared to the crack length and other geometric parameters, and therefore constitutive relation of the material can be assumed to follow Hook's law. In LEFM, especially in composites, strain energy release rate (SERR) is extensively used as a parameter to estimate the prediction of the failure of composites. Hence, it is important to know the background of SERR.

*Strain energy release rate (G)*: In 1920, Griffith developed the theoretical relation between fracture stresses to crack size for brittle materials. Strain energy release rate is defined as the release of energy per unit area of crack extension and denoted by *G*. Griffith used the first law of thermodynamics to develop a fracture theory based on simple energy balance. Griffith's model accurately predicted the relation between fracture strength and flaw size in glass materials, but for metals, the concept failed. In 1957, Irwin modified Griffith's theory by including the energy during the plastic deformation with the strain energy primarily considered by Griffith in order to be applicable to both brittle and ductile materials. The amount of energy release rate at the moment of crack initiation is called critical SERR ($G_c$), which is independent of the geometry and material properties of the cracked component and shows resistance to crack growth.

## 1.3 Research motivation

Since ply break and impact induced delamination are extremely important and need to be addressed in analyzing a laminate subjected to loading, it is important to investigate the ways to improve the performance of a laminate in the presence of such laminate. Both ply break and embedded delamination propagate leading to the catastrophic failure of the laminate at a load level much below the strength of the laminate. Therefore, it is important to improve the interlaminar strength of such laminates to resist delamination initiation and propagation. These interlaminar strengths are matrix dominated properties and hence it is worth investigating whether modifying the matrix could lead to better resistance against such failure modes. This led to the motivation of this study where three phase carbon/(CNT+epoxy) composites have been studied to understand how modifying the matrix by addition of CNTs to epoxy in such composites actually influences the behavior of such laminates against resistance to such defects. Before undertaking this investigation, a detailed literature survey was planned to understand the state of the art in this broad area which would help defining the specific objectives of the present work and justify the relevance and is presented in the next chapter.

# CHAPTER 2

# Literature Review

In order to understand the potential of three phase CNT/polymer composites, extensive literature review has been performed and this chapter presents the works reported in the broad area of CNTs and three phase CNT/polymer composites in general and failure analysis of three phase CNT/polymer composites in particular. Based on this, research gaps have been identified, and specific objectives for the present thesis work have been presented.

For better understanding of the state of the art in this area, literatures have been categorized based on the nature of the work as shown in **Fig. 2.1** and presented in the different sections of this chapter.

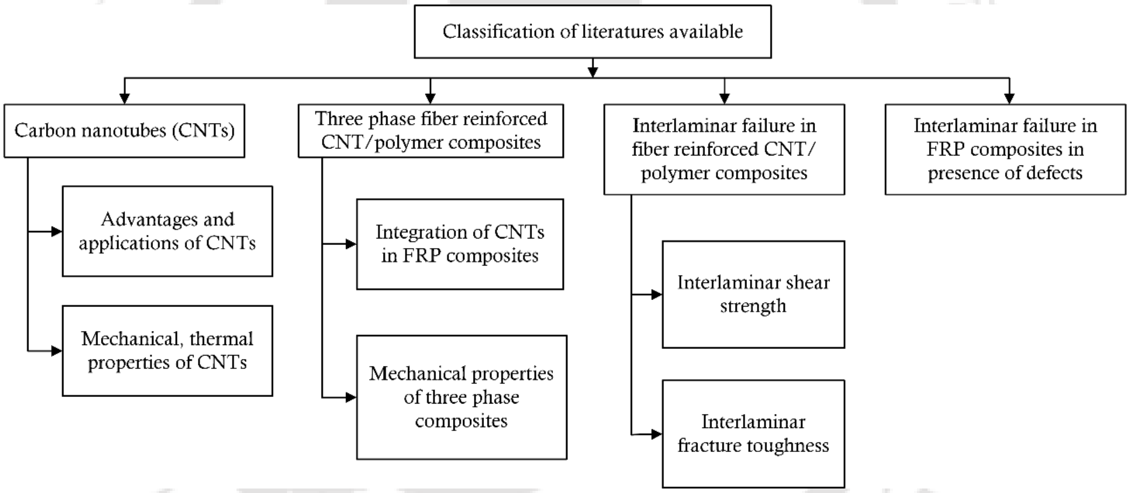

**Figure 2.1:** A flow chart showing the classification of available literatures

## 2.1 Carbon nanotubes

Iijima [4] used the arc discharge method in 1991 to develop a novel class of finite carbon structures made of needle like tubes. The discovery of carbon nanotubes led to research in different nanoscale areas. CNTs are classified as single-wall CNTs and multi-wall CNTs on the basis of the fabrication process and chiral, armchair, and zigzag on the basis of chirality. Dresselhaus et al. [16] have studied carbon nanotubes and presented the basic relations governing the geometry of carbon nanotubes. The authors defined the general CNTs in terms of the tube diameter and chiral angles.

CNTs can be made using the arc discharge method, laser ablation, chemical vapor deposition, and flame synthesis method. In synthesizing nanotubes, Bethune et al. [17] used thin electrodes with drilled holes as anodes filled with a combination of pure powdered metals (Fe, Ni, or Co) and graphite and Journet et al. [18] used this method to produce CNTs in larger quantities. Thess et al. [19] developed SWCNTs in yields larger than 70% by laser ablation of graphite rods with small concentrations of Ni and Co at 1,200°C. These two synthesis methods however have two major limitations, large-scale and ordered synthesis [20]. However, a chemical vapor deposition method was discovered in 1996 to synthesize nanotubes where, the reaction chamber is filled with a mixture of hydrocarbon gas, such as methane, acetylene, or ethylene, the hydrocarbon decomposes at temperatures between 700°C and 900°C and at atmospheric pressure and nanotubes are formed on the substrate [7]. In flame synthesis, hydrocarbon flames are used to initiate and grow CNTs and in order to deposit solid black carbon, catalysts must also provide reaction sites [21].

It has been reported in the literature that CNTs are very strong in the axial direction but weak in the radial direction [22]. They have high elastic modulus ranging from 270-950 GPa, and high tensile strength ranging from 11-63 GPa and it is reported that elastic modulus depends on the diameter of CNTs, and is independent of tube chirality [23]. In addition to their mechanical properties, CNTs have good thermal properties and isolated CNTs at high temperatures have approximately the same specific heat as a two dimensional (2D) graphene sheet [24]. Theoretical and experimental observations confirmed that thermal conductivity at room temperature varies from 1800-6000 W/mK [25]. Literature shows that CNTs have good conductive properties and the electronic properties of CNTs depend on the chirality, diameters, defects, and degree of crystallinity of the tubular structure [26]. Based on the chirality type, CNTs are classified as conductive and semi-conductive [27].

Most of the literature addressed the applications of carbon nanotubes in the areas of nanotechnology, actuators, capacitors, transistors, and membranes. Lu and Han [28] described the manufacturing, characterization, physical properties, and applications of CNTs and their composites. This review stated that in the future, nanotechnology could be one of the rising technologies that would play an important role in developing future space vehicles. Ibrahim [29] gave a detailed review of the properties, synthesis, applications, and functionalization of CNTs.

## 2.2 Three phase CNT/Polymer composites

Ajayan et al. [30] stated that even though there are constraints in optimizing the properties of composite polymers by adding conventional micrometer scale fillers. The filler content in polymer composites is usually 10 to 70 wt%, which leads to a higher density than that of the neat polymer matrix. In addition, microscopic defects and voids formation due to the high volume fraction of filler often lead to the failure of composites.

Compared to conventional polymer composites with microscale fillers, CNT/polymer composites are fabricated by incorporating nanoscale carbon nanotubes (CNTs) as an additive in a polymer resin. Ajayan et al. [31] made the first report on the preparation of CNT/polymer nanocomposites in 1994, and stated that CNT/polymer composites are finding potential applications in emerging areas due to their superior physical, mechanical and functional properties of CNTs are finding enormous potential applications of CNT/polymer composites. Du et al. [32] classified CNT/polymer composites into structural and functional composites based on the area of applications. In structural composites, improved mechanical properties of CNTs, such as high modulus, tensile strength, and strain to fracture are examined. Jojibabu et al. [33] provided a detailed review describing the works reported on epoxy based nanocomposites as adhesive materials and summarized the future research directions.

## 2.3 Integration of CNTs in FRP composites

The improvement in different properties of a composite with addition of CNTs majorly depends on how CNTs are added into three phase multiscale composites. The nanoscale CNTs are integrated with traditional microscale fiber reinforcements in a polymer matrix and can be obtained by modifying i) matrix resin or ii) the fiber reinforcement with CNTs or iii) interface with CNT-made buckypapers.

### 2.3.1 Matrix resin modification by dispersing CNTs in polymer

Matrix modification is considered the most direct and popular method for incorporating CNTs into FRP composites due to ease of preparation and operation [34]. When CNTs are added to epoxy, they act as a bridge between the resin and fiber interface, which transfers the stress effectively, prevents crack growth, and strengthens the matrix and interface. As a result, CNTs may significantly enhance the mechanical properties of the composite material. Many works reported on the techniques developed for the dispersion of CNTs into a polymer matrix. Generally, two methods are used for CNT dispersion: mechanical methods and a combination of mechanical dispersion and functionalization.

Several works described the mechanical dispersion methods of CNTs in epoxy resin, such as ultrasonication [35], calendaring [36], ball milling [37], shear mixing [38], and extrusion [39]. A brief detail of these methods are shown in **Table 2.1**. Many recent studies have used a combination of these techniques, such as ultrasonication plus extrusion by Isayev et al. [40], Moniruzzaman et al. [41], and ultrasonic plus ball milling by Ma et al. [42]. Jain et al. [43]

dispersed CNTs in resin matrix by sonication and fabricated multiscale carbon fiber epoxy composite by vacuum assisted resin infusion molding (VARIM).

**Table 2.1:** Comparison of different methods of CNT dispersion in nanocomposites

| Method | Damage to CNTs | Polymer matrix | Controlling parameters | Remarks |
|---|---|---|---|---|
| **Ultrasonication [35]** | Yes | Oligomer or low viscous polymer, monomer, soluble polymer | Sonication duration, mode, and power of sonicator | Operation is easy; cleaning is easy after use; commonly used in laboratories |
| **Calendering [36]** | No | Monomer, oligomer or liquid polymer | Distance between two rollers, roller speed | Training is required for operation; cleaning is difficult after use |
| **Ball Milling [37]** | Yes | Powder | Size of balls, milling time, balls/CNT ratio, rotation speed | Operation is easy; cleaning is required after use |
| **Shear mixing [38]** | Yes | Oligomer or low viscous polymer, monomer, soluble polymer | Viscosity of the liquid, mixing time and speed, size and shape of the propeller | Operation is easy; cleaning is easy after use; commonly used in laboratories |
| **Extrusion [39]** | Yes | Thermoplastics | Rotation speed of screw, configuration, temperature | Training is required for operation; cleaning is difficult after use; large-scale production |

CNTs are difficult to dissolve or disperse in volatile organic solvents or polymeric matrices. The dispersion of CNTs is not just dependent on the geometrical parameters of the CNTs; rather, it requires a method that separates and stabilizes individual CNTs from highly entangled and agglomerated CNTs in a polymer matrix to prevent further agglomeration [44]. As a result, chemical modification of the side walls of the surfaces of CNTs called functionalization is required to increase their solubility or dispersion in solvents or polymers as well as their interaction and reactivity with polymers [45].

Different functionalization methods include mechano-chemical [46], electro-chemical [47], chemical [48], and plasma [49] in nature. Out of these methods chemical functionalization is the most commonly used in which strong acids are used to shorten the length and remove end caps of CNTs. In addition, oxide groups such as carbonyl, hydroxyl, and carboxylic acids are added to the ends to find the defect sites of CNTs. Pristine and functionalized MWCNTs have been used by Qiu et al. [11] to prepare multiscale glass fiber reinforced epoxy composites with the help of an infiltration based vacuum assisted resin transfer molding (VARTM) process where multi-walled carbon nanotubes (MWNTs) were infused through and between glass fiber tows along through the thickness direction. Sadeghian et al. [50] reported that surface treated CNF/resin matrix showed uniform dispersion in resin matrix compared with untreated CNF/resin matrix. Experiments have been conducted to understand the influence of CNF concentration on CNF filtration, micro-void formation, and resin viscosity and results reveal that CNFs with more than 1wt% lead to a filtering effect and formation of micro-voids in the composite. Gojny et al. [51] reported that functionalization reduced agglomeration and improved interaction between the CNTs and the epoxy resin. Vaisman et al. [52] used a noncovalent method in which a few surfactants physically coat CNTs to improve the dispersion of CNTs in epoxy resin. However, CNTs treated with different surfactants may reduce the contact between CNTs, leading to a decrease in the conductive properties of CNT/polymer composites.

### 2.3.2 Addition of CNTs on reinforcing fibers

Other than the traditional techniques to disperse the CNTs into the resin matrix, there are some methods to fabricate advanced FRPs such as grafting, attachment, or growth of CNTs on reinforcing fibers or fabrics. Bekyarova et al. [53] deposited CNTs on the surface of a carbon woven fabric using an electrophoretic deposition (EPD) process. The carbon fiber/CNT preforms have been infiltrated with epoxy resin using VARTM and confirm that there is an improvement in electrical properties and out-of-plane mechanical properties of the multiscale hybrid composites. Warrier et al. [54] incorporated carbon nanotubes in glass fiber epoxy composites by adding CNTs in the fiber sizing formulation, in the matrix, or in both leading to an increase of 10% in glass transition temperature and a significant reduction of 31% in the coefficient of thermal expansion of the composites. Khan et al. [55] grafted CNTs by a chemical vapor deposition (CVD) process on the surface of carbon fabric in two different cases and reported that CNT grafting leads to improvement in mechanical properties. Awan et al. [56] deposited MWCNTs on carbon fibers using various methods such as hand layup, dip coating, EPD, and spray up and reported that the EPD method had achieved uniform dispersion in comparison with other methods. Xiao et al. [57] deposited MWCNTs on the T300 carbon fibers to make carbon/epoxy laminated composites using the aqueous suspension deposition method and reported significant improvement in the mechanical properties. Functionalized CNTs were grown by Yao et al. [58] on the surface of the carbon fiber fabric by CVD at different temperatures and the experimental results showed that ILSS has been improved compared with neat carbon fiber fabric composites.

CNT forests were grown by Veedu et al. [59] at the interface of multilayer three dimensional (3D) composite in order to improve the multifunctional properties along the thickness direction. De Resende et al. [60] used the CVD process to grow aligned multi-walled CNT forests on carbon fibers with an amorphous Si interface and the results confirm that mechanical, electrical, and thermal properties of the interface of the composite can be modified by using this method. Falzon et al. [61] grown aligned multi-walled CNTs forests on a silicon substrate with the help of the CVD process and after that CNT forests were transferred to a pre-impregnated carbon epoxy composite. The fracture test results revealed that through-the-thickness fracture toughness has been improved by the growth of CNT forests.

### 2.3.3 Addition of CNT interleaves or CNT buckypaper at the interface

Interleaving is one of the traditional methods in which a thin layer of material is incorporated at the interface of FRP composite laminates to improve multi-functional properties. Sun et al. [62] implemented an epoxy/CNT thin film approach to place CNTs at different locations inside a VARTM composite offering low cost, improvement in quality, and viscosity-related issues have been minimized. Bilge et al. [63] used an electrospinning process to get MWCNT interlayers on carbo/epoxy neat prepreg surfaces and confirmed that the mechanical properties of the laminate were enhanced significantly. Zheng et al. [64] fabricated carbon nanotubes/polysulfone nanofiber (CNTs/PSF) paper using the vacuum filtration method to improve the interlaminar properties of carbon epoxy composite laminates. Xin et al. [65] used MWCNT sheets for interleaving in cross-ply carbon fiber epoxy composite laminate and their experimental results confirm that impact properties, interlaminar properties, and flexural properties are enhanced by the interleaving of MWCNT sheets. Ou et al. [66] studied the influence of CNT veil interleave thickness on the interlaminar properties of CFRP woven composite laminates and reported that the thickness of the CNT veil had a significant effect on the interlaminar properties

Buckypaper (BP) is known as carbon nanotube paper or carbon nanotube film first developed in 1998. Liu et al. [67] reported different methods to prepare BP and BP composites, and their wide range of applications. Organic polymer solutions such as polystyrene, polyvinyl alcohol, and polyvinyl pyrrolidone were introduced into single-wall CNT sheets by Coleman et al. [68] and results show that mechanical properties such as strength, elastic modulus, and toughness were enhanced by 3, 9, and 38 times respectively. Liu and Shen [69] introduced CNT buckypaper in the middle interface of a carbon/epoxy laminate using a positive pressure filtration method and the experimental results confirm that interlaminar properties were enhanced with CNT buckypaper. Shin and Kim [70] used CNT buckypaper as interleaves in CFRP composite laminate and the results from the experiments show an improvement in interlaminar fracture toughness.

## 2.4 Mechanical properties of three phase CNT/polymer composites

Multi-scale CFRP composite laminates were prepared by mixing CNTs in epoxy resin using VARIM and tensile test results show an improvement of 17% in ultimate tensile strength with 0.3 wt% of CNTs [42]. Qiu et al. [11] conducted tensile tests on glass/MWCNT-epoxy composites and reported that with 1% MWCNT loading, tensile strength and Young's modulus are increased by 14% and 20% respectively, in comparison with glass fiber reinforced composites. Andrews et al. [71] fabricated carbon fiber/CNT-resin composite by dispersing MWCNTs in isotropic petroleum pitch matrix and their experimental results confirm that, with an addition of 5 wt% CNT, tensile strength, Young's modulus, and electrical conductivity were enhanced by 90%, 150%, and 340% respectively. Sanchez et al. [72] fabricated carbon fiber composites using vacuum assisted resin infusion molding (VARIM), where the matrix is modified by CNTs with different contents (0.1, 0.2, and 0.3 wt%) and for different surface conditions (non-functionalized and amino-functionalized). Tensile tests and flexural tests reported that the addition of amino-functionalized CNTs in epoxy resin improves mechanical properties such as tensile strength and flexural strength. Sharma and Shukla [73] fabricated carbon/CNT/epoxy three phase composites by adding different weight percentages of MWCNTs such as 0%, 0.25%, 0.5%, 1%, and 1.5% in epoxy. By conducting tensile tests and flexural tests, results confirmed that mechanical properties of three phase composite increase up to 1% MWCNT and beyond that decreases, and mixing 1% MWCNTs in resin matrix leads to an increase in Young's modulus, tensile strength, and flexural strength by 49%, 52%, and 37% respectively. In their work, Halpin-Tsai model along with the principle of micromechanics were used for computing the mechanical properties of three phase fiber reinforced CNT+epoxy composites.

Islam et al. [74] used three roll shear mixtures to disperse 0.3 wt% MWCNTs in epoxy to prepare a three phase carbon/MWCNT-epoxy composite. Three-point bending tests have been conducted and results confirm that the addition of MWCNTs leads to an increase in flexural strength and flexural modulus by 19% and 15% respectively. Sheth et al. [75] fabricated three phase CNT/CF/epoxy by adding 0.5%, 1%, 1.5%, and 2% weight percentages of CNTs in epoxy. Experimental results show that tensile strength and flexural strength were increased by 10% and 13% respectively up to 1 wt% of CNT and beyond that, the strength decreases. Khan et al. [76] dispersed MWCNTs in an epoxy resin and studied the alignment of MWCNTs originating from the application of a direct current (DC) electric field during composite curing.

Dynamic mechanical analysis (DMA) has been performed and results reported that, at 0.3 wt% CNT alignment, elastic modulus, and fracture toughness were increased by 40% and 50% respectively, and beyond 0.3 wt% mechanical properties decreased.

Awan et al. [56] fabricated three phase CF/MWCNT-epoxy composites by coating MWCNTs on the carbon fibers using electrophoretic deposition (EPD) method. It has been observed by conducting flexural tests that, due to MWCNTs coating, the flexural strength and flexural modulus were increased by 41% and 16% respectively in comparison with CF/epoxy composites. Xiao et al. [57] deposited MWCNTs on T300-grade carbon fibers by the aqueous deposition method. With the deposition of 0.1% MWCNTs, by conducting tensile tests and flexural tests, results reported that tensile strength and flexural strength were increased by 15% and 17% respectively. Gong et al. [77] integrated CNTs in resin to understand their effect on the mechanical properties of three phase CNT/polymer composites. Addition of 1 wt% CNTs with surfactants led to an increase in glass transition temperature and elastic modulus by 40% and 30% respectively. Whereas, the addition of CNTs without the surfactants has a moderate effect on mechanical properties and on the glass transition temperature. Allaoui et al. [78] integrated MWCNTs of 1 wt% and 4 wt% into epoxy resin by chemical vapor deposition method (CVD). Experimental results show that, for both weight percentages, yield strength and Young's modulus were increased by two times and four times respectively in comparison with those for neat epoxy. Kumar et al. [79] fabricated polypropylene/nano carbon fiber composites with conventional melt spinning equipment and tensile and compressive tests reported that, at 5 wt% nano carbon fiber loading, elastic modulus, and compressive strength are increased by 50% and 100%. Kanagaraj et al. [80] coated CNTs with different volume fractions (0, 0.11, 0.22, 0.33, and 0.44) on high-density polyethylene (HDPE) pallets. Tensile tests were conducted and results confirm that, with the addition of CNTs, mechanical properties such as Young's modulus, ultimate strength, and strain at fracture increased by 22%, 4%, and 24% respectively, in comparison with no addition of CNTs.

Single-wall CNT sheets were soaked in polymers and tensile tests on intercalated sheets confirmed a 3, 9, and 38 times improvement in strength, elastic modulus, and toughness respectively, which shows that the load transmission among CNTs enhanced with intercalated polymer [68]. Polystyrene-co-glycidyl methacrylate P(St-co-GMA)/MWCNT interlayers have been introduced on the surfaces of carbon/epoxy prepreg using an electrospinning process and flexural test results confirming that flexural strength and flexural modulus were enhanced by 25% and 29% respectively with interlayer addition [63]. A carbon nanotubes/polysulfone nanofiber (CNTs/PSF) paper has been used as an interleaf at the interface of carbon epoxy composite laminates and experimental results confirm that flexural strength and flexural modulus were substantially increased by 27% and 29% respectively with interleafs [64]. **Table 2.2** shows a summary of published literature on the mechanical properties of CNT-FRP composites.

**Table 2.2:** Mechanical properties of multiscale CNT-FRP composites

| **Fiber/matrix** | **CNTs Type** | **CNT integration method** | **% increase in tensile properties (CNT wt%)** | | **% increase in flexural properties (CNT wt%)** | |
|---|---|---|---|---|---|---|
| | | | **Tensile Strength** | **Tensile Modulus** | **Flexural Strength** | **Flexural Modulus** |
| Glass/epoxy [11] | MWCNT | Entire matrix | 14% (1) | 20% (1) | - | - |
| Carbon/epoxy [42] | MWCNT | Entire matrix | 17% (0.3) | - | - | - |
| Carbon/Petrol [73] | SWCNT | Entire matrix | 90% (5) | 150% (5) | - | - |
| Carbon/epoxy [75] | MWCNT | Entire matrix | 52% (1) | 49% (1) | 37% (1) | - |
| Carbon/epoxy [76] | MWCNT | Entire matrix | - | - | 19% (0.3) | 15% (0.3) |
| Carbon/epoxy [77] | MWCNT | Entire matrix | 10% (1) | - | 13% (1) | - |
| Carbon/epoxy [58] | MWCNT | Electrophoresis | - | - | 41% | 16% |
| Carbon/epoxy [59] | MWCNT | Coating on fibers | 15% (0.1) | - | 17% (0.1) | - |
| Carbon/epoxy [70] | SWCNT | Interleaves | 3X | 9X | - | - |
| Carbon/epoxy [65] | MWCNT | Interlayer | - | - | 25% | 29% |
| Carbon/epoxy [66] | MWCNT | Interleaves | - | - | 27% | 29% |

CNT: carbon nanotube, MWCNT: multi-walled CNT, SWCNT: single-walled CNT.

## 2.5 Interlaminar failure in fiber reinforced CNT/polymer composites

In FRP composite laminates, interlaminar failure commonly occurs due to weak fiber matrix interfacial bonds. This might lead to delamination at the interface, which results in strength and stiffness degradation, leading to catastrophic failure of the whole structure. The fracture resistance of fiber reinforced composite to various modes of crack propagation determines its structural performance. Since one of the most important design requirements for FRPs in structural applications is their ability to absorb enough fracture energy, it is therefore important to enhance the ILSS and fracture toughness of FRP composite laminates by incorporating nanofillers such as CNTs and CNFs. A large number of works have reported the influence of CNTs on ILSS and fracture toughness and are discussed in this section.

### 2.5.1 Interlaminar shear strength (ILSS)

Qiu et al. [11] reported an infusion-based VARTM technique in which nanocomposites containing a strong acid-a mixture of nitric and sulphuric acid-functionalized MWCNTs and epoxy resin were infused into glass fabrics in the thickness direction. Short beam tests results showed that, with only 1 wt% CNT loading, the ILSS of the multiscale composites enhanced by 8%. As reported in [43] an improvement of 28% in ILSS has been observed by dispersing 0.3 wt% of CNTs in resin of multiscale CFRP composite laminate. Evaluation of the modulus gradient across the interface showed that the addition of the nanofiller improved the stability of the interface. Gojny et al. [81] fabricated multiscale glass/CNT-epoxy by resin transfer molding (RTM) technique and their experimental results confirm that with the addition of 0.3 wt% amino-functionalized double-walled carbon nanotubes (DWCNTs), ILSS enhanced by 20%. A similar observation was reported by Wichmann et al. [82] confirmed that the ILSS of GFRPs was increased by 16% by modifying the matrix with 0.3 wt% of DWCNTs. Godara et al. [83] fabricated multiscale CFRPs by mixing various types of CNTs in resin matrix. Short beam tests were conducted and results showed that all composites containing 0.5 wt% CNTs had a clear reduction in ILSS, regardless of whether they were pristine, small, or amino-functionalized. Unidirectional CFRP composite laminates were fabricated by dispersing MWCNTs in epoxy resin and experimental results show an improvement of 77% in ILSS with 0.5 wt% of MWCNTs [84].

Bekyarova et al. [53] conducted experiments to show that composites containing 0.25 wt% MWCNTs leads to 27% increase in ILSS without affecting the in-plain mechanical properties including tensile strength and modulus. Khan et al. [55] made multiscale carbon/epoxy composites (i) by coating only the top surface of the fabric with CNTs (type-1) and (ii) by coating both surfaces of the fabric with CNTs (type-2). Experimental results show an enhancement in ILSS of type 1 and type 2 composite laminates by 32% and 102%, respectively. A 12.6% enhancement in ILSS has been observed by the deposition of 0.1 wt% of MWCNTs on the carbon fibers to fabricate carbon/epoxy composites. The mechanisms for interface enhancement are resin toughening and interfacial properties [57]. Sharma and Lakkad [85] prepared multiscale carbon/epoxy composites by growing MWCNTs on surface-treated carbon fibers using the CVD process. Experimental results reported that CNTs growth on CF leads to a 35% increase in ILSS Khan and Kim [86] studied the influence of buckypaper interleaves made from carbon nanofiber (CNF) on the mechanical properties of carbon fiber reinforced epoxy composites (CFRPs). Experimental results show that, with the addition of 10 wt% CNF buckypaper interleaves, ILLS is enhanced by 31%.

**Table 2.3** shows a summary of published literature on interlaminar shear strength of CNT-FRP multiscale composites. Wu et al. [87] fabricated hybrid carbon fiber reinforced composites by in situ deposition of a multi-walled carbon nanotube bukcypaper (i-MBP) on the surface of functionalized CF fabric (PCF). Short beam shear (SBS) test results reported that the ILSS increased by 68.6% for i-MBP-PCF hybrid fiber mat in comparison with the CF/EP composite. By scanning electron microscopy (SEM) analysis and nanoindentation tests, it has been observed that the mechanical properties enhanced due to in situ deposition of i-MBP on the PCF fabric, which not only increases the strength of the epoxy but also improves the interfacial adhesion between the fiber and epoxy resin.

**Table 2.3:** ILSS of multiscale CNT-FRP composites

| Fiber/matrix | CNTs Type | CNT integration method | % increase in ILSS (CNT wt%) |
|---|---|---|---|
| Glass/epoxy [11] | MWCNT | Entire matrix | 8% (1) |
| Carbon/epoxy [43] | MWCNT | Entire matrix | 28% (0.3) |
| Glass/epoxy [81] | DWCNT | Entire matrix | 20% (0.3) |
| Glass/epoxy [82] | DWCNT | Entire matrix | 16% (0.3) |
| Carbon/epoxy [84] | MWCNT | Entire matrix | 77% (0.5) |
| Carbon/epoxy [53] | MWCNT | Electrophoresis | 27% (0.25) |
| Carbon/epoxy [55] | MWCNT | Surface coating | 32% (Type1), 102% (Type2) |
| Carbon/epoxy [57] | MWCNT | Coating on fibers | 12.6% (0.1) |
| Carbon/epoxy [85] | MWCNT | Grown on fibers | 35% |
| Carbon/epoxy [86] | CNF | Buckypaper | 27% |
| Carbon/epoxy [87] | MWCNT | Buckypaper | 68.6% |

ILSS: interlaminar shear strength, CNT: carbon nanotube, MWCNT: multi-walled CNT, SWCNT: single-walled CNT, DWCNT: double-walled CNTs, CNF: carbon nanofiber.

## 2.5.2 Interlaminar fracture toughness

A large number of works have reported the influence of CNTs on mode I and mode II interlaminar fracture toughness of three phase fiber-CNT composites. Yokozeki et al. [88] prepared multiscale CFRP composites by mixing cup-stacked CNTs in resin matrix. Double cantilever beam (DCB) and end notch flexure (ENF) tests were conducted and results confirmed that with the addition of 5 wt% cup-stacked CNTs, mode I fracture toughness $(G_{Ic})$ and mode II interlaminar fracture toughness $(G_{IIc})$ of CFRP composites enhanced by 98% and

30% respectively. In a similar study, Karapappas et al. [89] fabricated hybrid unidirectional CFRP composites by integrating the MWCNTs into the epoxy resin. Experimental results show that with addition of 1 wt% and 0.5 wt% of CNTs, $G_{Ic}$ and $G_{IIc}$ enhanced by 60% and 75% respectively. Romhany et al. [90] fabricated a 10-ply unidirectional multiscale CFRP laminate by the dispersion of MWCNTs in epoxy resin using three-roll milling. DCB tests were conducted for mechanical characterization and experimental results confirmed that with the addition of 0.3 wt% non-functionalized MWCNTs, average $G_{Ic}$ enhanced by 13% compared with neat specimens.

Almuhammadi et al. [91] prepared an MWCNTs-liquid solution and sprayed it onto 16-ply unidirectional CFRP laminates and results confirmed that the addition of 0.5 wt% COOH-MWCNTs led to a 17% increase in mode I fracture toughness. Borowski et al. [92] fabricated CFRP composite specimens by modifying the matrix with carboxyl-functionalized MWCNTs. Experimental results of the DCB tests indicate an enhancement of 25%, 20%, and 17% in $G_{Ic}$ for 0.5 wt%, 1 wt%, and 1.5 wt% respectively. FE simulations were performed and are in good agreement with experimental results. Quan et al. [93] fabricated CFRP composite laminate by adding MWCNTs in epoxy resin. Double cantilever beam (DCB) and end-loaded split (ELS) tests were conducted and results confirm that $G_{Ic}$ increased by 8% and 25% for 0.5% and 1% MWCNTs respectively, and the average $G_{IIc}$ increased by 68% and 171% for 0.5% and 1% MWCNTs respectively. Troung and Choi [94] added COOH-functionalized short MWCNTs (S-MWCNT-COOH) in epoxy resin of woven CFRP composite laminates. Mode I tests have been conducted and results confirmed that with the addition of 0.5 wt%, 1 wt%, and 1.5 wt% S-MWCNT-COOH, $G_{Ic}$ has been enhanced by 1.6%, 31%, and 31.7% respectively.

Sadeghian et al. [50] integrated the surface-treated carbon nanofibers (CNFs) in polyester resin and then the CNF-resin mixture was injected to impregnate a glass fiber preform using vacuum-assisted resin transfer molding. DCB tests confirmed that mode I critical strain energy release rate ($G_{IC}$) increased by 100% by adding 1 wt% CNFs. In a similar study, Tsantzalis et al. [95] prepared hybrid CFRP laminates by doping with CNFs and/or piezoelectric (PZT) particles. Mode I tests reported that addition of 1 wt% CNFs to resin matrix leads to a 100% increase in interlaminar fracture energy.

Nanofillers were directly grown on the surface of the main reinforcement which leads to improvement in various properties of FRP composites. For example, Veedu et al. [59] showed improvement in hardness, delamination resistance, in-plane mechanical properties, and damping capability by growing CNTs on the surface of silicon carbide (SiC) cloth plies. In addition, $G_{Ic}$ and $G_{IIc}$ enhanced by 348% and 54% respectively for 2 wt% of MWCNTs without compromising the in-plane mechanical properties. In a similar study, Wicks et al. [96] used a modified thermal chemical vapor deposition method (CVD) to grow CNTs directly on the surface of the alumina woven cloth. Experimental results confirmed that with the direct growth of CNTs, both initiation and steady state fracture toughness increased by 67% and 76% respectively. Davis et al. [97] prepared multiscale 20-ply CFRP laminates by depositing the fluorine-functionalized carbon nanotubes (f-CNTs) onto the carbon fabric with the help of the H-VARTM method. The four-point ENF tests reported that average initiation and propagation fracture toughness increased by 23% and 27% respectively, in specimens containing 0.5 wt% f-CNTs. It was observed from the fracture surfaces of the specimens, the functionalization of CNTs binds the fiber and epoxy resin, which makes the toughened fiber matrix interface strengths to get improved through thickness mechanical properties. Multi-walled CNTs forests were introduced in a pre-impregnated carbon epoxy composite by the CVD process and conducted DCB and four-point bending tests and results show an improvement of 61% in $G_{Ic}$ , and 161% in $G_{IIc}$ respectively [61]. Naito and Nagai [98] made carbon fiber reinforced polymer composite laminates by directly applying MWCNTs with different vol% (1, 3, 5, and 7) to the interface in the dry state. DCB and ENF tests were conducted and the results show that for 1% MWCNTs, $G_{Ic}$ and $G_{IIc}$ were increased in comparison with the neat specimen, but further increase in vol% of MWCNTs leads to the reduction in both fracture toughnesses.

Li et al. [99] manually distributed the vapor-grown carbon fiber (VGCF) nanofiller at the mid-plane of unidirectional laminates in order to prepare hybrid CFRP/VGCF laminate. Experimental results confirmed that the addition of VGCF interlayer at the mid-plane leads to a significant increase in mode I delamination resistance. Arai et al. [100] fabricated unidirectional CFRP/CNF hybrid laminates by inserting the carbon nanofiber reinforcement between the middle layer of the prepregs. By conducting DCB and ENF tests, it was observed that $G_{Ic}$ and $G_{IIc}$ increased by 1.5 times and 2 times respectively in comparison with neat composites. Khan and Kim [86] incorporated the partially cured CNF-epoxy buckypaper interleaf at the mid-plane of CFRP laminates improved $G_{IIc}$ by 104%. Mode II fracture toughness tests were conducted on carbon/epoxy prepreg composite laminates and the results confirmed that $G_{IIc}$ was enhanced by 70% with P(St-co-GMA)/MWCNT interlayer [63]. A CNTs/PSF has been used as an interleaf in carbon epoxy composite laminates. Double cantilever beam (DCB) and end notch flexure (ENF) tests have been conducted and results confirm that $G_{Ic}$ for 5% and 10% CNTs/PSF interleaves have been improved by 41% and 53% respectively than that of neat resin, and $G_{IIc}$ for 5% and 10% CNTs/PSF interleaves have been improved by 25% and 34% respectively than that of neat resin [64].

**Table 2.4:** Mode I ( $G_{Ic}$ ) and mode II ( $G_{IIc}$ ) interlaminar fracture toughness of multiscale CNT-FRP composites

| **Fiber/matrix** | **CNTs Type** | **CNT integration method** | **% increase in $G_{Ic}$ (CNT wt%)** | **% increase in $G_{IIc}$ (CNT wt%)** |
|---|---|---|---|---|
| Carbon/epoxy [88] | CSCNT | Entire matrix | 98% (5) | 30% (5) |
| Carbon/epoxy [89] | MWCNT | Entire matrix | 60% (1) | 75% (0.5) |
| Carbon/epoxy [90] | MWCNT | Entire matrix | 13% (0.3) | - |
| Carbon/epoxy [91] | MWCNT | Entire matrix | 17% (0.5) | - |
| Carbon/epoxy [92] | MWCNT | Entire matrix | 25% (0.5), 20% (1), 17% (1.5) | - |
| Carbon/epoxy [93] | MWCNT | Entire matrix | 8% (0.5), 25% (1) | 68% (0.5), 171% (1) |
| Carbon/epoxy [94] | SMWCNT | Entire matrix | 1.6% (0.5), 31% (1), 31.7% (1.5) | - |
| Glass/polyester [50] | CNF | Entire matrix | 100% (1) | - |
| Carbon/epoxy [95] | CNF | Entire matrix | 100% (1) | - |
| SiC/epoxy [59] | MWCNT | Grown on fibers | 348% (2) | 54% (2) |
| Alumina/epoxy [96] | MWCNT | Grown on fibers | 67% ( $G_{Ic}$ onset)<br>76% ( $G_{Ic}$ prop) | - |
| Carbon/epoxy [97] | MWCNT | Grown on fibers | - | 23% (0.5) ( $G_{IIc}$ onset)<br>27% (0.5) ( $G_{IIc}$ prop) |
| Carbon/epoxy [61] | MWCNT | Grown on fibers | 61% | 161% |
| Carbon/epoxy [100] | CNF | Interlayer | 1.5X | 2X |
| Carbon/epoxy [86] | CNF | Buckypaper | - | 104% |
| Carbon/epoxy [63] | MWCNT | Interlayer | - | 70% |
| Carbon/epoxy [64] | CNT/PSF | Interleaf | 41% (5), 53% (10) | 25% (5), 34% (10) |
| Glass/vinyl ester [101] | MWCNT | Entire matrix | 0% (0.1) ( $G_{Ic}$ onset)<br>-40% (0.1) ( $G_{Ic}$ prop) | 8% (0.1) |
| Glass/epoxy [54] | MWCNT | Fiber sizing | 10% (0.5) ( $G_{Ic}$ onset)<br>-53% (0.5) ( $G_{Ic}$ prop) | - |
| Carbon/epoxy [102] | SWCNT | Entire matrix | -46% (0.5) | 35% (0.5) |

CNT: carbon nanotube, CSCNT: cup-stacked CNT, MWCNT: multi-walled CNT, SMWCNT: short MWCNT, SWCNT: single-walled CNT, SiC: silicon carbide, PSF: polysulfone, CNF: carbon nanofiber

Despite the moderate to large enhancements in interlaminar fracture toughness that have been mentioned above as a result of CNT integration in FRP composites, a few adverse effects have also been reported. For example, Seyhan et al. [101] fabricated hybrid glass fiber reinforced polymer (GFRP) composites by dispersing 0.1 wt% amino-functionalized MWCNTs in resin using the VARTM process. Experimental results reported that the CNT reinforcement had no beneficial impact on mode I initiation fracture toughness, but it had a negative effect on propagation fracture toughness, which was reduced by nearly 40%. It was expected that the presence of CNTs restrained fiber bridging. However, other interlaminar properties, such as $G_{IIc}$ (by 8%) and the ILSS (by 9%) were improved. The CNT content of 0.1 wt% appears to be too low to draw any conclusion about the underlying mechanisms that can determine the interlaminar properties described above. In a similar study, Warrier et al. [54] integrated 0.5% MWCNTs into glass fiber composites by fiber sizing formulation. Experimental results showed that $G_{Ic}$ increased by 10% due to CNTs in the sizing, but propagation fracture toughness was reduced by 53%. They reported that the adverse effects on crack propagation fracture toughness were caused by the bundling of glass fibers during the fiber sizing process, thereby reducing the chance for crack bridging by the individual glass fibers. Burkov and Eremin [102] fabricated unidirectional CFRP composite laminates by modifying the resin with SWCNTs in the range of 0.1-0.5 wt%. DCB and ENF tests were conducted and the results confirm that with the addition of SWCNTs, $G_{Ic}$ has a negative effect due to the brittle tensile behavior of SWCNT-epoxy and $G_{IIc}$ has been increased by 35%. **Table 2.4** shows a summary of published literature on the mode I and mode II interlaminar fracture toughness of CNT-FRP composites.

Wicks et al. [96], Blanco et al. [103] and Tong et al. [104] developed various theoretical models to predict mode I interlaminar fracture toughness of FRP hybrid composites consisting of CNT reinforcements. These include mechanistic models based on molecular dynamics and closed-form analytical models based on energy approach. These theoretical studies show that increasing the length, density, volume fraction, and interfacial shear strength of CNT-fiber multiscale composites will result in higher mode I interlaminar fracture toughness.

## 2.6 Interlaminar failure in FRP composites in presence of defects

There has been a good number of works reported in analyzing the FRP composites having defects like ply break and interfacial delaminations. Wisnom [105] fabricated unidirectional GFRP composites with central plies cut normal to fiber direction across the full width. By conducting tensile tests, the fracture energy of specimens with 8 cut 32 continuous plies was observed to have increased by 69% compared to specimens with 1 cut and 4 continuous plies. In a similar study, Tian and Swanson [106] studied the effect of internal fiber breakage (or buried crack) on the tensile strength of carbon/epoxy composites. The residual strength of laminate was observed to have decreased due to internal fiber cuts. Finite element results showed that, as the tension load increases, induced delamination propagates in pure mode II only. In addition, this study confirmed that the principal load-carrying ply criterion can be used to predict the residual strength of laminates consisting of internal cut fibers. Darby et al. [107] used the shear-lag model to calculate the stress distribution around the ply break in a single carbon fiber under tension. Theoretical results revealed that the presence of discontinuous plies decreases the mean failure stress in continuous plies by 15% as compared to specimens without defects, regardless of the number of discontinuous plies.

Wisnom [108] prepared tapered specimens of unidirectional glass epoxy with dropped plies and also studied the induced delamination with the help of tension tests and finite element analysis and experimental results also showed that, due to the discontinuity caused by the cut, untapered specimens with cut plies have high interlaminar stresses. However, delamination does not occur until the strain energy release rate is high sufficient to drive delamination. Chakraborty and Pradhan [109] carried out a 3D FE analysis in order to determine the delamination initiation stress and critical strain energy release rate of unidirectional glass/epoxy and graphite epoxy laminates having one or more central ply/plies broken. Numerical results showed that only mode II delamination occurs when the unidirectional laminate is subjected to uniaxial loading.

Many researchers investigated impact induced delamination in fiber reinforced composite laminates and it has been identified that in low velocity impact, delamination is the major damage mode and interlaminar strength can be determined by the relationship between delamination and loading. Hong and Liu [110] fabricated thin glass/epoxy composite plates and they were subjected to low velocity impact. Experimental results confirmed that in low velocity impact, the delamination area per unit impact energy is similar to the critical strain energy release rate. As a result, analysis of strain energy release rates along the delamination front can help to describe interlaminar fracture in composite laminates. In a similar study, Liu and Malvern [111] observed that in addition to delamination, matrix cracking and fiber breakage were the other type of failure in fiber reinforced composites under low velocity impact. Experimental results confirmed that impact induced delamination can also occur in quasi-static central loading. As a result, static analysis has been employed by Hong [112] to investigate the relationship between interlaminar stresses and the onset of delamination. It was found that stacking sequence, fiber orientation, and laminate thickness had a great influence on delamination resistance.

Lu and Liu [113] performed a 3D FE analysis by introducing penny-shaped delamination at the center of the composite laminates which was considered to have a very low modulus to prevent penetration between delaminated surfaces due to central loading. Strain energy release rate components were calculated along the delamination front. Numerical results revealed that interlaminar normal stresses were negative thereby mode I failure is absent in central loading and mode II failure is dominant compared with mode III. They also observed that the strain energy release rate along the delamination front is different in different directions due to the anisotropy of the composite laminae. Hence, the initiation of central delamination is not self-similar and it is considered that this can lead to anisotropic delamination. In a similar study, Mukherjee et al. [114] developed a 3D finite element model to calculate delamination initiation stress and strain energy release rates around a delamination of glass epoxy layered composite. Experiments were conducted in order to understand delamination growth between the layered composite and it has been observed that the preliminary results of the experiments and numerical simulations are in good agreement.

Yashiro and Ogi [115] studied the effect of initially cut fibers (slits) on the fracture behavior of cross ply CFRP composite laminates with alternate or identical slit angle $\pm\theta$ in the $0^{\circ}$ plies. Experiments were conducted to understand damage near the slit in detail, and numerically estimated the damage progress by damage analysis with cohesive elements and a damage law. The predicted damage extension to the final failure agreed with the observations. Wisnom [116] performed open-hole tension and over-height compact tension tests with constant plane dimensions in order to understand the failure of FRP composites due to delamination. Experimental results demonstrated that when ply block thickness increases, the failure mechanism shifts from fiber-dominated fracture to complete delamination. Cameselle-Molares et al. [117] conducted experiments in order to investigate the behavior of 2D delamination along a circular embedded pre-crack at the center and mid-plane of GFRP composite laminates under quasi-static out-of-plane opening loading. Wang et al. [118] used FE analysis to examine two-dimensional (2D) delamination growth in fiber reinforced polymer (FRP) laminates with in-plane isotropy under mode I loading conditions. Depending on the different stages of fracture, two different sizes of plate models have been considered. Cohesive elements were used to simulate the fracture behavior with large-scale bridging (LSB). The effects of pre-crack shape/area, loading zone shape/area, and fracture resistance were investigated parametrically. It was identified during crack initiation and early propagation that neither a flatter pre-crack shape nor a flatter loading zone shape could lead to higher initial structural stiffness and less uniform distribution of the strain energy release rate (SERR) along the pre-crack perimeter.

There has been a good number of works available in the direction of simulating the delamination growth in laminated composites using cohesive zone modeling (CZM) as well as the virtual crack closure technique (VCCT) [119]. In CZM, the critical strain energy release rate needs to be known to capture the initiation and propagation of delamination. Whereas the modeling effort and computational time required are much higher in the CZM approach, the VCCT and CZM approach provides a similar prediction of delamination at the interface [120]. Therefore, in the present work, the VCCT method could be advantageously used when deciding the SERR components as well as critical SERR for estimating the resistance to delamination at the interface.

## 2.7 Summary of literature review and research gaps

From the exhaustive literature review, it was clear that CNTs have already emerged as an important element in the enhancement of important properties in traditional laminated FRP composites due to their exceptional mechanical, electrical, and thermal properties. From the existing literature, it was reported that ILSS and fracture toughness of conventional FRP composites were enhanced by the addition of CNTs in different forms. It is expected that in coming days with the improvement in manufacturing methods of CNTs, these may also be used as reinforcing members replacing conventional fibers.

There have been a large number of works reported on the broad area of multiscale CNT-reinforced composites in recent times. From a thorough review of the literature, the following important observations have been made.

- From a large number of works, it has been concluded that carbon nanotubes can be used as reinforcing fibers in structural components.
- Large number of works has been focused on fabrication, characterization, strength and load carrying capability of CNT-reinforced composites.
- Most of the literatures reported that the addition of CNTs in FRP composite leads to improvement in mechanical properties such as tensile strength, flexural strength and fracture toughness.
- In the existing literature, many researchers conducted experiments in order to study the fracture behavior of CNT composites and the influence of important parameters with the aim of improving interlaminar shear strength and fracture toughness.
- There are also a few works focused on predicting the behavior of delamination initiation and propagation at the interface of CNT-reinforced composites using numerical techniques such as virtual crack closure technique (VCCT) and cohesive zone modeling (CZM) and reported that both techniques provide a similar prediction.

- In the existing literature, most of the works reported the critical strain energy release rate as an important parameter in understanding the failure behavior of CNT-reinforced composites using VCCT.
- From the literature it has been observed that to estimate the initiation and propagation of delamination, modeling effort and computational time required are much higher in the CZM approach. Therefore, the VCCT approach could be advantageously used when estimating the resistance to delamination at the interface.
- A large number of works have been reported on failure analysis of FRP composites which consists of different failure modes such as fiber break, matrix cracking, delamination, etc.
- There are also a few works reported that fiber debonding, pull out, etc. were failure modes in multiscale CNT-reinforced composites, but no work is reported to date on the analysis of three phase CNT composites with ply break or embedded delamination.

## 2.8 Objectives of the present work

From the exhaustive literature review, it was clear that CNTs have already emerged as main elements in the enhancement of important properties in traditional laminated FRP composites due to their exceptional mechanical, electrical, and thermal properties. In view of the fact that matrix properties play an important role in the interlaminar failure of FRP laminated composites, three phase (fiber/(CNT+epoxy)) where matrix is modified by adding CNTs to it gained importance and practical use to strengthen against such interlaminar failure. There have been a large number of works available in the three phase CNT composites where effect of adding CNTs to the matrix on the enhancement of properties are reported. In addition, there have been papers reporting the investigation of defects like ply break and impact induced interfacial delamination in conventional FRP laminated composites where it was shown that delamination usually precedes the final fracture in such laminates with defects. It was therefore felt important to understand the delamination initiation and such internal flaws in three phase CNT composites for assessing the performance of such three phase composites having internal flaws. More importantly, it was felt important to understand the role of CNTs in enhancing the resistance against failure initiation from such flaws both qualitatively and quantitatively. It was also reported that due to anisotropic material properties at the interface, the delamination ahead of such flaws at the interface is not self-similar and a complete three dimensional finite element analysis could be advantageously used for accurate assessment of stresses and displacement. However, no work has been reported where three phase fiber/(CNT+epoxy) composite laminates with internal flaws like ply break and interfacial delamination are analysed to assess the chances of delamination initiation from such flaws and to understand the influence of CNTs on enhancement of resistance to such delamination.

In view of the above observations from literature review, it was felt important to investigate the behavior of three phase fiber/(CNT+epoxy) composite laminates with internal defects like ply break and delamination where 3D FEA would be used along with the concept of LEFM to assess the chances of delamination from such defects and to understand the influence of adding CNTs to the epoxy. Therefore, in the present study the specific objectives have been laid down as follows:

1. A full 3D FEA of a carbon/(CNT+epoxy) three phase composite laminates with a central ply broken part-through-the-width to
    - (i) Determine the interlaminar stresses responsible for delamination and their distribution around the ply break.
    - (ii) Determine the strain energy release rate components ahead of the ply break using the stresses and displacement and VCCI.
    - (iii) Study the influence of CNTs and other important parameters on the SERR components.
    - (iv) Determine the critical SERR using QSC and VCCI and to study the influence of CNT wt% on the critical SERR.

2. A full 3D FEA of a carbon/(CNT+epoxy) three phase composite laminates with a through the width broken ply to
    - (i) Evaluate the interlaminar stresses responsible for delamination and their distribution around the ply break.
    - (ii) Evaluate the strain energy release rate components ahead of the ply break using the stresses and displacement and VCCI to understand the mixed mode nature of the delamination initiation.
    - (iii) Investigate the influence of CNTs and other important parameters like resin thickness, ply angle at the interface etc. on the SERR components
    - (iv) Evaluate the critical SERR using QSC and VCCI and to study the influence of CNT wt% on the critical SERR.

3. 3D FE model of a three phase carbon/(CNT+epoxy) composite laminate having an elliptical delamination at the interface of two laminae (due to low velocity impact) and to study the post impact behavior of such laminates subjected to loading to
    - (i) Determine the interlaminar stress (responsible for delamination) distribution along the curved delamination front.
    - (ii) Determine the components of strain energy release rates along the curved delamination front to understand the mixed mode delamination initiation.
    - (iii) Study the influence of CNT wt% and other important parameters like size and shape of delamination, ply angle etc. on the components of SERR.
    - (iv) Determine the critical SERR using QSC and VCCI along with the 3D FEA and to understand the influence of CNT wt% on the critical SERR.

4. 3D FE model of a three phase carbon/(CNT+epoxy) composite laminate having two neighboring elliptical delaminations at the interface of two laminae (due to low velocity impact) and to study the post impact behavior of such laminates subjected to loading to
    - (i) Understand the interaction of such neighboring delaminations by assessing the interlaminar stresses and SERR components especially, to study whether they grow as one single delamination or two separate delaminations.
    - (ii) Understand the influence of important parameters like separating distance, size and shape of delaminations etc. on the inetractions of the delaminations.
    - (iii) Study the influence of CNT wt% on the behavior of such interacting delaminations.

The methodologies adopted for predicting the delamination initiation in three phase carbon/(CNT+epoxy) composites with ply break or embedded delamination to realise the objectives of thesis have been discussed in details in Chapter 3.

## CHAPTER 3

# Theoretical background – FEA of three phase composite laminates with defects

This chapter presents the theoretical background for the finite element analysis of the three phase CNT composites with ply break and embedded delamination. Starting with stress-strain relationship for an orthotropic lamina, evaluation of effective properties of carbon/(CNT+epoxy) lamina using micromechanics has been presented. This chapter also presents the FE modeling and the elements used for the FEA of three phase CNT composites with defects.

## 3.1 Stress-strain relationship for orthotropic materials

In a general continuum, the state of stress at a point of a body can be represented by nine stress components $\sigma_{ij}$ acting on the sides of an elemental cube with sides parallel to the axes $x$, $y$, and $z$ of a global coordinate system as shown in **Fig. 3.1**. In a similar manner, the state of deformation is represented by nine strain components, $\varepsilon_{kl}$ . In general, the stress and strain components are related by the generalized Hooke's law [121] as given by the following equation:

$$\sigma_{ij} = C_{ijkl}\varepsilon_{kl} \qquad (i,\ j,\ k,\ l = 1,\ 2,\ 3) \tag{3.1}$$

$$\varepsilon_{ij} = S_{ijkl}\sigma_{kl} \tag{3.2}$$

Where $\sigma_{ij}$ and $\varepsilon_{kl}$ are the second order tensors, $C_{ijkl}$ and $S_{ijkl}$ are fourth order tensors. $C_{ijkl}$ is called a stiffness matrix comprising the elastic constants relating to stress and strain. $S_{ijkl}$ is called as compliance matrix which is the inverse of the stiffness matrix. Hence, a total 81 number of elastic constants are required to characterize a fully anisotropic material. However, due to the symmetry of stress and strain tensors ($\sigma_{ij} = \sigma_{ji}$, $\varepsilon_{ij} = \varepsilon_{ji}$), the number of elastic constants is reduced to 36. In a matrix form the reduced Eq. 3.1 can be written as

$$\begin{Bmatrix} \sigma_x \\ \sigma_y \\ \sigma_z \\ \tau_{xy} \\ \tau_{yz} \\ \tau_{zx} \end{Bmatrix} = \begin{bmatrix} C_{11} & C_{12} & C_{13} & C_{14} & C_{15} & C_{16} \\ C_{21} & C_{22} & C_{23} & C_{24} & C_{25} & C_{26} \\ C_{31} & C_{32} & C_{33} & C_{34} & C_{35} & C_{36} \\ C_{41} & C_{42} & C_{43} & C_{44} & C_{45} & C_{46} \\ C_{51} & C_{52} & C_{53} & C_{54} & C_{55} & C_{56} \\ C_{61} & C_{62} & C_{63} & C_{64} & C_{65} & C_{66} \end{bmatrix} \begin{Bmatrix} \varepsilon_x \\ \varepsilon_y \\ \varepsilon_z \\ \gamma_{xy} \\ \gamma_{yz} \\ \gamma_{zx} \end{Bmatrix} \tag{3.3(a)}$$

$$\{\sigma\} = [C]\{\varepsilon\} \tag{3.3(b)}$$

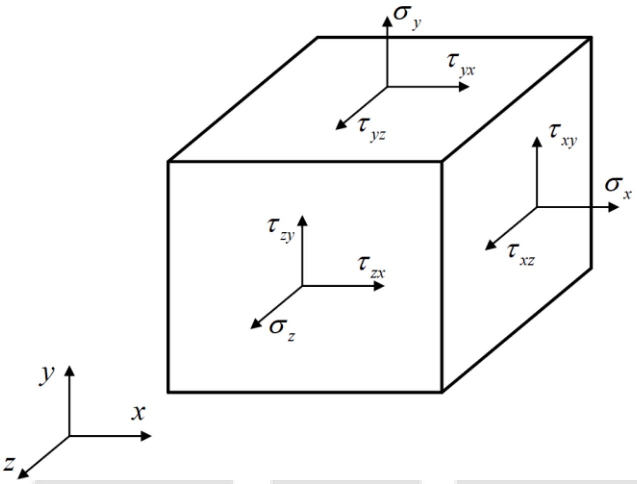

**Figure 3.1:** 3D state of stress at a point of a body

In the case of a single lamina of a continuous fiber reinforced composite, it is appropriate to use an orthogonal coordinate system in which one axis is aligned with the direction of fibers. The study of a single lamina stress-strain behavior is equivalent to finding out the relations between the stresses applied to lamina-bounding surfaces as a whole. It can be believed that a single homogeneous material can replace the two-material-fiber-matrix system thus simplifying the analysis. It should be evident that this single material might not have the same material properties in all directions. An orthotropic material has three mutually perpendicular planes of material symmetry as shown in **Fig. 3.2(a)**. This reduces the [*C*] matrix to 9 independent elastic constants.

A transversely isotropic material as shown in **Fig. 3.2(b)** has symmetric properties about an axis which is normal to a plane of material isotropy in an orthotropic body. If all the planes in an orthotropic body are identical then the properties are the same throughout the body is called an isotropic material as shown in **Fig. 3.2(c)**.

$$[C]=\begin{bmatrix} C_{11} & C_{12} & C_{13} & 0 & 0 & 0 \\ C_{21} & C_{22} & C_{23} & 0 & 0 & 0 \\ C_{31} & C_{32} & C_{33} & 0 & 0 & 0 \\ 0 & 0 & 0 & C_{44} & 0 & 0 \\ 0 & 0 & 0 & 0 & C_{55} & 0 \\ 0 & 0 & 0 & 0 & 0 & C_{66} \end{bmatrix} \tag{3.4}$$

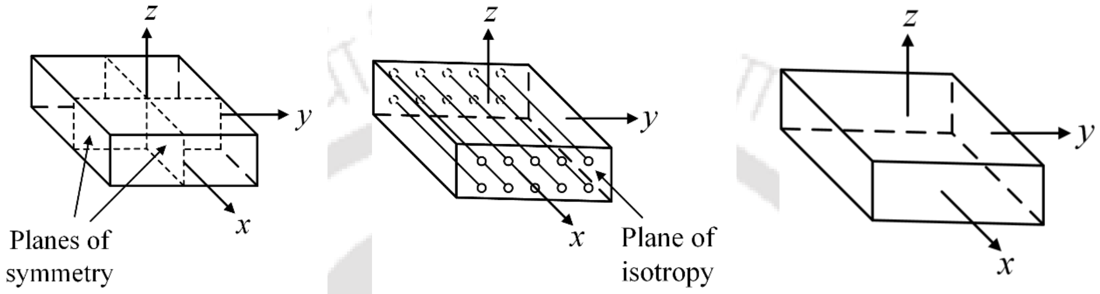

(a) Orthotropic body (b) Transversely isotropic body (c) Isotropic body

**Figure 3.2:** Material types based on symmetry in properties

In order to find the independent elastic constants of orthotropic material, a single lamina having unidirectional fibers with a reference coordinate system 1-2-3 is considered as shown in **Fig. 3.3**. In the 1-2-3 plane, Axis-1 is aligned with the direction of the fiber, axis-2 is perpendicular to the direction of fiber and in the plane of the lamina, and axis-3 is perpendicular to the plane of the lamina.

Unidirectional fibers were reinforced in a repeating pattern as shown in **Fig. 3.3** and plane 2-3 is a plane of material isotropy. Due to this transverse isotropy, the properties in the two directions perpendicular to the fiber are the same. In an isotropic material, the properties in all three directions are the same.

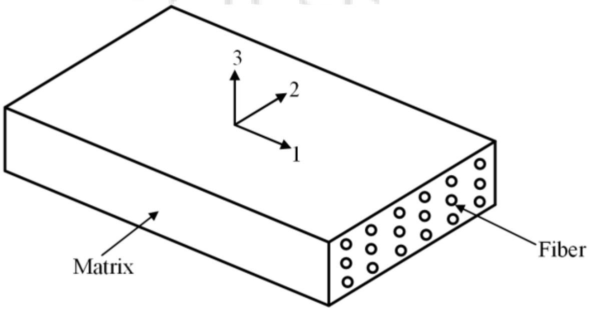

**Figure 3.3:** A single lamina with unidirectional fibers

The terms of [*C*] matrix can be computed for the given material properties in three directions such as $E_1$, $E_2$, $E_3$, $\nu_{12}$, $\nu_{23}$, $\nu_{13}$, $G_{12}$, $G_{23}$, and $G_{13}$ where $E$ represents Young's modulus, $\nu$ represent Poisson's ratio, and $G$ represents rigidity modulus. The relations among the material properties were given by the Maxwell-Betti Reciprocal theorem as

$$\frac{\nu_{12}}{E_1} = \frac{\nu_{21}}{E_2};\ \frac{\nu_{13}}{E_1} = \frac{\nu_{31}}{E_3};\ \frac{\nu_{23}}{E_2} = \frac{\nu_{32}}{E_3} \tag{3.5}$$

Hence, the constant terms can be calculated using the following relations

$$\begin{aligned} &C_{11} = \frac{1-\nu_{23}\nu_{32}}{E_2E_3\Delta}; && C_{22} = \frac{1-\nu_{13}\nu_{31}}{E_1E_3\Delta}; && C_{33} = \frac{1-\nu_{12}\nu_{21}}{E_1E_2\Delta}; \\ &C_{12} = C_{21} = \frac{\nu_{21}+\nu_{23}\nu_{31}}{E_2E_3\Delta}; && C_{13} = C_{31} = \frac{\nu_{31}+\nu_{21}\nu_{32}}{E_2E_3\Delta}; && C_{23} = C_{32} = \frac{\nu_{32}+\nu_{12}\nu_{31}}{E_1E_3\Delta}; \\ &C_{44} = G_{12}; && C_{55} = G_{23}; && C_{66} = G_{31} \end{aligned} \tag{3.6}$$

where $\Delta = \dfrac{1-\nu_{12}\nu_{21}-\nu_{23}\nu_{32}-\nu_{13}\nu_{31}-2\nu_{21}\nu_{32}\nu_{13}}{E_1E_2E_3}$

### 3.1.1 Stress transformation relations

Material constants for isotropic materials do not change with changing the coordinate axes but for anisotropic materials, the constants in a particular direction change with changing the coordinate axes. The transformation relations find their application when the ply-material axes do not coincide with the global coordinate axes. As shown in **Fig. 3.4**, the x-y-z system is the global coordinate system, the 1-2-3 system is the material coordinate system or local coordinate system, and both are orthogonal to each other.

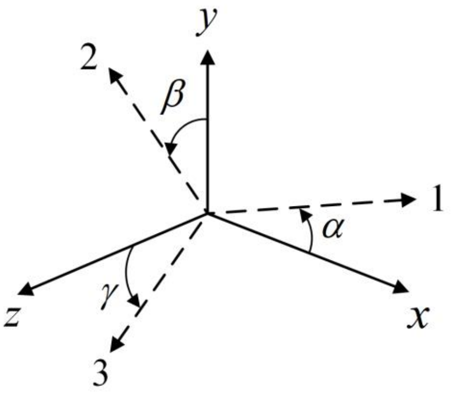

**Figure 3.4:** Representation of global and material axes

From Figure 3.4, it can be seen that α, β, and γ are the angles made by 1, 2, and 3 axes with respect to the x, y, and z axes respectively. The direction cosines between the axes are shown in **Table 3.1** and these can be represented by the matrix form which is given by [*l*]

**Table 3.1:** Direction cosines between axes

| Axes | $x$ | $y$ | $z$ |
|---|---|---|---|
| 1 | $l_1$ | $m_1$ | $n_1$ |
| 2 | $l_2$ | $m_2$ | $n_2$ |
| 3 | $l_3$ | $m_3$ | $n_3$ |

$$[l]=\begin{bmatrix} l_1 & m_1 & n_1 \\ l_2 & m_2 & n_2 \\ l_3 & m_3 & n_3 \end{bmatrix} \tag{3.7}$$

The engineering strains can be transformed from the global axes to local axes by the following relation

$$\begin{Bmatrix} \varepsilon_1 \\ \varepsilon_2 \\ \varepsilon_3 \\ \gamma_{12} \\ \gamma_{23} \\ \gamma_{31} \end{Bmatrix} = [T] \begin{Bmatrix} \varepsilon_x \\ \varepsilon_y \\ \varepsilon_z \\ \gamma_{xy} \\ \gamma_{yz} \\ \gamma_{zx} \end{Bmatrix} \tag{3.8}$$

where [T] is the 6×6 transformation matrix given by

$$[T]=\begin{bmatrix} l_1^2 & m_1^2 & n_1^2 & l_1 m_1 & m_1 n_1 & n_1 l_1 \\ l_2^2 & m_2^2 & n_2^2 & l_2 m_2 & m_2 n_2 & n_2 l_2 \\ l_3^2 & m_3^2 & n_3^2 & l_3 m_3 & m_3 n_3 & n_3 l_3 \\ 2l_1 l_2 & 2m_1 m_2 & 2n_1 n_2 & l_1 m_2 + l_2 m_1 & m_1 n_2 + m_2 n_1 & n_1 l_2 + n_2 l_1 \\ 2l_2 l_3 & 2m_2 m_3 & 2n_2 n_3 & l_2 m_3 + l_3 m_2 & m_2 n_3 + m_3 n_2 & n_2 l_3 + n_3 l_2 \\ 2l_3 l_1 & 2m_3 m_1 & 2n_3 n_1 & l_3 m_1 + l_1 m_3 & m_3 n_1 + m_1 n_3 & n_3 l_1 + n_1 l_3 \end{bmatrix} \tag{3.9}$$

The stress transformation relation is given by

$$\begin{Bmatrix} \sigma_1 \\ \sigma_2 \\ \sigma_3 \\ \tau_{12} \\ \tau_{23} \\ \tau_{31} \end{Bmatrix} = [T]^{-T} \begin{Bmatrix} \sigma_x \\ \sigma_y \\ \sigma_z \\ \tau_{xy} \\ \tau_{yz} \\ \tau_{zx} \end{Bmatrix} \tag{3.10}$$

From Eq. 3.3 the stress-strain relation can be written as $\{\sigma\}_{xyz} = [C]\{\varepsilon\}_{xyz}$ in global coordinate system or as $\{\sigma\}_{123} = [\bar{C}]\{\varepsilon\}_{123}$ in the local coordinate system. So, if $[\bar{C}]$ is the constitutive relationship matrix in the fiber direction is known and by using equations 3.9, 3.10 and the relation $\{\sigma\}_{123} = [\bar{C}]\{\varepsilon\}_{123}$ the global material matrix $[C]$ can be obtained by using the following relation

$$[C] = [T]^T [\bar{C}][T] \tag{3.11}$$

## 3.2 Methods to predict delamination initiation in composites

It is widely known that composite structure laminates are highly prone to crack initiation and propagation along the interfaces of the laminae in different modes of failure. Defects such as ply break, matrix cracking and delamination generally occurs in fiber reinforced laminated composites due to external loading on structure such as static tension or compression, bending, in fatigue or impact, while manufacturing or in service. High interlaminar stresses near the ply break leads to delamination initiation at the interface of the broken ply and adjacent intact ply, as it can result in a significant reduction in in-plane strength and stiffness of the composite laminate, eventually leading to catastrophic failure of the whole structure [1, 2].

Interlaminar stresses ($\tau_{xz}$, $\tau_{yz}$ and $\sigma_{zz}$) at the interface are responsible for delamination initiation. Hence, the calculation of interlaminar stresses is important. There are two different types of approaches to compute the interlaminar stresses at the interface of composite laminate. Numerical methods namely finite difference [122] and finite elements [123–124] were used. Earlier analytical approaches majorly concentrated on one component at a time. Pagano and Pipes [125] developed an analytical model for a rough approximation of interlaminar normal stress by assuming a stress distribution and imposing force and moment equilibrium at the free edge. Pagano and Soni [126] formulated a variational method in order to calculate interlaminar stresses in composite parts. The approach is similar to sub-structuring in the conventional finite element method.

The state of the interlaminar stresses at the interface is significant in delamination initiation. However, there has been a debate over how the concept of interlaminar stress state can be included in the prediction of delamination onset. Delamination is an initiation, growth, and final fracture process. Delamination onset always need not lead to a final fracture. It may propagate gradually even after the initiation. There are two methodologies for predicting the delamination initiation namely strength of materials approach and fracture mechanics approach.

### 3.2.1 Strength of materials approach

In strength of materials approach, the local stress state at the interface is compared to relevant strengths. Many researchers implemented different approaches to predict the onset of delamination. Maximum stress failure theory is based on the maximum normal stress theory by Rankine and the maximum shearing stress theory by Tresca as applied to isotropic materials. Failure of the lamina is predicted when any of the local normal and shear stress state of the lamina is equal to or exceeds the relevant ultimate strengths of the unidirectional lamina. Similarly, maximum strain failure theory also predicts failure when any of the local normal and shear strain state of the lamina is equal to or exceeds the relevant ultimate strains of the unidirectional lamina. This theory is based on the maximum normal strain theory by St. Venant and maximum shear stress theory by Tresca as applied to isotropic materials. Tsai and Hill [127–128] developed a failure theory for anisotropic materials based on the Von Mises distortion energy. Failure of lamina takes place when the distortion energy is greater than the failure distortion energy of the material. In this theory, the interaction between three unidirectional lamina strength parameters is considered and it does not differentiate between the tensile and compressive strengths in its equations. Similarly, Tsai-Wu [129] formulated a failure theory based on the Beltrami total strain energy. This theory distinguishes between the compressive and tensile strengths of a lamina.

Whitney and Nuismer [130] calculated the stress at the edge of a hole in a composite plate and implemented the average stress concept to predict failure. Theoretical longitudinal stress ($\sigma_{11}$) is averaged across a distance from the edge of the hole. The average stress criterion is given by:

$$\bar{\sigma}_{ij} = \frac{1}{x_{avg}} \int_{0}^{x_{avg}} \sigma_{ij} \, dx \tag{3.12}$$

where, $\sigma_{ij}$ is the stress component, $\bar{\sigma}_{ij}$ is the average stress component, $x$ is the distance from the reference edge, $x_{avg}$ is the averaging dimension. If this stress reaches the critical value, then failure will take place.

Similarly, before delamination onset, theoretical interlaminar shear and normal stresses considerably exceed reasonable strength parameters. As a result, Kim and Soni [131] tried to compare delamination onset with an average value of interlaminar normal stress. They averaged the stress over one nominal ply thickness and used the transverse strength of the unidirectional composite to estimate the interlaminar normal strength. Delamination initiation criterion is given by:

$$\bar{\sigma}_{zz} = Y^{t} \tag{3.13}$$

where: $Y^{t}$ is the in-plane transverse strength of the unidirectional composite. They identified that tensile interlaminar normal stress is responsible for delamination initiation. Their results revealed that the theoretical value of interlaminar normal stress was significantly more than the estimated strength.

In a further study, Soni and Kim [132] investigated the effect of interlaminar shear strength. They calculated the interlaminar shear strength as the in-plane shear strength of a unidirectional composite by averaging this shear component over one nominal ply thickness. According to the criterion proposed by them, delamination initiates when the absolute magnitude of the average interlaminar shear stress reaches the estimated shear strength:

$$\left| \bar{\sigma}_{xz} \right| = \mathrm{S} \tag{3.14}$$

where: S is unidirectional composite in-plane shear strength. They did not mention about how to choose between the proposed two criteria.

After that, Soni and Kim [133] developed a general criterion in which the effects of all interlaminar stresses were considered. By this criterion, delamination initiates when:

$$F_{zz}\bar{\sigma}_{zz}^{2} + F_{tt}\bar{\sigma}_{xz}^{2} + F_{uu}\bar{\sigma}_{yz}^{2} + F_{z}\bar{\sigma}_{zz} + F_{t}\bar{\sigma}_{xz} + F_{u}\bar{\sigma}_{yz} = 1 \tag{3.15}$$

where the coefficients can be obtained by conducting relevant in-plane shear and transverse strength tests. By eliminating terms based on shear stress sign, the criterion reduced to:

$$F_{zz}\bar{\sigma}_{zz}^{2} + F_{tt}\bar{\sigma}_{xz}^{2} + F_{uu}\bar{\sigma}_{yz}^{2} + F_{z}\bar{\sigma}_{zz} = 1 \tag{3.16}$$

The linear term in interlaminar stress is fairly important. It indicates that average compressive normal interlaminar stress can delay delamination initiation in cases where interlaminar shear stress dominates.

Brewer and Lagace [134] developed a quadratic stress criterion (QSC) to predict the delamination. This criterion is based on average interlaminar stresses computed over a very small length ($\Delta a$). However, the evaluation of average stresses over a small length depends on the material properties of the interface. They conducted experiments to find delamination initiation stress in graphite/epoxy laminates. By using the strength data available in the literature, they fit in the equation and identified that the optimum value of small length is approximately equal to single-ply thickness. The value of $\Delta a$ is very small compared to other dimensions of the laminate. Hence, accurate computation of interlaminar stresses is achieved. In the present work, this criterion is used and it states that delamination will initiate when:

$$Q\left( = \left[\frac{\bar{\sigma}_{z}}{Z}\right]^{2} + \left[\frac{\bar{\tau}_{xz}}{X}\right]^{2} + \left[\frac{\bar{\tau}_{yz}}{Y}\right]^{2}\right) \geq 1 \tag{3.17}$$

where, the mean interlaminar normal stress ($\bar{\sigma}_{z}$) and interlaminar shear stresses ($\bar{\tau}_{xz}$ and $\bar{\tau}_{yz}$) are obtained by taking average over a small distance ($\Delta a$) ahead of the delamination front as follows

$$\left(\bar{\sigma}_{z}, \bar{\tau}_{xz}, \bar{\tau}_{yz}\right) = \frac{1}{\Delta a}\int_{0}^{\Delta a}\left(\sigma_{z}, \tau_{xz}, \tau_{yz}\right)dx \tag{3.18}$$

and *Z, X* and *Y* are the corresponding interlaminar normal and shear strengths from the experiments.

Lu et al. [135] have used the same criterion to predict the failure of the fiber yarn-matrix interface of 2.5D woven composites subjected to quasi-static tension. Similarly, Munoz-Reja et al. [136] used the same criterion to predict the crack initiation and propagation at fiber-matrix elastic interfaces of carbon/epoxy and glass/epoxy composites under biaxial loading.

In a similar study, Lorriot et al. [137] proposed a model to predict the delamination initiation at the interface of a carbon/epoxy T800/914 composite by conducting edge delamination tests and the results are in good agreement with QSC results.

### 3.2.2 Fracture mechanics approach

Delamination can be considered as interlaminar cracks at the interface of the laminated composites. This motivated several researchers to study the delamination initiation and growth using fracture mechanics approach. There are two approaches in fracture mechanics namely linear elastic fracture mechanics (LEFM) and elastic-plastic fracture mechanics (EPFM). LEFM is based on the concept of small-scale yielding (SSY). In SSY, the plastic zone size ahead of the crack tip is very small compared to the crack length and other geometric parameters, and therefore constitutive relation of the material can be assumed to follow Hook's law. Strain energy release rate (SERR) and stress intensity factor (SIF) was studied in order to assess delamination in LEFM. Whereas EPFM deals with the materials that have nonlinear behavior (i.e., plastic deformation) and time independent. J contour integral and crack tip open displacement (CTOD) were studied in order to predict the delamination in EPFM. The phenomenon of fracture clearly explained by three fundamental modes of fracture (first observed by Irwin (1957)) such as opening mode (mode I), sliding mode (mode II) and tearing mode (mode III). **Fig. 1.7(a)**, **1.7(b)**, and **1.7(c)** shows the mode I, mode II and mode III failures respectively.

## 3.3 Computation of strain energy release rate using FE

In the present work, strain energy release rate approach has been used in order to assess the delamination. The strain energy release rate is defined as the energy release per unit area of crack growth. Various finite element methods such as finite crack extension method, virtual crack extension method, equivalent domain integral method, crack closure method, and modified or virtual crack closure methods were used to determine the strain energy release rate.

Kruger et al. [138] developed a *finite crack extension method* which is a combination of two complete analyses. The crack gets advanced for a finite length ahead of the second analysis, the crack advances for a finite length. This method calculates the global energy release rate which is the energy available to extend the crack by multiplying global forces on a structural level by global deformations. The *virtual crack extension method* is a one complete analysis used by different researchers [139–141] to determine the deformations of the structure. The total strain energy release rate is calculated locally at the crack front and the computation requires an additional calculation of the stiffness matrix of the elements caused by the virtual crack extension. This method calculates the total strain energy release rate as a function of virtual crack extension direction, providing information probably on growth direction. Ishikawa [142] and George [143] have made some modifications to this method in order to allow the mode separation for 2D analysis. In some of the literature [144–146], an *equivalent domain integral method* is used to solve both linear and nonlinear problems and it also provides mode separation information additionally. The virtual crack closure technique [147–148] is often used for calculating energy release rates for delamination in laminated composite structures where the failure criterion is largely dependent on the mixed-mode ratio and propagation occurs in the laminate plane.

The crack closure method computes the strain energy release rate components based on Irwin's crack closure integral. This method assumes that the energy released by the extension of the crack from $a$ to $a+\Delta a$ is equal to the energy required for the crack closure. The modified or virtual crack closure method (VCCT) considers the same assumptions of *crack closure method*. Additionally, it is assumed that a crack extension of $\Delta a$ from $a+\Delta a$ to $a+2\Delta a$ does not alter the state of the crack tip [149]. These methods can also extend to compute energy release rates in multi-scale laminated composites.

### 3.3.1 SERR along the flat crack front

**Figure 3.5** represents the FE calculation of SERR by Irwin's crack closure integral in 3D. For an existing crack length of $a$ , three components of SERR can be calculated using virtual crack closure integral (VCCI) as

$$G_I = \lim_{\Delta a \to 0} \frac{1}{2.\Delta a.\mathrm{c}} \int_{-c/2}^{c/2} \int_{0}^{\Delta a} \sigma_z (w_t - w_b)\, dxdy \tag{3.19}$$

$$G_{II} = \lim_{\Delta a \to 0} \frac{1}{2.\Delta a.\mathrm{c}} \int_{-c/2}^{c/2} \int_{0}^{\Delta a} \tau_{xz} (u_t - u_b)\, dxdy \tag{3.20}$$

$$G_{III} = \lim_{\Delta a \to 0} \frac{1}{2.\Delta a.\mathrm{c}} \int_{-c/2}^{c/2} \int_{0}^{\Delta a} \tau_{yz} (v_t - v_b)\, dxdy \tag{3.21}$$

Here, $a$ is the crack length, $c$ is the width of the delamination, $\Delta a$ is the virtual crack extension length. $u_t, v_t, w_t$ and $u_b, v_b, w_b$ are the nodal displacements along x, y and z directions of the top surface and bottom surface respectively of the delaminated region at a distance of $\Delta a$ behind the delamination front. $\sigma_z$ is the interlaminar normal stress and $\tau_{xz}$, $\tau_{yz}$ are the interlaminar shear stresses at the interface.

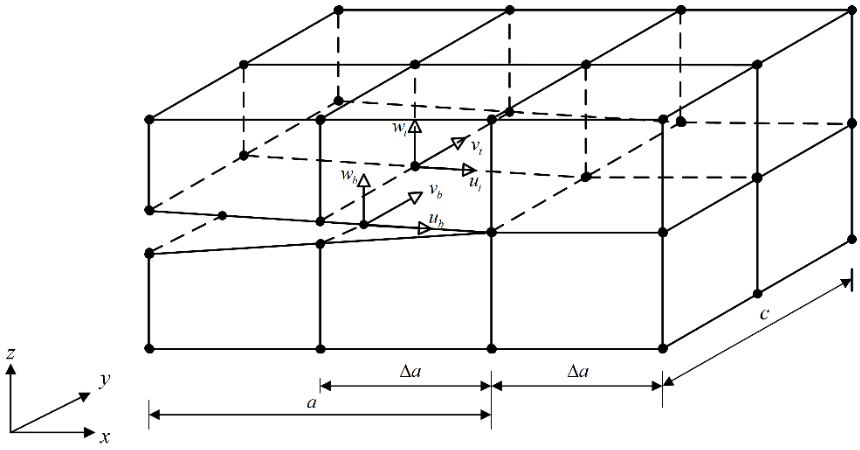

**Figure 3.5:** FE computation of SERR using Irwin's crack closure integral (3D)

### 3.3.2 SERR along the curved crack front

The delamination front in case of circular or elliptical delamination is curved one as shown in **Fig. 3.6**. On a curved delamination front, coordinate transformation on displacements and stresses can be carried out to calculate strain energy release rate components. At any point, the crack closure integral's integrand can be computed along the delamination fronts normal. Interlaminar stresses ($\sigma_{zz}$ , $\tau_{zn}$ , and $\tau_{zt}$) and the corresponding displacements could be obtained using a 3D FE analysis. At any point $P$ on the delamination front, strain energy release rate ($G_I$, $G_{II}$ and $G_{III}$) components can be computed using the following equations:

$$G_I = \lim_{\Delta a \to 0} \frac{1}{2c\Delta a} \int_0^{\Delta a} \int_0^c \sigma_{zz} \delta u_z (n - \Delta a)\; dndt \tag{3.22}$$

$$G_{II} = \lim_{\Delta a \to 0} \frac{1}{2c\Delta a} \int_0^{\Delta a} \int_0^c \tau_{zn} \delta u_n (n - \Delta a)\; dndt \tag{3.23}$$

$$G_{III} = \lim_{\Delta a \to 0} \frac{1}{2c\Delta a} \int_0^{\Delta a} \int_0^c \tau_{zt} \delta u_t (n - \Delta a)\; dndt \tag{3.24}$$

Where $\tau_{zn}$ and $\tau_{zt}$ can be computed using the following equations

$$\tau_{zn} = \tau_{xz} \cos\phi - \tau_{yz} \sin\phi \tag{3.25}$$

$$\tau_{zt} = \tau_{xz} \sin\phi + \tau_{yz} \cos\phi \tag{3.26}$$

Where $\phi$ is the angle considered normal to the point P

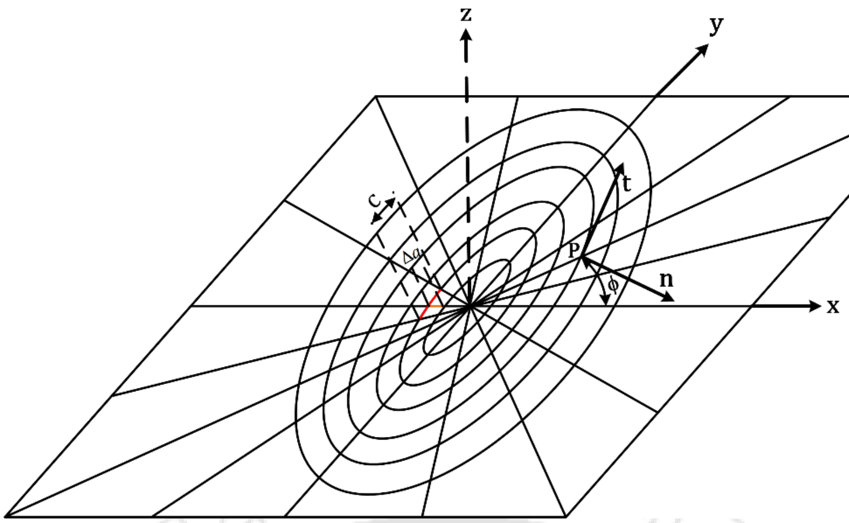

**Figure 3.6:** FE computation of SERR along elliptical delamination front

### 3.3.3 Critical strain energy release rate

For a ply break or intefacial delamination, considering the delamination front as the crack front, delamination initiation for a given loading occurs if the total SERR ( $G = G_I + G_{II} + G_{III}$ ) is greater than critical SERR ( $G_c$ ). Using the stress based approach, QSC, the condition $Q$ = 1 represents the delamination initiation and using LEFM, $G = G_c$ represents the delamination initiation. So, at the instant of delamination knowing the stresses , we could calculate $G_c$ .

## 3.4 Characteristics of elements used in FE modeling

In the present work, SOLID 185 and CONTA 178 elements are used in finite element modeling of the composite laminates. The characteristics of the both the elements are given in below sections.

### 3.4.1 SOLID 185 element

In ANSYS, SOLID 185 [150] is a 3D brick element as shown in **Fig. 3.7**, which is widely used for modeling of solid structures. It is defined by eight number of nodes having three translation degrees of freedom at each node in the nodal $x$, $y$, and $z$ directions. The element has creep, large deflection, plasticity, hyper elasticity, large strain capabilities and large deflection.

Solid 185 is available in two forms such as homogeneous structural solid and layered structural solid. Irregular regions can be modeled with help of structural solids in the form of degenerated prism, tetrahedral, and pyramid shapes. Layered SOLID 185 used to model the layered thick shells or solids. **Figure 3.7(a)** and **3.7(b)** shows the coordinate system, geometry, and node locations of the homogeneous and layered structural solid respectively.

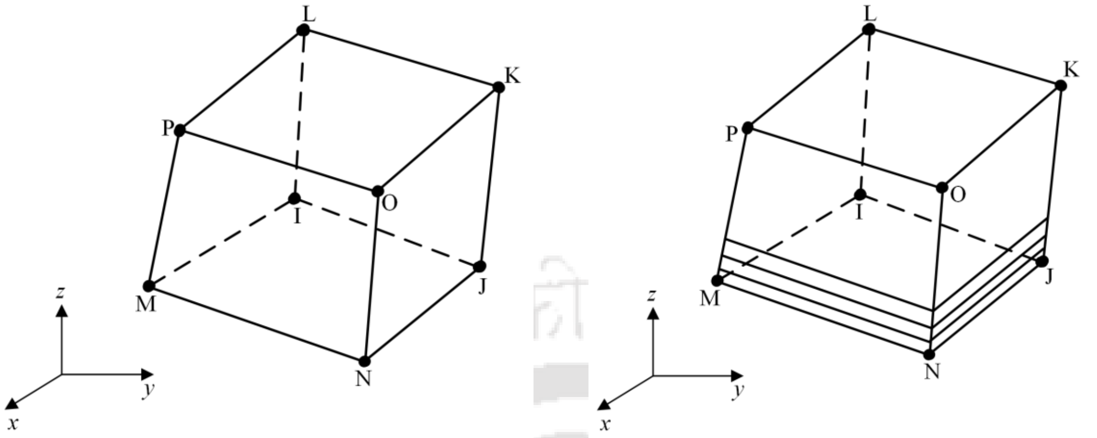

(a) (b)

**Figure 3.7:** FE geometry of (a) homogeneous structural solid (b) layered structural solid

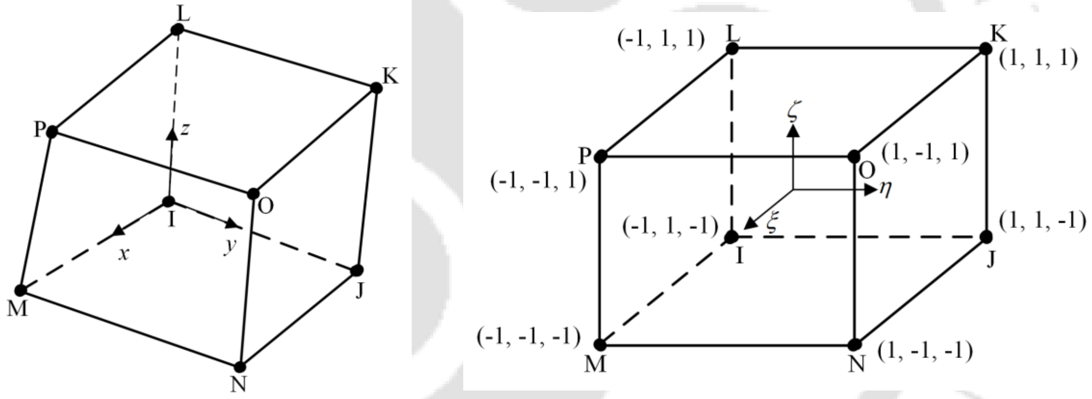

(a) (b)

**Figure 3.8:** Representation of SOLID 185 in (a) global coordinates (b) natural coordinates

In finite element analysis, the isoparametric elements are used to map the curved boundaries in global coordinate system into regular traingular and regular elements in natural coordinate system. **Figure 3.8(a)** and **3.8(b)** represents the structural solid in global and natural coordinates respectively. The mapping is done with help of interpolation functions called as shape functions. The shape functions for the SOLID 185 is given by the following equation

$$\begin{aligned}
N_I &= \frac{1}{8}(1-\xi)(1-\eta)(1-\zeta) & N_J &= \frac{1}{8}(1+\xi)(1-\eta)(1-\zeta) \\
N_K &= \frac{1}{8}(1+\xi)(1+\eta)(1-\zeta) & N_L &= \frac{1}{8}(1-\xi)(1+\eta)(1-\zeta) \\
N_M &= \frac{1}{8}(1-\xi)(1-\eta)(1+\zeta) & N_N &= \frac{1}{8}(1+\xi)(1-\eta)(1+\zeta) \\
N_O &= \frac{1}{8}(1+\xi)(1+\eta)(1+\zeta) & N_P &= \frac{1}{8}(1-\xi)(1+\eta)(1+\zeta)
\end{aligned} \tag{3.27}$$

In a simplified form the shape functions can be written as

$$N_i = \frac{1}{8}(1+\xi\xi_i)(1+\eta\eta_i)(1+\zeta\zeta_i) \qquad i = 1,\ 2,\ 3,\ldots\ldots 8 \tag{3.28}$$

### 3.4.2 CONTA 178 element

CONTA 178 [150] element is node to node contact element which provides contact and sliding between two nodes of any type of elements. The element is defined by two nodes having three translation degrees of freedom at each node in the nodal *x*, *y*, and *z* directions. It can also be employed in 2D and axisymmetric models by constraining translational degree of freedom in *z* direction. The element can be able to support compression in contact normal direction and Coulomb friction in tangential direction.

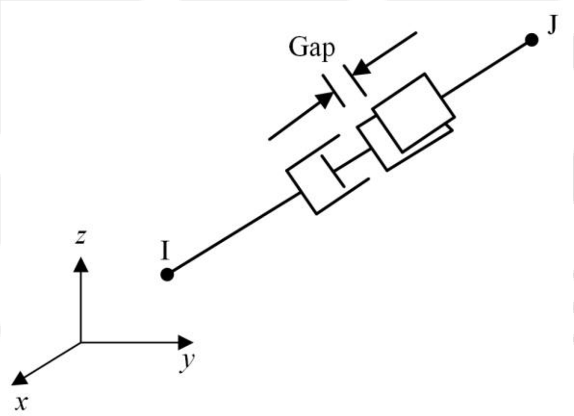

**Figure 3.9:** CONTA 178 element geometry and coordinate system

**Figure 3.9** represents geometry of the CONTA 178 element. The element supports four different contact algorithms named as Pure penalty method, Augmented Lagrange method, Pure Lagrange multiplier method, and Lagrange multiplier on contact normal penalty on frictional direction. In the present work, Augmented Lagrange method is used in which the parameters such as contact normal stiffness, maximum allowable penetration, and maximum allowable slip needs to be defined.

The normal contact force is given by

$$F_n = \begin{cases} K_n u_n + \lambda_{i+1} & \text{if } u_n \le 0 \\ 0 & \text{if } u_n > 0 \end{cases} \tag{3.29}$$

where $K_n$= contact normal stiffness, $u_n$ = contact gap size, and $\lambda_{i+1}$= Lagrange multiplier force at iteration $i+1$ is given by

$$\lambda_{i+1} = \begin{cases} K_n u_n + \tau_i & \text{if } |u_n| > \varepsilon_t \\ \tau_i & \text{if } |u_n| \le \varepsilon_t \end{cases} \tag{3.30}$$

where $\varepsilon_t$ = user-defined compatibility tolerance

## 3.5 FE modeling of ply break and embedded delamination

In the case of ply break, a full 3D FE modeling has been done in order to capture the interlaminar stresses responsible for delamination at the interface. The laminate has been modeled as number of sub-laminates above using the layered solid element and the ply break has been modeled by considering a particular ply cut throughout the width or part-through-the-width. Since the delamination ahead of the ply break actually initiates and propagates through a very thin resin rich layer [151–152], the two interfaces (above and below the broken ply) between the broken and the adjacent intact plies are modeled as thin (0.1 times the ply thickness) resin rich layers. At the interface of the broken and continuous ply, a small amount delamination is assumed to exist and the straight delamination front is considered as the crack front for delamination of SEER components. Duplicate nodes have been defined along the interface and are connected by the multi-point constraint (MPC) equations. Along the small delaminated zone ahead of the ply break these MPCs are released. However, these nodes at the delaminated zone have been connected by the contact element to prevent the undesirable interpenetration [150] of the top and bottom nodes in FEA. These contact elements are active when the two surfaces are in contact and prevent any interpenetration. However, the friction between the delaminated surfaces is neglected in the present modeling and the branching of the crack is ignored assuming the delamination plane is the weakest plane.

While modeling the defects in the form of an embedded sub surface delamination (elliptical shape) at the interface, the laminate is modeled as two sub laminates above and below the interface where the delamination exists. Again, the interface is modeled as thin (0.1 times the ply thickness) resin rich layer and the elliptical delamination has been modeled by deleting elements from the layer and separating the two sub-laminates at the delamination. In the delaminated region, the top and the bottom surface nodes are connected by the contact elements which prevent the undesirable interpenetration of the two surfaces in contact.

ANSYS parametric design language has been used to create the model and from the solution and post-processing the displacements, stresses, and strains are obtained. In the post-processing, macros have been written for implementing the QSC and calculations of SERR components using VCCI. Depending upon the delamination front (straight or curved), appropriate transformations of displacements and stresses have been performed before using those for the determination of SERR components.

## 3.6 Calculation of properties of carbon/(CNT+epoxy) composite

The laminae properties are evaluated by first computing the properties of the matrix (CNT+epoxy) with the help of Halpin-Tsai relations [153] and then the carbon/(CNT+epoxy) composite properties are evaluated using the rule of mixtures. For composites in which CNTs are considered to be randomly oriented and uniformly distributed throughout the resin matrix, the Halpin-Tsai equations are more elaborate and correlate specific geometric characteristics of CNTs, and the relative modulus of elasticity of a composite is related to the mechanical properties of its constituents by the following equation

$$E_c = \left( \frac{3}{8} \frac{1+\zeta\eta_L V_{CNT}}{1-\eta_L V_{CNT}} + \frac{5}{8} \frac{1+2\eta_T V_{CNT}}{1-\eta_T V_{CNT}} \right) E_m \tag{3.31}$$

where $\zeta = 2l_{CNT} / d_{CNT}$, $\eta_L$ and $\eta_T$ are the parameters which are represented by

$$\eta_L = \frac{(E_{CNT} / E_m) - 1}{(E_{CNT} / E_m) + (2l_{CNT} / d_{CNT})} \tag{3.32}$$

$$\eta_T = \frac{(E_{CNT} / E_m) - 1}{(E_{CNT} / E_m) + 2} \tag{3.33}$$

where $E_C$ = elastic modulus of the (CNT+epoxy), $E_{CNT}$ = elastic modulus of CNTs = 400 GPa, $E_m$ = elastic modulus of neat epoxy = 3.1 GPa, $l_{CNT}$ = length of CNTs = 30 μm, $d_{CNT}$ = diameter of CNTs = 20 nm and $V_{CNT}$ = volume fraction of CNTs given by the following equation

$$V_{CNT} = \frac{1}{[(\rho_{CNT} / \rho_m) \times (M_m / M_{CNT})] + 1} \tag{3.34}$$

where $\rho_{CNT}$ = density of CNTs = 2.1 g/cc, $\rho_m$ = density of epoxy matrix = 1.2 g/cc, $M_m$ is the mass fraction of epoxy matrix, and $M_{CNT}$ is the mass fraction of CNTs. As the mass fraction of CNTs is small, Poisson's ratios of the epoxy and CNT composite were considered to be the same. The shear modulus for the matrix (CNT+epoxy) is calculated as

$$G_m = \frac{E_c}{2\ (1+\nu)} \tag{3.35}$$

These properties of modified matrix (CNT+epoxy) obtained using Halpin-Tsai equations along with the properties of carbon fibers are then used to compute the properties of carbon/(CNT+epoxy) lamina using micromechanics rule of mixture.

# CHAPTER 4

# Three phase carbon/(CNT+epoxy) laminates with part through the width ply break

This chapter presents the FE analysis of a three phase carbon/(CNT+epoxy) laminate having a defect in the form of part-through-the-width ply break. Different configurations of laminates have been considered to understand the factors influencing the delamination at the interface of broken and intact ply. Influence of CNT wt% on the delamination has been investigated and presented in this chapter.

## 4.1 Introduction

One of the common defects in a laminate subjected to loading is fiber breakage especially when a laminate is subjected to impact load. Once the weakest fiber breaks, the adjacent fibers in that lamina get over stressed and break thus forming a part-through-the-width ply break in the laminate. Once such a ply break occurs, the adjacent plies experience more stress and there are high interfacial shear and normal stresses at the interface ahead of the ply break causing delamination initiation and propagation and leading to the final fracture of the laminate. More importantly, these types of part-through-the-width ply breaks are not visible from outside and resemble a buried sub-surface crack which is the cause of failure in many laminates. It is therefore important to enhance the resistance to such delamination arising from ply break.

## 4.2 Laminate specimen and FE modeling

**Fig. 4.1** shows a three phase $\left[0_2/\pm\theta/\bar{0}\right]_s$ carbon/(CNT+epoxy) laminate with the central lamina partly broken through the width. It is considered that the laminate is made of epoxy resin mixed with CNTs as the matrix and carbon fiber as the primary reinforcement (60% fiber volume fraction). In order to understand the effect of ply break width, four different widths ($c$ = 2, 8, 16 and 20 mm) have been considered. In addition, in order to understand the effect of fiber orientation of adjacent intact ply, five different ply angles ($\theta = 0^\circ, 30^\circ, 45^\circ, 60^\circ$ and $90^\circ$) have been considered. Different weight percentages (wt%) (0%, 0.25%, 0.5%, 1%, and 1.5%) of CNTs are considered to have mixed with the epoxy to investigate the influence of CNTs on the resistance to delamination at the interface. Due to the fact that delamination at the interface actually propagates through a very thin resin rich layer, adding CNTs to the epoxy may actually result in an increase in the thickness of this resin rich layer. Hence, in the present study, three different resin layer thickness (0.005 mm, 0.01 mm and 0.015 mm) has been considered in order to study the influence of resin layer thickness on delamination resistance. Elastic properties of CNT+epoxy (matrix) and carbon/(CNT+epoxy) composite laminates were shown in **Table 4.1**, which were calculated using Halpin-Tsai equations and the rule of mixtures principle in micromechanics [73] as discussed in section 3.6 of Chapter 3.

A high magnitude of interlaminar stresses induced near the ply break might lead to delamination at the interface of such broken ply and adjacent continuous ply. When such a ply break occurs, it separates from the adjacent intact ply by a very small length. Hence, very small delamination ahead of the ply break at the interface is considered. In order to assess the delamination growth at the interface, stress based criteria and fracture mechanics based criteria could be used. **Figures 4.1(a)** and **4.1(b)** show an exploded view of a laminate with the central ply broken partly through the width and delamination fronts (PQ and RS) respectively.

At the delamination fronts, interlaminar stresses and displacements could be obtained by performing a full three dimensional finite element analysis. Delamination growth at the interface could be assessed by using the obtained out-of-plane stresses $\tau_{xz}$, $\tau_{yz}$, $\sigma_z$ and by using the proper failure criterion. Additionally, the strain energy release rate could be evaluated to assess the propensity of the delamination growth by considering the delamination as an existing crack.

**Table 4.1:** Elastic properties of carbon/(CNT+epoxy) composites [73]

| | Matrix (CNT+epoxy) | | | Composite (Carbon fiber (60%) + (CNT+epoxy)) | | | |
|---|---|---|---|---|---|---|---|
| CNT wt% in epoxy | Tensile modulus (GPa) | Poisson's ratio | Shear modulus (GPa) | Longitudinal tensile modulus $E_1$ (GPa) | Transverse tensile modulus $E_2$ (GPa) | In-plane Poisson's ratio $\nu_{12}$ | In-plane shear modulus $G_{12}$ (GPa) |
| 0.0% | 3.10 | 0.35 | 1.15 | 98.92 | 7.59 | 0.284 | 2.75 |
| 0.25% | 3.46 | 0.35 | 1.28 | 124.48 | 8.46 | 0.284 | 3.07 |
| 0.50% | 3.83 | 0.35 | 1.42 | 128.94 | 9.34 | 0.284 | 3.39 |
| 1.00% | 4.26 | 0.35 | 1.58 | 138.35 | 10.36 | 0.284 | 3.77 |
| 1.50% | 4.41 | 0.35 | 1.63 | 142.58 | 10.72 | 0.284 | 3.89 |

A full 3D FE analysis has been performed using ANSYS general purpose FE software. In order to model the laminate with part-through-the-width ply break (preprocessing) and for obtaining the solution, a code has been developed using ANSYS parametric design language (APDL). In addition, the same code has been used for calculating interlaminar stresses, displacements and components of strain energy release rate (SERR) using virtual crack closure integral (VCCI) (postprocessing).

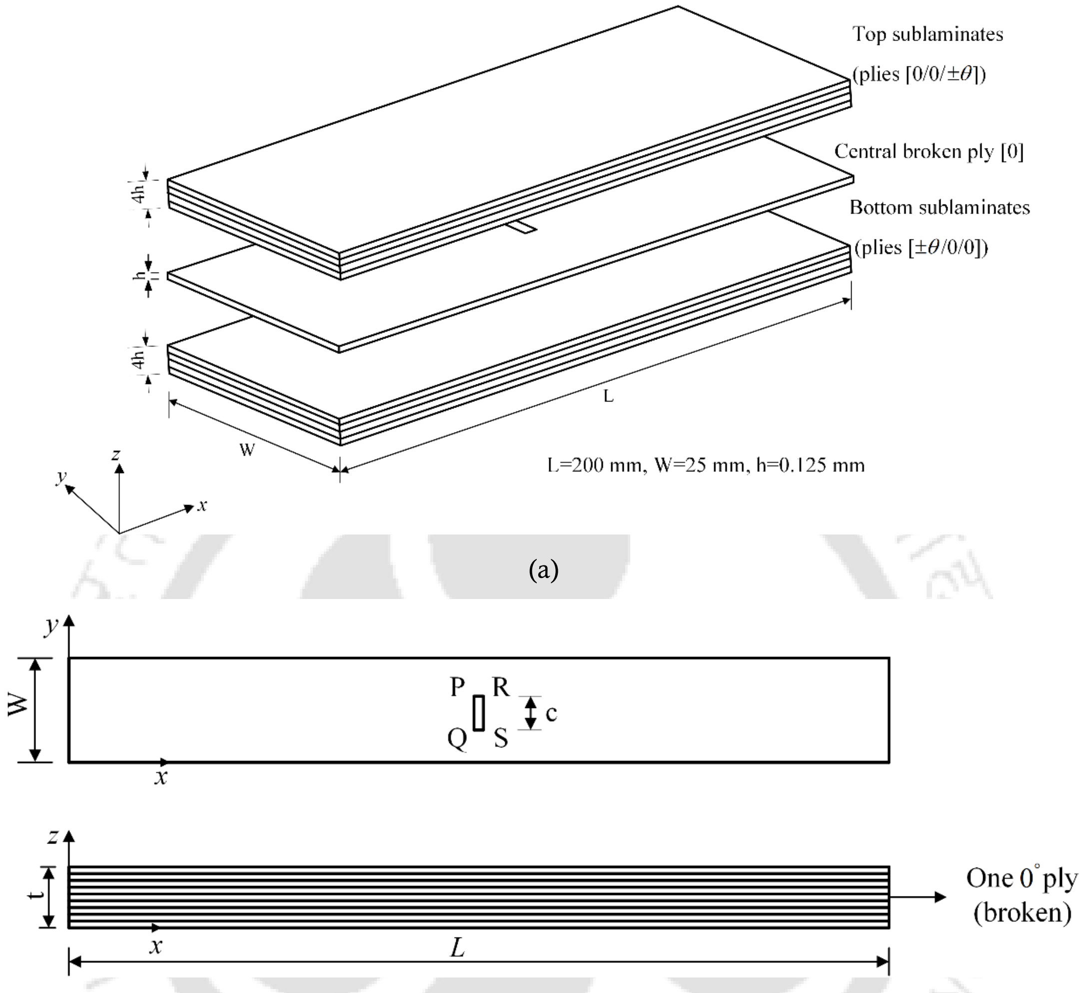

(a)

(b)

**Figure 4.1:** (a) Exploded view of the $\left[0_2/\pm\theta/\bar{0}\right]_s$ laminate with central 0° ply broken partly through the width (b) Front view and top view of laminate interface. PQ and RS are the delamination fronts

Eight noded solid elements (SOLID 185 in ANSYS) [150] with three translational degrees of freedom per node are used for modeling the laminate. The interface between the broken and continuous ply has been modeled in the present FE study with a thin (0.01 mm) resin rich layer since the delamination propagates through a very thin resin layer at the interface [151–152 ]. In order to avoid the interpenetration of the delaminated surfaces in FE analysis, these top and bottom nodes at the delaminated region are connected by bilinear node-to-node contact elements that are embodied in ANSYS as CONTA 178. CONTA 178 [150] is a two noded element with three translational degrees of freedom at each node, allowing small sliding contact and compression. By using the stresses and displacements obtained from the

FE analysis, SERR components are evaluated using the VCCI technique as discussed in section 3.3.1 of Chapter 3

## 4.3 Results and Discussions

A full 3D FE analyses have been performed for different configurations of three phase carbon/(CNT+epoxy) composite laminate consisting of four different weight percentages (0.25%, 0.5%, 1% and 1.5%) of CNTs mixed with epoxy, for four different widths of the ply break ($c$ = 2, 8, 16 and 20 mm), three different resin layer thicknesses ($t_r$ = 0.005, 0.01 and 0.015 mm), and for five different adjacent intact ply angles ($\theta = 0^\circ, 30^\circ, 45^\circ, 60^\circ$ and $90^\circ$).

However, before carrying out the FE analysis of the three phase laminated composite with ply break, validation and convergence of the FEA have been carried out to check the correct computation of SERR components and to decide on the required mesh refinement.

### 4.3.1 Convergence and validation

In order to validate the computation of SERR components using VCCI in the present FE analysis, a double cantilever beam (DCB) specimen (shown in **Fig. 4.2**) made of unidirectional orthotropic carbon/epoxy composite ($E_1$ = 135 GPa, $E_2$ = 10 GPa, $G_{12}$ = 5 GPa and $\nu_{12}$ = 0.3) has been considered. The dimensions (refer to **Fig. 4.2**) of the DCB specimen are 150 mm length (along $x$), 25 mm width ($B$, along $z$), 3 mm thickness ($2h$, along $y$) and 30 mm crack length ($a$). A 3D FE analysis is performed by applying a uniformly distributed load on the beam and mode I SERR ($G_I$) calculated from the present FEA is compared with the theoretical solution [154] given by

$$G_I = \frac{12P^2a^2}{B^2h^3E_1} \tag{4.1}$$

**Table 4.2** shows the convergence of the solution with successive mesh refinement and it agrees well with the analytical solution [154].

**Table 4.2:** Convergence and validation of FE model

| | $G_I$ (N/mm) | |
|---|---|---|
| Number of elements | Present FE solution | Reference analytical solution [154] |
| 1800 | 0.029 | 0.024 |
| 7200 | 0.028 | |
| 12600 | 0.027 | |
| 18000 | 0.026 | |
| 25200 | 0.024 | |
| 36000 | 0.024 | |

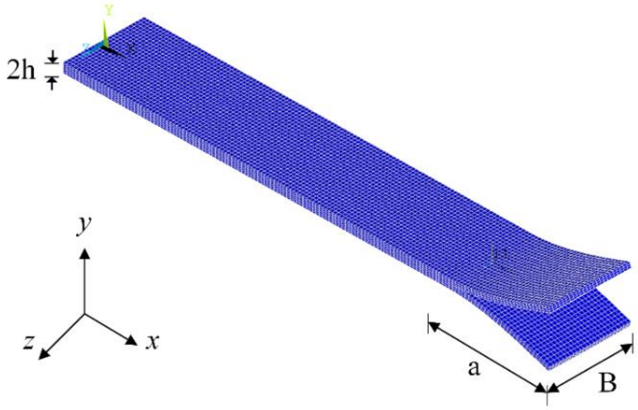

**Figure 4.2:** FE model of DCB orthotropic specimen for evaluating $G_I$

### 4.3.2 Stress distribution

The 3D FE model of the laminated specimen is shown in **Figure 4.3**. The centre ply contains a part-through-the-width ply break, which is embedded and not visible in the FE model. Stress concentration results from the redistribution of stresses near the vicinity of the ply break caused by the ply break. In order to capture the stress gradient of interlaminar stresses, which is necessary for computing SERR components using VCCI, a highly refined mesh near the break is used. The laminate shown in **Fig. 4.3(a)** is subjected to uniaxial loading, which is simulated by using the following boundary conditions.

At $x = 0$, for all nodes, $u_x = u_y = u_z = 0$ and at $x = L$ all the nodes are subjected to uniform axial load. From the current FE analysis, Interlaminar normal and shear stresses induced at the interface of the broken and intact plies are obtained for $\theta = 0^\circ$. With those interlaminar stresses and displacements computed from FEA, SERR components have been evaluated using VCCI as described in section 3.3.1 of Chapter 3.

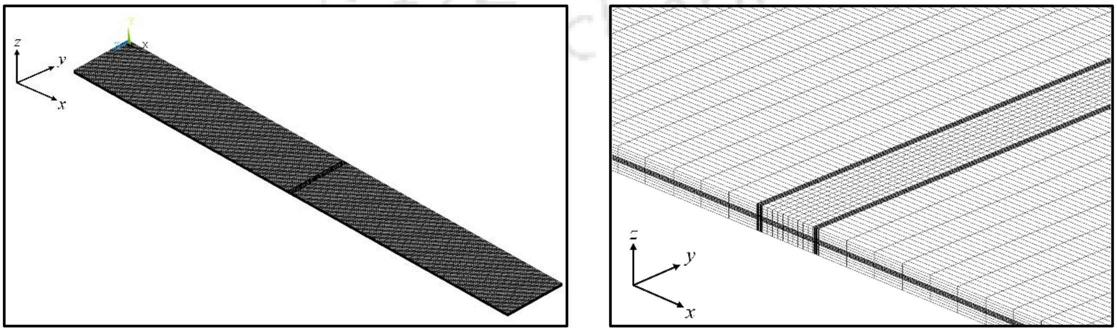

(a) (b)

**Figure 4.3**: (a) 3D FE model of the laminate (b) zoomed view near the ply break

In order to capture the interlaminar stresses accurately a highly refined mesh near the ply break has been used. **Figure 4.4** shows the convergence of interlaminar shear stress with successive mesh refinement and as listed in **Table 4.3**, there has not been any change in the magnitude of the maximum interlaminar stresses beyond 5,79,600 elements. Based on the convergence study, the laminate is modeled by 5,79,600 solid 185 elements and the top and bottom delaminated surfaces are connected by 396 CONTA 178 elements.

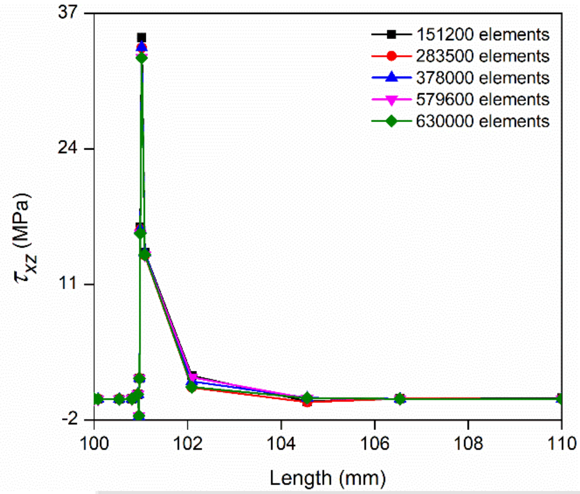

**Figure 4.4:** FE mesh convergence of a carbon/epoxy composite ($c$ = 2 mm, $\theta = 0^{\circ}$)

**Table 4.3:** Convergence of FE Mesh

| Mesh number | Number of elements | $\tau_{xz}$ (MPa) |
|---|---|---|
| 1 | 151200 | 34.6 |
| 2 | 283500 | 33.7 |
| 3 | 378000 | 33.7 |
| 4 | 579600 | 32.7 |
| 5 | 630000 | 32.7 |

#### 4.3.2.1 *Axial stresses along the length of plies*

In absence of a ply break, the axial load is equally shared by all the plies. But as a result of ply break, there is a redistribution of axial stresses near the ply break and the axial stresses on the adjacent intact plies increase. **Figure 4.5** shows the distribution of axial stress ($\sigma_x$) in the broken as well as in the intact plies of a $\left[0^{\circ}\right]_9$ carbon/epoxy laminate corresponding to a ply break width, $c$ = 2 mm. Since the stress distribution is symmetric on either side of the delamination, stress variation over only one half of the laminate length is shown. It is clear from the stress plot that the redistribution of axial stress takes place in the vicinity of the ply break only over a small length and it reaches the nominal value away from the break. **Figure 4.5** also shows that the stress in the broken ply is zero over a small distance near the ply break indicating that it is ineffective over that distance and as a result, the neighboring intact plies get overstressed with the adjacent ply experiencing the highest stress concentration of 1.2 increasing the chances of failure. However, at a small distance away from the ply break (in this case, it is 5 mm), the stress in the broken ply reaches the nominal stress and it could participate in load bearing.

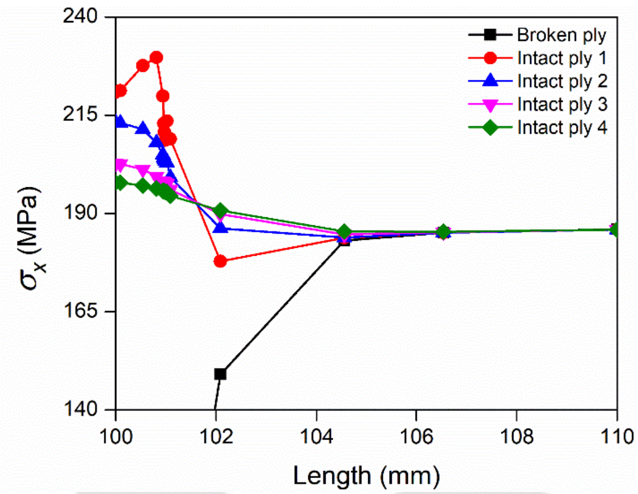

**Figure 4.5:** Variation of $\sigma_x$ along the length of broken and intact plies

### *4.3.2.2 Effect of ply break width on axial stresses of an adjacent intact ply*

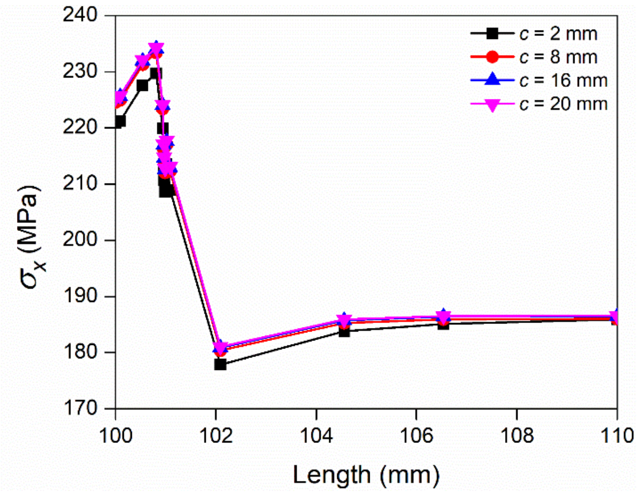

**Figure 4.6:** Variation of $\sigma_x$ along the length of adjacent intact ply

It could be clearly seen from **Fig. 4.5**, adjacent intact ply near to broken ply experiences stress concentration enhancing the chance of tensile failure of the adjacent ply. Hence, it is important to understand the influence of ply break width (*c*) on such stress concentration of axial stresses in adjacent intact plies. **Figure 4.6** shows the distribution of axial stress ($\sigma_x$) in the adjacent intact ply of carbon/epoxy laminate corresponding to different ply break widths.

It is clear from **Fig. 4.6** that as the ply break width increases, axial stress in the adjacent intact ply increases initially when the width increases from $c = 2$ mm to $c = 8$ mm but as the width approaches the full width, it is insignificant. In the present case, as the ply break width increases from $c = 2$ mm to $c = 8$ mm, the stress concentration increases from 1.2 to 1.24 and thereafter almost constant. This shows that a smaller width ply break grows to a larger width ply break.

### *4.3.2.3 Interlaminar stresses along the interface*

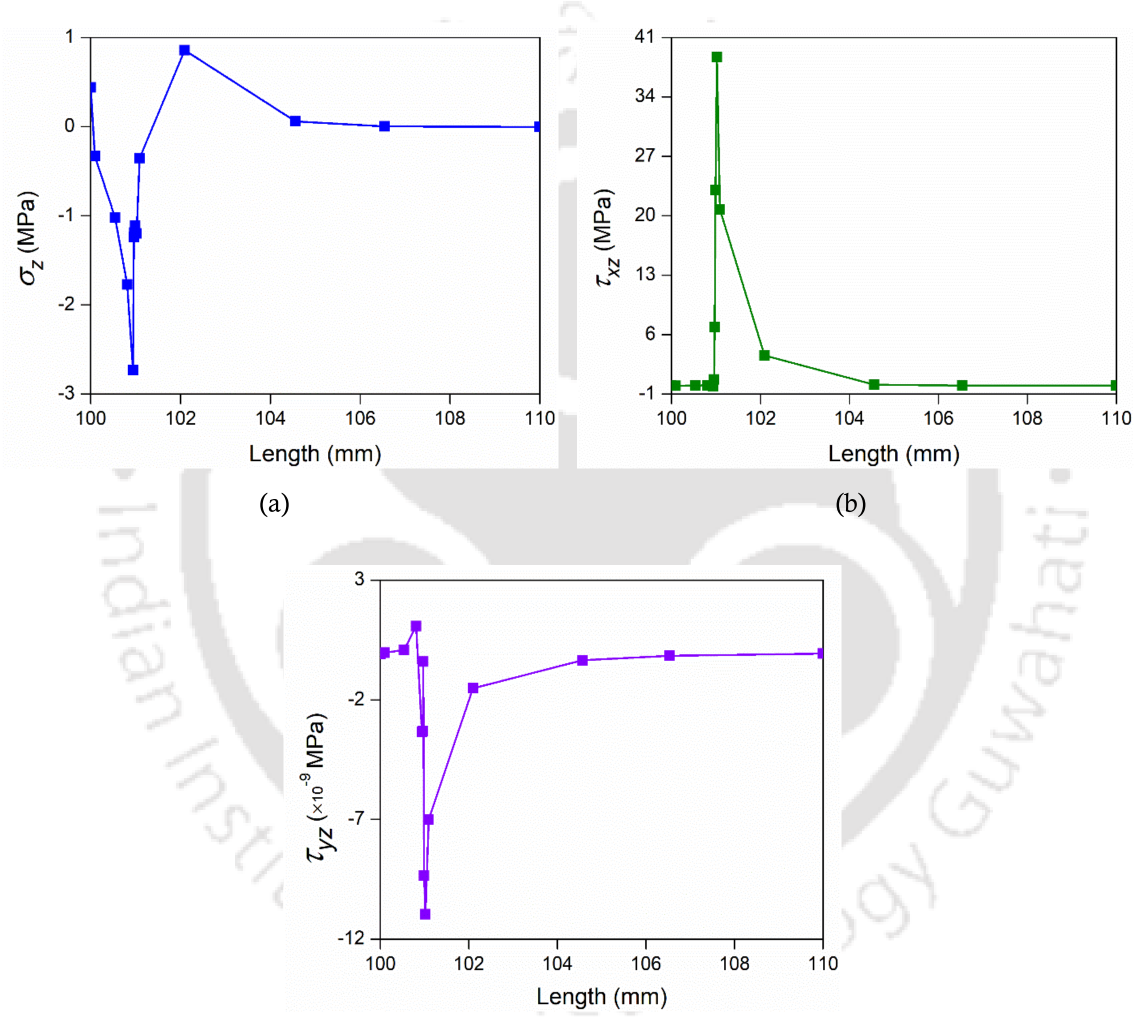

(a) (b)

(c)

**Figure 4.7:** Variation of (a) $\sigma_z$ (b) $\tau_{xz}$ (c) $\tau_{yz}$ along the interface

Since at the tip of the break, the axial stress in the broken ply is zero but at a certain distance ahead of the break, the axial stress is fully developed, therefore, interlaminar stresses are developed at the interface of the broken and intact plies near the ply break. **Figures 4.7(a), 4.7(b)** and **4.7(c)** show the distribution of interlaminar normal stress ($\sigma_z$), interlaminar shear stress, $\tau_{xz}$ and interlaminar shear stress, $\tau_{yz}$ respectively along the interface of the broken and intact plies for a ply break width of $c$ = 2 mm. It is observed that in all the cases, the magnitudes of interlaminar stresses ($\sigma_z$ , $\tau_{xz}$ and $\tau_{yz}$) at the interface increase sharply in the vicinity of the ply break and away from the break these stresses die down to zero. Since the interlaminar stresses exist only over a small length along the interface of the broken and adjacent intact plies, for a clear demonstration of interlaminar stress variation, the stresses are plotted over a small length along the interface instead of the full length. Beyond that length, the interlaminar stresses are zero. Interlaminar stresses $\sigma_z$, $\tau_{xz}$ and $\tau_{yz}$ are responsible for delamination at the interface. In the present case of axial loading of the laminate, $\tau_{xz}$ is significantly higher compared to $\sigma_z$ and $\tau_{yz}$. Also, negative value of $\sigma_z$ shows that opening mode of delamination is absent and a very small magnitude of $\tau_{yz}$ indicates that anti-plane shear mode is insignificant and the only dominant mode of delamination is shearing mode.

#### 4.3.2.4 *Effect of CNT wt% and resin thickness on interlaminar stresses*

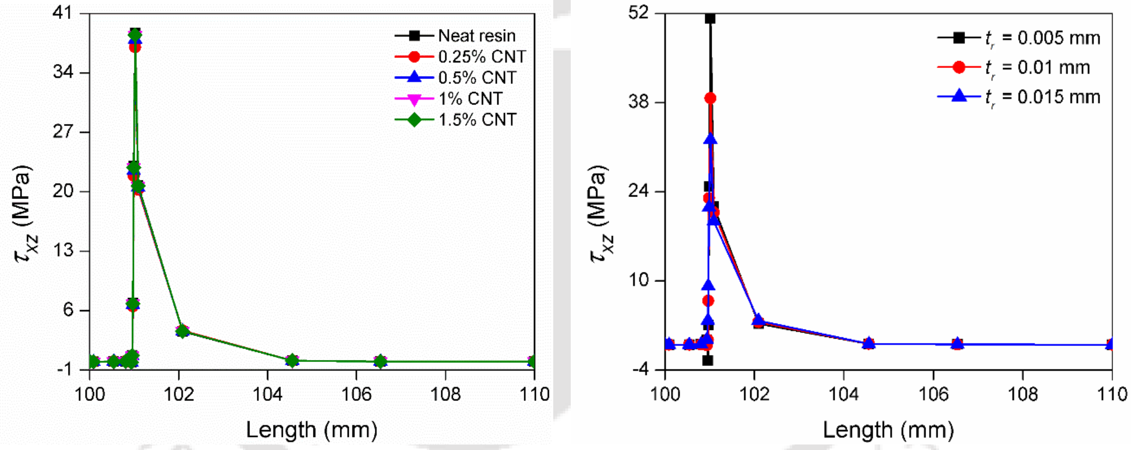

(a) (b)

**Figure 4.8:** Variation of $\tau_{xz}$ along the interface (a) for different CNT wt% (b) for different resin thickness

Since only $\tau_{xz}$ is the dominant interlaminar stress, variation of $\tau_{xz}$ along the interface of the broken and intact plies for different wt% of CNT in resin and for different resin thickness has been studied to understand the influence of CNT wt% and resin thickness on the interlaminar stresses. **Figure 4.8(a)** shows that magnitude of $\tau_{xz}$ does not change significantly with the inclusion of CNTs in the epoxy. This is due to the fact that the axial stress in the broken and continuous plies do not depend on the materials properties and the development of shear stress at the interface is due to the difference in axial stresses in the broken and intact plies. However, as shown in **Fig. 4.8(b)**, magnitude of $\tau_{xz}$ decreases significantly as the resin layer thickness is increased and as a result the chance of delamination at the interface of the broken and intact plies decreases. These figures are corresponding to a ply break width $c$ = 2 mm. However, similar trends were observed for other values of $c$ also.

### *4.3.2.5 Effect of ply break width and intact ply orientation on interlaminar stresses*

In order to understand the influence of ply break width, interlaminar stresses have been computed for carbon/epoxy neat composites having different ply break widths ($c$ = 2 mm, 8 mm, 16 mm and 20 mm) with a resin thickness of 0.01 mm. **Figure 4.9(a)** shows the variation of interlaminar stress ($\tau_{xz}$) with increasing ply break width and for corresponding to a resin thickness of $t_r$ = 0.01 mm. It could be clearly seen that even though the increase in $\tau_{xz}$ with the increase in ply break width is not that significant.

In order to understand the influence of adjacent intact ply angle, interlaminar stresses have been computed for carbon/epoxy neat composites having ply angles varying from $\theta = 0^{\circ}$ to $90^{\circ}$ with $t_r$ = 0.01 mm and $c$ = 2 mm is considered. **Figure 4.9(b)** shows the variation of $\tau_{xz}$ for different ply angles along the interface and it has been observed that there is a sharp rise in the magnitude of $\tau_{xz}$ near the ply break and decrease to zero away from the ply break. It could also be seen that $\tau_{xz}$ is maximum for $\theta = 30^{\circ}$ subjected to same axial loading.

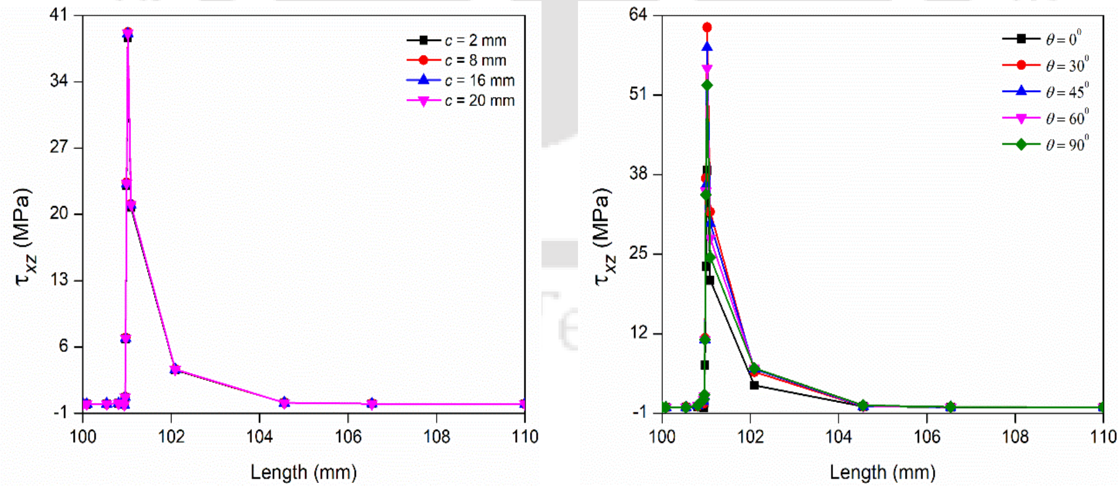

(a) (b)

**Figure 4.9:** Variation of $\tau_{xz}$ along the interface (a) for different ply break width (b) for different ply angle

### 4.3.3 Strain energy release rate around the ply break

Considering the delamination fronts (PQ and RS in **Fig. 4.1**) as the crack fronts, components of strain energy release rate ($G_I, G_{II}, G_{III}$) have been computed using VCCI as described in section 3.3.1 of Chapter 3 for laminates with different wt% of CNTs in epoxy.

#### *4.3.3.1 Effect of CNT wt% on strain energy release rate*

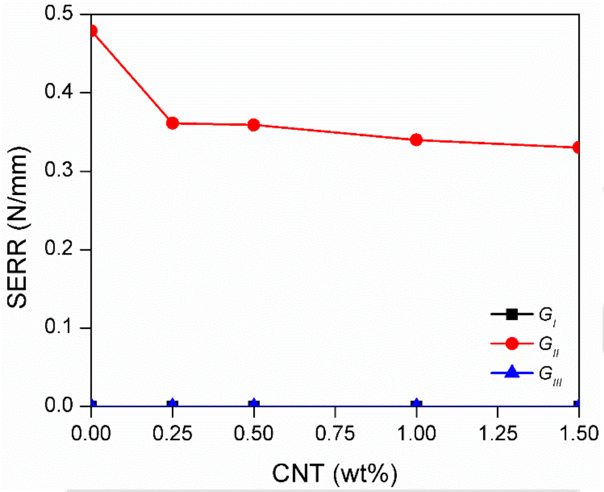

**Figure 4.10:** Variation of $G_I$, $G_{II}$ and $G_{III}$ with different CNT wt%

In order to understand the influence of CNT wt% on SERR, different wt% viz. 0%, 0.25%, 0.5%, 1% and 1.5% are considered and FE analysis have been carried out where components of SERR are calculated using VCCI. **Figure 4.10** shows the variation of $G_I$, $G_{II}$ and $G_{III}$ with different CNT wt% mixed with epoxy for a ply break width of $c$ = 2 mm. As already seen that the interlaminar stresses $\sigma_z$ and $\tau_{yz}$ are insignificant leading to $G_I$ and $G_{III}$ to be negligibly small compared to $G_{II}$ (due to $\tau_{xz}$) which happens to be the dominant mode. The same could be seen in **Fig. 4.10** where $G_I$ and $G_{III}$ are negligibly small compared to $G_{II}$. In addition, it could be seen that addition of CNTs to the epoxy leads to significant reduction in $G_{II}$. This is due to the fact that as the CNTs are mixed with the epoxy, the stiffness increases and as a result the SERR components decrease with the addition of CNTs to the epoxy.

#### *4.3.3.2 Effect of ply break width on strain energy release rate*

In order to understand the influence of ply break width, SERR has been computed for different ply break widths ($c$ = 2 mm, 8 mm, 16 mm and 20 mm) corresponding to different CNT wt%. **Figure 4.11(a)** show the variation of $G_{II}$ with increasing ply break width for different CNT wt% for resin thickness of $t_r = 0.01$ mm. It could be observed that, increase in $G_{II}$ with increasing ply break width is insignificant as was the case for interlaminar stress $\tau_{xz}$.

### 4.3.3.3 *Effect of resin layer thickness on strain energy release rate*

To understand the influence of resin layer thickness on $G_{II}$, $G_{II}$ has been calculated for different resin thicknesses ($t_r$ = 0.005 mm, 0.01 mm, and 0.015 mm) corresponding to the different wt% of CNTs. **Figure 4.11(b)** shows the variation of $G_{II}$ with increasing resin thickness for different wt% of CNTs for a ply break width of $c = 2$ mm. It has been observed that as the resin layer thickness increases, $G_{II}$ slightly increases and the increase is not significant.

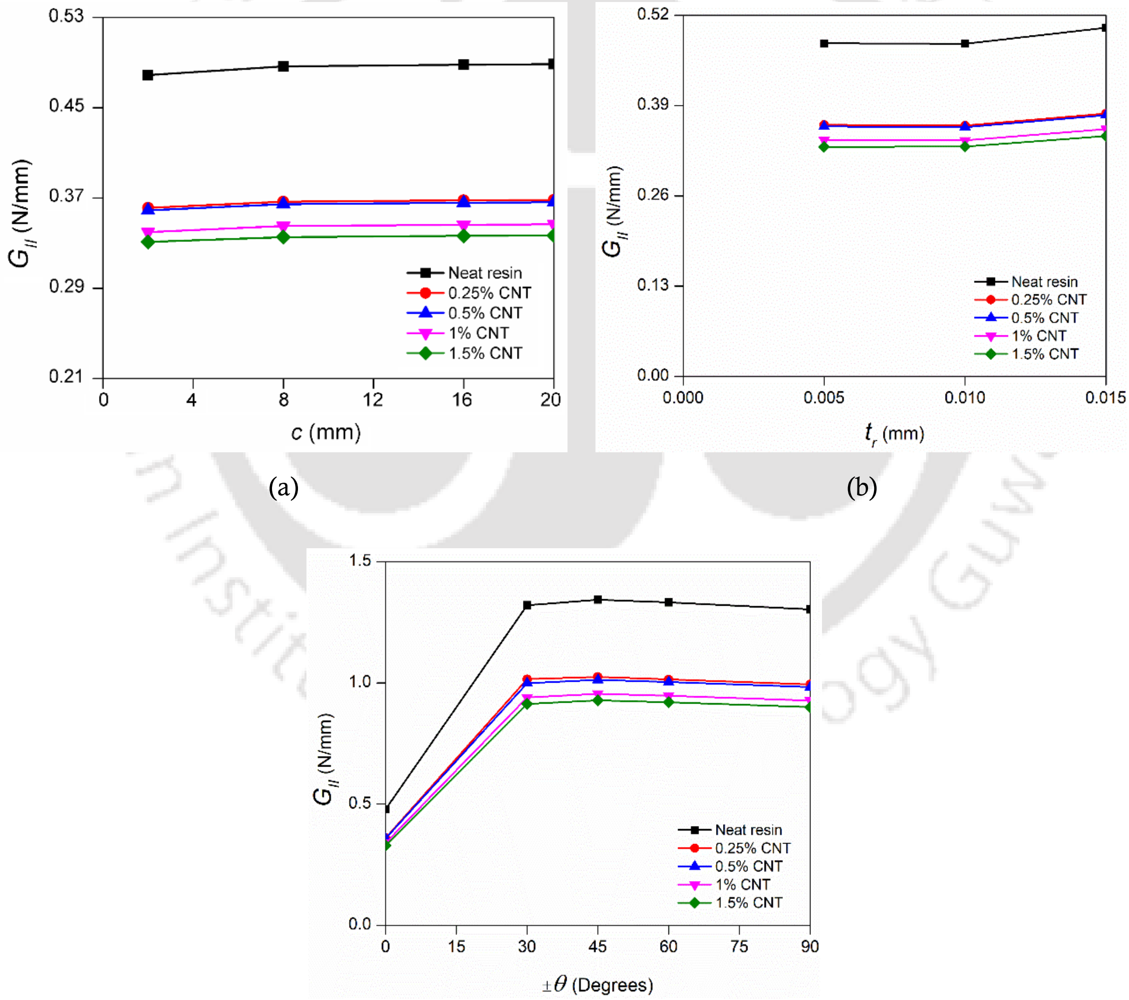

(a) (b)

(c)

**Figure 4.11:** Variation of $G_{II}$ with different (a) ply break width (b) resin thickness (c) ply angle

#### *4.3.3.4 Effect of adjacent intact ply orientation on strain energy release rate*

In order to understand the effect of fiber orientation of neighboring intact ply on $G_{II}$ , $G_{II}$ has been calculated for different fiber orientations ($\theta = 0^\circ$ to $90^\circ$) corresponding to the different wt% of CNTs. **Figure 4.11(c)** shows the variation of $G_{II}$ with increasing fiber orientation for different wt% of CNTs for a ply break width of $c$ = 2 mm. It could be seen that as the fiber orientation angle increases, $G_{II}$ increases significantly up to $\theta = 45^\circ$ and beyond that the increase is not that much significant. This is due to the property mismatch between the adjacent plies.

### 4.3.4 Critical strain energy release rate ($G_c$)

Critical SERR ($G_c$) has been computed for all these laminate configurations following the discussion in section 3.3.3 of Chapter 3 to understand the influence of CNT wt% in epoxy on the resistance to delamination.

#### *4.3.4.1 Effect of CNT wt% on critical SERR*

In order to study the effect of adding CNTs in epoxy on the critical SERR ($G_c$), $G_c$ has been computed for different wt% of CNTs viz. 0%, 0.25%, 0.5%, 1% and 1.5% and plotted as shown in **Fig. 4.12** corresponding to ply break width $c$ = 2 mm. **Figure 4.12** shows that with an increase in the wt% of CNTs, there is a significant increase in $G_c$ **Table 4.4** shows percentage increase in $G_c$ for different CNTs wt% in epoxy. The value of $G_c$ attains maximum corresponding to 1% CNTs which is 36% more than that corresponding to neat resin (0% CNTs). However, with an additional increase in weight % of CNTs beyond 1%, $G_c$ decreases again despite it being greater than that corresponding to neat resin. Hence, $G_c$ being a measure of the laminate's resistance to delamination at the interface, the results from the current study clearly confirm that addition of CNTs to the epoxy enhances the resistance to delamination at the interface of partly broken ply and intact plies. However, there is an upper limit to the weight percentage of CNTs to be added to the epoxy to achieve maximum resistance, which is 1% in the present case but may vary depending on the type of laminates. Similar results were also reported in the experimental results [155] where the interface strength of laminates was observed to increase with increase in carbon nanofillers only up to a certain weight percentage and in [156] where a full width ply break was considered.

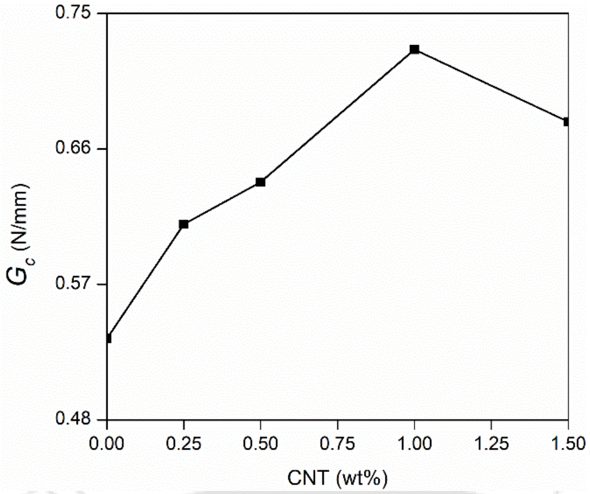

**Figure 4.12:** Variation of $G_c$ with CNT wt%

**Table 4.4:** Percentage increase in $G_c$ with CNT wt%

| S. No | % (weight) CNT | % increase in $G_c$ |
|---|---|---|
| 1 | 0 | -- |
| 2 | 0.25 | 14% |
| 3 | 0.5 | 19% |
| 4 | 1 | 36% |
| 5 | 1.5 | 27% |

### *4.3.4.2 Effect of ply break width on critical SERR*

**Figure 4.13(a)** shows the plot of $G_c$ computed for different ply break width and for different CNT wt%. It could be clearly seen that while the variation of $G_c$ with CNTs wt% show the similar trend for all the ply break widths, $G_c$ is independent of ply break width showing that $G_c$ is constant for a given laminate.

### *4.3.4.3 Effect of resin layer thickness on critical SERR*

Since addition of CNTs may lead to increase in thickness of the resin layer, influence of resin layer thickness on the critical SERR ($G_c$) has been studied by varying the thickness of resin layer at the interface between the broken and adjacent continuous plies between 0.05 to 0.15 times the ply thickness and $G_c$ is computed for all the cases. **Figure 4.13(b)** shows the variation of $G_c$ with resin layer thickness for different weight percentages of CNTs in epoxy. It is observed that in all the cases, when resin layer thickness is increased from 0.005 mm to 0.015 mm, $G_c$ increases by 42% showing that thicker the resin, more will be the resistance to delamination at the interface of the broken and intact ply in a three phase carbon/(CNT+epoxy) laminate having a part-through-the-width ply break.

#### 4.3.4.4 *Effect of adjacent intact ply orientation on critical SERR*

**Figure 4.13(c)** shows the effect of fiber orientation of adjacent lamina on $G_c$ of the laminate for different wt% of CNTs in epoxy. It could be clearly seen that in all cases, as the fiber orientation changed from $0^\circ$ to $90^\circ$, critical strain energy release rate increases (by 20%) significantly till $60^\circ$ and after that remains almost same which shows more resistance to delamination at the interface of the broken and intact ply of a laminate having a part-through-the-width ply break.

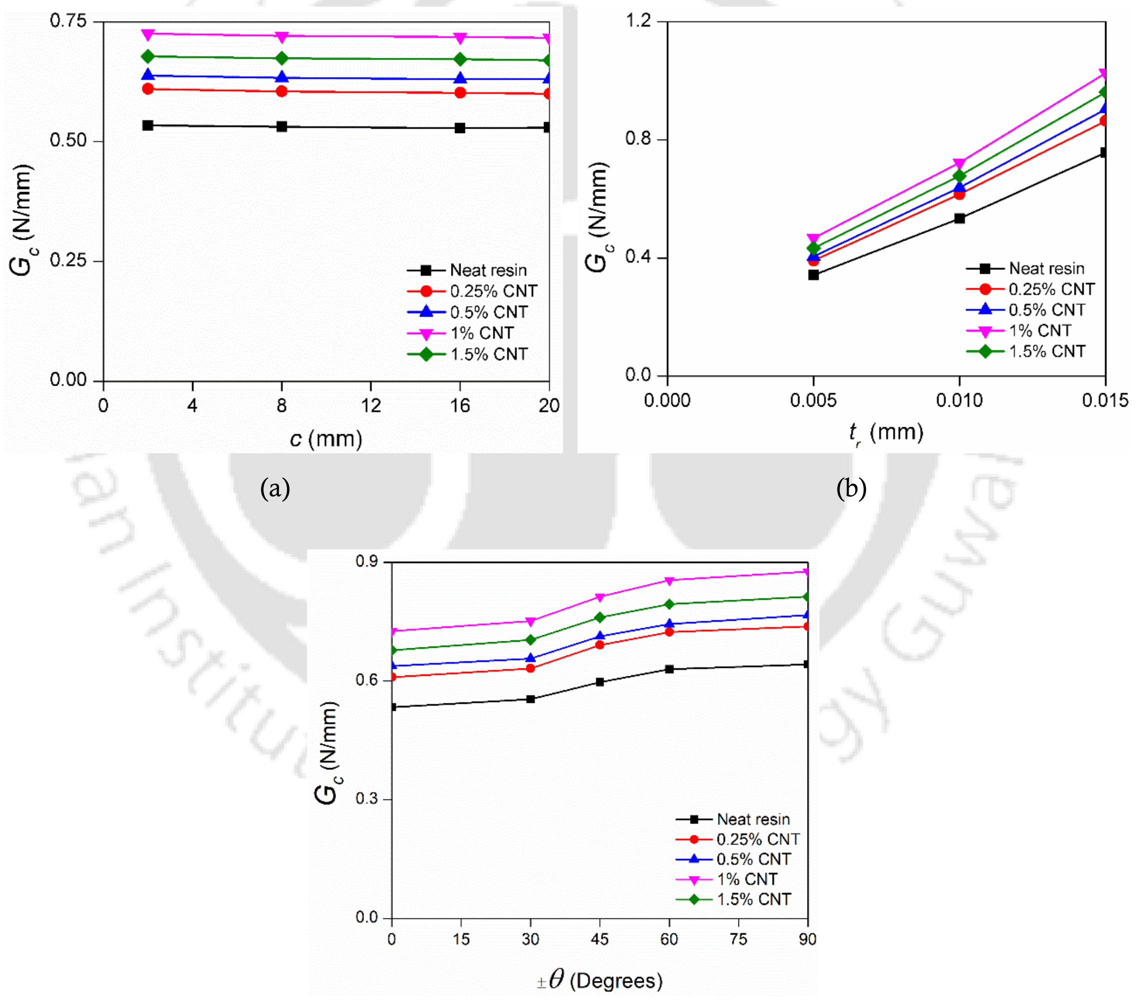

(a) (b)

(c)

**Figure 4.13:** Variation of $G_c$ with (a) different ply break width (b) different resin thickness (c) different ply angle

## 4.4 Summary

In the present chapter, the influence of adding CNTs to adhesive resin on the resistance to delamination at the interface of broken and continuous plies in a laminate having a part-through-the-width ply break has been studied. A full 3D finite element analysis has been carried out to compute interlaminar stresses and critical SERR to understand the influence of adding CNTs to epoxy on the resistance to delamination growth at the interface. The following important observations have been drawn from numerical results

- Both in-plane and out-of-plane stresses are induced at the interface of the broken and intact plies due to ply break. The stresses get redistributed in the vicinity of the ply break over a small length, leading to a stress concentration, and reach the nominal value away from the break.
- For smaller width ply break, as the ply break width increases the stress concentration in the adjacent intact ply increases but as the ply break width approaches the full width it is insignificant. In the present case, as the ply break width increases from $c$ = 2 mm to $c$ = 8 mm, the stress concentration increases from 1.2 to 1.24 and thereafter almost constant. This shows that a smaller width ply break grows to a larger width ply break.
- In the vicinity of the ply break at the interface between the broken and intact plies, though all the three out-of-plane interlaminar stresses are present, in the case of axial loading of the laminate, $\tau_{xz}$ is significantly higher compared to $\sigma_z$ and $\tau_{yz}$, which indicates the dominant mode of delamination is the shearing mode.
- The magnitude of $\tau_{xz}$ decreases with an increase in resin layer thickness showing that thicker the interfacial resin layer less is the chance of delamination.
- The magnitude of $\tau_{xz}$ does not change significantly with the inclusion of CNTs in the epoxy.
- The magnitude of $\tau_{xz}$ though does not change significantly with increasing ply break width however strongly influenced by the relative ply orientation ($\theta$) at the interface of broken and intact plies. This is same for all cases of CNT wt%.
- The fact that the interlaminar stresses $\sigma_z$ and $\tau_{yz}$ are insignificant compared to $\tau_{xz}$ is reflected in the SERR components and it was observed that $G_I$ (due to $\sigma_z$) and $G_{III}$ (due to $\tau_{yz}$) were negligibly small compared to $G_{II}$ (due to $\tau_{xz}$) which happens to be the dominant mode.

- The increase in mode II SERR $G_{II}$ with increasing ply break width is insignificant as was the case for interlaminar stress $\tau_{xz}$.
- As the resin layer thickness increases, $G_{II}$ increases and the increase is not very significant.
- As the adjacent intact ply angle increases, $G_{II}$ increases significantly up to $\theta = 45°$ and beyond that the increase is not much significant
- Variation of critical SERR with CNT wt% shows that modification of epoxy by the addition of CNTs to it significantly improves the resistance to delamination at the interface of broken and intact plies in FRP laminated composites. Therefore, the use of CNTs in epoxy is recommended in those cases where the laminate might encounter low velocity impact leading to ply break.
- Increase in CNT wt% added to epoxy leads to increase in resistance to delamination at the interface, up to a certain wt% of CNTs only, and adding CNTs to epoxy beyond that it leads to reduction in critical SERR.
- In the present case of carbon/(CNT+epoxy) with ply break, critical SERR was observed to increase with the addition of CNT wt% till 1 wt% of CNTs, and adding CNTs beyond 1% leads to a reduction in delamination resistance though it is still more than that corresponding to neat epoxy (0 wt% of CNT). Therefore, it is important to determine the optimum percentage of CNTs to be added to the epoxy to achieve the best resistance against delamination.
- Adding only 1 wt% of CNT to epoxy leads to 36% increase in resistance against delamination growth at the interface in case of broken ply.
- The resin rich layer between the plies plays an important role in resistance to delamination growth at the interface. Thicker is the resin rich layer more is the resistance to delamination growth.
- The fiber orientation of adjacent intact ply plays an important role in interfacial delamination growth. For a $\left[0_2/\pm\theta/\bar{0}\right]_s$ carbon/(CNT+epoxy) laminate, delamination resistance increases as the fiber orientation angle increases from $0^\circ$ to $90^\circ$ and is maximum for a ply orientation of $\theta = 60^\circ$.
- As expected, critical strain energy release rate is independent of ply break width reinforcing it as a property for a specific laminate.

# CHAPTER 5

# Three phase carbon/(CNT+epoxy) laminates with full width ply break

This chapter presents the FE analysis of three phase carbon/(CNT+epoxy) laminate having a defect in the form of full width ply break. Different configurations of the laminate have been considered to understand the influence of the broken and intact plies. In addition, CNT wt% has been considered to understand the influence of the CNT wt% on the delamination.

## 5.1 Introduction

Composite laminated structures are often subjected to low velocity impact, which may cause fiber/ply breakage in certain plies, which leads to partly through the thickness ply breakage. This ply break resembles an internal sub-surface crack (not visible) and as a result, the adjacent continuous plies experience stress concentration and a shear stress concentration occurs at the interface. The interface in the vicinity of ply break becomes the weakest point in the laminate and delamination initiates and propagates at the interface. This induced delamination causes degradation of the strength in the laminate, leading to the final fracture. Therefore, it is important to understand such delamination initiation and propagation and the factors affecting the same.

## 5.2 Laminate specimen and FE modeling

Due to the fact that at the interface of broken and continuous ply the out-of-plane normal and shear stresses cause delamination, a full three dimensional (3D) stress analysis needs to be carried out to model such delamination.

A $\left[0_2/\pm\theta/\bar{0}\right]_s$ three phase carbon/(CNT+epoxy) laminate (as shown in **Fig. 5.1**) has been considered where the central lamina is considered broken and the laminate is subjected to axial load. A full 3D finite element analysis has been carried out in ANSYS. A code has been developed using ANSYS parametric design language (APDL) for modeling the laminate with a ply break, to obtain the displacements, interlaminar stresses, and strain energy release rate (SERR) components using virtual crack closure integral (VCCI).

The laminate has been modeled using eight noded layered solid elements (SOLID 185 in ANSYS). As ply breaks, broken ply separates from the adjacent intact ply over a small length near the break. This is included in the present FE model by considering a small delaminated zone of length 0.1 mm ahead of the ply break. Additionally, a thin (0.01 mm) resin rich layer (CNT+epoxy) is modeled at the interface between the broken ply and the adjacent intact ply in the FE model, where delamination actually propagates. To avoid interpenetration of delaminated layers in the FE model, the top and bottom nodes in the small delaminated zone are connected by two noded contact elements (CONTA 178 in ANSYS).

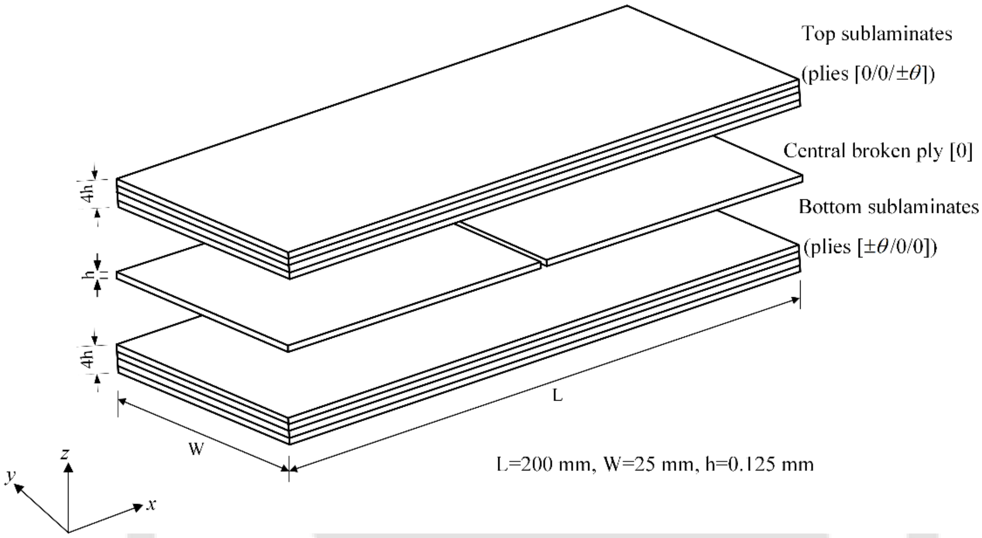

**Figure 5.1:** Exploded view of the laminate with a broken central ply

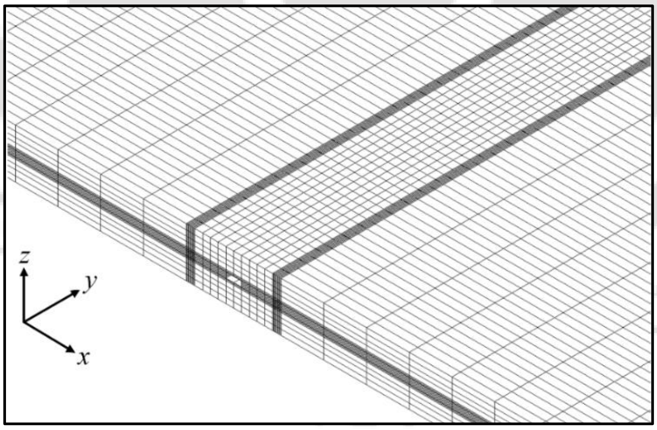

**Figure 5.2:** Zoomed view of FE mesh near the ply break

A 3D FE mesh of the laminate zoomed near the ply break is shown in **Fig. 5.2**. In order to capture the high stress gradient and to calculate SERR using VCCI, a highly refined mesh is used near the ply break. The nodes at one end of the laminate have all been constrained, and uniform axial loading has been applied to the nodes at the other end to simulate axial loading.

In the present work, carbon fiber is considered as the main reinforcement (60% fiber volume fraction) in the laminate, while epoxy mixed with CNTs used as a modified resin for binding fibers. To examine how CNTs influence the resistance to delamination at the interface of broken and intact plies, different weight percentages of CNTs in the epoxy are considered. To further investigate the impact of laminate thickness on the resistance to delamination initiation, the number of plies in the laminate is further varied (keeping the central ply broken). The properties considered in the present FE analysis are as shown in **Table 5.1** which have been calculated using Halpin-Tsai and rule of mixtures [73] as discussed in section 3.6 of Chapter 3. Halpin-Tsai equations were used to calculate the matrix properties corresponding to various CNT weight percentages [153] and using these matrix properties and the carbon fiber (T700) properties, the three phase carbon/(CNT+epoxy) composite properties were then calculated using the micromechanics rule of mixtures.

**Table 5.1:** Elastic properties of carbon/(CNT+epoxy) composites [73]

| | Matrix (CNT+epoxy) | | | Composite (Carbon fiber (60%) + (CNT+epoxy)) | | | |
|---|---|---|---|---|---|---|---|
| CNT wt% in epoxy | Tensile modulus (GPa) | Poisson's ratio | Shear modulus (GPa) | Longitudinal tensile modulus $E_1$ (GPa) | Transverse tensile modulus $E_2$ (GPa) | In-plane Poisson's ratio $\nu_{12}$ | In-plane shear modulus $G_{12}$ (GPa) |
| 0.0% | 3.10 | 0.35 | 1.15 | 98.92 | 7.59 | 0.284 | 2.75 |
| 0.25% | 3.46 | 0.35 | 1.28 | 124.48 | 8.46 | 0.284 | 3.07 |
| 0.50% | 3.83 | 0.35 | 1.42 | 128.94 | 9.34 | 0.284 | 3.39 |
| 1.00% | 4.26 | 0.35 | 1.58 | 138.35 | 10.36 | 0.284 | 3.77 |
| 1.50% | 4.41 | 0.35 | 1.63 | 142.58 | 10.72 | 0.284 | 3.89 |

## 5.3 Results and discussion

3D FE analyses have been performed for various configurations of the three phase carbon/(CNT+epoxy) composite laminate based on the FE model presented in section 5.2. The FE model has first been validated and then subsequently used to obtain the stresses and SERR for different configurations of the laminates.

### 5.3.1 Convergence and validation

In order to validate the computation of SERR components using VCCI in the present FE analysis, a double cantilever beam (DCB) specimen (shown in **Fig. 5.3**) made of unidirectional orthotropic carbon/epoxy composite ($E_1$ = 135 GPa, $E_2$ = 10 GPa, $G_{12}$ = 5 GPa and $\nu_{12}$ = 0.3) has been considered. The dimensions (refer to **Fig. 5.3**) of the DCB specimen are 150 mm length (along $x$), 25 mm width ($B$, along $z$), 3 mm thickness ($2h$, along $y$) and 30 mm crack length ($a$). A 3D FE analysis is performed by applying a uniformly distributed load on the beam and mode I SERR ($G_I$) calculated from the present FEA is compared with the theoretical solution [154] given by

$$G_I = \frac{12P^2a^2}{B^2h^3E_1} \tag{5.1}$$

**Table 5.2** shows the convergence of the solution with successive mesh refinement and it agrees well with the analytical solution [154].

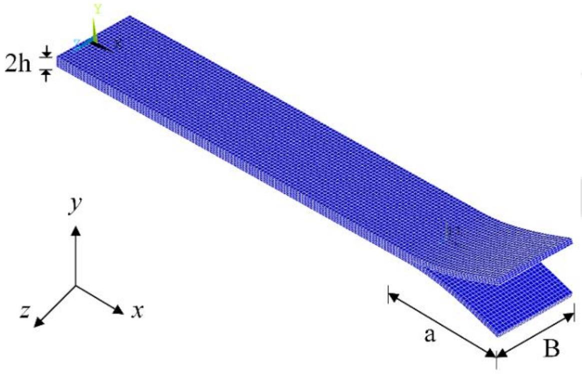

**Figure 5.3:** FE model of DCB orthotropic specimen for evaluating $G_I$

**Table 5.2:** Convergence and validation of FE model

| Number of elements | $G_I$ (N/mm) Present FE solution | Reference analytical solution [154] |
|---|---|---|
| 1800 | 0.029 | 0.024 |
| 7200 | 0.028 | |
| 12600 | 0.027 | |
| 18000 | 0.026 | |
| 25200 | 0.024 | |
| 36000 | 0.024 | |

### 5.3.2 Stress distribution

At the interface in the vicinity of the ply break, both in-plane as well as out-of-plane stresses are observed to have been induced showing that a complete 3D stress state exists there. Using the interlaminar stresses and displacements from the FEA, SERR components have been computed using VCCI as discussed in section 3.3.1 of Chapter 3.

In order to capture the interlaminar stresses accurately a highly refined mesh near the ply break has been used. **Figure 5.4** shows the convergence of interlaminar shear stress with successive mesh refinement and as listed in **Table 5.3**, there has not been any change in the magnitude of the maximum interlaminar stresses beyond 5,21,640 elements. Based on the convergence study, the laminate is modeled by 5,21,640 solid 185 elements and the top and bottom delaminated surfaces are connected by 396 CONTA 178 elements.

**Table 5.3:** Convergence of FE Mesh

| Mesh number | Number of elements | $\tau_{xz}$ (MPa) |
|---|---|---|
| 1 | 151200 | 46.6 |
| 2 | 283500 | 39.8 |
| 3 | 378000 | 39.7 |
| 4 | 521640 | 38.1 |
| 5 | 567000 | 38.1 |

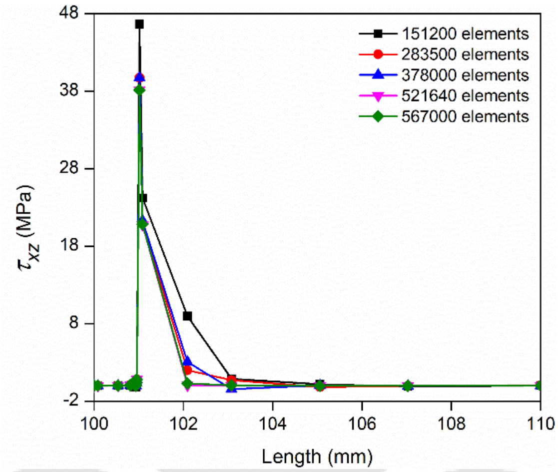

**Figure 5.4:** FE mesh convergence of a carbon/epoxy composite

### 5.3.2.1 *Axial stress along the length of the plies*

The axial stress in the broken and intact plies of the $\left[0_2/\pm\theta/\bar{0}\right]_s$ carbon/(CNT+epoxy) laminate, which corresponds to a 0.25% (weight) CNT and $\theta = 0^\circ$, is shown in **Fig. 5.5**. Only one-half of the laminate's length is shown due to the symmetry of the stress distribution. Additionally, the axial stress distribution is only plotted near the ply break to clearly show the nature of redistribution and the stress concentration in the adjacent plies because the stress is only redistributed over a small area near the ply break and away from the break the stress reaches the nominal stress. It could be observed from **Fig. 5.5** that broken ply experiences zero stress at the break and does not participate in load bearing. As a result, the intact plies experience stress concentration factor (SCF) which is highest for the adjacent ply (SCF=1.4). This shows how the failure of the adjacent intact ply might result in further overloading and failure of other plies. Additionally, it was observed that the broken ply might engage in load carrying at a distance of just 5 mm from the break, at which point the stress reaches the nominal stress. This is due to the ability of the matrix to transfer load between plies.

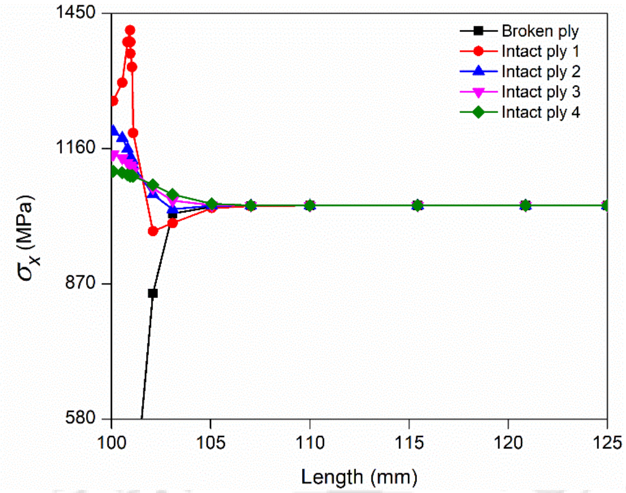

**Figure 5.5:** Axial stress variation along the length of the broken and intact plies

### *5.3.2.2 Interlaminar stresses along the interface*

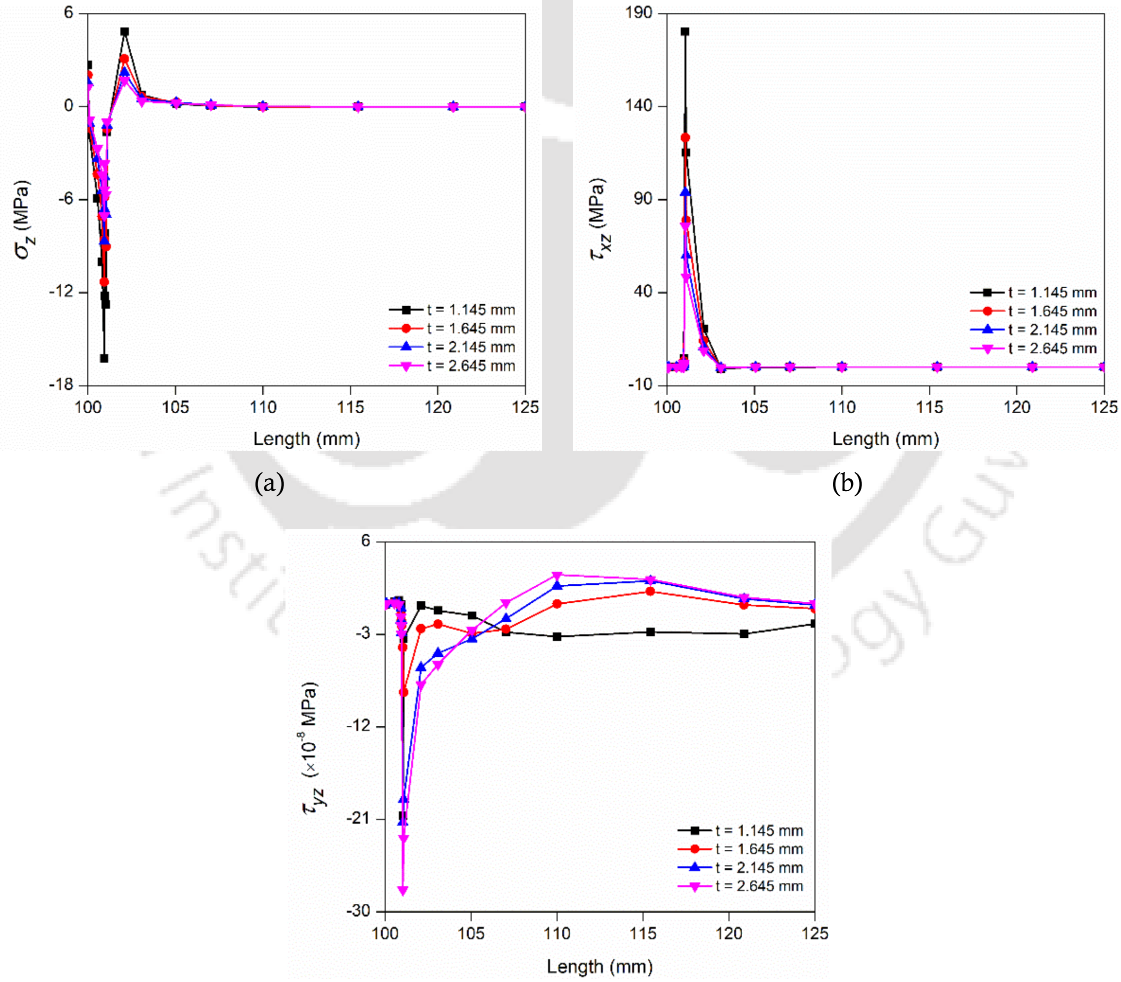

(a) (b)

(c)

**Figure 5.6:** Variation of interlaminar stresses (a) $\sigma_z$ (b) $\tau_{xz}$ (c) $\tau_{yz}$ along the interface of broken and intact plies

**Figures 5.6(a)**, **5.6(b)**, and **5.6(c)** show the variation of the interlaminar normal stress, $\sigma_z$ (opening mode), the interlaminar shear stress, $\tau_{xz}$ (shearing mode), and the interlaminar shear stress, $\tau_{yz}$ (tearing mode) along the interface of the broken and intact plies for various laminate thicknesses (corresponding $\left[0^{\circ}\right]_9$, $\left[0^{\circ}\right]_{13}$ $\left[0^{\circ}\right]_{17}$ and $\left[0^{\circ}\right]_{21}$), where in each case the central ply is considered to be broken. It is evident that there is a sharp increase in magnitudes near the ply break in each case of interlaminar stresses ($\sigma_z$ , $\tau_{xz}$ and $\tau_{yz}$) at the interface, and away from the break, these stresses become zero. However, it is clear that the magnitude of $\tau_{xz}$ is far greater than that of $\sigma_z$ and $\tau_{yz}$. The presence of interlaminar stresses still suggests that there is a possibility of delamination at the interface. However, for the axial loading of the laminate under consideration, only shearing mode dominates, and the other two modes are insignificant. Additionally, it is observed that as the laminate thickness ($t$) increases, the magnitude of the interlaminar stresses decreases, indicating that thicker laminate, lesser is the chances of delamination at the interface of broken and intact plies.

### 5.3.3 Strain energy release rate ahead of ply break

Considering the delamination front at the interface of the broken and intact plies as the crack front, strain energy release rate components ($G_I, G_{II}, G_{III}$) at the delamination front have been calculated using VCCI (as discussed in section 3.3.1 of Chapter 3) for laminates with different weight percentages of CNTs in epoxy.

#### *5.3.3.1 Effect of CNT percentage on SERR components*

The variation of $G_I$, $G_{II}$ and $G_{III}$ with increasing CNT wt% and for different laminate thickness are shown in **Fig. 5.7(a)**, **5.7(b)** and **5.7(c)** respectively. In the present case, it could be seen that, the SERR component in the shear mode ($G_{II}$) is significantly higher than those in the opening mode ($G_I$) and tearing mode ($G_{III}$), which further strengthen that, for an axial loading of a laminate with a broken ply, the shearing mode alone dominates delamination at the interface of broken and intact plies. As the laminate thickness increases, the chances of delamination decrease as the SERR components decrease, which is consistent with variation of interlaminar stresses with thickness.

Most importantly, **Fig. 5.7(b)** shows that once CNTs are added to the epoxy, there is a substantial reduction in $G_{II}$. In fact, in the present case, adding merely 0.25% (weight) CNTs to the epoxy causes a 25% reduction in $G_{II}$ value compared to that of pure resin. With further addition of CNTs, $G_{II}$ decreases further though after 0.5% (weight) the reduction is not significant. This indicates that the addition of CNTs to epoxy reduces the chances of delamination at the interface of the broken and intact plies. However, the critical SERR value determines whether delamination will continue to grow or not and hence it is important to calculate $G_c$ for the same configuration of carbon/(CNT+epoxy) laminate.

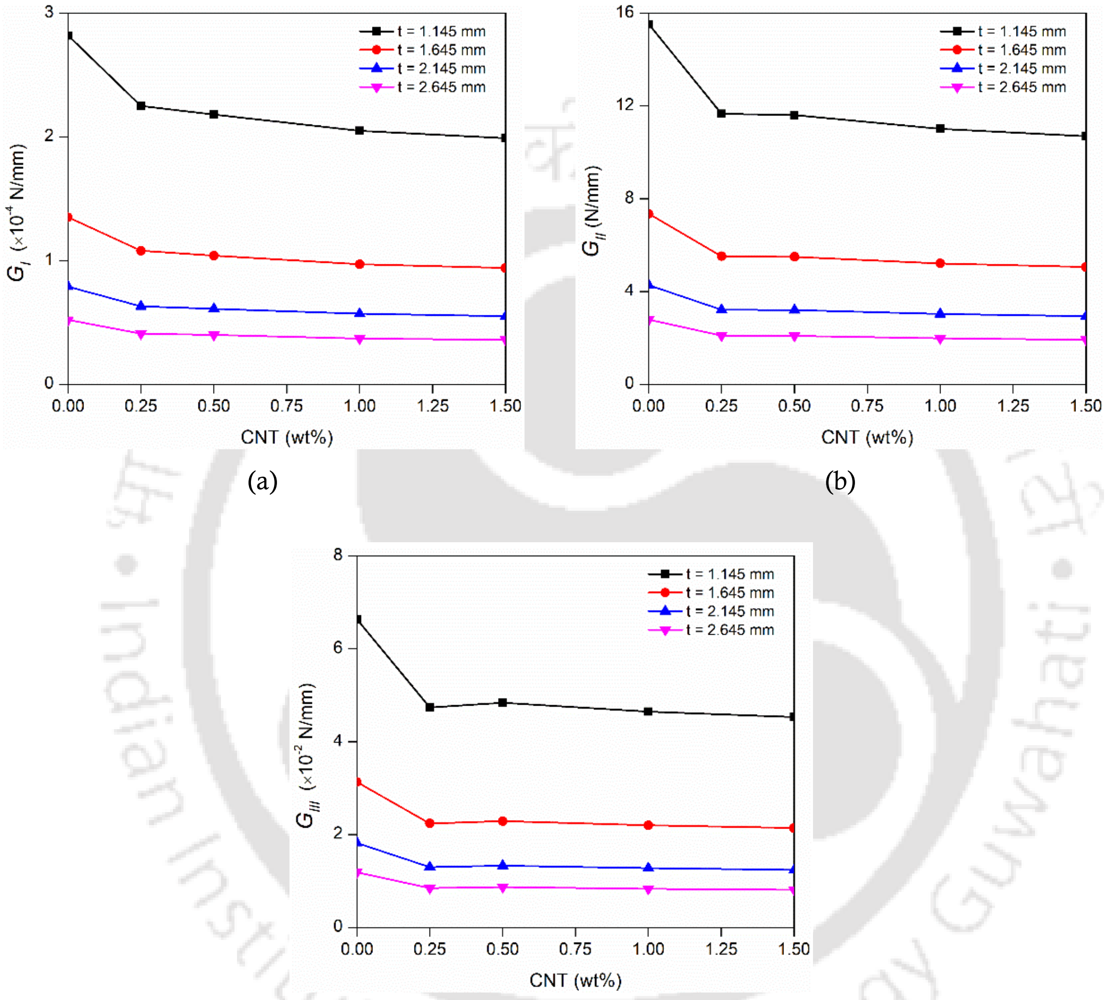

(a) (b)

(c)

**Figure 5.7:** Variation of (a) $G_I$ (b) $G_{II}$ (c) $G_{III}$ with CNT wt%

### 5.3.3.2 *Effect of resin layer thickness on SERR*

To understand the influence of resin layer thickness only the influence on $G_{II}$ has been shown as the other two components are insignificant. Different resin layer thicknesses ($t_r$ = 0.005 mm, 0.01 mm, and 0.015 mm) have been considered along with different wt% of CNTs to understand how the resin layer thickness actually influences the delamination at the interface of the broken and intact plies in a three phase carbon/(CNT+epoxy) composites.

**Figure 5.8(a)** shows the variation of $G_{II}$ with increasing resin thickness for all the wt% of CNTs considered. It has been observed that in all the cases, as the resin layer thickness increases, $G_{II}$ increases but the increase is not significant. However, for all resin layer thicknesses, $G_{II}$ decreases with the increase in CNT wt% indicating that the chances of delamination decreases at the interface.

#### 5.3.3.3 *Effect of adjacent intact ply orientation on SERR*

In order to understand the effect of fiber orientation of neighboring intact ply on mode II SERR, $G_{II}$ has been calculated for different fiber angles ($\theta = 0^\circ, 30^\circ, 45^\circ, 60^\circ$ and $90^\circ$) corresponding to the different wt% of CNTs with a resin layer thickness $t_r = 0.01$ mm. **Figure 5.8(b)** shows the variation of $G_{II}$ with increasing fiber angle for different wt% of CNTs. It could be seen that as the fiber angle increases, $G_{II}$ increases significantly up to $\theta = 45^\circ$ and beyond that the increase is not that much significant. However, for all fiber angles, $G_{II}$ decreases with the increase in CNT wt% indicating that the chances of delamination decreases at the interface.

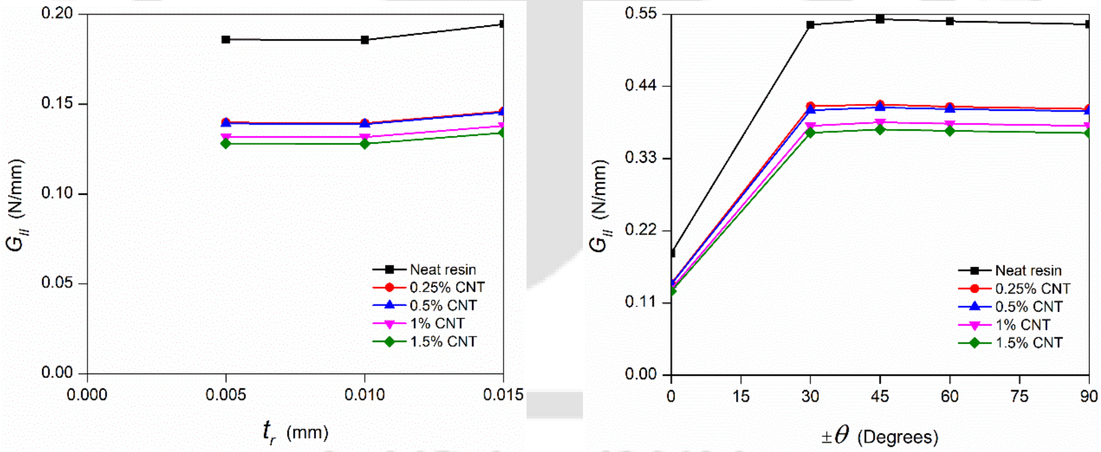

(a) (b)

**Figure 5.8:** Variation of $G_{II}$ (a) with resin layer thickness (b) with intact ply orientation

### 5.3.4 Critical strain energy release rate ($G_c$)

Critical strain energy release rate ($G_c$) value determines whether delamination will continue to grow or not and hence it is important to calculate $G_c$ for all of these laminate configurations using the quadratic stress criteria and VCCI, as discussed in section 3.3.3 of Chapter 3.

### 5.3.4.1 *Effect of CNT wt% on* $G_c$

**Figure 5.9** shows the variation of critical SERR ($G_c$) with CNT wt% in the epoxy in the three phase carbon/(CNT+epoxy) composite laminate. It could be observed that as the CNT wt% increases, there is a significant increase in $G_c$ and the value reaches to its maximum corresponding to 1%, which is 31% higher than that corresponding to of neat resin (0% CNT). **Table 5.4** shows the percentage increase $G_c$ with the addition of CNTs in the epoxy. However, with further increase in CNT wt% beyond 1%, $G_c$ decreases again even though it is more than that of the neat resin. Since $G_c$ in the present case is a measure of resistance of the laminate to delamination at the interface, results from the present study clearly show that adding the CNTs to the epoxy increases the resistance to delamination at the interface of broken and intact plies. However, there is an optimum weight percentage of CNTs to be added to the epoxy in order to obtain the maximum resistance, which is 1% in the present case, but may vary depending on the type of laminates.

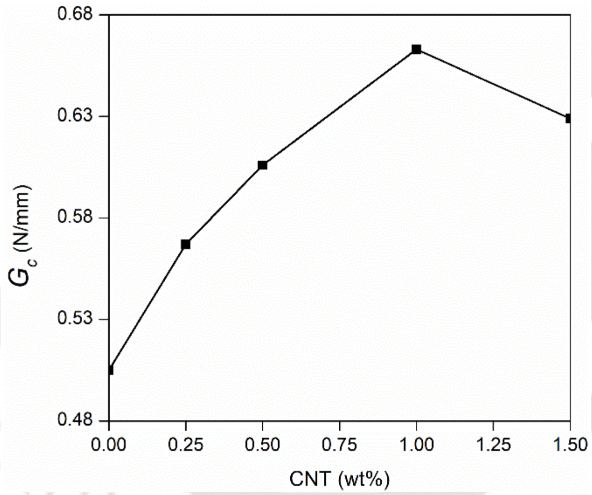

**Figure 5.9:** Variation of $G_c$ with CNT wt%

**Table 5.4:** Percentage increase in $G_c$ with CNT wt%

| S. No | % (weight) CNT | % increase in $G_c$ |
|---|---|---|
| 1 | 0 | -- |
| 2 | 0.25 | 12% |
| 3 | 0.5 | 20% |
| 4 | 1 | 31% |
| 5 | 1.5 | 25% |

#### 5.3.4.2 *Effect of laminate thickness on* $G_c$

**Figure 5.10** shows the variation of $G_c$ with thickness of the laminate for different weight percentages of CNTs in the epoxy. It could be seen that as the thickness of the laminate increases, $G_c$ remains constant in all the cases for a given configuration of the laminate which further shows that $G_c$ for a specific laminate configuration is a property of the laminate.

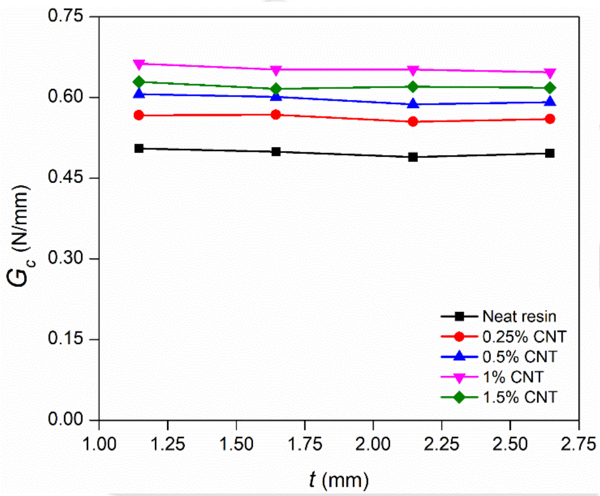

**Figure 5.10:** Variation of $G_c$ with laminate thickness

#### 5.3.4.3 *Effect of resin layer thickness on* $G_c$

**Figure 5.11(a)** shows the variation of $G_c$ with increasing resin layer thickness for different CNT wt% in the epoxy. It could be seen that in all cases, when the thickness of the resin layer is increased from 0.005 mm to 0.015 mm, $G_c$ increased by 43%, indicating that the thicker the resin, the greater the resistance to delamination at the interface of the broken and neighbouring intact ply in a carbon/(CNT+epoxy) composite with central ply broken through the width.

#### 5.3.4.4 *Effect of adjacent intact ply orientation on* $G_c$

**Figure 5.11(b)** shows the effect of fiber orientation of adjacent lamina on $G_c$ of the laminate for different wt% of CNTs in epoxy. It could be clearly seen that in all cases, as the fiber orientation changed from $0^\circ$ to $90^\circ$, critical strain energy release rate increases till $60^\circ$, and beyond that it almost remains same or insignificant change in $G_c$. Similar results were also observed for the part through the thickness ply break also.

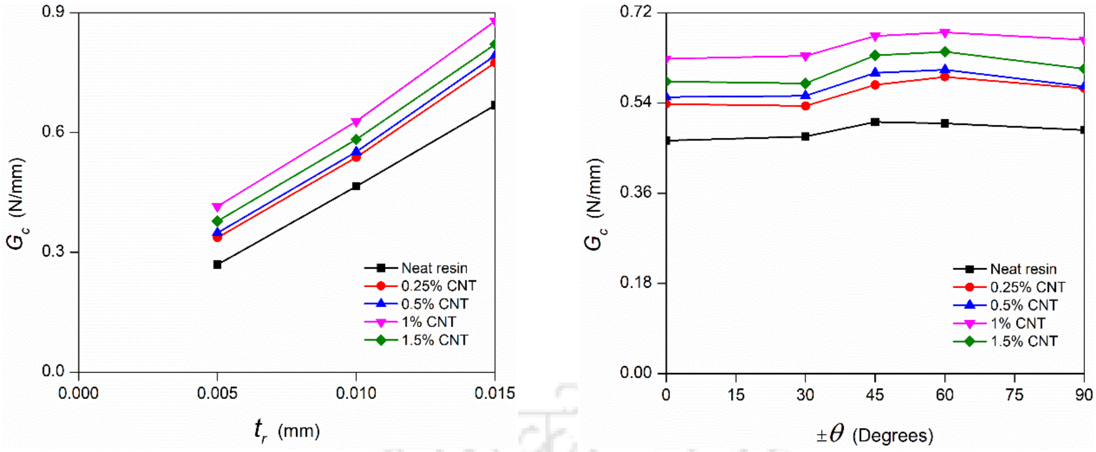

(a) (b)

**Figure 5.11:** Variation of $G_c$ (a) with resin layer thickness (b) with intact ply orientation

## 5.4 Summary

In the present chapter, it has been investigated how CNTs influenced the resistance to delamination at the interface of broken and intact plies in a three phase carbon/(CNT+epoxy) laminated composites where one of the plies has been considered broken through the width. A three dimensional finite element analysis has been performed in order to compute the interlaminar stresses and subsequently, SERR to assess the propensity of the delamination at the interface. In order to understand the influence of CNTs on resistance to interfacial delamination, critical strain energy release rate has also been evaluated for different wt% of CNTs in the epoxy. Some of the important observations from the present study are as follows.

- Due to ply break, at the interface of the broken and intact plies, both in-plane and out-of-plane stresses are induced. Over a small length, in the vicinity of the ply break, the stresses are redistributed leading to a stress concentration, and reach the nominal value away from the break.
- In the case of axial loading, for a 0.25wt% CNT, the intact plies experience stress concentration factor (SCF) which is highest for the adjacent ply (SCF=1.4). This indicates that breaking of one ply results to the overloading of the adjacent intact plies leading to the successive failure of the other plies and hence the laminate.
- Though all the three out-of-plane interlaminar stresses are present in the vicinity of the ply break at the interface between the broken and intact plies, under axial loading of the laminate, $\tau_{xz}$ is much higher compared to $\sigma_z$ and $\tau_{yz}$, showing that the shearing mode is the dominant mode.

- The shear mode SERR ($G_{II}$) is significantly higher than the opening mode SERR ($G_I$) and tearing mode SERR ($G_{III}$), which further strengthens that, for an axial loading of a laminate with a broken ply, the shearing mode alone dominates delamination at the interface of broken and intact plies.
- As the laminate thickness increases, SERR components decreases showing that the chances of delamination decreases, which is consistent with the way interlaminar stresses vary with thickness.
- Addition of CNTs with epoxy leads to a significant reduction in magnitudes of SERR, indicating that the chances of delamination at the interface are reduced significantly. In the present case, adding only 0.25% (weight) of CNTs to the epoxy leads to a 25% reduction in mode II SERR ($G_{II}$).
- The addition of CNTs to epoxy improves the critical SERR ($G_c$), a property of a laminate that measures the resistance to delamination. In the present case, $G_c$ increases by 31% when 1% (weight) CNTs is added to epoxy of the three phase carbon/(CNT+epoxy) laminate in comparison with carbon/epoxy laminate (with neat epoxy).
- Although addition of CNTs with epoxy increases delamination resistance, but beyond a certain limit, further addition of CNTs with epoxy leads to reduction in $G_c$. In the present case of three phase carbon/(CNT+epoxy) composites, it is 1% however, it may change based on the materials used for reinforcement and matrix.
- As the thickness of the laminate increases, $G_c$ remains constant for all the cases of given laminate configurations.
- The resin rich layer at the interface has a significant influence in resisting delamination initiation and growth at the interface. The resistance to delamination initiation and growth increase with the increase in thickness of the resin rich layer.
- Critical SERR depends upon the fiber orientation of intact ply adjacent to broken plies. In the present case of three phase carbon/(CNT+epoxy) composites, critical SERR is observed to increase as the fiber orientation angle increases from $0^\circ - 90^\circ$, reaches maximum at $60^\circ$ and thereafter almost remains constant.

## CHAPTER 6

# Three phase carbon/(CNT+epoxy) laminates with an embedded elliptical delamination

This chapter presents the FEA of a three phase carbon/(CNT+epoxy) laminate having an elliptical embedded delamination at the interface (caused due to low velocity impact) to study the behavior under post impact axial or transverse load. In addition to investigating the important factors affecting growth of such delamination, more importantly it also presents the influence of CNTs on the resistance to delamination from such internal flaws.

## 6.1 Introduction

FRP laminates develop elliptical embedded delaminations at the interface when experiencing low velocity impact. Such delaminations are small in size, more importantly are sub-surface in nature and many a time go unnoticed. However, in post impact loading these grow leading to sudden failure. It is therefore important to study the behavior of a three carbon/(CNT+epoxy) laminate having an embedded delamination, various factors affecting the delamination growth and to understand how adding CNTs to epoxy might lead to improving the resistance to growth of such delaminations at the interface thus preventing catastrophic failure of such laminates.

## 6.2 Problem statement

A square laminate made of carbon/(CNT+epoxy) with stacking sequence $[0/\pm\theta/90]_s$ is considered. An elliptical delamination is considered at the $[0/+\theta]$ interface. The laminate is considered subjected to loading and the influence of adding CNTs to the epoxy in improving the resistance to further growth of such delamination is studied. **Figure 6.1** shows the exploded view of the laminate where the delamination is shown in the thin resin layer between the $[0/+\theta]$ lamina.

## 6.3 Geometry of the specimen and material properties

As shown in **Fig. 6.1**, a three phase carbon/(CNT+epoxy) laminated composite specimen having embedded elliptical delamination is considered. It is reported [157] that under low velocity impact delamination occurs at the interface and is generally elliptical. Therefore, in this case, a square $[0/\pm\theta/90]_s$ laminate is considered and $[0/+\theta]$ the interface has been modeled by a thin resin rich layer containing an elliptical delamination as shown in **Fig. 6.1**. The laminated specimen is of 100 mm length (*L*), 100 mm wide (*W*) and the ply thickness is 0.127 mm. The embedded elliptical delamination has a major axis (*a*), and a minor axis (*b*), and the aspect ratio of delamination is $e = a/b$.

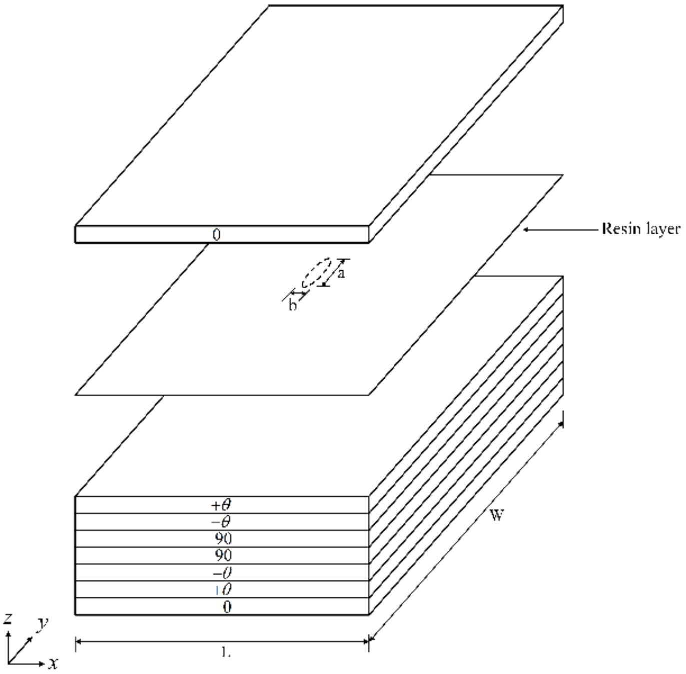

**Figure 6.1:** Exploded view of the laminate with an embedded elliptical delamination

The laminate is considered to be made of carbon/(CNT+epoxy) laminate with a 60% fiber volume fraction and carries an axial tension. Mechanical properties of the matrix (CNT+epoxy) and carbon/(CNT+epoxy) composite for different wt% (0, 0.25, 0.5, 1, and 1.5) of CNTs are calculated using Halpin-Tsai equations and rule of mixtures as described in section 3.6 of Chapter 3 are presented in **Table 6.1**.

**Table 6.1:** Carbon/(CNT+epoxy) composites properties

| | Matrix (CNT+epoxy) | | | Composite (Carbon fiber (60%) + (CNT+epoxy)) | | | |
|---|---|---|---|---|---|---|---|
| CNT wt% in epoxy | Tensile modulus (GPa) | Poisson's ratio | Shear modulus (GPa) | Longitudinal tensile modulus $E_1$ (GPa) | Transverse tensile modulus $E_2$ (GPa) | In-plane Poisson's ratio $\nu_{12}$ | In-plane shear modulus $G_{12}$ (GPa) |
| 0.0% | 3.10 | 0.35 | 1.15 | 139.24 | 7.59 | 0.284 | 2.75 |
| 0.25% | 3.31 | 0.35 | 1.23 | 139.33 | 8.11 | 0.284 | 2.93 |
| 0.50% | 3.53 | 0.35 | 1.31 | 139.41 | 8.62 | 0.284 | 3.11 |
| 1.00% | 3.95 | 0.35 | 1.46 | 139.58 | 9.63 | 0.284 | 3.46 |
| 1.50% | 4.38 | 0.35 | 1.62 | 139.75 | 10.65 | 0.284 | 3.81 |

## 6.4 Results and discussions for axial loading of the laminate

The laminate with an embedded elliptical delamination has been modeled using SOLID 185 and CONTA 178 elements in ANSYS by developing an APDL code. Interlaminar stresses have been evaluated at the interface and components of SERR are calculated using VCCI. Since near the vicinity of the embedded delamination, a stiff stress gradient exists, therefore a very fine mesh is used there. Thus the FE mesh convergence study has been done and the computed SERR using VCCI has been validated before using the FE APDL program.

### 6.4.1 FEA of the laminate with an embedded delamination

In the present FEA, the laminate specimen has been modeled as layers viz. the top and bottom sub-laminates as two layers and a thin resin rich layer (thickness = 0.1 times the ply thickness) representing the interface. SOLID 185 elements in ANSYS (three dimensional, eight noded, layered) are used in discretizing the laminate having an embedded delamination at the interface, and layer wise orthotropic properties have been input. It is reported [158] that the FEA solutions might lead to inaccurate results due to delaminated layers interpenetrating each other and hence in the present FEA, the top and bottom nodes of the delaminated region are connected through a bi-linear contact element (CONTA 178) in ANSYS ensuring no interpenetration of delaminated layers. The resin rich interface has been modeled by providing the isotropic properties of resin (CNT+epoxy) as input and the elliptical delamination has been modeled by deleting elements from the resin layer.

**Table 6.2:** FE mesh convergence of interlaminar shear stress

| Mesh number | Number of elements | $\tau_{zn}$ (MPa) |
|---|---|---|
| 1 | 10752 | 20.3 |
| 2 | 16128 | 21.9 |
| 3 | 21504 | 22.8 |
| 4 | 26880 | 23.3 |
| 5 | 32256 | 23.9 |
| 6 | 37632 | 23.8 |
| 7 | 43008 | 23.8 |

**Figures 6.2(a)** and **6.2(b)** show the full 3D FE mesh of a square laminate and zoomed view of mesh near embedded elliptical delamination respectively. In order to capture the stiff stress gradient at the delamination front, highly refined mesh near the delamination front has been used. The convergence of interlaminar shear stress with progressive mesh refinement is shown in **Table 6.2**. In the present case, the mesh convergence has been attained with a mesh size of 37632 elements near the delamination front as shown in **Fig. 6.3**. Uniform axial loading is simulated by fixing laminate's one edge and by subjecting the opposite edge to

axial displacement ($\varepsilon = 0.005$). Different values of the aspect ratio of the embedded elliptical delamination have been considered to understand the effect of the delamination shape.

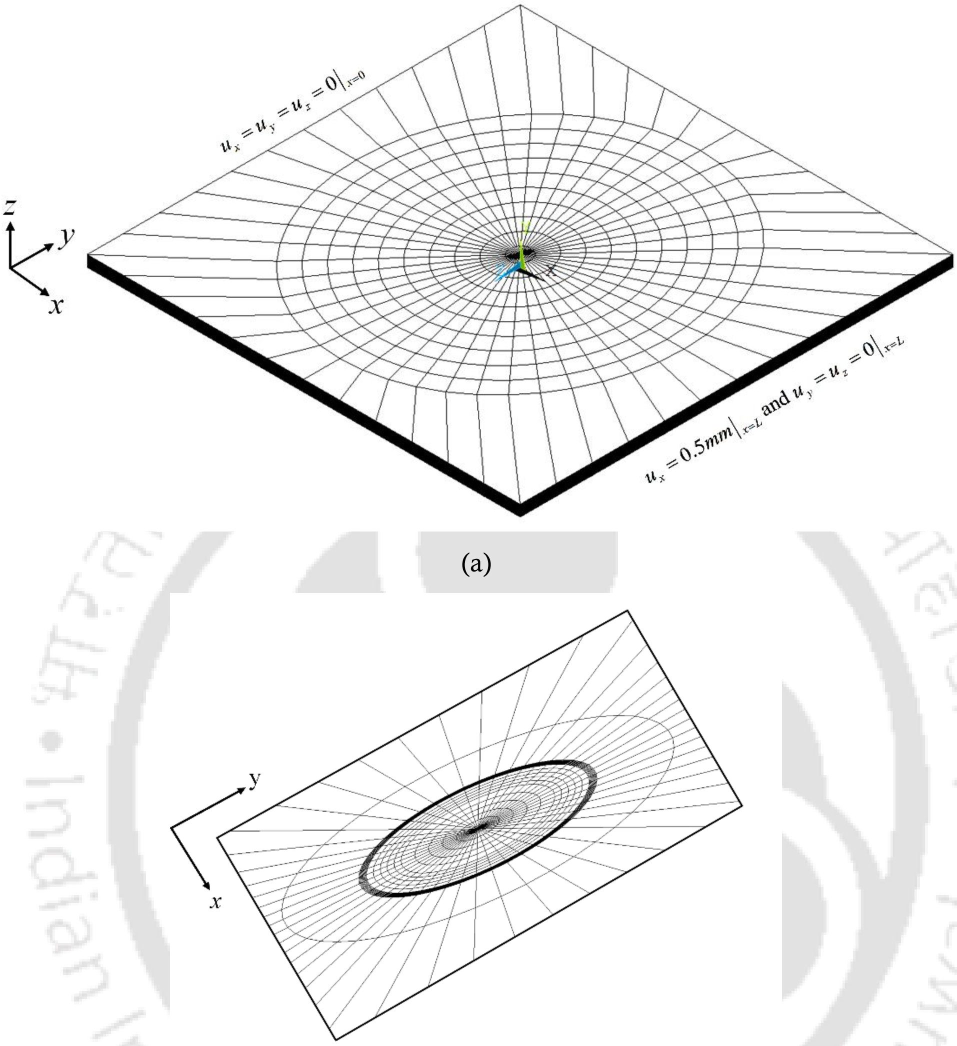

(a)

(b)

**Figure 6.2:** (a) 3D FE mesh of square laminate and (b) zoomed mesh near delamination

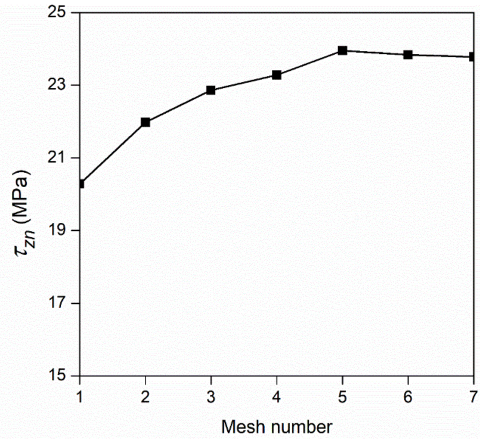

**Figure 6.3:** Convergence of FE mesh for carbon/epoxy composite ($e = 1,\ \theta = 0^{\circ}$)

### 6.4.2 Validation

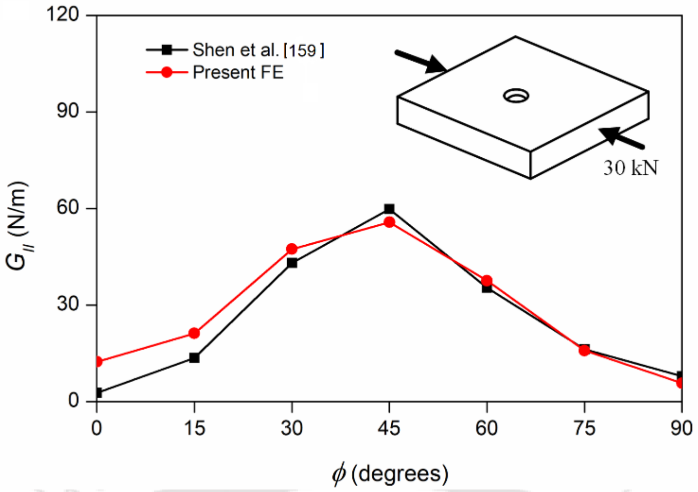

**Figure 6.4:** $G_{II}$ around a circular delamination front

In order to validate the computed SERR using the present FE analysis and VCCI, a $[(0/+45/-45)_3]_s$ square laminate with side 50 mm, and a centrally located through hole of 5 mm in diameter, and a circular delamination of 20 mm in diameter is considered. The properties of the composite are [159] as $E_1 = 134$ GPa, $E_2 = E_3 = 10.2$ GPa, $G_{12} = G_{13} = 5.5$ GPa, $G_{23} = 3.4$ GPa, $\nu_{12} = \nu_{13} = 0.23$ and $\nu_{23} = 0.49$. A 3D FE analysis is carried out by applying a compression load of 30 kN on the laminate and mode II SERR ($G_{II}$) computed using the VCCI is compared with [159] as shown in **Fig. 6.4** and a similar qualitative trend in variation of $G_{II}$ with $\phi$ could be seen excepting at a few points where the present FE estimates higher values of $G_{II}$.

### 6.4.3 Stress distribution and SERR along the delamination front

Even though the laminate is loaded axially, due to centrally located embedded delamination at the interface, in-plane, as well as out-of-plane stresses are induced along the delamination. Using the 3D FEA, considering the delamination front near the elliptical delamination as the crack front, the interlaminar stresses at the interface are computed using Eq. 3.18 as discussed in section 3.2.1 of Chapter 3, using the displacements of the top and bottom nodes behind the delamination, SERR components have been computed following VCCI as discussed in section 3.3.2 of Chapter 3.

#### *6.4.3.1 Influence of delamination shape*

In order to understand how the delamination shape at the interface influences the interlaminar stresses and the SERR, the delamination shape ($e = a/b$) is varied from to 1 to 2.5 and interlaminar stresses and SERR are computed.

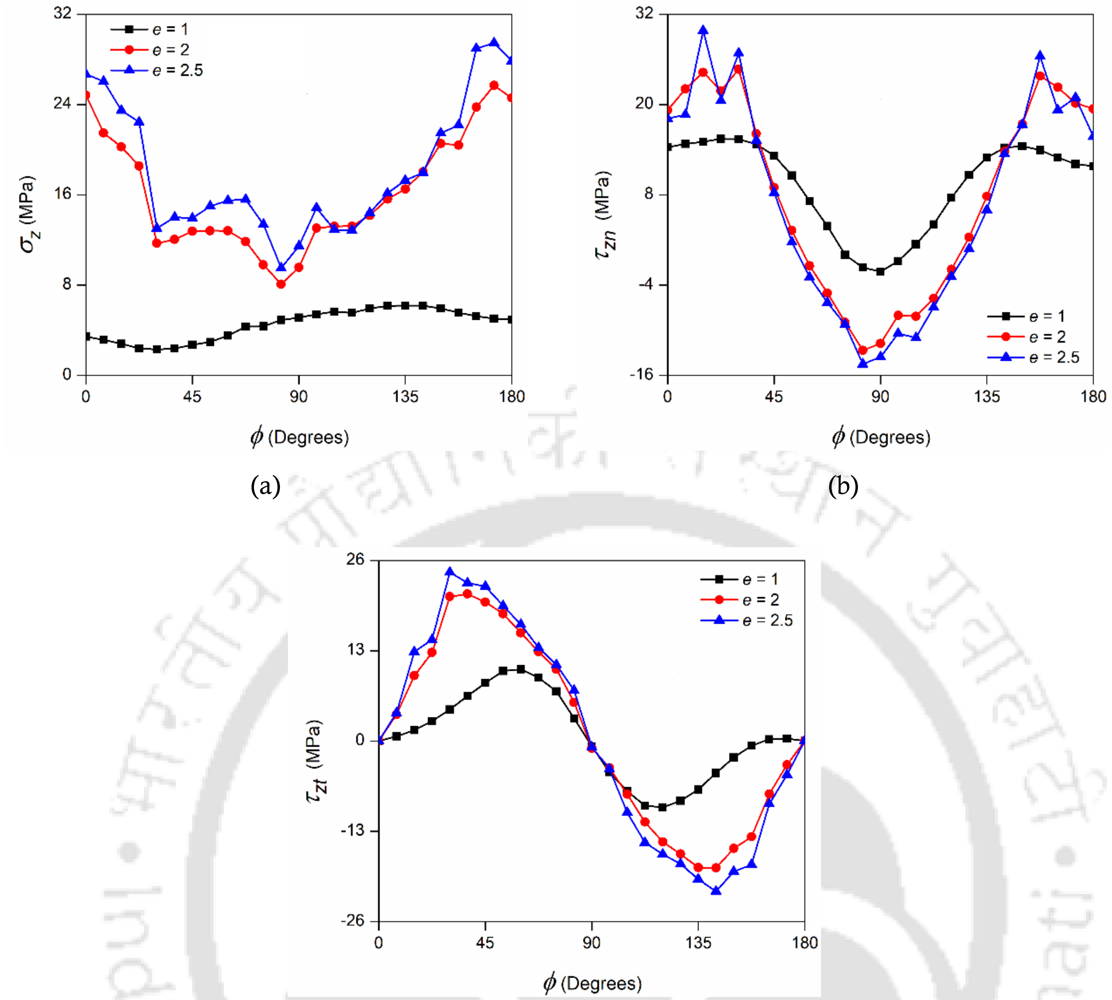

(a) (b)

(c)

**Figure 6.5:** Variation of (a) $\sigma_z$ , (b) $\tau_{zn}$ and (c) $\tau_{zt}$ along delamination front

**Figures 6.5(a)**, **6.5(b)**, and **6.5(c)** show the variation of $\sigma_z$ , $\tau_{zn}$ and $\tau_{zt}$ respectively along the delamination front (represented by angle measured from to X-axis as in **Fig. 6.2**) for a $[0/\pm\theta/90]_s$ carbon/(CNT+epoxy) laminate having an embedded delamination with an adjacent ply orientation of $\theta = 0^\circ$ . All these stresses are average stresses measured over a very small distance in front of the delamination front as in Eq. 3.18 discussed in section 3.2.1 of Chapter 3. Due to the symmetry, stress variation along half of the total delamination front $(0-180^\circ)$ has been shown. Existence of all the three out-of-plane components of the interlaminar stresses at the delamination front clearly shows a 3D state of stress at the delamination front. Thus it could be inferred that the delamination at the interface will be mixed mode even though the applied load is purely axial. In addition, it could also be noted that the magnitudes of these interlaminar stresses vary along the delamination front differently showing that even the relative magnitudes of those stresses are also different at different location along the delamination front.

It could be seen that with the increase in aspect ratio *e*, interlaminar stresses $\sigma_z$ and $\tau_{zt}$ increase, and $\tau_{zn}$ decreases, for a laminate subjected to same axial loading. However, both $\sigma_z$ and $\tau_{zn}$ are maximum at $\phi = 180^\circ$ and $\phi = 0^\circ$ respectively but $\tau_{zt}$ is maximum at $\phi = 30^\circ$ showing that not only the delamination growth is mixed mode, but also the location of delamination growth along the elliptical front is decided by the relative values of the out-of-plane stresses. Even though these results corresponding to interface between $0$ and $\pm\theta$ where $\theta = 0^\circ$, the same trend has been observed for other values of $\theta$ as well. Though these results correspond to the neat resin, the same trend has been observed even for different wt% of CNTs mixed with epoxy.

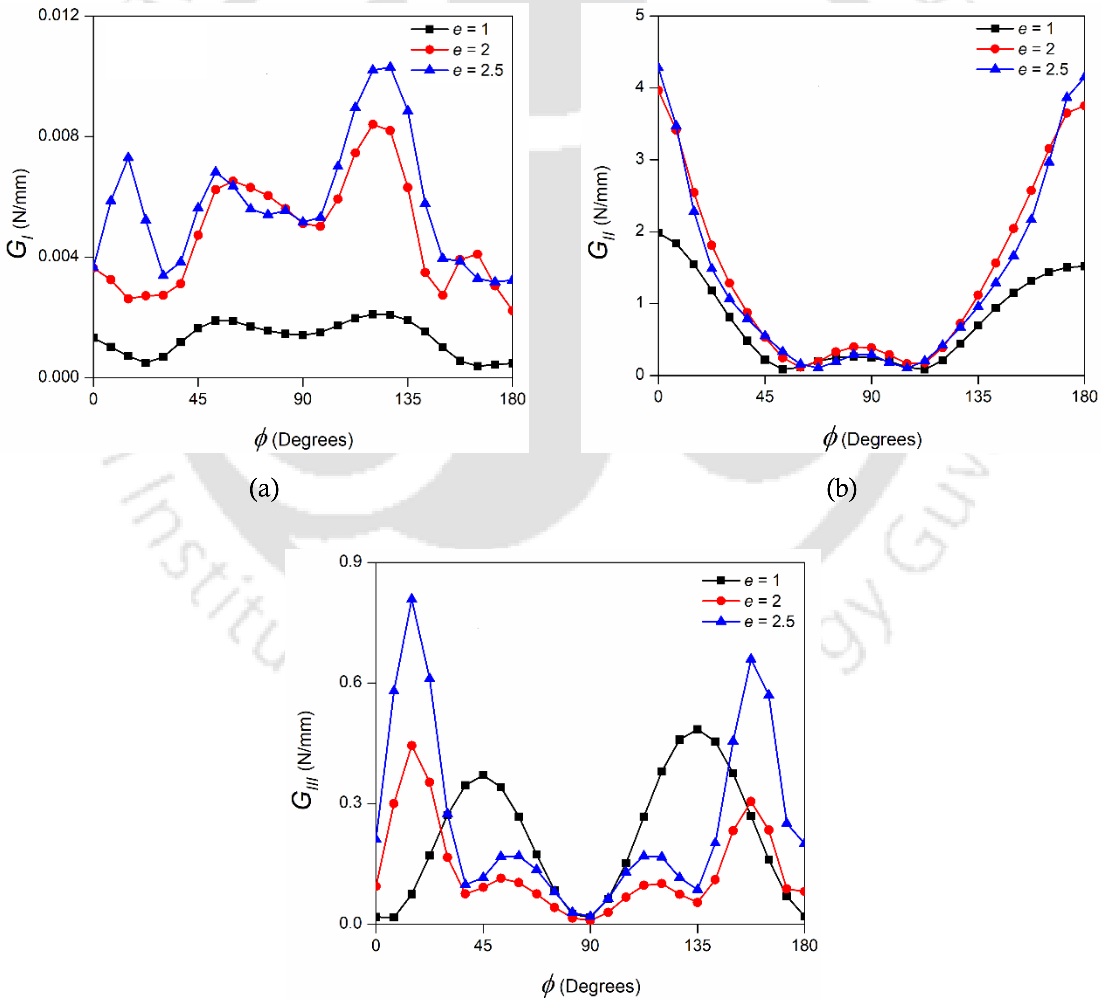

(a)

(b)

(c)

**Figure 6.6:** Variation of (a) $G_I$, (b) $G_{II}$ and (c) $G_{III}$ along delamination front

In order to understand the propensity of delamination growth at the interface, the SERR components are calculated at the delamination front using VCCI and are plotted around the elliptical delamination front (angular location with reference to X-axis with reference to **Fig. 6.2**). **Figures 6.6(a)**, **6.6(b)** and **6.6(c)** show the variation of $G_I$, $G_{II}$ and $G_{III}$ respectively around the elliptical delamination front for different aspect ratio. In the present case, as the aspect ratio of delamination increases, magnitude of $G_I$, $G_{II}$ and $G_{III}$ increases. It could be observed that in accordance with the variation of interlaminar stresses, the components of SERR also vary following a similar trend around the delamination front. Similar to the stress variation, the maximum magnitude of SERR components also occur at different locations showing that it is the combination of $G_I$, $G_{II}$ and $G_{III}$ that will decide whether the delamination will further grow or not. However, it could be noted that the magnitude of $G_I$ is much smaller compared to those of $G_{II}$ and $G_{III}$ showing that mode II and mode III will dominate the delamination growth. It could be seen that not only the delamination growth a mixed mode phenomenon, but the mode mix ratio is also different at different locations. It is therefore difficult to predict the delamination growth in such a situation.

**Figure 6.7** shows the variation of maximum magnitudes of $G_{II}$ and $G_{III}$ with increasing aspect ratio, *e* (= *a*/*b*) for $\theta = 0^\circ$ degrees. In the present case, with the increase in *e*, there is a substantial increase in both maximum mode II SERR ($G_{II\max}$) and maximum mode III SERR ($G_{III\max}$) showing that the chances of delamination along the delamination front increases with the increase in aspect ratio.

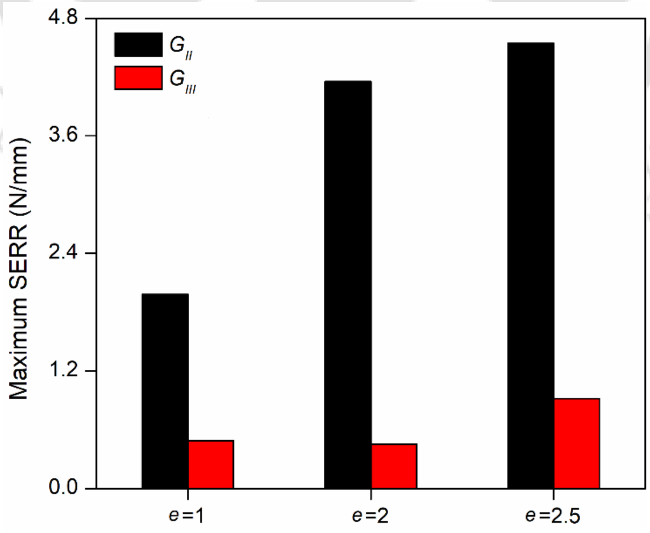

**Figure 6.7:** Maximum SERR for different aspect ratio of the delamination

### 6.4.3.2 *Influence of fiber orientation*

In order to understand how the relative fiber orientation of the adjacent laminae at the interface influences the interlaminar stresses and the SERR, the fiber orientation angle ($\theta$) of the adjacent lamina is varied from $0^{\circ}$ to $90^{\circ}$. Results in the previous section 6.4.3.1 showed that SERR is maximum for an aspect ratio of 2.5. Hence, in the present case, interlaminar stresses and SERR are computed for $e$ = 2.5. Again, mode I SERR is small compared with other two modes, hence $G_I$ and corresponding interlaminar stress $\sigma_z$ are neglected in the present case.

**Figures 6.8(a)** and **6.8(b)** depict the variation of $\tau_{zn}$ and $\tau_{zt}$ respectively along the delamination front for a $[0/\pm\theta/90]_s$ three phase carbon/(CNT+epoxy) laminate having an embedded delamination. In all the cases, it could be observed that the magnitude of interlaminar stresses is minimum for $\theta = 0^{\circ}$ and it increases with increase in $\theta$. However, $\tau_{zn}$ is maximum at $\phi = 0^{\circ}$ and $\phi = 180^{\circ}$ but $\tau_{zt}$ is maximum corresponding to $\phi = 45^{\circ}$ and $\phi = 135^{\circ}$ showing that not only the delamination growth is mixed mode, but also the location of delamination growth along the elliptical front is decided by the relative values of the out-of-plane stresses. Though these results correspond to the neat resin, the same trend has been observed even for different wt% of CNTs mixed with epoxy.

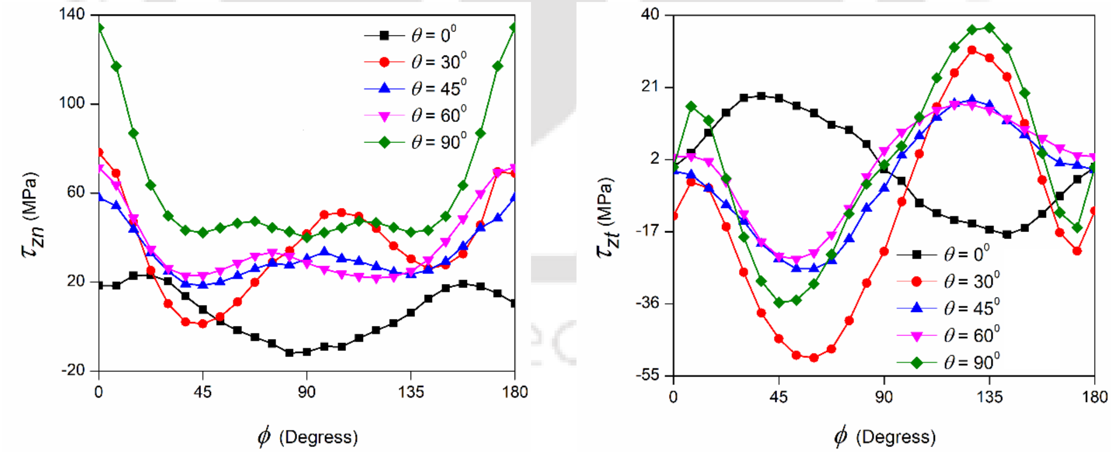

(a) (b)

**Figure 6.8:** Variation of (a) $\tau_{zn}$ and (b) $\tau_{zt}$ along delamination front

**Figures 6.9(a)** and **6.9(b)** show the variation of $G_{II}$ and $G_{III}$ respectively around the elliptical delamination front for different fiber orientation. It could be seen that $G_{II}$ is always maximum at $\phi = 0^{\circ}$ but the maximum value of $G_{II}$ changes with fiber orientation. On the other hand, the magnitude as well as the location of maximum $G_{III}$ also changes with the fiber orientation.

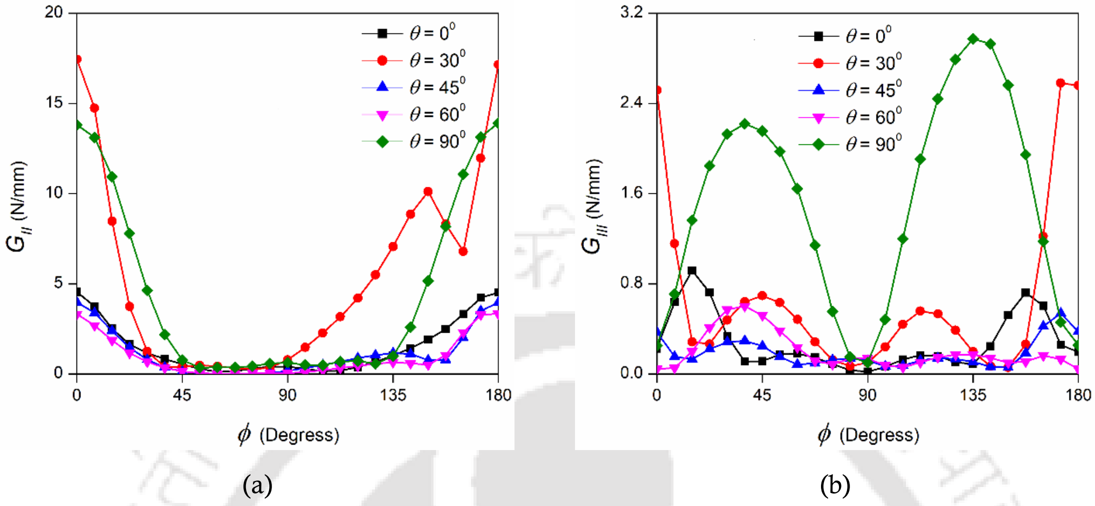

(a) (b)

**Figure 6.9:** Variation of (a) $G_{II}$ and (b) $G_{III}$ along delamination front

**Figure 6.10** show the variation of $G_{II\max}$ and $G_{III\max}$ with the fiber orientation angle, $\theta$. It has been observed that there is a significant increase in $G_{II\max}$ is maximum for $\theta = 30^{\circ}$ and $G_{III\max}$ is maximum for $\theta = 90^{\circ}$. The reason for $G_{II\max}$ to be maximum for $\theta = 30^{\circ}$ is because the property mismatch causing $\tau_{zn}$ is maximum corresponding to $0^{\circ}/30^{\circ}$ interface. Similarly, the reason for $G_{III\max}$ to be maximum for $\theta = 90^{\circ}$ is because the property mismatch causing $\tau_{zt}$ is maximum corresponding to $0^{\circ}/90^{\circ}$ interface. Similar experimental results have been observed where SERR increases with the increase in fiber orientation [160].

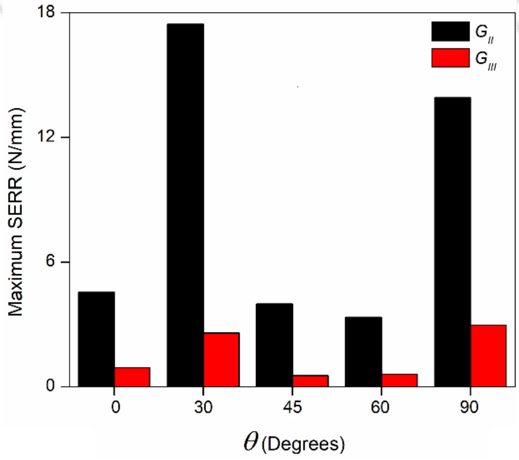

**Figure 6.10:** Maximum SERR for different fiber orientation

#### 6.4.3.3 *Influence of CNT wt%*

To understand the effect of CNT wt% on interlaminar stresses and SERR, different CNT wt% viz. 0%, 0.25%, 0.5%, 1% and 1.5% are considered. It was observed from section 6.4.3.1 that SERR is maximum for an aspect ratio of $e$ = 2.5 and also observed from section 6.4.3.2 that for $e$ = 2.5, $G_{II\max}$ is maximum for $\theta = 30^\circ$ and $G_{III\max}$ is maximum for $\theta = 90^\circ$. Hence, in the present case, interlaminar stresses and SERR are computed for the above stated combinations.

**Figures 6.11(a)**, and **6.11(b)** show the variation of $\tau_{zn}$ and $\tau_{zt}$ respectively along the delamination front for different wt% of CNT in epoxy. It could be observed that though the magnitudes of $\tau_{zn}$ and $\tau_{zt}$ change with CNT wt% but the change is not that significant except at some specific locations. It may be noted here that the change in stress magnitude is due to the change in property mismatch between the adjacent laminae due to addition of CNTs.

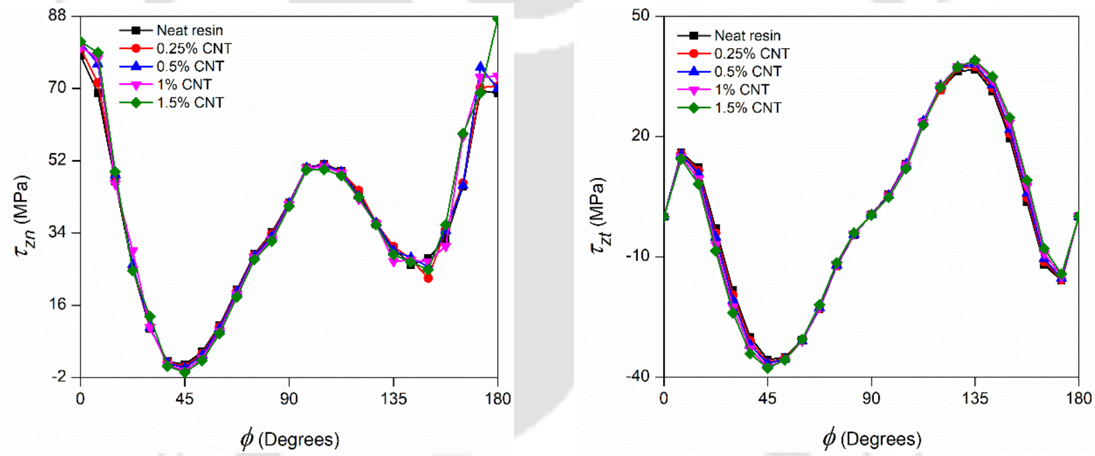

(a) (b)

**Figure 6.11:** Variation of (a) $\tau_{zn}$ and (b) $\tau_{zt}$ along delamination front

**Figures 6.12(a)**, and **6.12(b)** show the variation of $G_{II}$ and $G_{III}$ respectively along the delamination front with increasing CNT weight percentage in a three phase (CNT+epoxy). It could be seen that $G_{II}$ is always maximum at $\phi = 0^\circ$ and $G_{III}$ is always maximum at $\phi = 135^\circ$. It could be seen that as the wt% of CNTs in the epoxy increases, there is a reduction in maximum magnitudes of both $G_{II}$ and $G_{III}$. This indicates that adding CNTs to epoxy reduces the chances of interfacial delamination growth from an existing embedded delamination in the post impact loading.

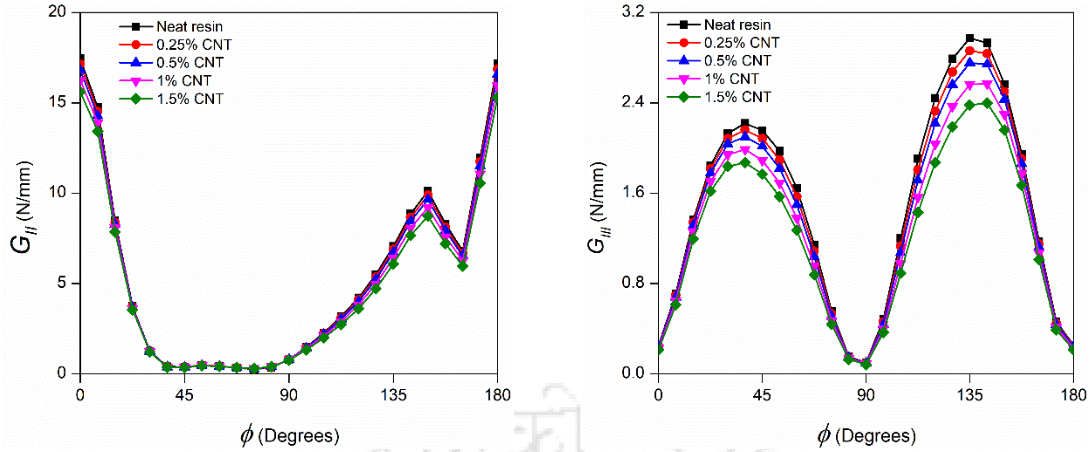

(a) (b)

**Figure 6.12:** Variation of (a) $G_{II}$ and (b) $G_{III}$ along delamination front

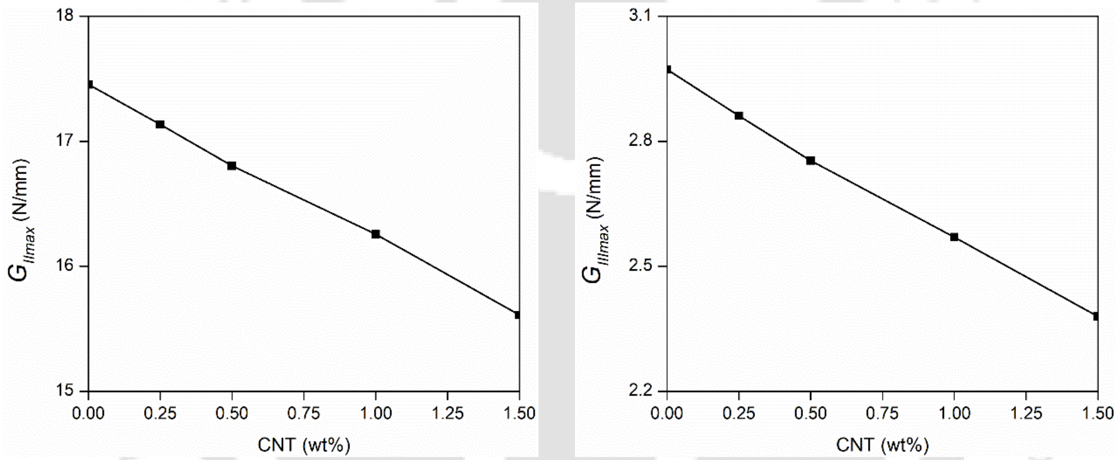

(a) (b)

**Figure 6.13:** Maximum SERR (a) $G_{II\max}$ , and (b) $G_{III\max}$ variation with CNT wt%

**Figures 6.13(a)**, and **6.13(b)** show the variation of $G_{II\max}$ and $G_{III\max}$ respectively on the delamination front with increasing CNT wt%. Since $G_{II}$ is maximum for $\theta = 30^{\circ}$, therefore variation in $G_{II\max}$ with CNT wt% is shown only for $\theta = 30^{\circ}$. Similarly, the variation of $G_{III\max}$ with CNT wt% is shown only for $\theta = 90^{\circ}$. In both the cases variation is shown for $e$ = 2.5. It could be observed that both $G_{II\max}$ and $G_{III\max}$ values show reduction with increasing CNT wt% in the epoxy. It has been observed that $G_{II\max}$ and $G_{III\max}$ values are reduced by 11% and 20% respectively compared to those for to neat resin with the addition of 1.5 wt% CNTs in epoxy. This indicates that adding CNTs to epoxy reduces the chances of interfacial delamination growing further from an existing embedded delamination. However, the value of critical SERR ($G_c$) decides whether delamination will grow further or not, and thus it is essential to calculate $G_c$ for the same laminate.

### 6.4.4 Critical SERR ($G_c$) and influence of CNT wt%

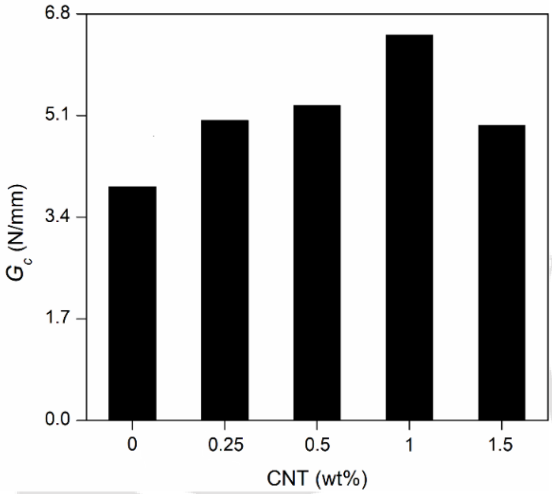

**Figure 6.14.** Variation of $G_c$ with CNT wt%

Preceding discussions reveal that the delamination growth is mix mode phenomenon and SERR components vary along the delamination front differently. This means that the mode mix also varies along the delamination front. Since the critical SERR components are also decide by the mode mix ratio, it is difficult to assess critical SERR components for such a case. Therefore, as discussed in section 3.3.3 of Chapter 3 total Critical SERR ($G_c$) as a measure of resistance to delamination growth has been computed using QSC and VCCI. In the present case, $G_c$ has been calculated for different CNT wt% in three phase (CNT+epoxy) to understand how the addition of CNTs to the epoxy actually enhances the resistance to the further growth of embedded delamination. Since the SERR is maximum corresponding to $e$ = 2.5 and for $\theta = 30^{\circ}$, therefore the variation of $G_c$ with CNT wt% has been computed corresponding to $e$ = 2.5 and $\theta = 30^{\circ}$, and **Fig. 6.14** shows the variation with different CNT wt%. It could be seen from **Fig. 6.14** that as CNT wt% increases, the magnitude of $G_c$ increases substantially and reaches a maximum at 1 wt%. However, with the further increase in CNT beyond 1 wt%, value of $G_c$ decreases though it is still more than that corresponding to the case of neat resin. It could be observed that the corresponding to 1 wt% of CNT, increase in $G_c$ is 65% more than that corresponding to neat resin. Therefore, it could be inferred that addition of CNT to epoxy leads to significant enhancement in the resistance to further growth of delamination in the post impact loading, but there is a limit to CNT wt% to which this enhancement is maximum which is 1% in the present case.

## 6.5 Results and discussions for transverse loading of the laminate

The same $[0/\pm\theta/90]_s$ carbon/(CNT+epoxy) laminate with an embedded elliptical delamination is considered subjected to transverse load at the centre with all the four edges fixed. The material properties are considered from **Table 6.1** for the present FE analysis.

### 6.5.1 FEA of the laminate with embedded delamination

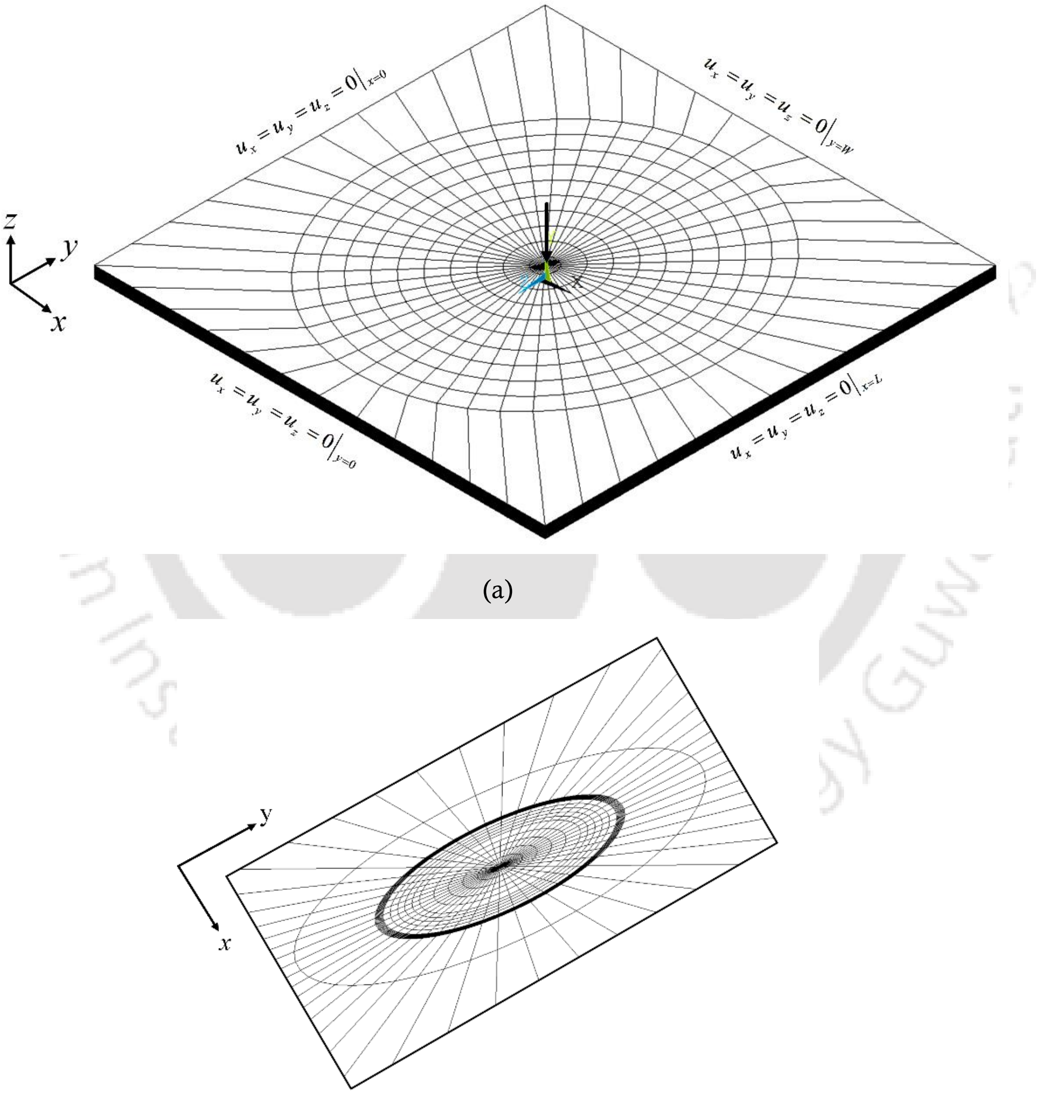

(a)

(b)

**Figure 6.15:** (a) 3D FE mesh of square laminate and (b) zoomed mesh near delamination

FE modeling of the laminate with embedded delamination is same as for the case of axial loading. **Figures 6.15(a)** and **6.15(b)** show the full 3D FE mesh of a square laminate and zoomed view of mesh near embedded elliptical delamination respectively. In order to capture the stiff stress gradient at the delamination front, highly refined mesh near the delamination front has been used. The convergence of interlaminar shear stress with progressive mesh refinement is shown in **Table 6.3**. In the present case, the mesh convergence has been attained with a mesh size of 32256 elements near the delamination front as shown in **Fig. 6.16**. A transverse loading is simulated by fixing all the edges of the laminate and subjected to a transverse loading of 500N at the center. Different values of the aspect ratio of the embedded elliptical delamination have been considered to understand the effect of the delamination shape.

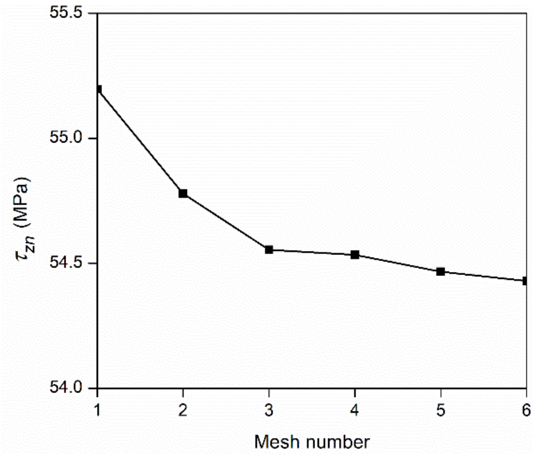

**Figure 6.16:** Convergence of FE mesh for carbon/epoxy composite ( $e=1, \theta=0^{\circ}$ )

**Table 6.3:** FE mesh convergence of interlaminar shear stress

| Mesh number | Number of elements | $\tau_{zn}$ (MPa) |
|---|---|---|
| 1 | 10752 | 55.2 |
| 2 | 16128 | 54.8 |
| 3 | 21504 | 54.6 |
| 4 | 26880 | 54.5 |
| 5 | 32256 | 54.4 |
| 6 | 37632 | 54.4 |

### 6.5.2 Stress distribution and SERR along the delamination front

Using the 3D FEA, considering the delamination front near the elliptical delamination as the crack, the interlaminar stresses at the interface are computed using Eq. 3.18 as discussed in section 3.2.1 of Chapter 3 and using the displacements of the top and bottom nodes behind the delamination, SERR components have been computed using VCCI as discussed in section 3.3.2 of Chapter 3.

### 6.5.2.1 *Influence of delamination shape*

In order to understand how the delamination shape at the interface influences the interlaminar stresses and the SERR, the delamination shape (*e* = *a*/*b*) is varied from to 1 to 2.5 and interlaminar stresses and SERR are computed.

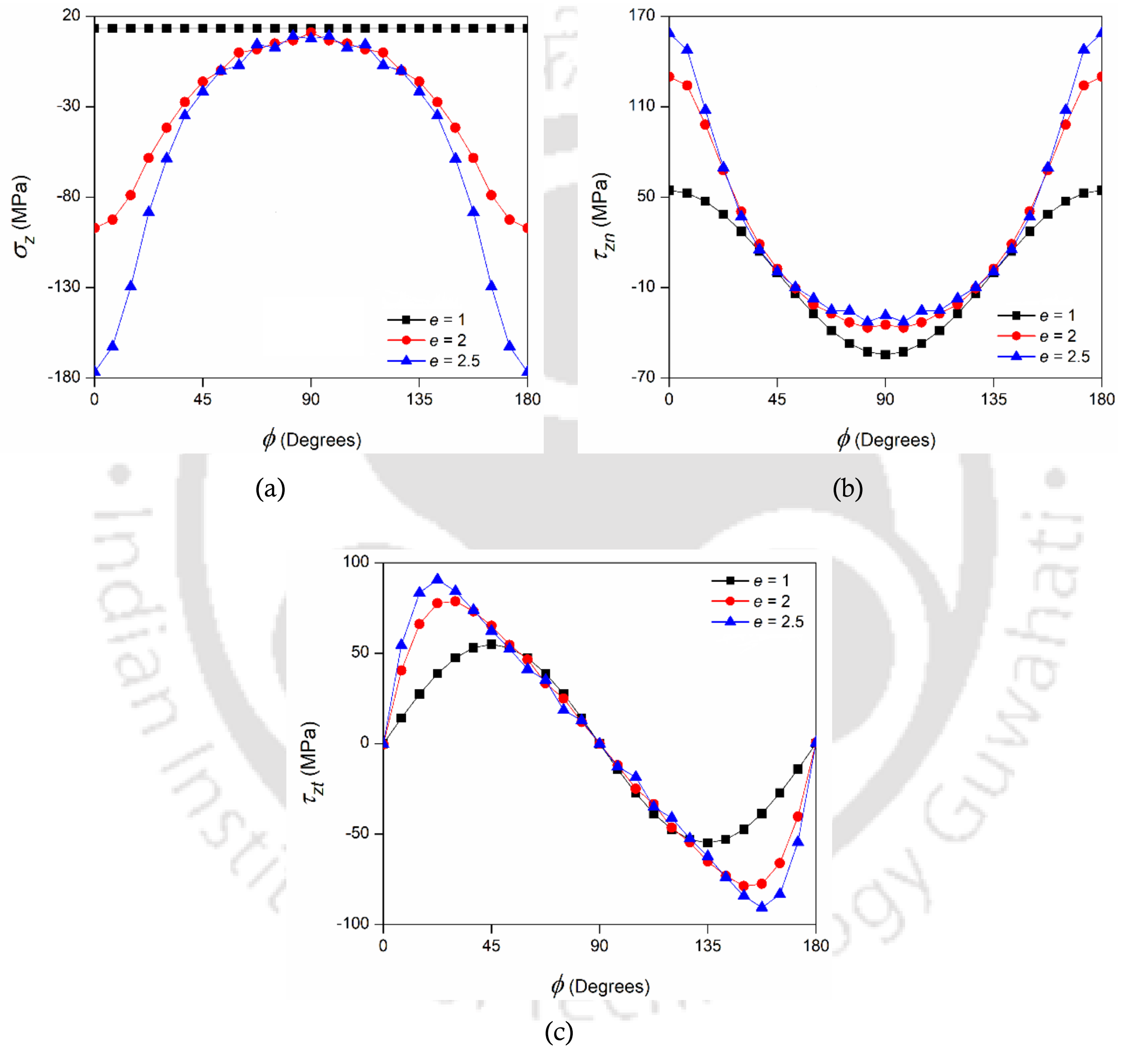

(a) (b)

(c)

**Figure 6.17:** Variation of (a) $\sigma_z$ , (b) $\tau_{zn}$ and (c) $\tau_{zt}$ along delamination front

**Figures 6.17(a)**, **6.17(b)**, and **6.17(c)** show the variation of $\sigma_z$ , $\tau_{zn}$ and $\tau_{zt}$ respectively along the delamination front (represented by angle measured from to X-axis) for a $[0/\pm\theta/90]_s$ carbon/(CNT+epoxy) laminate having an embedded delamination with an adjacent ply orientation of $\theta = 0^\circ$ . All these stresses are average stresses measured over a very small distance in front of the delamination front as in Eq. 3.18. Due to the symmetry, stress variation along half of the total delamination front $(0-180^{\circ})$ has been shown. The presence of all three out-of-plane components of interlaminar stresses at the delamination front clearly shows a three dimensional (3D) stress state at that location. As a result, it can be inferred that the delamination occurring at the interface will be a mixed mode phenomenon.

It could be seen that with the increase in aspect ratio *e*, interlaminar stresses $\sigma_z$ and $\tau_{zt}$ increase, and $\tau_{zn}$ decrease, for a laminate subjected to same transverse loading. However, both $\sigma_z$ and $\tau_{zn}$ are maximum at $\phi=0^{\circ}$ but $\tau_{zt}$ is maximum at $\phi=30^{\circ}$ showing that not only the delamination growth is mixed mode, but also the location of delamination growth along the elliptical front is decided by the relative values of the out-of-plane stresses. Even though these results corresponding to interface between $0$ and $\pm\theta$ where $\theta=0^{\circ}$, the same trend has been observed for other values of $\theta$ as well. Though these results correspond to the neat resin, the same trend has been observed even for different wt% of CNTs mixed with epoxy. It may be noted that $\sigma_z$ being negative actually does not contribute to the delamination growth and therefore only $\tau_{zn}$ and $\tau_{zt}$ are responsible for delamination growth under transverse loading.

In order to understand the propensity of delamination growth at the interface the SERR components are calculated at the delamination front using VCCI and are plotted around the elliptical delamination front (angular location with reference to X-axis as shown in **Fig. 6.15**). **Figures 6.18(a)**, **6.18(b)** and **6.18(c)** show the variation of $G_I$, $G_{II}$ and $G_{III}$ respectively around the elliptical delamination front for different aspect ratio. In the present case, as the aspect ratio of delamination increases, magnitude of $G_I$, $G_{II}$ and $G_{III}$ increases. It could be observed that in accordance with the variation of interlaminar stresses, the components of SERR also vary following a similar trend around the delamination front. Similar to the stress variation, the maximum magnitude of SERR components also occur at different locations showing that it is the combination of $G_I$, $G_{II}$ and $G_{III}$ that will decide where the delamination will further grow or not. However, it could be noted that the magnitude of $G_I$ is negative in accordance with the compressive nature of the interlaminar normal stress $\sigma_z$. Thus $G_I$ does not contribute to the delamination growth and showing that mode II and mode III will dominate the delamination growth.

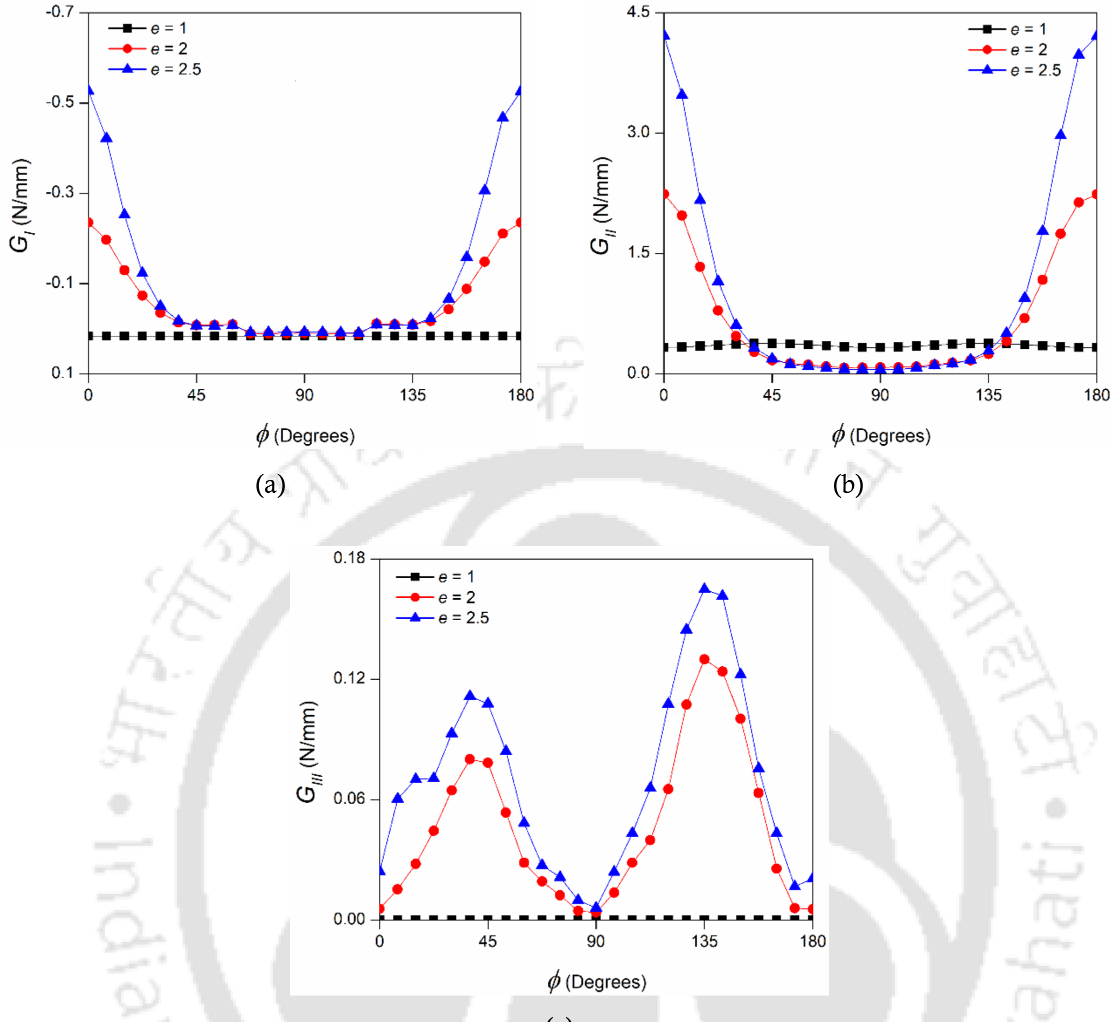

(a) (b)

(c)

**Figure 6.18:** Variation of (a) $G_I$, (b) $G_{II}$ and (c) $G_{III}$ along delamination front

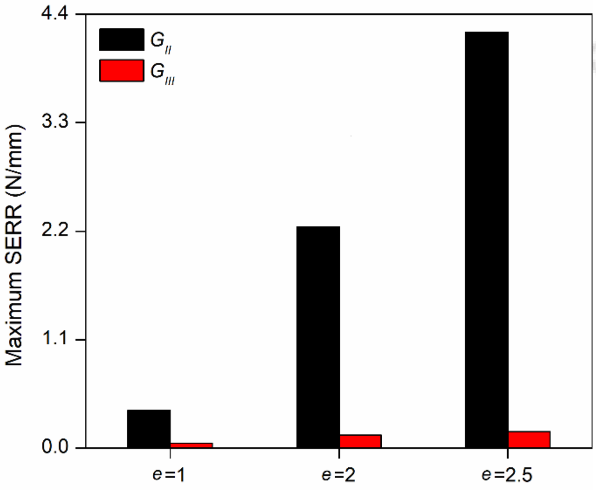

**Figure 6.19:** Maximum SERR for different aspect ratio of the delamination

**Figure 6.19** shows the variation of maximum magnitudes of $G_{II}$ and $G_{III}$ with increasing aspect ratio, *e* (= $a/b$) for $\theta = 0^{\circ}$ degrees. In the present case, with the increase in *e*, there is a substantial increase in both maximum mode II SERR ($G_{II\max}$) and maximum mode III SERR ($G_{III\max}$) showing that the chances of delamination along the delamination front increases with the increase in aspect ratio.

### *6.5.2.2 Influence of fiber orientation*

In order to understand how the relative fiber orientation of the adjacent laminae at the interface influences the interlaminar stresses and the SERR, the fiber orientation angle ($\theta$) of the adjacent lamina is varied from $0^{\circ}$ to $90^{\circ}$. From the previous section 6.5.2.1, it has been observed that SERR is maximum for an aspect ratio of 2.5. Hence, in the present case, interlaminar stresses and SERR are computed for *e* = 2.5. Similarly, mode I SERR is small compared with other two modes, hence $G_I$ and corresponding interlaminar stress $\sigma_z$ are neglected in the present case.

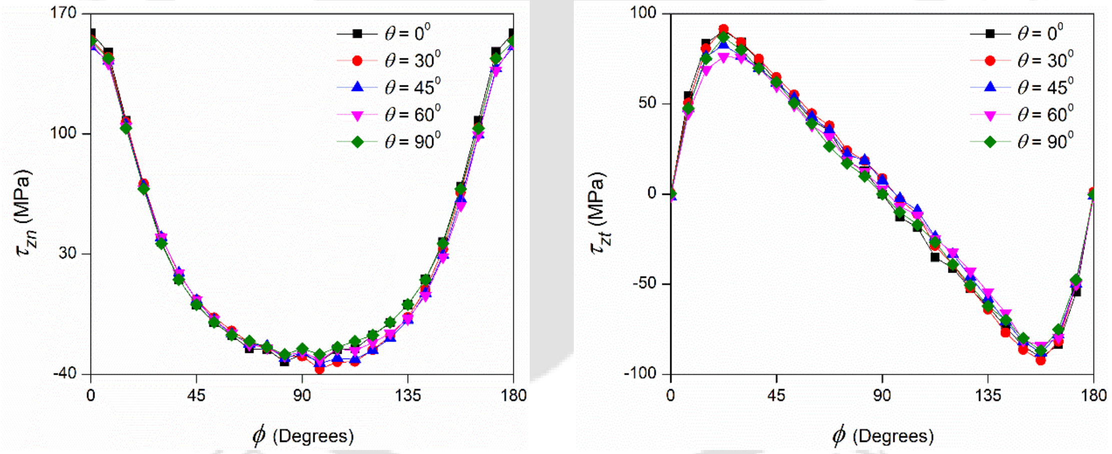

(a) (b)

**Figure 6.20:** Variation of (a) $\tau_{zn}$ and (b) $\tau_{zt}$ along delamination front

**Figures 6.20(a)** and **6.20(b)** depict the variation of $\tau_{zn}$ and $\tau_{zt}$ respectively along the delamination front for a $[0/\pm\theta/90]_s$ carbon/(CNT+epoxy) laminate having an embedded delamination. In all the cases, it could be observed that the magnitude of interlaminar stresses is minimum for $\theta = 0^{\circ}$ and it increases with increase in $\theta$. However, both $\tau_{zn}$ is maximum at $\phi = 0^{\circ}$ and $\phi = 180^{\circ}$ but $\tau_{zt}$ is maximum corresponding to $\phi = 45^{\circ}$ and $\phi = 135^{\circ}$ showing that not only the delamination growth is mixed mode, but also the location of delamination growth along the elliptical front is decided by the relative values of the out-of-plane stresses. Though these results correspond to the neat resin, the same trend has been observed even for different wt% of CNTs mixed with epoxy.

**Figures 6.21(a)** and **6.21(b)** show the variation of $G_{II}$ and $G_{III}$ respectively around the elliptical delamination front for different fiber orientations. It could be seen that $G_{II}$ is always maximum at $\phi = 0^{\circ}$ but the maximum value of $G_{II}$ changes with fiber orientation. On the other hand, the magnitude as well as the location of maximum $G_{III}$ also changes with the fiber orientation.

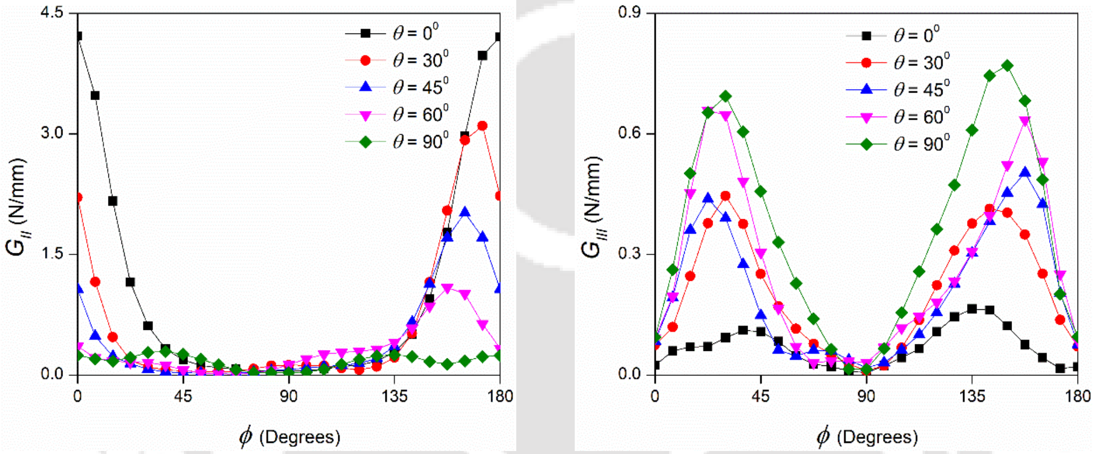

(a) (b)

**Figure 6.21:** Variation of (a) $G_{II}$ and (b) $G_{III}$ along delamination front

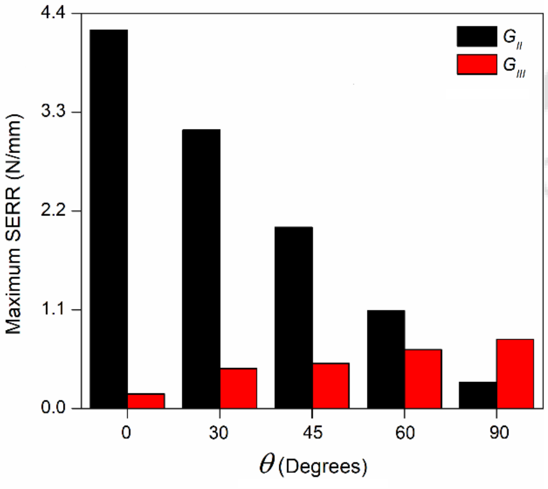

**Figure 6.22:** Maximum SERR for different fiber orientation

**Figure 6.22** show the variation of $G_{II\max}$ and $G_{III\max}$ with the fiber orientation angle, $\theta$. It has been observed that there is a significant decrease in $G_{II\max}$ and increase in $G_{III\max}$ with increase in fiber orientation. It has also been observed that $G_{II\max}$ and $G_{III\max}$ are maximum for $0^{\circ}$ and $90^{\circ}$. However, in all the cases, the magnitude of $G_{II\max}$ is significantly higher compared to that of $G_{III\max}$. Similar experimental results have been observed where SERR increases with the increase in fiber orientation angle [160].

#### *6.5.2.3 Influence of CNT wt%*

To understand the effect of CNT wt% on interlaminar stresses and SERR, different CNT wt% viz. 0%, 0.25%, 0.5%, 1% and 1.5% are considered. It was observed from previous sections 6.5.2.1 and 6.5.2.2 that mode II SERR is maximum for $e$ = 2.5 and $\theta = 0^{\circ}$, similarly mode III SERR is maximum for $e$ = 2.5 and $\theta = 90^{\circ}$. Hence, in the present case, interlaminar stresses and SERR are computed for both the combinations.

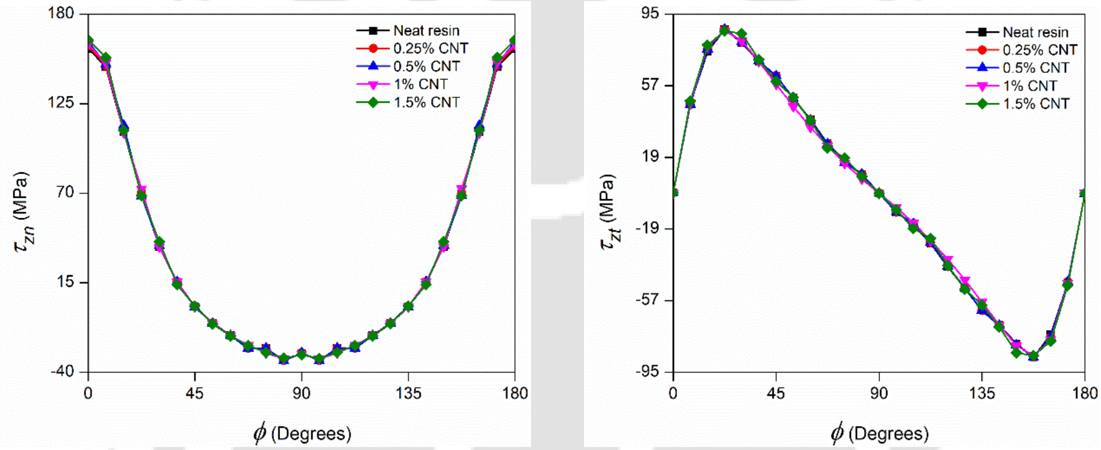

(a) (b)

**Figure 6.23:** Variation of (a) $\tau_{zn}$ and (b) $\tau_{zt}$ along delamination front

**Figures 6.23(a)**, and **6.23(b)** show the variation of $\tau_{zn}$ and $\tau_{zt}$ respectively along the delamination front for different wt% of CNT in epoxy. It could be observed that though the magnitudes of $\tau_{zn}$ and $\tau_{zt}$ change with CNT wt% but the change is not that significant except at some specific locations. It may be noted here that the change in stress magnitude is due to the change in property mismatch between the adjacent laminae due to addition of CNTs.

**Figures 6.24(a)**, and **6.24(b)** show the variation of $G_{II}$ and $G_{III}$ respectively along the delamination front with increasing CNT weight percentage in (CNT+epoxy). It could be seen that $G_{II}$ is always maximum at $\phi = 0^{\circ}$ and $G_{III}$ is always maximum at $\phi = 135^{\circ}$. It could be seen that as the wt% of CNTs in the epoxy increases, there is a significant reduction in both $G_{II}$ and $G_{III}$. This indicates that adding CNTs to epoxy reduces the chances of interfacial delamination growth from an existing embedded delamination caused by low velocity impact in the post impact loading.

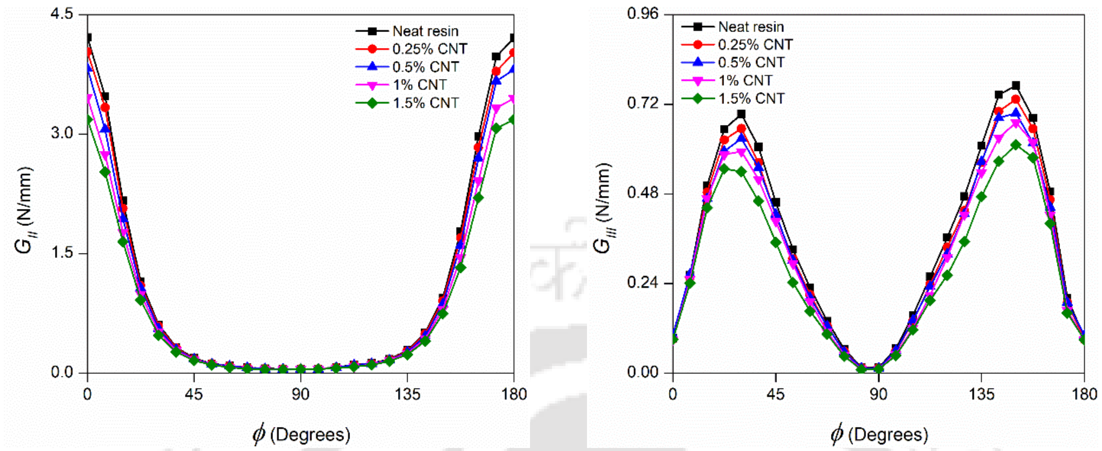

(a) (b)

**Figure 6.24:** Variation of (a) $G_{II}$ and (b) $G_{III}$ along delamination front

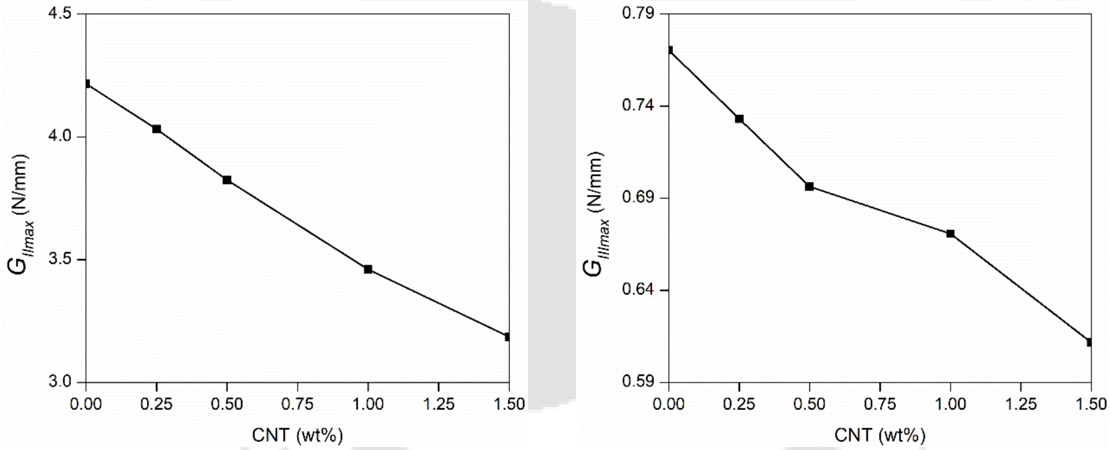

(a) (b)

**Figure 6.25:** Maximum SERR (a) $G_{II\max}$, and (b) $G_{III\max}$ variation with CNT wt%

**Figures 6.25(a)**, and **6.25(b)** show the variation of $G_{II\max}$ and $G_{III\max}$ respectively on the delamination front with increasing CNT wt% for $e = 2.5$. Since $G_{II}$ is maximum for $\theta = 0^\circ$, therefore variation in $G_{II\max}$ with CNT wt% is shown only for $\theta = 0^\circ$. Similarly, the variation of $G_{III\max}$ with CNT wt% is shown only for $\theta = 90^\circ$. It could be observed that $G_{II\max}$ and $G_{III\max}$ values are significantly reduced with increasing wt% of CNTs. It has been observed that both $G_{II\max}$ and $G_{III\max}$ values are reduced by 25% and 21% respectively compared to those for neat resin with the addition of 1.5 wt% CNTs in epoxy. The growth of delamination in a laminate largely depends on the critical SERR ($G_c$). Determining the critical SERR value is crucial because it determines whether the delamination will continue to grow or not. Therefore, it is essential to calculate $G_c$ specifically for the same laminate.

### 6.5.3 Critical SERR ($G_c$) and influence of CNT wt%

As discussed, critical SERR ($G_c$) has been computed using QSC and VCCI as discussed in section 3.3.3 of Chapter 3. In the present case, $G_c$ has been calculated for different wt% of CNT in (CNT+epoxy) to know the effect of addition of CNTs in the epoxy actually enhances the resistance to the further growth of embedded delamination. Since the SERR is maximum corresponding to e = 2.5 and for $\theta = 0^\circ$, therefore the variation of $G_c$ with CNT wt% has been computed corresponding to $e$ = 2.5 and $\theta = 0^\circ$, and **Fig. 6.26** shows the variation with different CNT wt%. It could be seen from **Fig. 6.26** that as CNT wt% increases, the magnitude of $G_c$ increases substantially and reaches a maximum at 1 wt%. However, with the further increase in CNT beyond 1 wt%, value of $G_c$ decreases though still more than that corresponding to the case of neat resin. It could be observed that the corresponding to 1 wt% of CNT, increase in $G_c$ is 50% more than that of neat resin. Therefore, it could be inferred that addition of CNT to epoxy leads to significant enhancement in the resistance to further growth of delamination in the post impact loading, but there is a limit to CNT wt% to which this enhancement is maximum which is 1% in the present case.

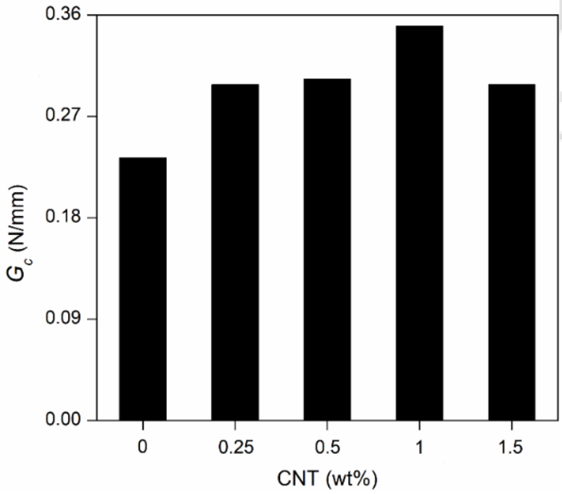

**Figure 6.26:** $G_c$ variation with wt% of CNT

As could be seen that the critical SERR computed under transverse load is less than that corresponding to axial loading. This is due to the fact that there is a huge difference in mode mixity at the delamination front. While for axial loading it is almost like pure mode II but in case of transverse loading it is mix of all the three modes at some locations and hence the difference. In general, it could be summarized that in post impact loading, the laminate is tougher against axial load than against transverse load.

## 6.6 Summary

The present chapter aimed at investigating the enhancement of resistance to growth of delamination by adding CNTs with epoxy in the post impact loading of a laminate having an embedded elliptical delamination caused due to low velocity impact. Using VCCI and stress based criterion, 3D FEAs are carried out to calculate the total critical SERR as a measure of resistance to delamination growth corresponding to different CNT wt% and the following important observations have been drawn.

- In-plane, as well as out-of-plane stresses are induced along the delamination, due to centrally located embedded delamination at the interface of laminate, when the laminate is loaded.
- Existence of all the three out-of-plane components of the interlaminar stresses at the delamination front clearly shows a 3D state of stress at the delamination front. Thus it could be inferred that the delamination at the interface will be mixed mode even if the applied load is purely axial.
- In both cases of laminate with axial and transverse loading, the maximum magnitudes of interlaminar stresses $\sigma_z$ , $\tau_{xz}$ and $\tau_{yz}$ occurs at different locations of the delamination front and these increases with increase in aspect ratio (*e*) of the embedded delamination as well as increase in adjacent intact ply orientation.
- In both cases of laminate with axial and transverse loading, similar to the stress variation, the maximum magnitude of individual components of SERR also occur at different locations showing that it is the combination of $G_I$ , $G_{II}$ and $G_{III}$ that will decide whether the delamination will further grow or not. In other words, not only the $G_I$ , $G_{II}$ and $G_{III}$ vary along the delamination front but the mode mix ratio is also different.
- In case of laminate with axial loading, the magnitude of $G_I$ is much smaller compared to those of $G_{II}$ and $G_{III}$ showing that mode II and mode III will dominate the delamination growth.

- In case of laminate with transverse loading, $G_I$ is absent due to compressive nature of interlaminar normal stress, and $G_{II}$ is higher compared to $G_{III}$ showing mode II will dominate the delamination.
- In both cases of laminate with axial loading and transverse loading, both maximum mode II SERR ($G_{II\max}$) and maximum mode III SERR ($G_{III\max}$) increases with the increase in aspect ratio of delamination.
- In both cases of laminate with axial and transverse loading, addition of CNTs to the epoxy leads to substantial improvement in resistance to growth of delamination from an existing embedded delamination at the interface in post impact loading.
- In both cases of laminate with axial and transverse loading, the magnitudes of SERR components decrease with the addition of CNTs to the epoxy indicating that the chance for delamination to grow at the interface could be reduced.
- In the case of axial loading, addition of 1 wt% CNTs in epoxy indicates a reduction of $G_{II\max}$ and $G_{III\max}$ values by 11% and 20% respectively compared to those for neat epoxy (without CNT).
- In the case of transverse loading, addition of 1 wt% CNTs in epoxy indicates a reduction of $G_{II\max}$ and $G_{III\max}$ values by 25% and 21% respectively compared to those for neat epoxy (without CNT).
- Critical SERR as a measure of the resistance to delamination growth is significantly increased by the addition of CNTs to epoxy for both axial and transverse loading respectively in comparison to carbon/epoxy laminate without CNTs.
- Even though the critical SERR of such laminated composites with embedded elliptical delamination at the interface is a function of shape (aspect ratio) of the delamination as well as the relative fiber orientation at the interface, however, in all the cases, the addition of CNTs has shown to improve resistance to delamination growth significantly.
- Adding CNTs to epoxy leads to enhancement in delamination resistance though, there is a limit beyond which further addition of CNTs to epoxy leads to a reduction in critical SERR. Thus, in order to achieve maximum resistance to delamination growth of an embedded elliptical delamination, it is necessary to identify the optimum amount of CNT wt% to be added with the epoxy. In the present case, it is 1% but it may vary based on different laminate configurations.
- In post impact loading, the laminate is tougher against axial loading compared to transverse loading.

# CHAPTER 7

# Three phase carbon/(CNT+epoxy) laminates with multiple embedded elliptical delamination

This chapter presents the FEA of a three phase carbon/(CNT+epoxy) laminates having two neighboring delaminations at the interface to study the interactions of such delamination under loading. Dependence of their interaction on the separating distance has been presented in addition to the influence of CNTs on such delamination.

## 7.1 Introduction

Laminated composite structures are very often subjected to multiple impacts leading to multiple delaminations at the interface. Once such delaminations are identified, it becomes important to understand whether two closely spaced delaminations actually behave as a single large delamination or as individual small delaminations. It is equally important to address how the matrix properties could be modified by adding CNTs so that resistance against merging of two delaminations could be enhanced.

## 7.2 Geometry of the specimen and material properties

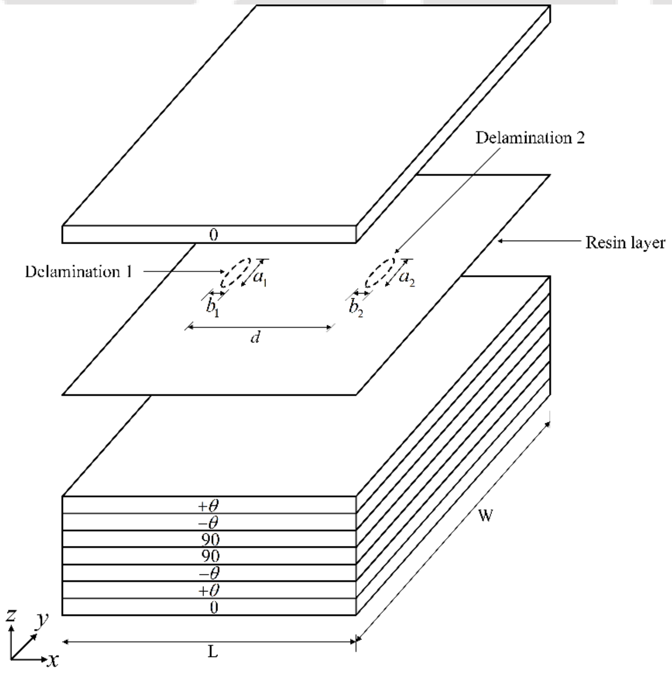

**Figure 7.1:** Two interfacial elliptical delaminations in a laminate

**Figure 7.1** shows the three phase carbon/(CNT+epoxy) laminates having two neighboring delaminations at the interface. A $[0/\pm\theta/90]_s$ laminate configuration has been considered and the delaminations were considered to be present at the $[0/+\theta]$ interface in a thin resin layer.

As shown in **Fig. 7.1**,

$L$ = length = 100 mm
$W$ = width = 100 mm
$a_1, a_2$ = major axes of delamination 1 and 2
$b_1$, $b_2$ = minor axes of the delamination 1 and 2
$e = a / b$ = aspect ratio
$d$ = separating distance between two delaminations.

Elastic properties of CNT+epoxy (matrix) and carbon/(CNT+epoxy) composite laminates have been computed using Halpin-Tsai equations and the rule of mixtures (discussed in section 3.6 of Chapter 3) and are shown in **Table 7.1**.

**Table 7.1:** Carbon/(CNT+epoxy) composites properties

| | Matrix (CNT+epoxy) | | | Composite (Carbon fiber (60%) + (CNT+epoxy)) | | | |
|---|---|---|---|---|---|---|---|
| CNT wt% in epoxy | Tensile modulus (GPa) | Poisson's ratio | Shear modulus (GPa) | Longitudinal tensile modulus $E_1$ (GPa) | Transverse tensile modulus $E_2$ (GPa) | In-plane Poisson's ratio $\nu_{12}$ | In-plane shear modulus $G_{12}$ (GPa) |
| 0.0% | 3.10 | 0.35 | 1.15 | 139.24 | 7.59 | 0.284 | 2.75 |
| 0.25% | 3.31 | 0.35 | 1.23 | 139.33 | 8.11 | 0.284 | 2.93 |
| 0.50% | 3.53 | 0.35 | 1.31 | 139.41 | 8.62 | 0.284 | 3.11 |
| 1.00% | 3.95 | 0.35 | 1.46 | 139.58 | 9.63 | 0.284 | 3.46 |
| 1.50% | 4.38 | 0.35 | 1.62 | 139.75 | 10.65 | 0.284 | 3.81 |

## 7.3 FEA of the laminate with two embedded delaminations

The laminate has been modeled with the top and bottom sub laminates and the interface is represented by a thin (0.1 times ply thickness) resin layer. Delamination is reported to originate at the interface of the resin layer and neighboring laminae [152], which supports the modeling of the interface with a resin rich layer. Additionally, it was reported that the introduction of a thin resin layer eliminates the oscillatory stress singularity that occurs at the interface in layered FRP composites [106]. The laminate having embedded delaminations at the interface is discretized using 3D, eight noded, layered element (SOLID 185 in ANSYS), and layer wise orthotropic properties are input. It has been reported [158] that FEA solutions could produce inaccurate results due to the interpenetration of delaminated layers and therefore, in the present FE analysis, the top and bottom nodes of the delaminated region are connected through a bi-linear contact element (CONTA 178 in ANSYS) ensuring no interpenetration of delaminated layers.

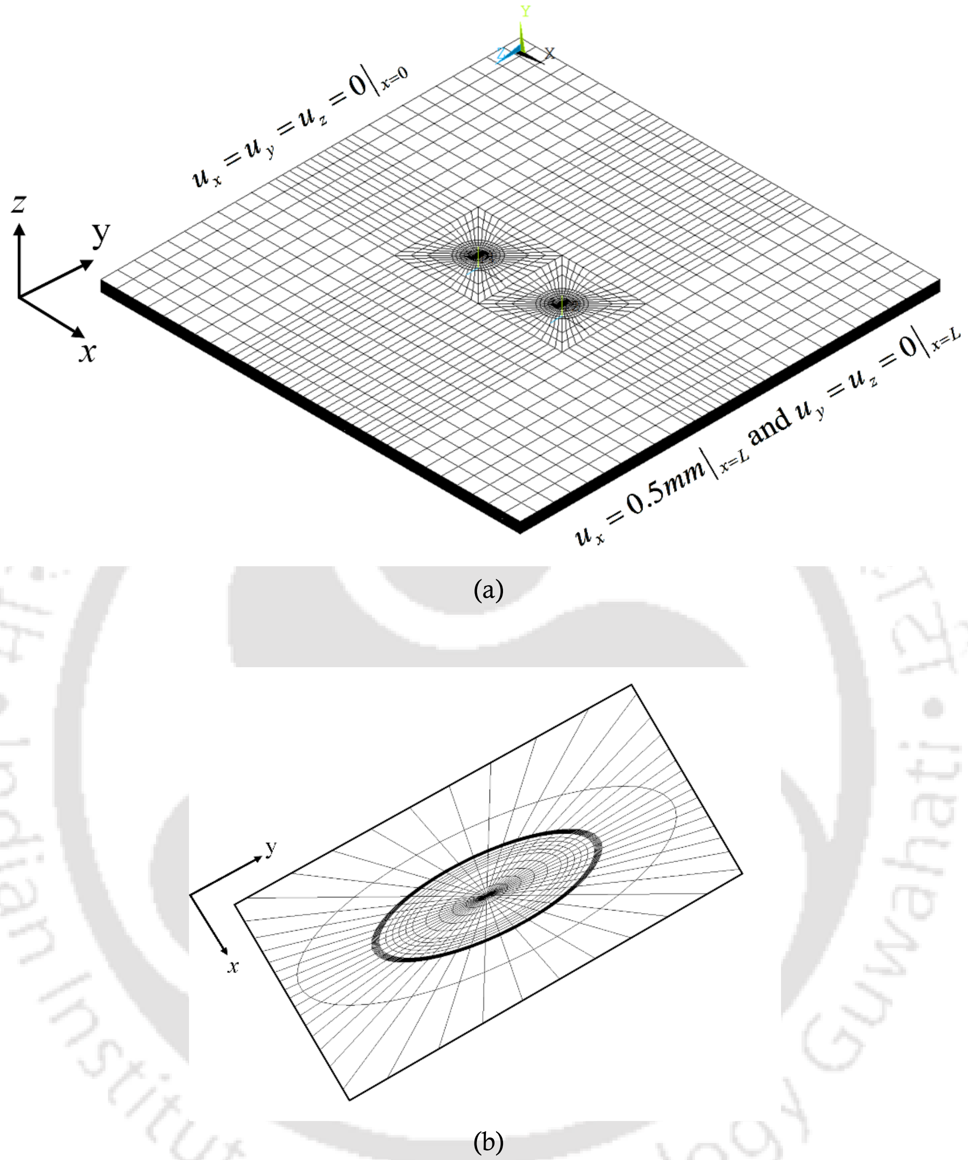

(a)

(b)

**Figure 7.2:** (a) 3D FE mesh of square laminate (b) zoomed mesh near delamination ($e$ = 2.5)

**Figures 7.2(a)** and **7.2(b)** show the 3D FE mesh of the laminate specimen and zoomed view of the mesh close to embedded elliptical delamination respectively. After performing a mesh refinement study, a highly refined mesh close to the delamination front has been used to capture the stiff stress gradient at the delamination front. The convergence of interlaminar shear stress ($\tau_{zn}$) for gradual mesh refinement is shown in **Figure 7.3**. There has been no change in the magnitude of $\tau_{zn}$ beyond 81984 elements as shown in **Table 7.2**. The laminate is modeled using 81984 elements (SOLID 185) and top and bottom delaminated surfaces are connected with 960 elements (CONTA 178).

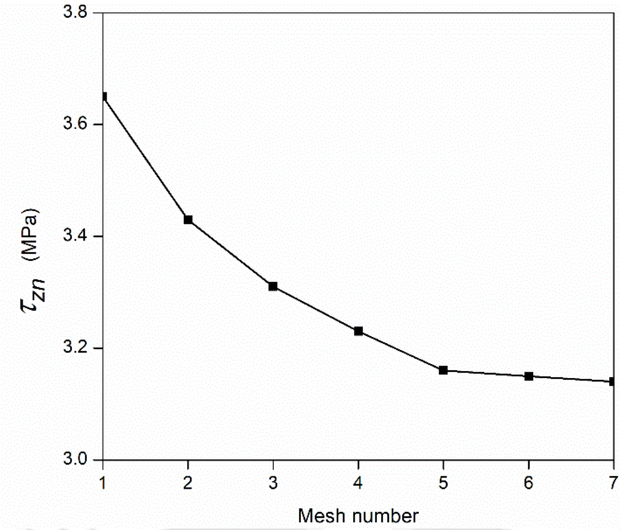

**Figure 7.3:** Finite element mesh convergence ($e = 1$, $d = 20$ mm, and $\theta = 0^{\circ}$)

**Table 7.2:** Finite element mesh convergence of $\tau_{zn}$

| Mesh number | Number of elements | $\tau_{zn}$ (MPa) |
|---|---|---|
| 1 | 28224 | 3.65 |
| 2 | 38976 | 3.43 |
| 3 | 49728 | 3.31 |
| 4 | 60480 | 3.23 |
| 5 | 71232 | 3.16 |
| 6 | 81984 | 3.15 |
| 7 | 92736 | 3.15 |

## 7.4 Results and discussions for axial loading of the laminate

A three phase carbon/(CNT+epoxy) laminate with two interfacial delaminations of elliptical shape has been modeled in ANSYS using SOLID 185 and CONTA 178 elements by developing an APDL code. Interlaminar stresses have been computed using the 3D FE analysis and the components of SERR are computed using virtual crack closure integration (VCCI) technique. Since a stiff stress gradient exists near the vicinity of the embedded delamination, a highly refined mesh is used there. The VCCI based evaluation of SERR has been validated before using the same for analysis of the embedded delamination. Different configurations of the laminate have been considered in the study to understand the effect of adding CNTs to the epoxy on the propensity of the delamination to grow further under loading.

### 7.4.1 Validation

In order to validate the computed SERR around a circular delamination front using the present FE analysis and virtual crack closure integral, a $[(0/+45/-45)_3]_s$ square laminate with a side of 50 mm, and a centrally located through hole of 5 mm in diameter, is considered following the work of Shen et al. [159]. Mode II SERR computed using VCCI from the present FE analysis is compared with that of Shen et al. [159] as shown in **Fig. 7.4**. and a similar qualitative trend in variation of $G_{II}$ with $\phi$ could be seen excepting at a few points where the present FE estimates higher values of $G_{II}$.

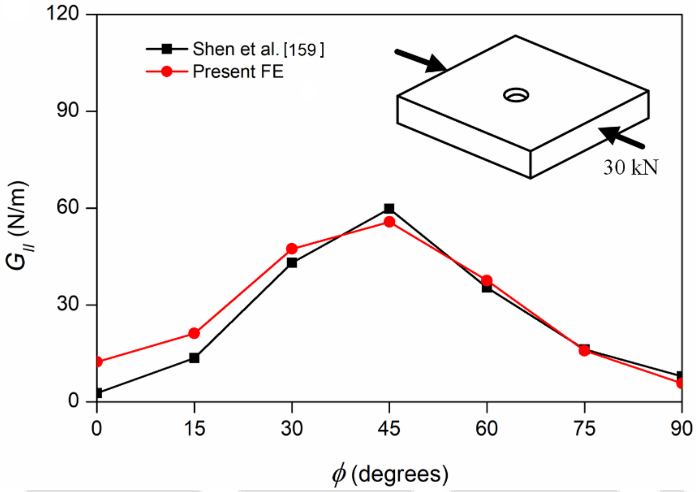

**Figure 7.4:** Mode II SERR around a circular delamination front

### 7.4.2 Interlaminar stresses along embedded delaminations 1 and 2

The variation of interlaminar stresses $\sigma_z$ , $\tau_{zn}$ and $\tau_{zt}$ along the delamination front 1 and 2 (represented by angles measured from the X-axis as in **Fig. 7.2**) for a separating distance of 20 mm between the two delaminations in a $[0/\pm\theta/90]_s$ carbon/epoxy laminate are shown in **Fig. 7.5(a)**, **7.5(b)**, and **7.5(c)** respectively. These are stresses near the delamination front averaged over a very small distance. Stress variation has been shown along half of the total delamination front $(0-180^\circ)$ due to the symmetry. The presence of all three out-of-plane interlaminar stresses shows a 3D state of stress at the delamination fronts leading to mixed mode delamination. The magnitudes and variation of interlaminar stresses for both the delaminations are same excepting slight difference in the case of $\sigma_z$ .

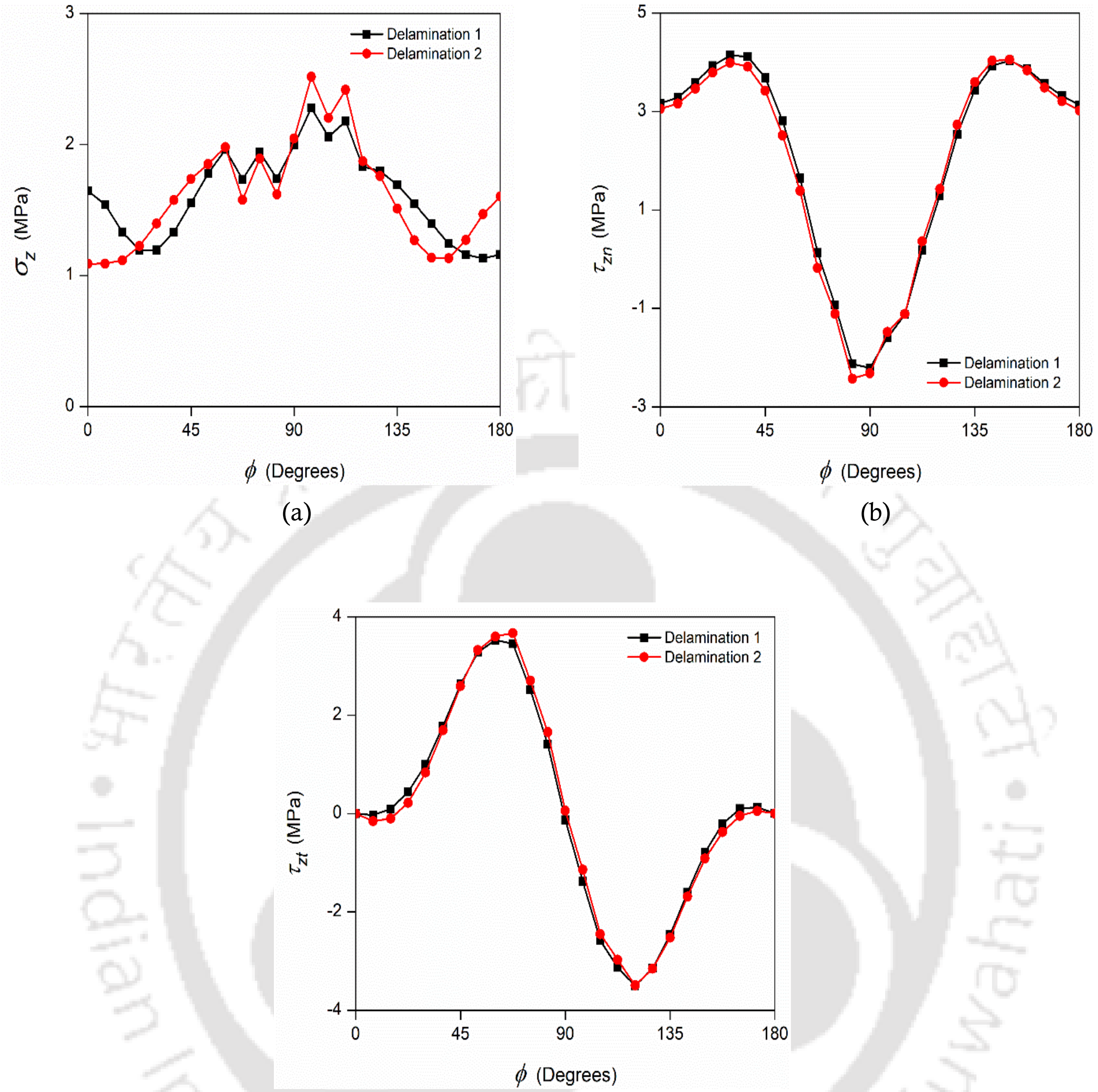

(a) (b)

(c)

**Figure 7.5:** Variation of (a) $\sigma_z$ , (b) $\tau_{zn}$ and (c) $\tau_{zt}$ along delamination fronts 1 and 2 ($e = 1$, $d = 20$ mm, and $\theta = 0^\circ$)

### 7.4.3 Strain energy release rate along the delamination front

By performing 3D FE analysis, considering the delamination front near the elliptical delamination as the crack front, required interlaminar stresses and displacements are evaluated to compute SERR components for different separating distances, different delamination shapes, and different fiber orientations using VCCI as discussed in section 3.3.2 of Chapter 3.

#### *7.4.3.1 Effect of relative spacing between two delaminations*

In order to understand how relative spacing or separating distance between two delaminations at the interface influences the strain energy release rate, different center distances (*d*) viz. 20, 40 and 60 mm are considered. SERRs are computed using VCCI along both the delamination fronts but the variation is shown only for delamination front 1 due to symmetry of geometry.

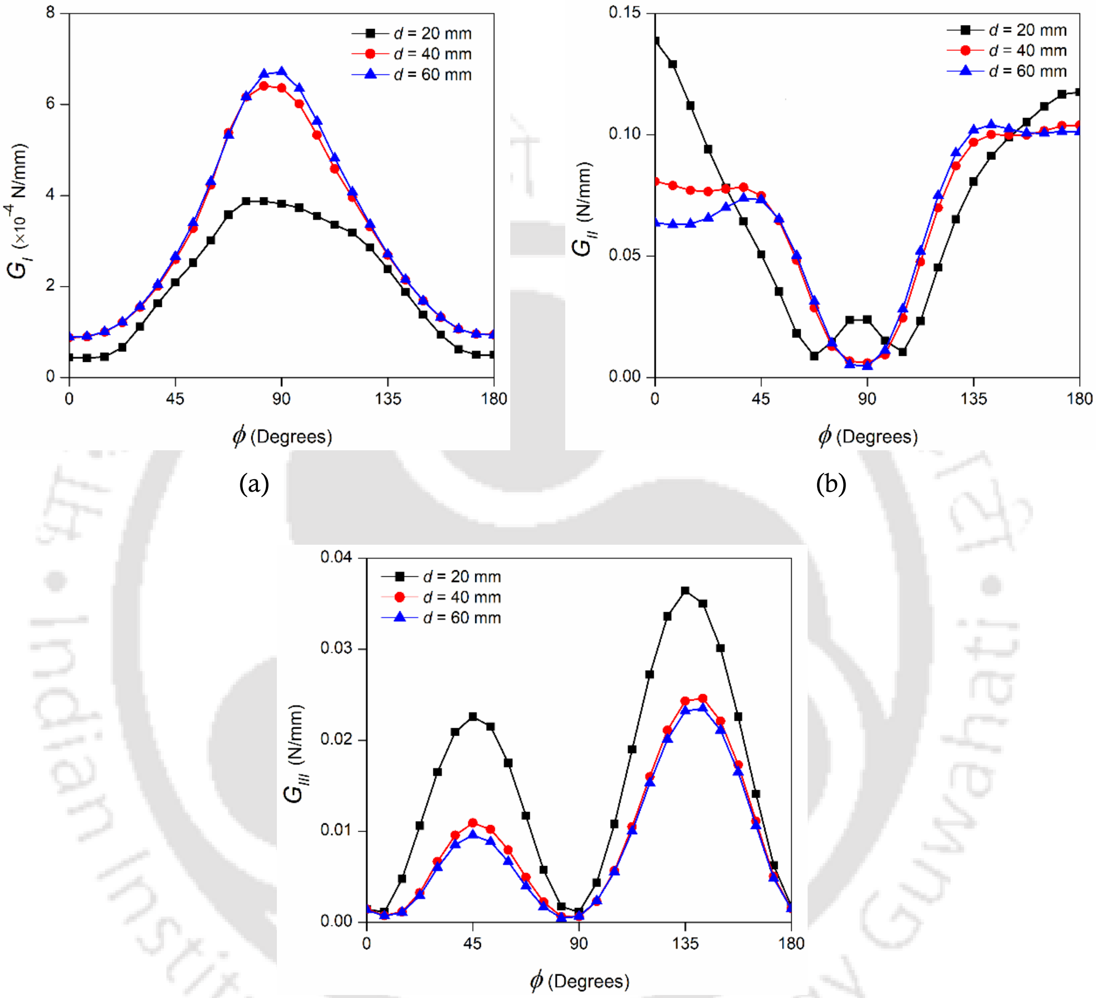

(a)

(b)

(c)

**Figure 7.6:** Variation of (a) $G_I$ ,(b) $G_{II}$ , and (c) $G_{III}$ along delamination front 1

**Figures 7.6(a)**, **7.6(b)**, and **7.6(c)** show the variation of SERR components, $G_I$ , $G_{II}$ , and $G_{III}$ respectively for delamination 1 with different separating distances for $e$ = 1 and $\theta = 0^{\circ}$ degrees. It could be observed that in accordance with the variation of interlaminar stresses (**Fig. 7.5**), the components of SERR also vary following a similar trend along the delamination front. Similar to the stress variation, the maximum magnitude of SERR components also occur at different location showing that it is the combination of $G_I$ , $G_{II}$ and $G_{III}$ that will decide whether the delamination will grow or not. However, it could be observed that the magnitude of $G_I$ is much smaller compared to those of $G_{II}$ and $G_{III}$ showing that mode II and mode III will dominate the delamination growth. Also $G_{II} > G_{III}$ by an order of magnitude showing that $G_{II}$ is the dominant mode even though $G_{III}$ also contributes.

It could be seen that location of maximum value of $G_{II}$ is at $0^{\circ}$ for smaller separating distance ($d$ = 20 mm) and for larger separating distance the location shifts to $180^{\circ}$. This shows that for a smaller separating distance the two delaminations act as one big delamination and tend to progress towards the edge. Whereas for larger separating distance, the two delaminations grow towards each other and finally coalesce into one.

The maximum magnitudes of $G_{II}$ and $G_{III}$ for different separating distances have been shown in **Fig. 7.7**. It has been observed that as separating distance between the two delaminations increases, there is a substantial reduction in both maximum mode II SERR ( $G_{II\max}$ ) and maximum mode III SERR ( $G_{III\max}$ ) when the separating distance is increased from 20 mm to 40 mm. But when the separating distance is increased further the values almost remain same.

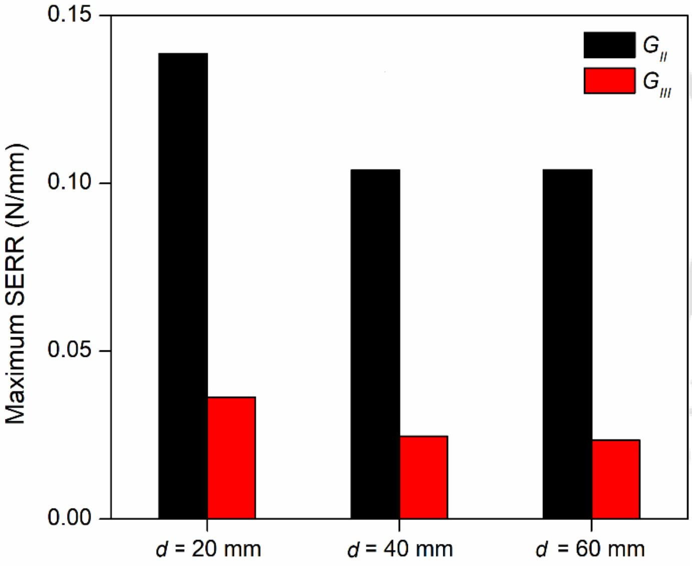

**Figure 7.7:** Maximum SERR for different separating distances

### *7.4.3.2 Effect of shape of delamination*

To study the influence of delamination shape at the interface on the SERR along the delamination front 1, the delamination shape ($e = a/b$) is varied from to 1 to 2.5 and the SERRs are computed for different separating distances.

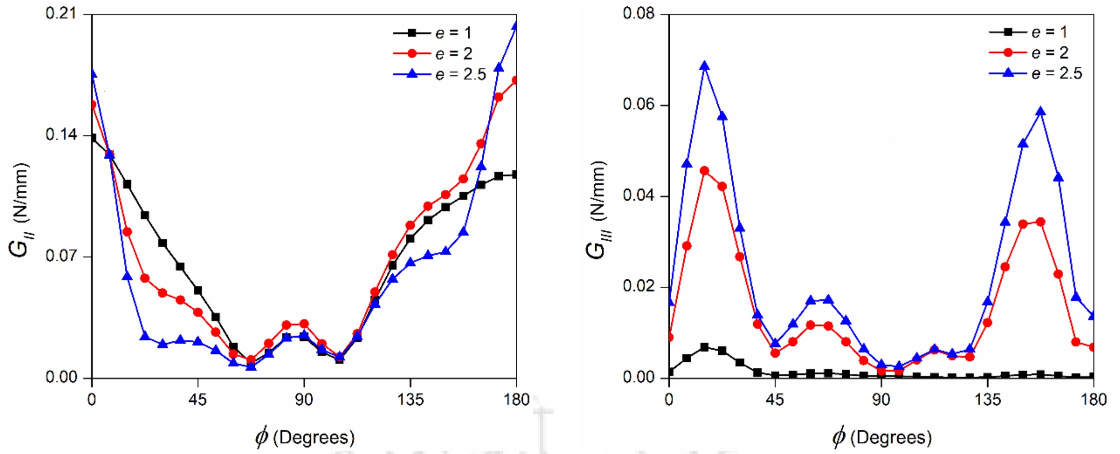

(a) (b)

**Figure 7.8:** Variation of (a) $G_{II}$ , and (b) $G_{III}$ along delamination front 1

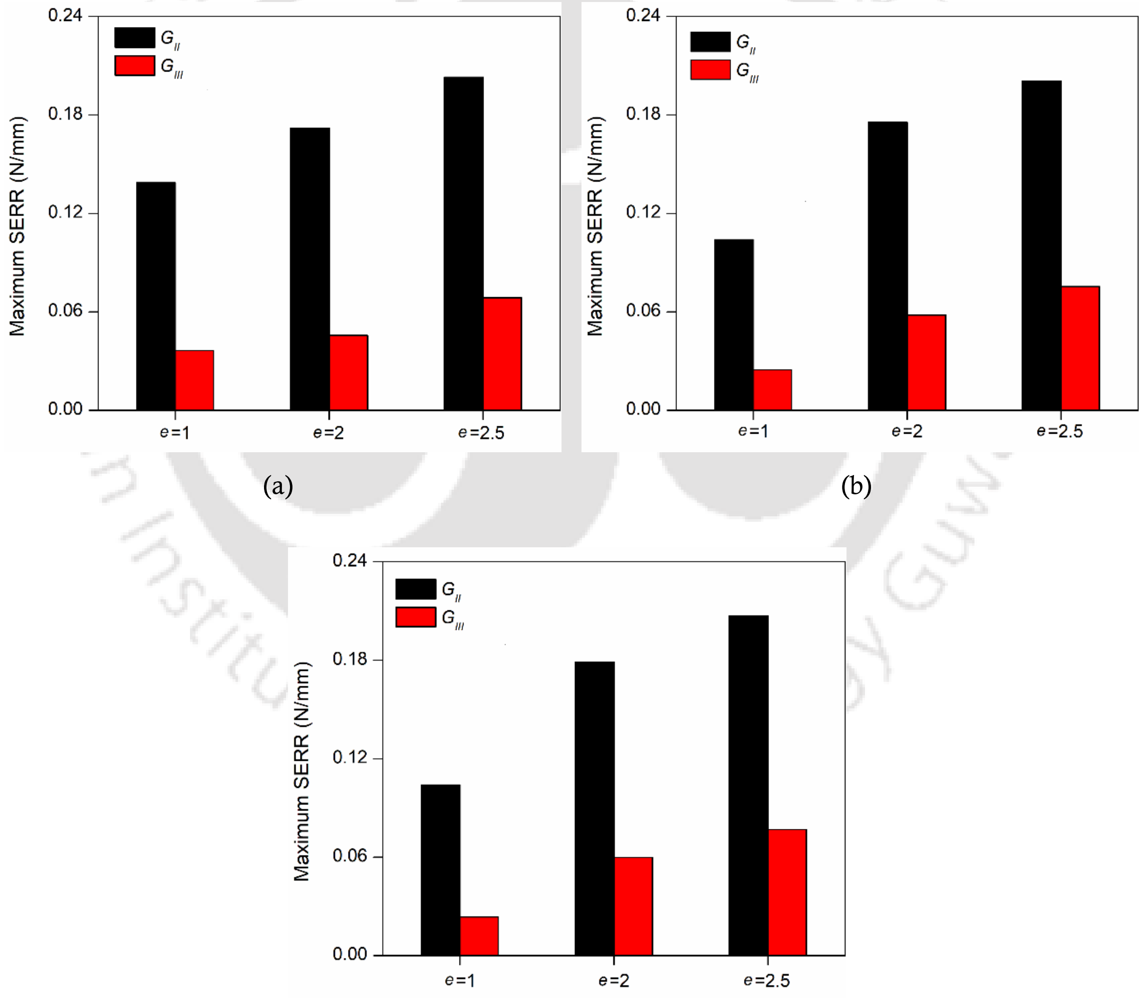

(a) (b)

(c)

**Figure 7.9:** Maximum SERR with different aspect ratio of the delamination for (a) $d = 20$ mm, (b) $d = 40$ mm, and (c) $d = 60$ mm

**Figures 7.8(a)**, and **7.8(b)** show how $G_{II}$ , and $G_{III}$ respectively vary along the curved delamination with increasing aspect ratio, $e$ (= $a/b$) for $d$ = 20 mm and $\theta = 0^{\circ}$ degrees. In the present case, with the increase in $e$, magnitude of $G_{II}$ and $G_{III}$ increases. With the increase of the aspect ratio, $e$, the point at which delamination starts to grow (at which $G_{II}$ and $G_{III}$ reach maximum value) changes along the delamination front. Here also $G_{II} > G_{III}$ for all values of $e$, location of $G_{II}$ suggest that for $d$ = 20 mm, the two delaminations act as one single delamination and grow towards the edge of the laminate.

**Figure 7.9(a)**, **7.9(b)**, and **7.9(c)** show the variation of both $G_{II\max}$ and $G_{III\max}$ for $\theta = 0^{\circ}$ degrees with increasing aspect ratio, $e$ (= $a/b$) for $d$ = 20 mm, $d$ = 40 mm, and $d$ = 60 mm respectively. In all the cases, $G_{II\max}$ and $G_{III\max}$ increases substantially with the increase in $e$, showing that the chances of delamination along the delamination front increases with the increase in aspect ratio.

### *7.4.3.3 Effect of fiber orientation*

In order to understand how the fiber orientation at the interface influences the SERR, the fiber orientation angle ($\theta$) of the adjacent lamina is varied from $0^{\circ}$ to $90^{\circ}$. From the previous section 7.4.3.2 it has been observed that SERR is maximum for an aspect ratio of $e$ = 2.5. Hence, in the present case, SERR is computed for $e$ = 2.5 and $d$ = 20 mm.

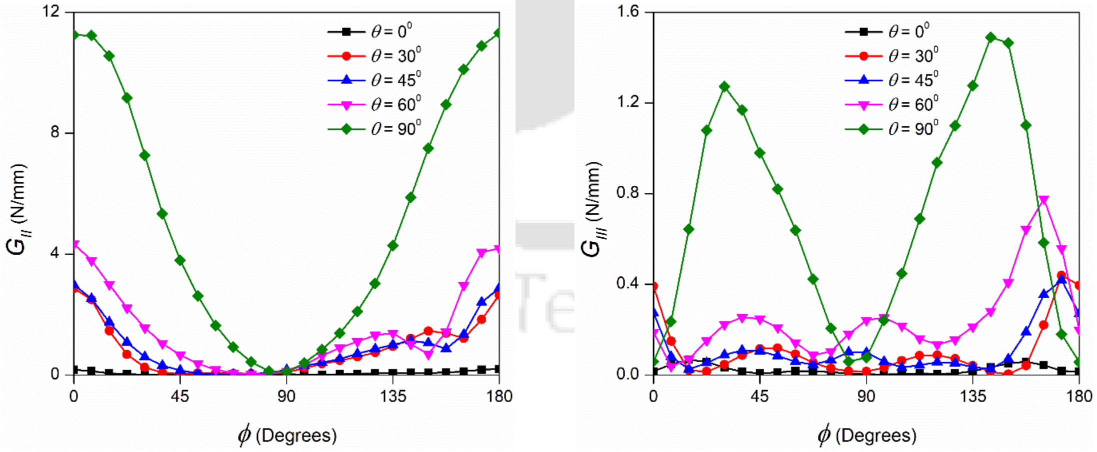

(a) (b)

**Figure 7.10:** Variation of (a) $G_{II}$ and (b) $G_{III}$ along delamination front 1

**Figures 7.10(a)**, and **7.10(b)** show the variation of $G_{II}$ and $G_{III}$ respectively around the elliptical delamination front for different orientation of fiber at the interface. While $G_{II}$ is maximum at $\phi = 0^{\circ}$ for all the cases, and the maximum value of $G_{III}$ changes with fiber orientation. As could be seen that the magnitude of $G_{II}$ is more than that of $G_{III}$. $G_{II}$ is maximum at $\phi = 0^{\circ}$ in all the cases but the $G_{II\max}$ is highest for $\theta = 90^{\circ}$. Similarly, $G_{III\max}$ is also highest for $\theta = 90^{\circ}$.

**Figures 7.11** shows the variation of $G_{II\max}$ and $G_{III\max}$ with the fiber orientation angle, $\theta$. It has been observed that as $\theta$ increases, there is a significant increase in $G_{II\max}$ and $G_{III\max}$ and for $\theta = 90^{\circ}$, $G_{II\max}$ and $G_{III\max}$ values are the highest though $G_{II\max}$ is much higher compared to $G_{III\max}$. This is because the property mismatch is maximum at $0^{\circ}/90^{\circ}$ indicating higher chances of delamination along the delamination front. Similar experimental results have been observed where SERR increases with the increase in fiber orientation [160].

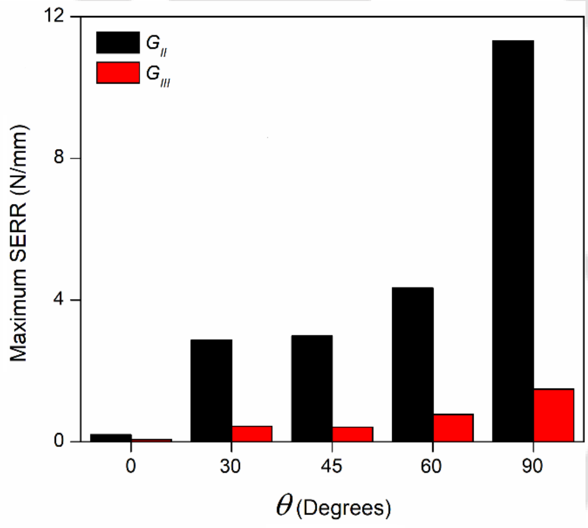

**Figure 7.11:** Maximum SERR for different fiber orientations

### 7.4.4 Effect of CNT wt% in epoxy on SERR

Having observed that the SERR components in case of two interacting delaminations depend upon many factors viz., the separating distance, the shape and size of the delamination and the relative fiber orientation at the interface, it is clear that delamination progress is a complex mixed mode phenomenon and is not easy to estimate. However, the objective here has been to investigate whether using a modified matrix in the form of (CNT+epoxy) could actually mitigate the chances of delamination progress. Therefore, in order to study the influence of CNTs on the delamination growth from the impact induced delaminations at the interface, different weight percentages (0%, 0.25%, 0.5%, 1%and 1.5%) of CNTs are considered and finite element analysis has been performed in which the components of SERR are computed using VCCI. It has been observed from the results in the previous section 7.4.3.3 that SERR is maximum corresponding to fiber orientation of $90^{\circ}$ and aspect ratio of 2.5. Hence, the influence of CNT wt% on SERR for these combinations has been presented here though similar trends have also been observed for other cases also.

**Figures 7.12(a)**, and **7.12(b)** show the variation of $G_{II}$ and $G_{III}$ respectively along the elliptical delamination front with increasing CNT wt% at the interface in the presence of a neighboring delamination with separating distance, $d$ = 20 mm. In all the cases, $G_{II}$ is maximum at $\phi = 0^{\circ}$. It could be observed that both $G_{II\max}$ and $G_{III\max}$ show significant reductions with increase in CNT wt%.

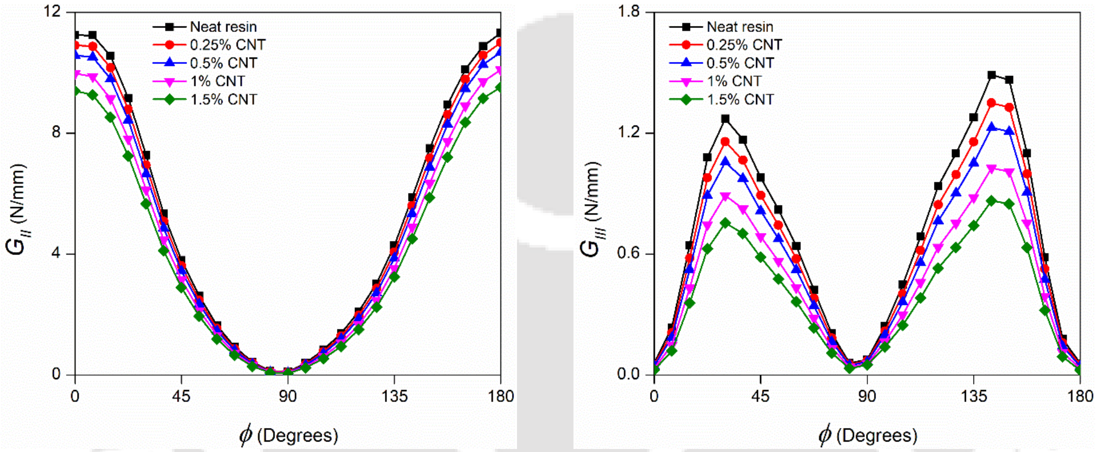

(a) (b)

**Figure 7.12:** Variation of (a) $G_{II}$ and (b) $G_{III}$ along delamination front 1

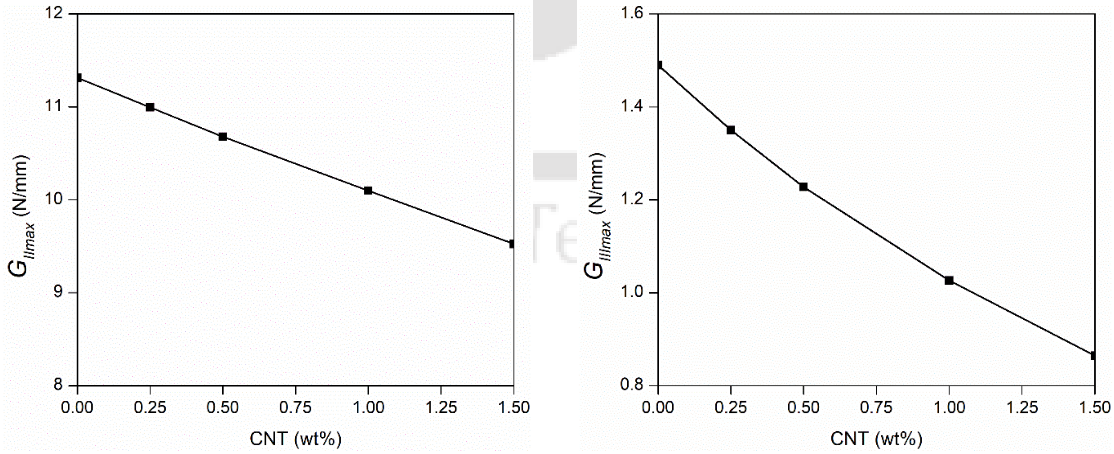

(a) (b)

**Figure 7.13:** Maximum SERR (a) $G_{II\max}$, and (b) $G_{III\max}$ variation with CNT wt%

**Figures 7.13(a)**, and **7.13(b)** show the variation of $G_{II\max}$ and $G_{III\max}$ respectively on the elliptical delamination front 1 with increasing CNT wt% for ply angle of $90^{\circ}$ at the interface.

It has been observed that as the CNT wt% increases, $G_{II\max}$ and $G_{III\max}$ decreases and a maximum reduction of 16% in $G_{II\max}$ and 42% in $G_{III\max}$ has been observed for 1.5 wt% in epoxy. This shows that with the addition of CNT wt%, the chances of multiple delaminations growing as a single delamination at the interface are reduced significantly.

## 7.5 Results and discussions for transverse loading of the laminate

Interlaminar stresses have been computed using the 3D FE analysis and the components of SERR are computed using virtual crack closure integration technique. The same laminate used for axial loading analysis is considered here and different configurations of the laminate have been considered in the study to understand the effect of adding CNTs to the epoxy on the propensity of the delamination to grow further under transverse loading.

### 7.5.1 FE analysis with embedded delamination

FE modeling of the laminate with two interacting embedded delaminations is same as for the case of axial loading. **Figures 7.14(a)** and **7.14(b)** show the 3D FE mesh of the laminate specimen and zoomed view of the mesh close to embedded elliptical delamination respectively. After performing a mesh refinement study, a highly refined mesh close to the delamination front has been used to capture the stiff stress gradient at the delamination front. The convergence of interlaminar shear stress ( $\tau_{zn}$ ) for gradual mesh refinement is shown in **Figure 7.15**. There has been no change in the magnitude of $\tau_{zn}$ beyond 71232 elements as shown in **Table 7.3**. The laminate is modeled using 71232 elements (SOLID 185) and top and bottom delaminated surfaces are connected with 960 elements (CONTA 178). Transverse loading is simulated by clamping all the edges of the laminate and applying transverse loading of 500N at centre. Different values of the relative spacing between delamination 1 and delamination 2 have been considered.

**Table 7.3:** Finite element mesh convergence of $\tau_{zn}$

| Mesh number | Number of elements | $\tau_{zn}$ (MPa) |
|---|---|---|
| 1 | 28224 | -6.91 |
| 2 | 38976 | -8.04 |
| 3 | 49728 | -8.91 |
| 4 | 60480 | -9.15 |
| 5 | 71232 | -9.27 |
| 6 | 81984 | -9.27 |

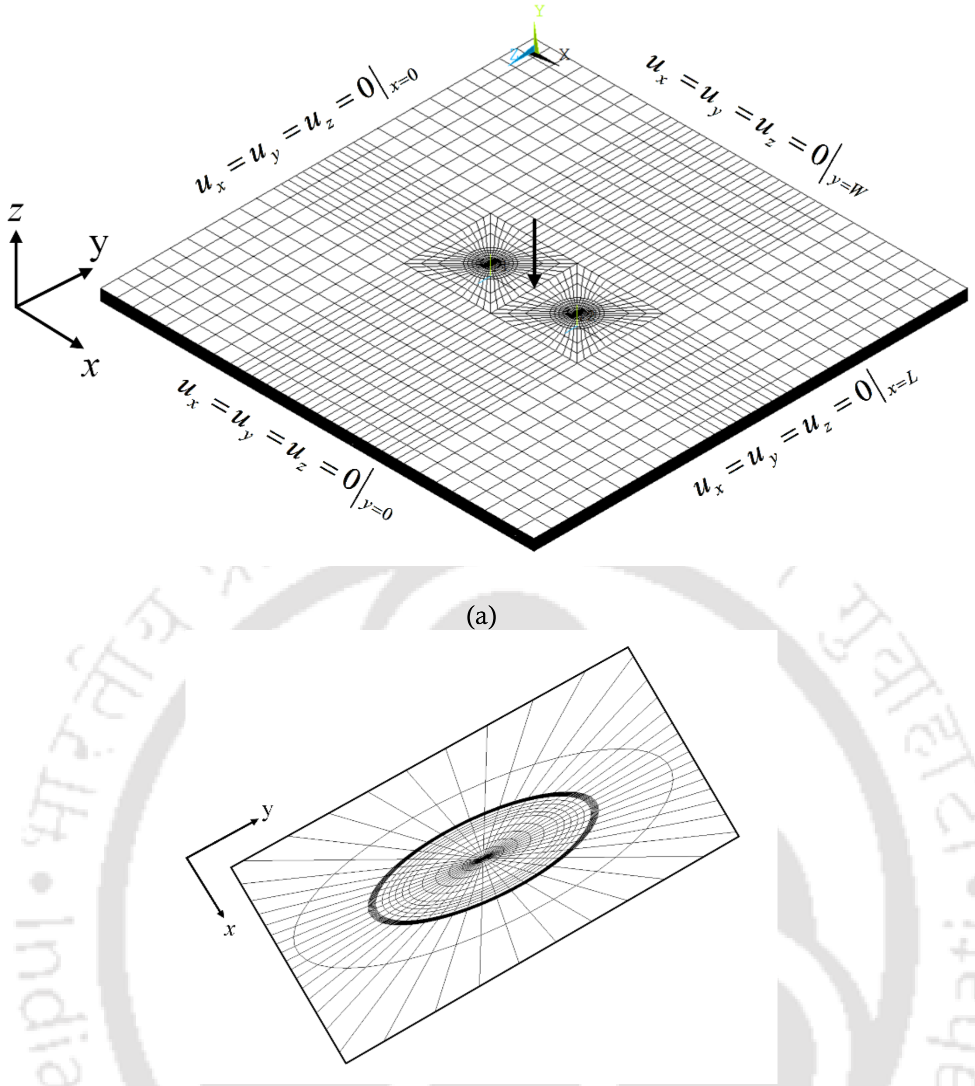

(a)

(b)

**Figure 7.14:** (a) 3D FE mesh of square laminate (b) zoomed mesh near delaminations ($e = 2.5$)

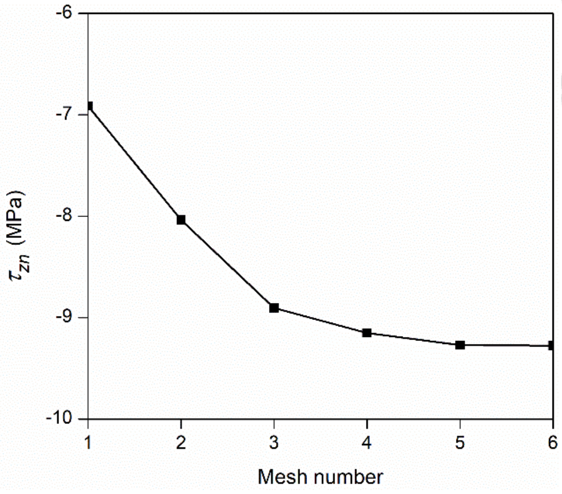

**Figure 7.15:** Finite element mesh convergence ($e = 1$, $d = 20$ mm, and $\theta = 0^{\circ}$)

### 7.5.2 Interlaminar stresses along embedded delaminations 1 and 2

The variation of interlaminar stresses $\sigma_z$ , $\tau_{zn}$ and $\tau_{zt}$ along the delamination front 1 and 2 (represented by angles measured from the X-axis with reference to **Fig. 7.14**) for a separating distance of 20 mm between the two delaminations in a $[0/\pm\theta/90]_s$ carbon/epoxy laminate are shown in **Fig. 7.16(a)**, **7.16(b)**, and **7.16(c)** respectively. These are the stresses near the delamination front averaged over a very small distance. Stress variation has been shown along half of the total delamination front ($0-180^\circ$) due to the symmetry. The presence of all the three out-of-plane interlaminar stresses shows a 3D state of stress at the delamination fronts leading to mixed mode delamination. The magnitudes and variation of interlaminar stresses for both the delaminations are exactly identical due to the symmetric locations and symmetric loading.

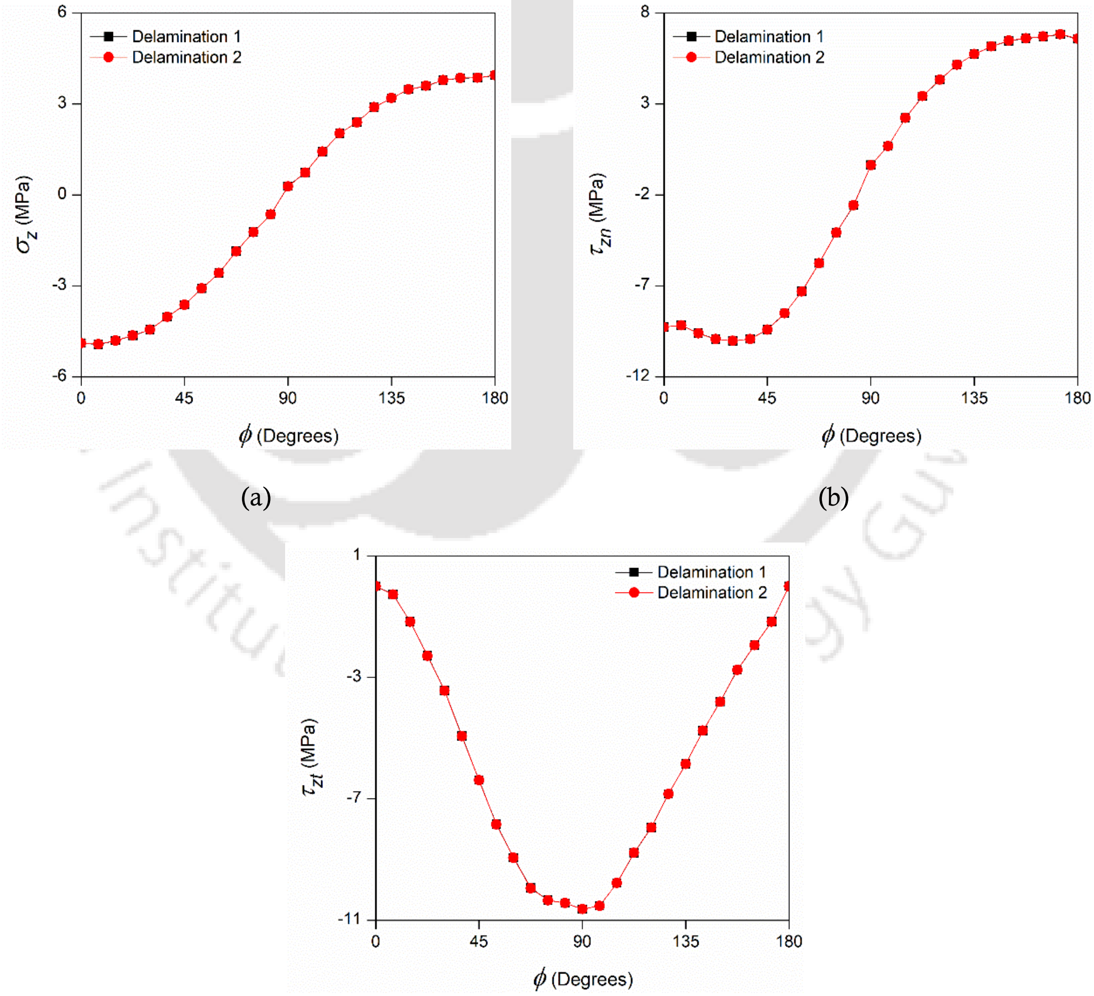

(a) (b)

(c)

**Figure 7.16:** Variation of (a) $\sigma_z$ , (b) $\tau_{zn}$ and (c) $\tau_{zt}$ along delamination fronts 1 and 2 ($e$ = 1, $d$ = 20 mm, and $\theta = 0^\circ$)

### 7.5.3 Strain energy release rate along the delamination front

By performing 3D FE analysis, considering the elliptical delamination front as the crack front, required interlaminar stresses and displacements are evaluated to compute SERR components for different separating distances, different delamination shapes, and different fiber orientations using VCCI as discussed in section 3.3.2 of Chapter 3

#### *7.5.3.1 Effect of relative spacing between two delaminations*

In order to understand how relative spacing between the two delaminations at the interface influences the strain energy release rate, different separating distances (*d*) viz. 20, 40 and 60 mm are considered. Components of SERRs are computed using VCCI along both the delamination fronts but the variation is shown only for delamination 1 due to identical variation.

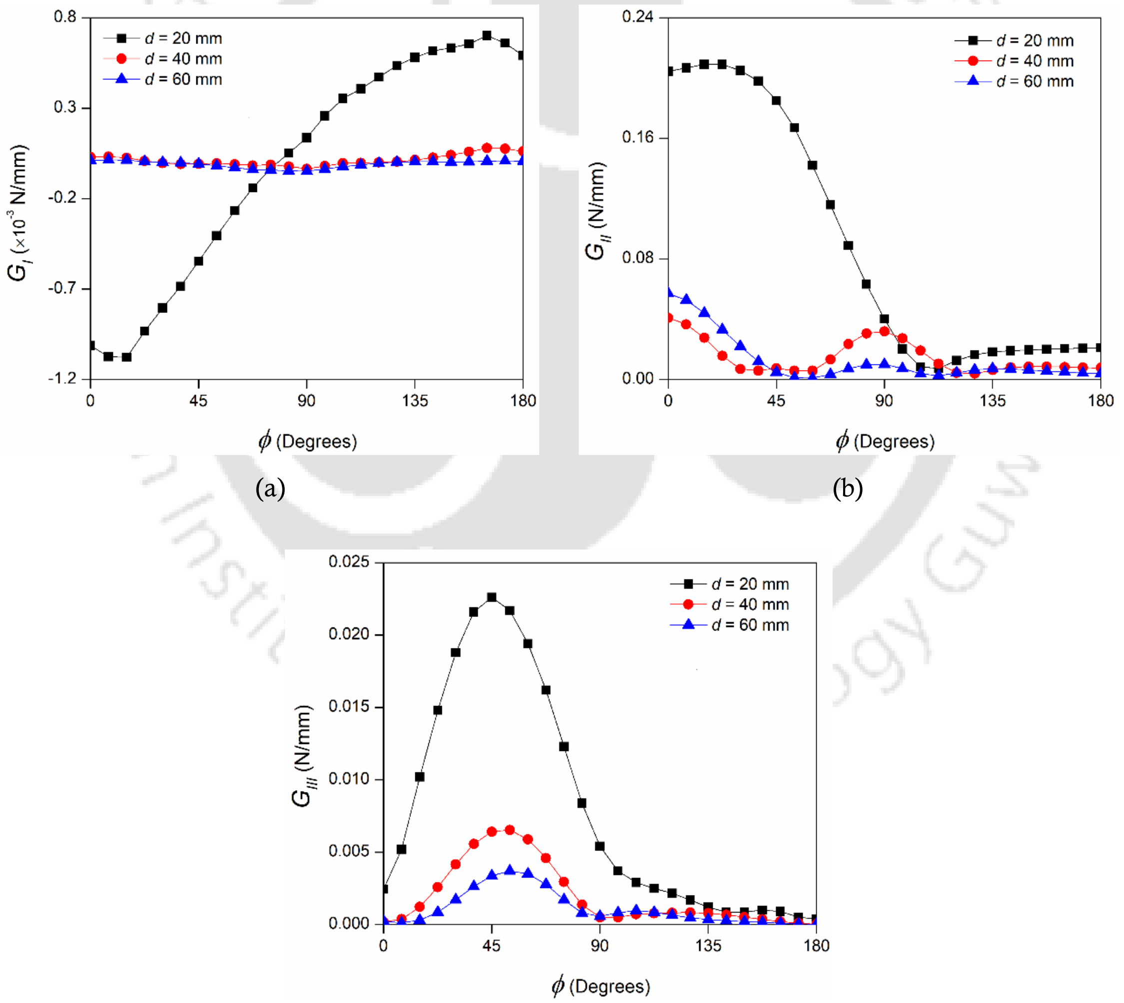

(a)

(b)

(c)

**Figure 7.17:** Variation of (a) $G_I$ , (b) $G_{II}$ , and (c) $G_{III}$ along delamination front 1

**Figures 7.17(a)**, **7.17(b)**, and **7.17(c)** show the variation of SERR components, $G_I$, $G_{II}$, and $G_{III}$ respectively for delamination 1 with different separating distances for $e$ = 1 and $\theta = 0^\circ$ degrees. It could be observed that in accordance with the variation of interlaminar stresses (**Fig. 7.16**), the components of SERR also vary following a similar trend along the delamination front. Similar to the stress variation, the maximum magnitude of SERR components also occur at different location showing that it is the combination of $G_I$, $G_{II}$ and $G_{III}$ that will decide whether the delamination will grow or not. However, it could be observed that the magnitude of $G_I$ is much smaller compared to those of $G_{II}$ and $G_{III}$ showing that mode II and mode III will dominate the delamination growth. It could be observed that except for $d$ = 20 mm, $G_I = 0$ for all the cases showing that mode I is absent, mode II and mode III are the dominant modes. It could also be observed that while $G_I$ (for $d$ = 20 mm) is maximum at $\phi = 180^\circ$, $G_{II}$ is maximum at $\phi = 0^\circ$ and $G_{III}$ is maximum at $\phi = 45^\circ$. This shows that growth of delamination is not self-similar and is decided by $G_I$, $G_{II}$ and $G_{III}$. It is therefore not very clear how the two neighboring delaminations will interact. However, it could be seen that in all the cases of separating distances, $G_{II}$ is maximum at $\phi = 0^\circ$ and $G_{III}$ is maximum at $\phi = 45^\circ$ and therefore unlike axial loading, here the nature of interaction is same for all the cases of separating distances studied here. In addition, the fact that $G_{II} > G_{III}$ and $G_{II}$ is always maximum at $\phi = 0^\circ$ indicates that the two delaminations will always grow as one large delamination and progress towards the edge of the laminate.

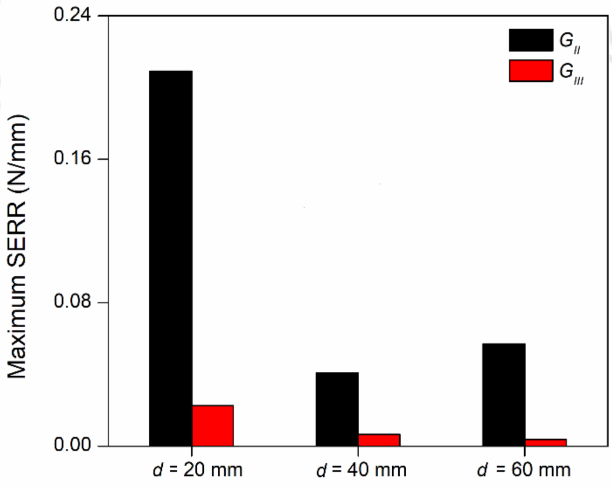

**Figure 7.18:** Maximum SERR for different separating distances

The maximum magnitudes of $G_{II}$ and $G_{III}$ for different separating distances have been shown in **Fig. 7.18**. It has been observed that as separating distance between the two delaminations increases, there is a substantial reduction in both $G_{II\max}$ and $G_{III\max}$ when the separating distance is increased from 20 mm to 40 mm. But when the separating distance is increased further the values almost remain same.

### *7.5.3.2 Effect of shape of delamination*

To study the influence of delamination shape at the interface on the SERR along the delamination front 1, the delamination shape ($e = a/b$) is varied from to 1 to 2.5 and the SERRs are computed for different separating distances.

**Figures 7.19(a)**, and **7.19(b)** show how $G_{II}$ , and $G_{III}$ respectively vary along the curved delamination with increasing aspect ratio, $e$ (= $a/b$) for $d$ = 20 mm and $\theta = 0^{\circ}$ degrees. In the present case, with the increase in $e$, the magnitude of $G_{II}$ decreases and that of $G_{III}$ increases. With the increase of the aspect ratio, $e$, the point at which delamination starts to grow (at which $G_{II}$ and $G_{III}$ reach maximum value) changes along the delamination front. As could be seen, for $e$ = 1, $G_{II}$ is maximum at $\phi = 0^{\circ}$ but for $e$ = 2 and $e$ = 2.5, $G_{II}$ is maximum at $\phi = 45^{\circ}$. Similarly, there is a slight shift in location of maximum value of $G_{III}$ with increasing $e$. However, since $G_{II}$ is maximum between $\phi = 0^{\circ}$ and $\phi = 45^{\circ}$, it could still be inferred that the two delaminations will act as one single delamination and grows outward.

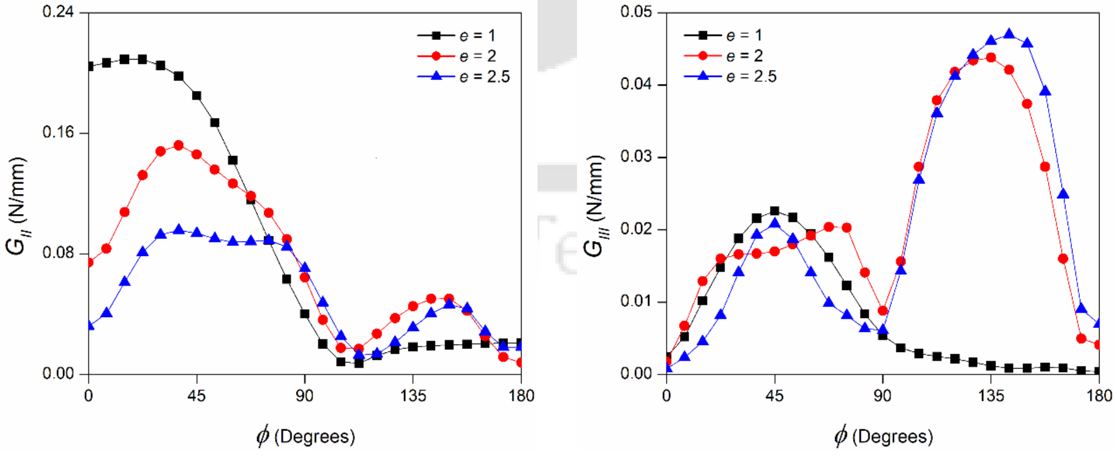

(a) (b)

**Figure 7.19:** Variation of (a) $G_{II}$ , and (b) $G_{III}$ along delamination front 1

**Figure 7.20(a)**, **7.20(b)**, and **7.20(c)** shows the variation of both $G_{II\max}$ and $G_{III\max}$ for $\theta = 0^{\circ}$ degrees with increasing aspect ratio, $e$ (= $a/b$) for $d$ = 20 mm, $d$ = 40 mm, and $d$ = 60 mm respectively. For a separating distance of *d* = 20 mm, with the increase in *e*, $G_{II\max}$ decreases and $G_{III\max}$ increases. Whereas for a separating distance of *d* = 40 mm, both $G_{II\max}$ and $G_{III\max}$ increases with increasing aspect ratio. But in case of larger separating distance of *d* = 40 mm, both $G_{II\max}$ and $G_{III\max}$ increases up to *e* = 2 and for *e* = 2.5 both $G_{II\max}$ and $G_{III\max}$ decrease. For *d* = 20 mm, though $G_{II\max}$ shows substantial reduction with the increasing values of *e,* and $G_{III\max}$ shows marginal increase , but since $G_{II\max}$ is much higher than $G_{III\max}$ , the chances of delamination along the delamination front decreases with the increase in aspect ratio. However, for higher separating distances, $G_{II\max}$ and $G_{III\max}$ are much less and the change with increasing *e* is also not that significant.

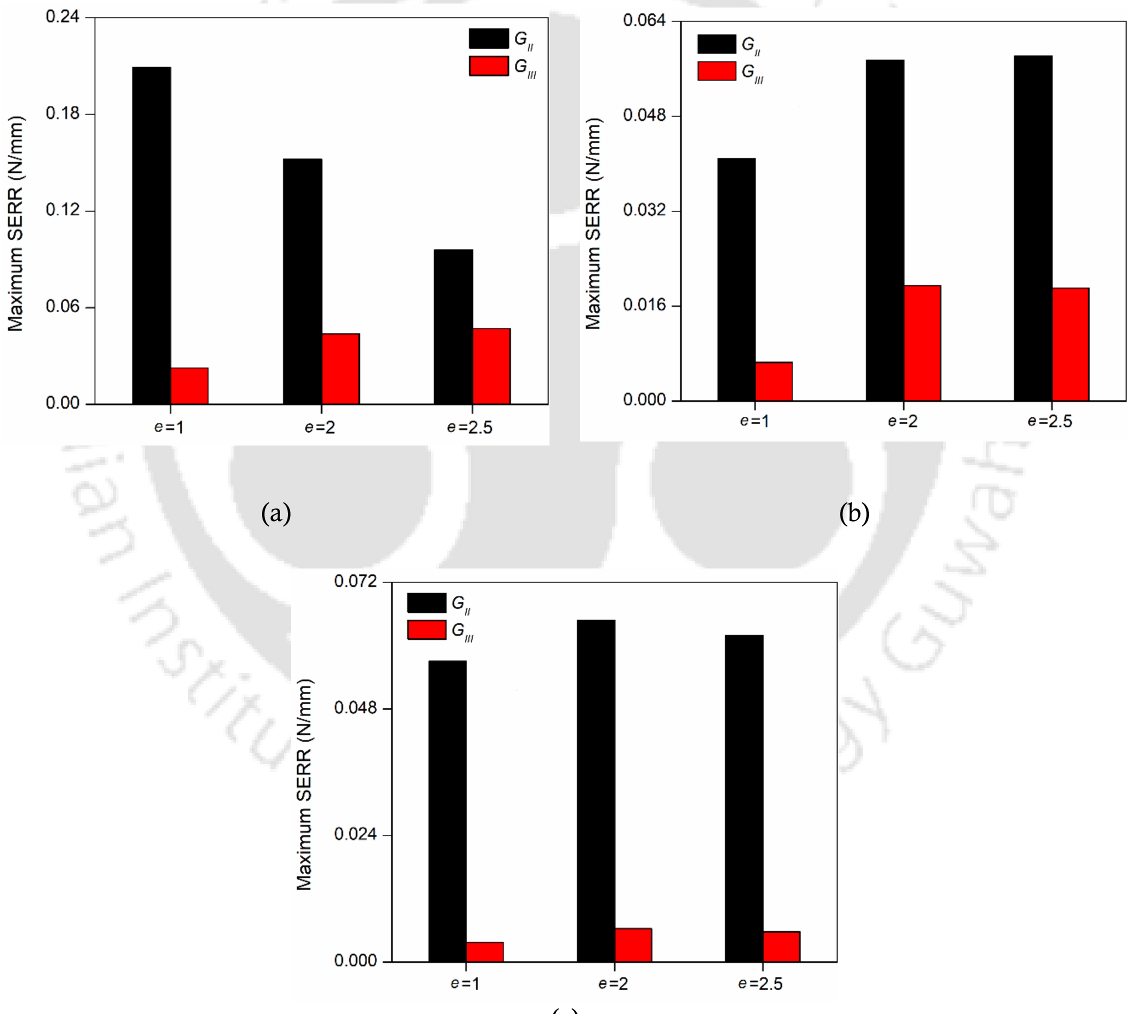

(a) (b)

(c)

**Figure 7.20:** Maximum SERR with different aspect ratios of the delamination for (a) *d* = 20 mm (b) *d* = 40 mm, and (c) *d* = 60 mm

### *7.5.3.3 Effect of fiber orientation*

In order to understand how the fiber orientation at the interface influences the SERR, the fiber orientation angle ($\theta$) of the adjacent lamina is varied from $0^\circ$ to $90^\circ$. From the previous section 7.5.3.2 it has been observed that SERR is maximum for an aspect ratio of 1. Hence, in the present case, SERR is computed for $e$ = 1 and $d$ = 20 mm.

**Figures 7.21(a)**, and **7.21(b)** show the variation of $G_{II}$ and $G_{III}$ respectively around the elliptical delamination front with the orientation of fiber at the interface. It could be seen that not only the magnitudes of $G_{II}$ and $G_{III}$ changes with the fiber orientation angle $\theta$, but also the location of $G_{II\max}$ and $G_{III\max}$ are different for different $\theta$. As could be observed that $G_{II}$ is maximum for $\theta = 0^\circ$ and it is at $\phi = 0^\circ$ but with increase in $\theta$, the location shifts and for $\theta = 90^\circ$, it is at $\phi = 45^\circ$. Similarly, $G_{III}$ is maximum for $\theta = 45^\circ$ and is at $\phi = 0^\circ$, but for other values of $\theta$ it is at $\phi = 45^\circ$.

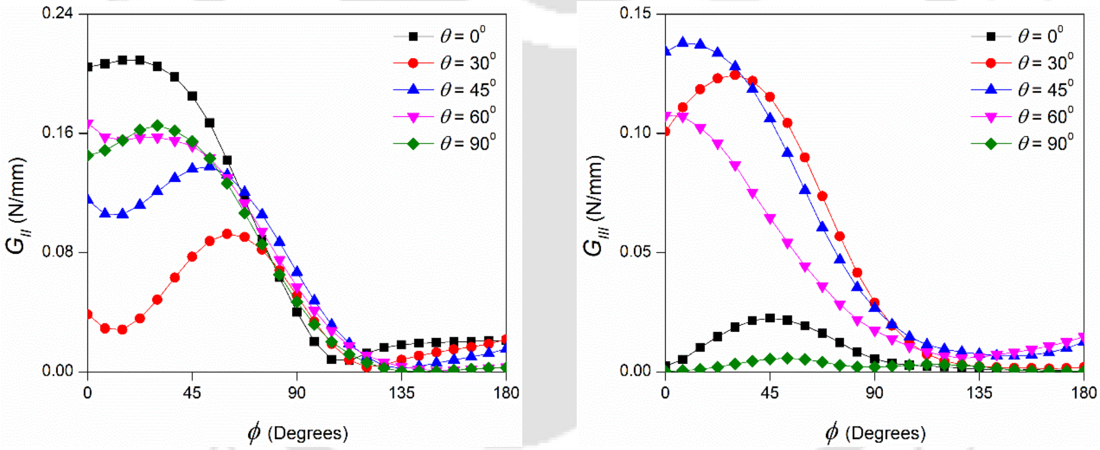

(a) (b)

**Figure 7.21:** Variation of (a) $G_{II}$ and (b) $G_{III}$ along delamination front 1

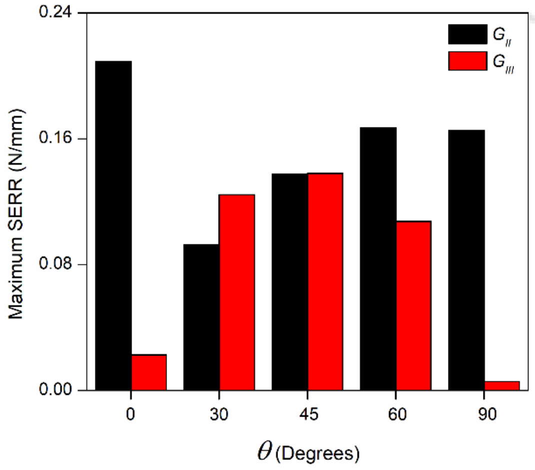

**Figure 7.22:** Maximum SERR for different fiber orientation

**Figures 7.22** show the variation of $G_{II\max}$ and $G_{III\max}$ with the fiber orientation angle, $\theta$. It has been observed that the magnitude of $G_{II\max}$ is higher compared to that of $G_{III\max}$. Similar experimental results have been observed where SERR increases with the increase in fiber orientation [160].

### 7.5.4 Effect of CNT wt% in epoxy on SERR

The behavior of SERR components in the case of two interacting delaminations depends on various factors, including the separating distance, the size and shape of the delamination, and the orientation of fibers at the interface, it is clear that progress of delamination is a complex mixed mode phenomenon and is challenging to predict accurately. However, the main objective here was to explore whether the use of a modified matrix in the form of (CNT+epoxy) could reduce the likelihood of growth of such delamination. Thus, to study the influence of CNTs on the growth of such delaminations from impact induced delaminations at the interface, different weight percentages (0%, 0.25%, 0.5%, 1%, and 1.5%) of CNTs were considered and FE analysis has been carried out in which components of SERR are computed using VCCI. It has been observed from the results in the previous section 7.5.3.3 that mode II and mode III SERRs are maximum for ply angle of $0^{\circ}$ and $45^{\circ}$ respectively for an aspect ratio of 1. Hence, the influence of CNT wt% on SERR for these combinations has been studied. **Figures 7.23(a)**, and **7.23(b)** show the variation of $G_{II}$ and $G_{III}$ respectively on the elliptical delamination front with increasing CNT wt%. As could be seen that there has been a significant reduction in $G_{II}$ and $G_{III}$ around the delamination front with increase in CNT wt%.

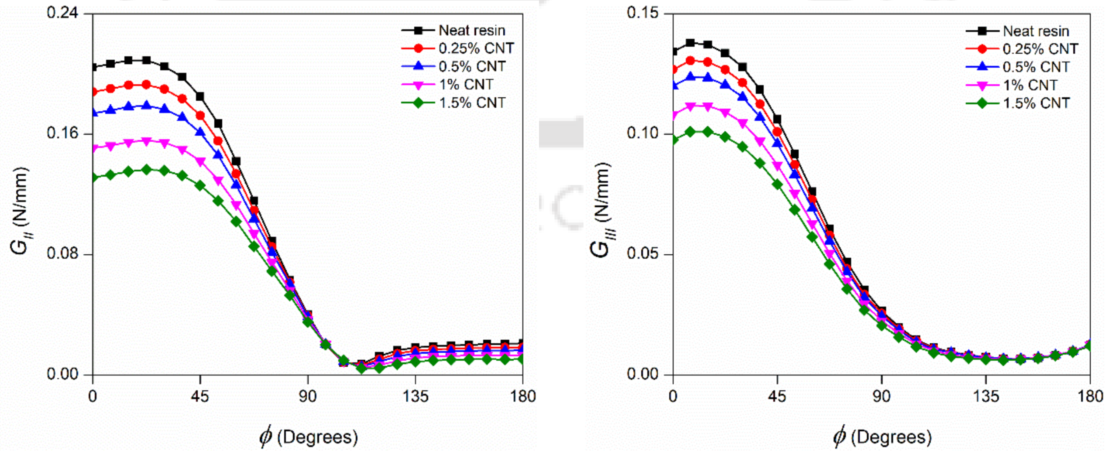

(a) (b)

**Figure 7.23:** Variation of (a) $G_{II}$ and (b) $G_{III}$ along delamination front 1

**Figures 7.24(a)**, and **7.24(b)** show the variation of $G_{II\max}$ for $\theta = 0^{\circ}$ and $G_{III\max}$ for $\theta = 45^{\circ}$ respectively on the elliptical delamination front with increasing CNT wt%. It has been observed that as the CNT wt% increases, $G_{II\max}$ and $G_{III\max}$ decreases and a maximum reduction of 35% in $G_{II\max}$ and 25% in $G_{III\max}$ has been observed for 1.5 wt% in epoxy. Hence, it has been confirmed that with the addition of CNT wt%, the chances of delamination growth at the interface will be reduced substantially. Similar trends have also been observed for other configurations also.

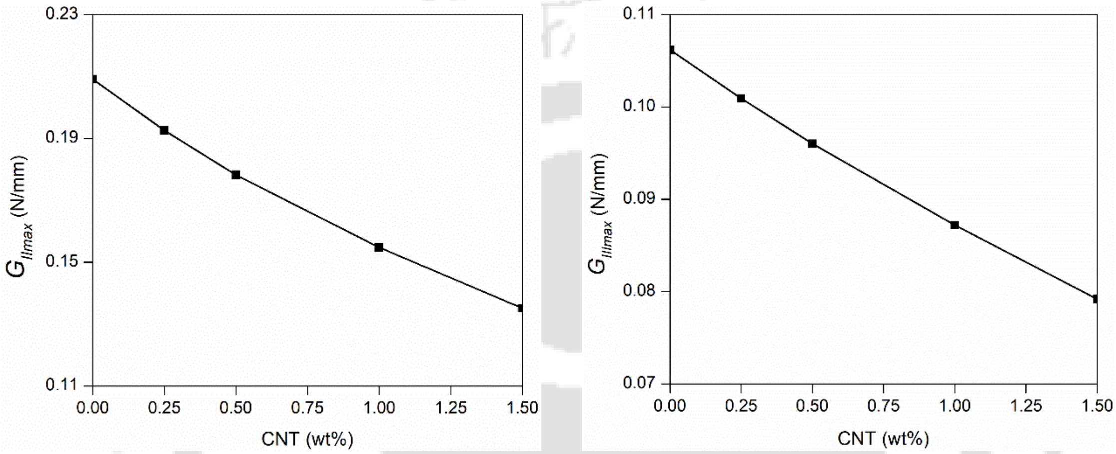

(a) (b)

**Figure 7.24:** Maximum SERR (a) $G_{II\max}$ , and (b) $G_{III\max}$ variation with CNT wt%

## 7.6 Summary

The present chapter aimed at the possibility of improving delamination resistance by adding CNTs with epoxy during the post-impact loading of a laminate having two interacting delaminations at the interface. A full three dimensional FE analysis is carried out to compute the SERR as a measure of resistance to delamination growth for different CNT wt%. The present numerical analysis resulted in the following observations:

- In both cases of axial and transverse loading of the three phase carbon/(CNT+epoxy) laminate, the presence of all the three out-of-plane interlaminar stresses shows a 3D state of stress at the delamination fronts leading to mixed mode delamination. The magnitudes and variation of interlaminar stresses for both the delaminations are same excepting slight difference in the case of interlaminar normal stress in case of the axial loading.

- In both cases of axial and transverse loading of the three phase carbon/(CNT+epoxy) laminate, the magnitudes of SERR vary following a similar trend of interlaminar stresses along the delamination front. Similar to the stress variation, the maximum magnitude of SERR components also occur at different locations showing that it is a mixed mode phenomenon and the combination of $G_I$, $G_{II}$ and $G_{III}$ will decide whether the delaminations will grow or not.
- In the case of two interacting delaminations at the interface, they grow further under post impact loading such as axial and transverse loading and it is a mixed mode phenomenon dictated by different factors like the shape and size of the delaminations, their separating distance, relative fiber orientation at the interface and is difficult to assess.
- In both cases of axial and transverse loading of the three phase carbon/(CNT+epoxy) laminate, the magnitude of $G_I$ is much smaller compared to those of $G_{II}$ and $G_{III}$. Also $G_{II} > G_{III}$ by an order of magnitude showing that $G_{II}$ is the dominant mode even though $G_{III}$ also contributes.
- In case of laminate with axial loading, for smaller separating distance (*d*=20 mm) the location maximum value of $G_{II}$ is $0^\circ$ and for larger separating distance the location shifts to $180^\circ$. This indicates that when the distance between the two delaminations is small, they behave as a single larger delamination and tend to grow towards the edge. On the other hand, when the separating distance is larger, the two delaminations grow towards each other and finally coalesce into one.
- In case of laminate with transverse loading, $G_{II}$ is maximum at $\phi = 0^\circ$ and $G_{III}$ is maximum at $\phi = 45^\circ$ for all the cases of separating distances and therefore unlike axial loading, here the nature of interaction is same for all the cases of separating distances. In addition, the fact that $G_{II} > G_{III}$ and $G_{II}$ is always maximum at $\phi = 0^\circ$ indicates that the two delaminations will always grow as one large delamination and progress towards the edge of the laminate.
- In case of the laminate with axial loading, for all values of aspect ratio of delamination, $G_{II} > G_{III}$ and the location of $G_{II}$ suggest that for smaller separating distance, the two delaminations act as a single delamination and grow towards the edge of the laminate.
- In case of the laminate with transverse loading, as the aspect ratio of delamination increases, $G_{II\max}$ decreases and $G_{III\max}$ increases substantially showing that the chances

of delamination along the delamination front decreases due to higher magnitude of $G_{II\max}$ compared to $G_{III\max}$.

- In case of axial loading, for all configuration of the laminate, the magnitude of $G_{II}$ is more than that of $G_{III}$. The maximum value of $G_{II}$ at $\phi = 0^{\circ}$ for all fiber orientation ($\theta$), and the maximum value of $G_{III}$ changes with $\theta$. $G_{II\max}$ and $G_{III\max}$ are highest for $\theta = 90^{\circ}$.
- In case of transverse loading, as the fiber orientation at the interface ($\theta$) changes, the magnitudes of $G_{II}$ and $G_{III}$ changes and location of $G_{II\max}$ and $G_{III\max}$ are different. $G_{II}$ is maximum for $\theta = 0^{\circ}$ and it is at $\phi = 0^{\circ}$ but with increase in $\theta$, the location shifts and for $\theta = 90^{\circ}$, it is at $\phi = 45^{\circ}$. Similarly, $G_{III}$ is maximum for $\theta = 45^{\circ}$ and is at $\phi = 0^{\circ}$, but for other $\theta$ it is at $\phi = 45^{\circ}$.
- In both cases of laminate with axial and transverse loading, the magnitudes of $G_{II}$ and $G_{III}$ decreases with increase in CNT wt%, indicating that the possibility of delamination to grow at the interface is substantially reduced.
- In case of axial loading, in the most sever case of two interacting delaminations, adding 1.5% CNT to epoxy leads to reduction in $G_{II\max}$ and $G_{III\max}$ by 16% and 42% respectively in comparison with those for neat epoxy.
- In case of transverse loading, in the most sever case of two interacting delaminations, adding 1.5% CNT to epoxy leads to reduction in $G_{II\max}$ and $G_{III\max}$ by 35% and 25% respectively in comparison with those for neat epoxy.

## CHAPTER 8

# Conclusions and further scope of work

Results obtained from the present thesis work on the FE analysis of the three phase carbon/(CNT+epoxy) composites having flaws like ply break and interfacial embedded delamination have been discussed in the previous chapters and some important conclusions could be drawn. Those conclusions are summarized in this chapter along with the further scope of extending this work.

## 8.1 Conclusions

The work in this thesis investigated the behavior of three phase carbon/(CNT+epoxy) composites with internal flaws like ply break and delamination with an objective of first understanding the important factors influencing the behavior of such laminates with flaws and then understanding how modifying the matrix with CNTs could improve the resistance to delamination from those defects. Three dimensional FE analyses have been performed first to understand the behavior of such three phase carbon/(CNT+epoxy) composite laminates in the presence of such flaws and important parameters affecting the behavior and then to investigate the influence of CNTs to enhance the resistance to failure due to delamination in presence of such flaws. Results from the investigation led to several conclusions. Some of these are general in nature and kind of observations and are classified as general conclusions. While some of the conclusions are more specific and bear significant importance from the view point of design of such composites and are classified as specific conclusions. These general and specific conclusions are presented in the subsequent sections.

## 8.2 General conclusions

The general conclusions are as follows

- Three phase composites such as carbon/(CNT+epoxy) laminates despite their better strengths may also experiences defects like ply break and interfacial delamination especially under low velocity impact. These defects are sub-surface in nature and many a time go unnoticed.
- In the post impact loading, both in-plane and out-of-plane stresses are induced in the vicinity of such defects causing interfacial delamination to initiate from such defects leading to catastrophic failure of the laminate.

- Existence of all the three out-of-plane components of the interlaminar stresses at the interface near the flaws shows a 3D state of stress and hence the delamination at the interface is a mixed-mode phenomenon irrespective of the nature of the applied load.
- Growth of such delamination is a complex phenomenon and influenced by many factors such as size of the ply break, size and shape of the embedded delamination, fiber orientation at the interface, properties and thickness of the resin layer etc.
- Interfacial resin layer has a significant influence on the delamination initiating from such flaws and needs due attention in design of such laminates.
- Adding CNTs to the epoxy enhances the resistance to delamination from such flaws but the appropriate percentage of CNTs needs to be decided.
- In the case of laminate with ply break, the stresses get redistributed in the vicinity of the ply break over a small length, leading to a stress concentration, and reach the nominal value away from the break. Adjacent intact plies get overstressed increasing the chances of breaking and the interface experiences high interlaminar stresses increasing the chances of delamination. However, adding CNTs to epoxy could significantly improve the resistance to such delamination.
- In case of laminate with impact induced embedded delamination, under post impact loading out–of–plane interlaminar stresses $\sigma_z$ , $\tau_{xz}$ and $\tau_{yz}$ are induced at the interface and the magnitudes of maximum value of those stresses occur at different locations along the boundary of the delamination and same is the case with the location of maximum value of SERR components. This shows that the delamination growth direction cannot be estimated and is complex. However, the addition of CNTs to epoxy actually reduces the magnitudes of SERR.
- For multiple neighboring delaminations, the situation is even more complex where two delaminations may act as one large delamination and grow or grow individually depending upon the separating distance between them.

## 8.3 Specific conclusion

### 8.3.1 Three phase carbon/(CNT+epoxy) laminates with ply break

- In case of ply break, two effects are clearly visible from the stress analysis viz. the intact adjacent ply experiences a high stress concentration and the interface of the broken and intact ply experiences high interlaminar stresses.
- For smaller width ply break, as the ply break width increases the stress concentration in the adjacent intact ply increases but as the ply break width

approaches the full width it is insignificant. In the present case, as the ply break width increases from $c = 2$ mm to $c = 8$ mm, the stress concentration increases from 1.2 to 1.24 and thereafter almost constant. This shows that a smaller width ply break grows to a larger width ply break.

- In the vicinity of the ply break at the interface between the broken and intact plies, though all the three out-of-plane interlaminar stresses are present, in the case of axial loading of the laminate, $\tau_{xz}$ is significantly higher compared to $\sigma_z$ and $\tau_{yz}$, which indicates the dominant mode of delamination is the shearing mode.
- The magnitude of $\tau_{xz}$ decreases with an increase in resin layer thickness showing that thicker the interfacial resin layer less is the chance of delamination.
- The magnitude of $\tau_{xz}$ though does not change significantly with increasing ply break width however strongly influenced by the relative ply orientation ($\theta$) at the interface of broken and intact plies. This is same for all cases of CNT wt%.
- The fact that the interlaminar stresses $\sigma_z$ and $\tau_{yz}$ are insignificant compared to $\tau_{xz}$ is reflected in the SERR components and it was observed that $G_I$ and $G_{III}$ were negligibly small compared to $G_{II}$ (due to $\tau_{xz}$) which happens to be the dominant mode.
- The increase in mode II SERR $G_{II}$ with increasing ply break width is insignificant as was the case for interlaminar stress $\tau_{xz}$.
- As the adjacent intact ply angle increases, $G_{II}$ increases significantly up to $\theta = 45°$ and beyond that the increase is not much significant.
- Addition of CNTs with epoxy leads to a significant reduction in magnitudes of SERR, which indicates that the chances of delamination at the interface are reduced significantly. In the case of a full width ply break, adding only 0.25 wt% of CNTs with the epoxy leads to a 25% reduction in $G_{II}$.
- Variation of critical SERR with CNT wt% shows that modification of epoxy by the addition of CNTs to it significantly improves the resistance to delamination at the interface of broken and intact plies in FRP laminated composites.
- Increase in CNT wt% with epoxy leads to increase in resistance to delamination at the interface, up to certain wt% of CNTs only, and beyond that it decreases again.
- In the present case of carbon/(CNT+epoxy) with ply break, critical SERR was observed to increase with the addition of CNT wt% till 1 wt% of CNTs, and adding CNTs beyond 1% leads to a reduction in delamination resistance though it is still

more than that corresponding to neat epoxy (0 wt% of CNT). Therefore, it is important to determine the optimum percentage of CNTs to be added to the epoxy to achieve the best resistance against delamination.

- Adding only 1 wt% of CNT to epoxy leads to 36% increase in resistance against delamination growth at the interface in case of broken ply.
- The resin rich layer between the plies plays an important role in resistance to delamination growth at the interface. Thicker is the resin rich layer more is the resistance to delamination growth.
- The fiber orientation of adjacent intact ply plays an important role in interfacial delamination growth. For a $\left[0_2/\pm\theta/\bar{0}\right]_s$ carbon/(CNT+epoxy) laminate, delamination resistance is maximum for a ply orientation of $\theta = 90^{\circ}$ at the interface.
- As expected, the critical strain energy release rate is independent of ply break width and the laminate thickness for all the cases of given laminate configurations reinforcing it as a property for a specific laminate. However, it depends upon the fiber orientation of intact ply adjacent to broken plies.

### 8.3.2 Three phase carbon/(CNT+epoxy) laminates with a single embedded delamination

- In-plane, as well as out-of-plane stresses are induced along the delamination, due to centrally located embedded delamination at the interface of laminate, when the laminate loaded axially as well as transversely.
- Existence of all the three out-of-plane components of the interlaminar stresses at the delamination front clearly shows a 3D state of stress at the delamination front. Thus it could be inferred that the delamination at the interface will be mixed mode even though the applied load is purely axial and transverse.
- In both cases of laminate with axial and transverse loading, the maximum magnitudes of interlaminar stresses $\sigma_z$ , $\tau_{xz}$ and $\tau_{yz}$ occurs at different locations of the delamination front and these increases with increase in aspect ratio (*e*) of the embedded delamination as well as increase in adjacent intact ply orientation.
- In both cases of laminate with axial and transverse loading, similar to the stress variation, the maximum magnitude of individual components of SERR also occur at different locations showing that it is the combination of $G_I$, $G_{II}$ and $G_{III}$ that will decide where the delamination will further grow or not. In other words, not only the

$G_I$, $G_{II}$ and $G_{III}$ vary along the delamination front but the mode mix ratio is also different.

- In case of laminate with axial loading, the magnitude of $G_I$ is much smaller compared to those of $G_{II}$ and $G_{III}$ showing that mode II and mode III will dominate the delamination growth.
- In case of laminate with transverse loading, $G_I$ is neglected due to compressive nature of interlaminar normal stress, and $G_{II}$ is higher compared to $G_{III}$ showing mode II will dominate the delamination growth.
- In both cases of laminate with axial loading and transverse loading, both maximum mode II SERR ($G_{II\max}$) and maximum mode III SERR ($G_{III\max}$) increases with the increase in aspect ratio of delamination.
- In the both cases of laminate with axial and transverse loading, addition of CNTs to the epoxy leads to substantial improvement in resistance to growth of delamination from an existing embedded delamination at the interface in post impact loading.
- In the both cases of laminate with axial and transverse loading, the magnitudes of SERR components decrease with the addition of CNTs to the epoxy indicating that the chance for delamination to grow at the interface could be reduced.
- In the case of axial loading, in the most severe case of delamination, the addition of 1 wt% CNTs in epoxy indicates a reduction of $G_{II\max}$ and $G_{III\max}$ values by 11% and 20% respectively compared to those for neat epoxy (without CNT).
- In the case of transverse loading, in the most severe case of delamination, the addition of 1 wt% CNTs in epoxy indicates a reduction of $G_{II\max}$ and $G_{III\max}$ values by 25% and 21% respectively compared to those for neat epoxy (without CNT).
- Critical SERR as a measure of the resistance to delamination growth is significantly increased by the addition of CNTs in epoxy for both axial and transverse loading respectively in comparison to carbon/epoxy laminate.
- Even though the critical SERR of such laminated composites with embedded elliptical delamination at the interface is a function of shape (eccentricity) of the delamination as well as the relative fiber orientation at the interface, however, in all the cases, the addition of CNTs has shown significant improvement in resistance to growth of delamination.
- Adding CNTs to epoxy leads to enhancement in delamination resistance though, there is a limit beyond which further addition of CNTs to epoxy leads to a reduction in critical SERR. Thus, in order to achieve maximum resistance to delamination

growth at the interface from an embedded elliptical delamination, it is necessary to identify the optimum amount of CNT wt% to be added with the epoxy. In the present case, it is 1% but it may vary based on different laminate configurations.

- In post impact loading, the laminate is tougher against axial loading compared to transverse loading.

### 8.3.3 Three phase carbon/(CNT+epoxy) laminates with multiple embedded delamination

- For both axial and transverse loading of the three phase carbon/(CNT+epoxy) laminate, the presence of all the three out-of-plane interlaminar stresses shows a 3D state of stress at the delamination fronts leading to mixed mode delamination. The magnitudes and variation of interlaminar stresses for both the delaminations are same excepting slight difference in the case of interlaminar normal stress in case of the axial loading.
- In case of both axial and transverse loading of the three phase carbon/ (CNT+epoxy) laminate, the magnitudes of SERR vary following similar trend of interlaminar stresses along the delamination front. Similar to the stress variation, the maximum magnitude of SERR components also occur at different location showing that it is a mixed mode phenomenon and the combination of $G_I$ , $G_{II}$ and $G_{III}$ will decide whether the delamination will grow or not.
- In the case of two interacting delaminations at the interface, they grow further under post impact loading such as axial and transverse loading and it is a mixed mode phenomenon dictated by different factors like the shape and size of the delaminations, their separating distance, and relative fiber orientation at the interface and is difficult to assess.
- In both cases of axial and transverse loading of the three phase carbon/ (CNT+epoxy) laminate, the magnitude of $G_I$ is much smaller compared to those of $G_{II}$ and $G_{III}$ . Also $G_{II} > G_{III}$ by an order of magnitude showing that $G_{II}$ is the dominant mode even though $G_{III}$ also contributes.
- In case of laminate with axial loading, for smaller separating distance (*d*=20 mm) the location maximum value of $G_{II}$ is $0^{\circ}$ and for larger separating distance the location shifts to $180^{\circ}$ . This indicates that when the distance between the two delaminations is small, they behave as a single larger delamination and tend to grow towards the edge. On the other hand, when the separating distance is larger, the two delaminations grow towards each other and finally coalesce into one.

- In case of laminate with transverse loading, $G_{II}$ is maximum at $\phi = 0^{\circ}$ and $G_{III}$ is maximum at $\phi = 45^{\circ}$ for all the cases of separating distances and therefore unlike axial loading, here the nature of interaction is same for all the cases of separating distances. In addition, the fact that $G_{II}$ > $G_{III}$ and $G_{II}$ is always maximum at $\phi = 0^{\circ}$ indicates that the two delaminations will always grow as one large delamination and progress towards the edge of the laminate.
- In case of the laminate with axial loading, for all values of aspect ratio of delamination, $G_{II} > G_{III}$ and the location of $G_{II}$ suggest that for smaller separating distance, the two delaminations act as a single delamination and grow towards the edge of the laminate.
- In case of the laminate with transverse loading, as the aspect ratio of delamination increases, $G_{II\max}$ decreases and $G_{III\max}$ increases substantially showing that the chances of delamination along the delamination front decrease due to higher magnitude of $G_{II\max}$ compared to $G_{III\max}$.
- In case of axial loading, for all configuration of the laminate, the magnitude of $G_{II}$ is more than that of $G_{III}$. The maximum value of $G_{II}$ at $\phi = 0^{\circ}$ for all fiber orientation ($\theta$), and the maximum value of $G_{III}$ changes with $\theta$. $G_{II\max}$ and $G_{III\max}$ are highest for $\theta = 90^{\circ}$.
- In case of transverse loading, as the fiber orientation at the interface ($\theta$) changes, the magnitudes of $G_{II}$ and $G_{III}$ changes and location of $G_{II\max}$ and $G_{III\max}$ are different. $G_{II}$ is maximum for $\theta = 0^{\circ}$ and it is at $\phi = 0^{\circ}$ but with increase in $\theta$, the location shifts and for $\theta = 90^{\circ}$, it is at $\phi = 45^{\circ}$. Similarly, $G_{III}$ is maximum for $\theta = 45^{\circ}$ and is at $\phi = 0^{\circ}$, but for other $\theta$ it is at $\phi = 45^{\circ}$.
- In both cases of laminate with axial and transverse loading, the magnitudes of $G_{II}$ and $G_{III}$ decreases with increase in CNT wt%, indicating that the possibility of delamination to grow at the interface is substantially reduced.
- In case of axial loading, in the most sever case of two interacting delaminations, adding 1.5% CNT to epoxy leads to reduction in $G_{II\max}$ and $G_{III\max}$ by 16% and 42% respectively in comparison with those for neat epoxy.

- In case of transverse loading, in the most sever case of two interacting delaminations, adding 1.5% CNT to epoxy leads to reduction in $G_{II\max}$ and $G_{III\max}$ by 35% and 25% respectively in comparison with those for neat epoxy.

## 8.4 Major contributions

- Efficacy of adding CNTs to epoxies in a three phase carbon/(CNT+epoxy) composites in improving the resistance to interfacial delamination has been demonstrated by 3D finite element simulations.
- It is established that there exists a limit of CNT wt% to which it could be added to epoxy ensuring enhancement of resistance to delamination. Adding CNTs beyond this limit will lead to further reduction in delamination resistance.

## 8.5 Scope for future work

- The work done in the present research is limited to delamination growth of three phase composites with flaws subjected to static loading and the same could be extended to fatigue loading and combined thermo-mechanical loading.
- This research may be extended to develop a learning system where SERR could be predicted as a function of different important parameters like laminate dimensions, stacking sequence, CNT wt% etc.
- The three phase carbon/(CNT+epoxy) composites with flaws in the form of ply break and embedded delamination could be fabricated and experiments could be conducted to compare the numerical results with the experimental results.

# References

[1] Jones RM. Mechanics of composite materials. Second Edition, CRC Press; 2018, ISBN1-56032-712-X. https://doi.org/10.1201/9781498711067.

[2] Chen J, Yu Z, Jin H. Nondestructive testing and evaluation techniques of defects in fiber-reinforced polymer composites: A review. Front Mater 2022;9:1–29. https://doi.org/10.3389/fmats.2022.986645.

[3] Kim JK, Mai YW, Mai YW. Engineered interfaces in fiber reinforced composites. First edition, Elsevier 1998, ISBN978-0-08-042695-2. https://doi.org/10.1016/B978-0-08-042695-2.X5000-3.

[4] Sasidharan S, Anand A. Epoxy-Based Hybrid Structural Composites with Nanofillers: A Review. Ind Eng Chem Res 2020;59:12617–31. https://doi.org/10.1021/acs.iecr.0c01711.

[5] Iijima S. Helical microtubules of graphitic carbon. Nature 1991;354:56–8. https://doi.org/10.1038/354056a0.

[6] Zhu W, Bartos PJM, Porro A. Application of nanotechnology in construction Summary of a state-of-the-art report. Mater Struct Constr 2004;37:649–58. https://doi.org/10.1617/14234.

[7] Barkalina N, Charalambous C, Jones C, Coward K. Nanotechnology in reproductive medicine: Emerging applications of nanomaterials. Nanomedicine Nanotechnology, Biol Med 2014;10:e921–38. https://doi.org/10.1016/j.nano.2014.01.001.

[8] Lau KT, Lu M, Hui D. Coiled carbon nanotubes: Synthesis and their potential applications in advanced composite structures. Compos Part B Eng 2006;37:437–48. https://doi.org/10.1016/j.compositesb.2006.02.008.

[9] Thostenson ET, Ren Z, Chou T-W. Advances in the science and technology of carbon nanotubes and their composites: a review. Compos Sci Technol 2001;61:1899–912. https://doi.org/10.1016/S0266-3538(01)00094-X.

[10] Sakharova NA, Antunes JM, Pereira AFG, Fernandes J V. Developments in the evaluation of elastic properties of carbon nanotubes and their heterojunctions by numerical simulation. AIMS Mater Sci 2017;4:706–37. https://doi.org/10.3934/matersci.2017.3.706.

[11] Ali MH, Rubel RI. A comparative review of Mg/CNTs and Al/CNTs composite to explore the prospect of bimetallic Mg-Al/CNTs composites. AIMS Mater Sci 2020;7:217–43. https://doi.org/10.3934/matersci.2020.3.217.

---

[12] Qiu J, Zhang C, Wang B, Liang R. Carbon nanotube integrated multifunctional multiscale composites. Nanotechnology 2007;18. https://doi.org/10.1088/0957-4484/18/27/275708.

[13] Murjani BO, Kadu PS, Bansod M, Vaidya SS, Yadav MD. Carbon nanotubes in biomedical applications: current status, promises, and challenges. Carbon Lett 2022;32:1207–26. https://doi.org/10.1007/s42823-022-00364-4.

[14] Tornabene F, Bacciocchi M, Fantuzzi N, Reddy JN. Multiscale approach for three-phase CNT/polymer/fiber laminated nanocomposite structures. Polym Compos 2019;40:E102--E126. https://doi.org/10.1002/pc.24520.

[15] Yousefi AH, Memarzadeh P, Afshari H, Hosseini SJ. Agglomeration effects on free vibration characteristics of three-phase CNT/polymer/fiber laminated truncated conical shells. Thin-Walled Struct 2020;157:107077. https://doi.org/10.1016/j.tws.2020.107077.

[16] Dresselhaus MS, Dresselhaus G, Saito R. Physics of carbon nanotubes. Carbon 1995;33:883–91. https://doi.org/10.1016/0008-6223(95)00017-8.

[17] Bethune DS, Kiang CH, De Vries MS, Gorman G, Savoy R, Vazquez J, et al. Cobalt-catalysed growth of carbon nanotubes with single-atomic-layer walls. Nature 1993;363:605–7. https://doi.org/10.1038/363605a0.

[18] Journet C, Maser WK, Bernier P, Loiseau A, Lamy de la Chapelle M, Lefrant S, et al. Large-scale production of single-walled carbon nanotubes by the electric-arc technique. Nature 1997;388:756–8. https://doi.org/10.1038/41972.

[19] Thess A, Lee R, Nikolaev P, Dai H, Petit P, Robert J, et al. Crystalline ropes of metallic carbon nanotubes. Science 1996;273:483–7. https://doi.org/10.1126/science.273.5274.483.

[20] Mamalis AG, Vogtländer LOG, Markopoulos A. Nanotechnology and nanostructured materials: Trends in carbon nanotubes. Precis Eng 2004;28:16–30. https://doi.org/10.1016/j.precisioneng.2002.11.002.

[21] Hahm MG, Hashim DP, Vajtai R, Ajayan PM. A review: controlled synthesis of vertically aligned carbon nanotubes. Carbon Lett 2011;12:185–93. http://dx.doi.org/10.5714/CL.2011.12.4.185.

[22] Ruoff RS, Tersoff J, Lorents DC, Subramoney S, Chan B. Radial deformation of carbon nanotubes by van der Waals forces. Nature 1993;364:514–6. https://doi.org/10.1038/364514a0.

[23] Rafiee R, Heidarhaei M. Investigation of chirality and diameter effects on the Young's modulus of carbon nanotubes using non-linear potentials. Compos Struct 2012;94:2460–4. https://doi.org/10.1016/j.compstruct.2012.03.010.

[24] Meyyappan M. Carbon nanotubes: science and applications. First Edition, CRC press 2004, ISBN 9780849321115.

[25] Yi W, Lu L, Dian-Lin Z, Pan ZW, Xie SS. Linear specific heat of carbon nanotubes. Phys Rev 1999;59:9015–8. https://doi.org/10.1103/PhysRevB.59.R9015.

[26] Dai H, Wong EW, Lieber CM. Probing electrical transport in nanomaterials: conductivity of individual carbon nanotubes. Science 1996;272:523–6. https://doi.org/10.1126/science.272.5261.523.

[27] Schönenberger C, Bachtold A, Strunk C, Salvetat JP, Forró L. Interference and interaction in multi-wall carbon nanotubes. Appl Phys A Mater Sci Process 1999;69:283–95. https://doi.org/10.1007/s003390051003.

[28] Lu JP, Han J. Carbon nanotubes and nanotube-based nano devices. Int J High Speed Electron Syst 1998;9:101–23. https://doi.org/10.1142/S0129156498000063.

[29] Ibrahim KS. Carbon nanotubes? properties and applications: A review. Carbon Lett 2013;14:131–44. http://dx.doi.org/10.5714/CL.2013.14.3.131.

[30] Ajayan PM. Bulk metal and ceramics nanocomposites. Nanocompos Sci Tech 2003: 1–76. http://dx.doi.org/10.1002/3527602127.

[31] Ajayan PM, Stephan O, Colliex C, Trauth D. Aligned carbon nanotube arrays formed by cutting a polymer resin—nanotube composite. Science 1994;265:1212–4. https://doi.org/10.1126/science.265.5176.1212.

[32] Du JH, Bai J, Cheng HM. The present status and key problems of carbon nanotube based polymer composites. Express Polym Lett 2007;1:253–73. https://doi.org/10.3144/expresspolymlett.2007.39.

[33] Jojibabu P, Zhang YX, Prusty BG. A review of research advances in epoxy-based nanocomposites. Int J Adhes Adhes 2020;96:10254. https://doi.org/10.1016/j.ijadhadh.2019.102454.

[34] Xie G, Zhou G, Bao X. Mechanical behaviour of advanced composite laminates embedded with carbon nanotubes. Second Int. Conf. Smart Mater. Nanotechnol. Eng., vol. 7493, 2009, p. 652–71. https://doi.org/10.1117/12.836060.

[35] Sonifer Products. http://www.sonifier.com, Branson Ultrasonics Corp., (accessed June 2010).

[36] Thostenson ET, Chou TW. Processing-structure-multi-functional property relationship in carbon nanotube/epoxy composites. Carbon 2006;44:3022–9. https://doi.org/10.1016/j.carbon.2006.05.014.

[37] Kim YA, Hayashi T, Fukai Y, Endo M, Yanagisawa T, Dresselhaus MS. Effect of ball milling on morphology of cup-stacked carbon nanotubes. Chem Phy Lett 2002; 355:279-84. https://doi.org/10.1016/S0009-2614(02)00248-8.

[38] Sandler J, Shaffer P, Prasse T, Bauhofer W, Schulte K, Windle AH. Development of a dispersion process for carbon nanotubes in an epoxy matrix and the resulting electrical properties. Polymer 1999;40:5967–71. https://doi.org/10.1016/S0032-3861(99)00166-4.

[39] Villmow T, Pötschke P, Pegel S, Häussler L, Kretzschmar B. Influence of twin-screw extrusion conditions on the dispersion of multi-walled carbon nanotubes in a poly(lactic acid) matrix. Polymer (Guildf) 2008;49:3500–9. https://doi.org/10.1016/j.polymer.2008.06.010.

[40] Isayev AI, Kumar R, Lewis TM. Ultrasound assisted twin screw extrusion of polymer-nanocomposites containing carbon nanotubes. Polymer 2009;50:250–60. https://doi.org/10.1016/j.polymer.2008.10.052.

[41] Moniruzzaman M, Du F, Romero N, Winey KI. Increased flexural modulus and strength in SWNT/epoxy composites by a new fabrication method. Polymer 2006;47:293–8. https://doi.org/10.1016/j.polymer.2005.11.011.

[42] Ma PC, Wang SQ, Kim J-K, Tang BZ. In-situ amino functionalization of carbon nanotubes using ball milling. J Nanosci Nanotechnol 2009;9:749–53. https://doi.org/10.1166/jnn.2009.C017.

[43] Jain V, Jaiswal S, Dasgupta K, Lahiri D. Influence of carbon nanotube on interfacial and mechanical behavior of carbon fiber reinforced epoxy laminated composites. Polym Compos 2022;43:6344–54. https://doi.org/10.1002/pc.26943.

[44] Norizan MN, Moklis MH, Ngah Demon SZ, Halim NA, Samsuri A, Mohamad IS, et al. Carbon nanotubes: Functionalisation and their application in chemical sensors. RSC Adv 2020;10:43704–32. https://doi.org/10.1039/d0ra09438b.

[45] Bahun GJ, Wang C, Adronov A. Solubilizing single-walled carbon nanotubes with pyrene-functionalized block copolymers. J Polym Sci Part A Polym Chem 2006;44:1941–51. https://doi.org/10.1002/pola.21308.

[46] Nakonechna OI, Belyavina NN, Dashevskyi MM, Ivanenko KO, Revo SL. Novel $Ti_2CuC_x$ and $Ti_3Cu_2C_x$ carbides obtained by sintering of products of mechanochemical synthesis of Ti, Cu and carbon nanotubes. Phys Chem Solid State 2019;19:179–85. https://doi.org/10.15330/pcss.19.2.179-185.

[47] Quintero-Jaime AF, Cazorla-Amorós D, Morallón E. Electrochemical functionalization of single wall carbon nanotubes with phosphorus and nitrogen species. Electrochim Acta 2020;340. https://doi.org/10.1016/j.electacta.2020.135935.

[48] Maity KP, Patra A, Prasad V. Influence of the chemical functionalization of carbon nanotubes on low temperature ac conductivity with polyaniline composites. J Phys D Appl Phys 2020;53. https://doi.org/10.1088/1361-6463/ab5f18.

[49] Garzia Trulli M, Sardella E, Palumbo F, Palazzo G, Giannossa LC, Mangone A, et al. Towards highly stable aqueous dispersions of multi-walled carbon nanotubes: the effect of oxygen plasma functionalization. J Colloid Interface Sci 2017;491:255–64. https://doi.org/10.1016/j.jcis.2016.12.039.

[50] Sadeghian R, Gangireddy S, Minaie B, Hsiao KT. Manufacturing carbon nanofibers toughened polyester/glass fiber composites using vacuum assisted resin transfer molding for enhancing the mode-I delamination resistance. Compos Part A Appl Sci Manuf 2006;37:1787–95. https://doi.org/10.1016/j.compositesa.2005.09.010.

[51] Gojny FH, Nastalczyk J, Roslaniec Z, Schulte K. Surface modified multi-walled carbon nanotubes in CNT/epoxy-composites. Chem Phys Lett 2003;370:820–4. https://doi.org/10.1016/S0009-2614(03)00187-8.

[52] Vaisman L, Wagner HD, Marom G. The role of surfactants in dispersion of carbon nanotubes. Adv Colloid Interface Sci 2006;128–130:37–46. https://doi.org/10.1016/j.cis.2006.11.007.

[53] Bekyarova E, Thostenson ET, Yu A, Kim H, Gao J, Tang J, et al. Multiscale carbon nanotube-carbon fiber reinforcement for advanced epoxy composites. Langmuir 2007;23:3970–4. https://doi.org/10.1021/la062743p.

[54] Warrier A, Godara A, Rochez O, Mezzo L, Luizi F, Gorbatikh L, et al. The effect of adding carbon nanotubes to glass/epoxy composites in the fibre sizing and/or the matrix. Compos Part A Appl Sci Manuf 2010;41:532–8. https://doi.org/10.1016/j.compositesa.2010.01.001.

[55] Khan S, Singh Bedi H, Agnihotri PK. Augmenting mode-II fracture toughness of carbon fiber/epoxy composites through carbon nanotube grafting. Eng Fract Mech 2018;204:211–20. https://doi.org/10.1016/j.engfracmech.2018.10.014.

[56] Awan FS, Fakhar MA, Khan LA, Zaheer U, Khan AF, Subhani T. Interfacial mechanical properties of carbon nanotube-deposited carbon fiber epoxy matrix hierarchical composites. Compos Interfaces 2018;25:681–99. https://doi.org/10.1080/09276440.2018.1439620.

[57] Xiao C, Tan Y, Wang X, Gao L, Wang L, Qi Z. Study on interfacial and mechanical improvement of carbon fiber/epoxy composites by depositing multi-walled carbon nanotubes on fibers. Chem Phys Lett 2018;703:8–16. https://doi.org/10.1016/j.cplett.2018.05.012.

[58] Yao Z, Wang C, Lu R, Su S, Qin J, Wang Y, et al. Fracture investigation of functionalized carbon nanotubes-grown carbon fiber fabrics/epoxy composites. Compos Sci Technol 2020;195:108161. https://doi.org/10.1016/j.compscitech.2020.108161.

[59] Veedu VP, Cao A, Li X, Ma K, Soldano C, Kar S, et al. Multifunctional composites using reinforced laminae with carbon-nanotube forests. Nat Mater 2006;5:457–62. https://doi.org/10.1038/nmat1650.

[60] De Resende VG, Antunes EF, De Oliveira Lobo A, Oliveira DAL, Trava-Airoldi VJ, Corat EJ. Growth of carbon nanotube forests on carbon fibers with an amorphous silicon interface. Carbon N Y 2010;48:3655–8. https://doi.org/10.1016/j.carbon.2010.06.006.

[61] Falzon BG, Hawkins SC, Huynh CP, Radjef R, Brown C. An investigation of Mode I and Mode II fracture toughness enhancement using aligned carbon nanotubes forests at the crack interface. Compos Struct 2013;106:65–73. https://doi.org/10.1016/j.compstruct.2013.05.051.

[62] Sun L, Warren GL, Sue HJ. Partially cured epoxy/SWCNT thin films for the reinforcement of vacuum-assisted resin-transfer-molded composites. Carbon 2010;48:2364–7. https://doi.org/10.1016/j.carbon.2010.02.027.

[63] Bilge K, Ozden-Yenigun E, Simsek E, Menceloglu YZ, Papila M. Structural composites hybridized with epoxy compatible polymer/MWCNT nanofibrous interlayers. Compos Sci Technol 2012;72:1639–45. https://doi.org/10.1016/j.compscitech.2012.07.005.

[64] Zheng N, Huang Y, Liu HY, Gao J, Mai YW. Improvement of interlaminar fracture toughness in carbon fiber/epoxy composites with carbon nanotubes/polysulfone interleaves. Compos Sci Technol 2017;140:8–15. https://doi.org/10.1016/j.compscitech.2016.12.017.

[65] Xin W, Sarasini F, Tirillò J, Bavasso I, Sbardella F, Lampani L, et al. Impact and post-impact properties of multiscale carbon fiber composites interleaved with carbon nanotube sheets. Compos Part B Eng 2020;183. https://doi.org/10.1016/j.compositesb.2019.107711.

[66] Ou Y, Wu L, Hefetz M, González C, José Vilatela J. Improving interlaminar properties of woven carbon fibre composite laminates with industrial-scale carbon nanotube fibre interleaves. Compos Part A Appl Sci Manuf 2023;164. https://doi.org/10.1016/j.compositesa.2022.107283.

[67] Liu J, Rinzler AG, Dai H, Hafner JH, Kelley Bradley R, Boul PJ, et al. Fullerene pipes. Science 1998;280:1253–6. https://doi.org/10.1126/science.280.5367.1253.

[68] Coleman JN, Blau WJ, Dalton AB, Muñoz E, Collins S, Kim BG, et al. Improving the mechanical properties of single-walled carbon nanotube sheets by intercalation of polymeric adhesives. Appl Phys Lett 2003;82:1682–4. https://doi.org/10.1063/1.1559421.

[69] Liu L, Shen LL. Influence of cnt buckypaper on the interlaminar shear strength of laminates. 20th Int. Conf. Compos. Mater. Copenhagen, 2015, p. 19–24.

[70] Shin YC, Kim SM. Enhancement of the interlaminar fracture toughness of a Carbon-Fiber-Reinforced polymer using interleaved carbon nanotube Buckypaper. Appl Sci 2021;11:6821. https://doi.org/10.3390/app11156821.

[71] Andrews R, Jacques D, Rao AM, Rantell T, Derbyshire F, Chen Y, et al. Nanotube composite carbon fibers. Appl Phys Lett 1999;75:1329–31. https://doi.org/10.1063/1.124683.

[72] Sánchez M, Campo M, Jiménez-Suárez A, Ureña A. Effect of the carbon nanotube functionalization on flexural properties of multiscale carbon fiber/epoxy composites manufactured by VARIM. Compos Part B Eng 2013;45:1613–9. https://doi.org/10.1016/j.compositesb.2012.09.063.

[73] Sharma K, Shukla M. Three-phase carbon fiber amine functionalized carbon nanotubes epoxy composite: Processing, characterisation, and multiscale modeling. J Nanomater 2014. https://doi.org/10.1155/2014/837492.

[74] Islam ME, Mahdi TH, Hosur M V., Jeelani S. Characterization of carbon fiber reinforced epoxy composites modified with nanoclay and carbon nanotubes. Procedia Eng 2015;105:821–8. https://doi.org/10.1016/j.proeng.2015.05.078.

[75] Sheth D, Maiti S, Patel S, Kandasamy J, Chandan MR, Rahaman A. Enhancement of mechanical properties of carbon fiber reinforced epoxy matrix laminated composites with multiwalled carbon nanotubes. Fullerenes Nanotub Carbon Nanostructures 2020;29:288–94. https://doi.org/10.1080/1536383X.2020.1839424.

[76] Khan SU, Pothnis JR, Kim JK. Effects of carbon nanotube alignment on electrical and mechanical properties of epoxy nanocomposites. Compos Part A Appl Sci Manuf 2013;49:26–34. https://doi.org/10.1016/j.compositesa.2013.01.015.

[77] Gong X, Liu J, Baskaran S, Voise RD, Young JS. Surfactant-Assisted Processing of Carbon Nanotube / Polymer Composites. Chem Mater 2000; 12:1049–52. https://doi.org/10.1021/cm9906396.

[78] Allaoui A, Bai S, Cheng HM, Bai JB. Mechanical and electrical properties of a MWNT / epoxy composite. Compos Sci Technol 2002;62:1993–8. https://doi.org/10.1016/S0266-3538(02)00129-X.

[79] Kumar S, Doshi H, Srinivasarao M, Park JO, Schiraldi DA. Polymer Communication Fibers from polypropylene/nano carbon ®ber composites. Polymer 2002;43:1701–3. https://doi.org/10.1016/S0032-3861(01)00744-3.

[80] Kanagaraj S, Varanda FR, Zhil'tsova T V., Oliveira MSA, Simões JAO. Mechanical properties of high density polyethylene/carbon nanotube composites. Compos Sci Technol 2007;67:3071–7. https://doi.org/10.1016/j.compscitech.2007.04.024.

[81] Gojny FH, Wichmann MHG, Fiedler B, Bauhofer W, Schulte K. Influence of nano-modification on the mechanical and electrical properties of conventional fibre-reinforced composites. Compos Part A Appl Sci Manuf 2005;36:1525–35. https://doi.org/10.1016/j.compositesa.2005.02.007.

[82] Wichmann MHG, Sumfleth J, Gojny FH, Quaresimin M, Fiedler B, Schulte K. Glass-fibre-reinforced composites with enhanced mechanical and electrical properties - Benefits and limitations of a nanoparticle modified matrix. Eng Fract Mech 2006;73:2346–59. https://doi.org/10.1016/j.engfracmech.2006.05.015.

[83] Godara A, Mezzo L, Luizi F, Warrier A, Lomov S V., van Vuure AW, et al. Influence of carbon nanotube reinforcement on the processing and the mechanical behaviour of carbon fiber/epoxy composites. Carbon N Y 2009;47:2914–23. https://doi.org/10.1016/j.carbon.2009.06.039.

[84] Zhou HW, Mishnaevsky L, Yi HY, Liu YQ, Hu X, Warrier A, et al. Carbon fiber/carbon nanotube reinforced hierarchical composites: Effect of CNT distribution on shearing strength. Compos Part B Eng 2016;88:201–11. https://doi.org/10.1016/j.compositesb.2015.10.035.

[85] Sharma SP, Lakkad SC. Comparative study of the effect of fiber surface treatments on the flexural and interlaminar shear strength of carbon fiber-reinforced composites. Mater Today Commun 2020;24:101016. https://doi.org/10.1016/j.mtcomm.2020.101016.

[86] Khan SU, Kim JK. Interlaminar shear properties of CFRP composites with CNF-bucky paper interleaves. 18th Int. Conf. Compos. Mater., 2011.

[87] Wu Y, Cheng X, Chen S, Qu B, Wang R, Zhuo D, et al. In situ formation of a carbon nanotube buckypaper for improving the interlaminar properties of carbon fiber composites. Mater Des 2021;202. https://doi.org/10.1016/j.matdes.2021.109535.

[88] Yokozeki T, Iwahori Y, Ishiwata S, Enomoto K. Mechanical properties of CFRP laminates manufactured from unidirectional prepregs using CSCNT-dispersed epoxy. Compos Part A Appl Sci Manuf 2007;38:2121–30. https://doi.org/10.1016/j.compositesa.2007.07.002.

[89] Karapappas P, Vavouliotis A, Tsotra P, Kostopoulos V, Paipetis A. Enhanced fracture properties of carbon reinforced composites by the addition of multi-wall carbon nanotubes. J Compos Mater 2009;43:977–85. https://doi.org/10.1177/0021998308097735.

[90] Romhány G, Szebényi G. Interlaminar crack propagation in MWCNT/ fiber reinforced hybrid composites. Express Polym Lett 2009;3:145–51. https://doi.org/10.3144/expresspolymlett.2009.19.

[91] Almuhammadi K, Alfano M, Yang Y, Lubineau G. Analysis of interlaminar fracture toughness and damage mechanisms in composite laminates reinforced with sprayed multi-walled carbon nanotubes. Mater Des 2014;53:921–7. https://doi.org/10.1016/j.matdes.2013.07.081.

[92] Borowski E, Soliman E, Kandil UF, Taha MR. Interlaminar fracture toughness of CFRP laminates incorporating multi-walled carbon nanotubes. Polymers (Basel) 2015;7:1020–45. https://doi.org/10.3390/polym7061020.

[93] Quan D, Urdániz JL, Ivanković A. Enhancing mode-I and mode-II fracture toughness of epoxy and carbon fibre reinforced epoxy composites using multi-walled carbon nanotubes. Mater Des 2018;143:81–92. https://doi.org/10.1016/j.matdes.2018.01.051.

[94] Truong GT, Choi KK. Effect of short multi-walled carbon nanotubes on the mode I fracture toughness of woven carbon fiber reinforced polymer composites. Constr Build Mater 2020;259:119696. https://doi.org/10.1016/j.conbuildmat.2020.119696.

[95] Tsantzalis S, Karapappas P, Vavouliotis A, Tsotra P, Kostopoulos V, Tanimoto T, et al. On the improvement of toughness of CFRPs with resin doped with CNF and PZT particles. Compos Part A Appl Sci Manuf 2007;38:1159–62. https://doi.org/10.1016/j.compositesa.2006.04.016.

[96] Wicks SS, de Villoria RG, Wardle BL. Interlaminar and intralaminar reinforcement of composite laminates with aligned carbon nanotubes. Compos Sci Technol 2010;70:20–8. https://doi.org/10.1016/j.compscitech.2009.09.001.

[97] Davis DC, Whelan BD. An experimental study of interlaminar shear fracture toughness of a nanotube reinforced composite. Compos Part B Eng 2011;42:105–16. https://doi.org/10.1016/j.compositesb.2010.06.001.

[98] Naito K, Nagai C. Mode-I and mode-II interlaminar fracture properties of high modulus pitch-based carbon fiber reinforced polymers containing different nanostructures. J Compos Mater 2022;56:397–407. https://doi.org/10.1177/00219983211049289.

[99] Li Y, Hori N, Arai M, Hu N, Liu Y, Fukunaga H. Improvement of interlaminar mechanical properties of CFRP laminates using VGCF. Compos Part A Appl Sci Manuf 2009;40:2004–12. https://doi.org/10.1016/j.compositesa.2009.09.002.

[100] Arai M, Noro Y, Sugimoto K ichi, Endo M. Mode I and mode II interlaminar fracture toughness of CFRP laminates toughened by carbon nanofiber interlayer. Compos Sci Technol 2008;68:516–25. https://doi.org/10.1016/j.compscitech.2007.06.007.

[101] Seyhan AT, Tanoglu M, Schulte K. Mode I and mode II fracture toughness of E-glass non-crimp fabric/carbon nanotube (CNT) modified polymer based composites. Eng Fract Mech 2008;75:5151–62. https://doi.org/10.1016/j.engfracmech.2008.08.003.

[102] Burkov M, Eremin A. Evaluation of fracture toughness of hybrid CNT/CFRP composites. Mech Adv Mater Struct 2023;30:2872–81. https://doi.org/10.1080/15376494.2022.2064569.

[103] Blanco J, García EJ, Guzmán De Villoria R, Wardle BL. Limiting mechanisms of mode I interlaminar toughening of composites reinforced with aligned carbon nanotubes. J Compos Mater 2009;43:825–41. https://doi.org/10.1177/0021998309102398.

[104] Tong L, Sun X, Tan P. Effect of long multi-walled carbon nanotubes on delamination toughness of laminated composites. J Compos Mater 2008;42:5–23. https://doi.org/10.1177/0021998307086186.

[105] Wisnom MR. On the Increase in Fracture Energy with Thickness in Delamination of Unidirectional Glass Fibre-Epoxy with Cut Central Plies. J Reinf Plast Compos 1992;11:897–909. https://doi.org/10.1177/073168449201100802.

[106] Tian Z, Swanson SR. The Fracture Behavior of Carbon/Epoxy Laminates Containing Internal Cut Fibers. J Compos Mater 1991;25:1427–44. https://doi.org/10.1177/002199839102501103.

[107] Darby MI, Richards JM, Yates B. Effect of discontinuous plies on the tensile strength of CFRP laminates. J Mater Sci Lett 1985;4:203–6. https://doi.org/10.1007/BF00728077.

[108] Wisnom M. Delamination in tapered unidirectional glass fibre-epoxy under static tension loading. 32nd Struct. Struct. Dyn. Mater. Conf., 1991, p. 1142. https://doi.org/10.2514/6.1991-1142.

[109] Chakraborty D, Pradhan B. Critical strain energy release rate of broken ply composite laminates. J Reinf Plast Compos 1998;17:498–511. https://doi.org/10.1177/073168449801700602.

[110] Hong S, Liu D. On the relationship between impact energy and delamination area. Exp Mech 1989;29:115–20. https://doi.org/10.1007/BF02321362.

[111] Liu D, Malvern LE. Matrix cracking in impacted glass/epoxy plates. J Compos Mater 1987;21:594–609. https://doi.org/10.1177/002199838702100701.

[112] Hong S. Central delamination in glass/epoxy laminates. Ph.D. Thesis. Michigan State University 1991.

[113] Lu X, Liu D. Finite element analysis of strain energy release rate at delamination front. J Reinf Plast Compos 1991;10:279–92. https://doi.org/10.1177/073168449101000303.

[114] Mukherjee YX, Gulrajani SN, Mukherjee S, Netravali AN. A numerical and experimental study of delaminated layered composites. J Compos Mater 1994;28:837–70. https://doi.org/10.1177/002199839402800904.

[115] Yashiro S, Ogi K. Fracture behavior in CFRP cross-ply laminates with initially cut fibers. Compos Part A Appl Sci Manuf 2009;40:938–47. https://doi.org/10.1016/j.compositesa.2009.04.023.

[116] Wisnom MR. The role of delamination in failure of fibre-reinforced composites. Philos Trans R Soc A Math Phys Eng Sci 2012;370:1850–70. https://doi.org/10.1098/rsta.2011.0441.

[117] Cameselle-Molares A, Vassilopoulos AP, Keller T. Experimental investigation of two-dimensional delamination in GFRP laminates. Eng Fract Mech 2018;203:152–71. https://doi.org/10.1016/j.engfracmech.2018.05.015.

[118] Wang C, Vassilopoulos AP, Keller T. Numerical modeling of two-dimensional delamination growth in composite laminates with in-plane isotropy. Eng Fract Mech 2021;250:107787. https://doi.org/10.1016/j.engfracmech.2021.107787.

[119] Jokinen J, Kanerva M, Wallin M, Saarela O. The simulation of a double cantilever beam test using the virtual crack closure technique with the cohesive zone modelling. Int J Adhes Adhes 2019;88:50–8. https://doi.org/10.1016/j.ijadhadh.2018.10.015.

[120] Sindhu BR, Raju J, Kamath K. A comparative numerical study of standard 3D composite plate using virtual crack closure technique and cohesive zone modelling method. IOP Conf. Ser. Mater. Sci. Eng., vol. 561, 2019, p. 12048. https://doi.org/10.1088/1757-899X/561/1/012048.

[121] Kaw AK. Mechanics of composite materials. Second edition, Taylor & Francis 2006, ISBN 0-8493-1343-0.

[122] Pipes RB, Pagano NJ. Interlaminar stresses in composite laminates under uniform axial extension. J Compos Mater 1970;4:538–48. https://doi.org/10.1177/002199837000400409.

[123] Rybicki EF. Approximate three-dimensional solutions for symmetric laminates under inplane loading. J Compos Mater 1971;5:354–60. https://doi.org/10.1177/002199837100500305.

[124] Wang ASD, Crossman FW. Some new results on edge effect in symmetric composite laminates. J Compos Mater 1977;11:92–106. https://doi.org/10.1177/002199837701100110.

[125] Pagano NJ, Pipes RB. The influence of stacking sequence on laminate strength. J Compos Mater 1971;5:50–7. https://doi.org/10.1177/002199837100500105.

[126] Pagano NJ, Soni SR. Global-local laminate variational model. Int J Solids Struct 1983;19:207–28. https://doi.org/10.1016/0020-7683(83)90058-6.

[127] Tsai SW. Strength theories of filamentary structure. Fundam Asp Fiber Reinf Plast Compos 1968.

[128] Hill R. The mathematical theory of plasticity. Oxford Classic Series 1998.

[129] Tsai SW, Wu EM. A general theory of strength for anisotropic materials. J Compos Mater 1971;5:58–80. https://doi.org/10.1177/002199837100500106.

[130] Whitney JM, Nuismer RJ. Stress fracture criteria for laminated composites containing stress concentrations. J Compos Mater 1974;8:253–65. https://doi.org/10.1177/002199837400800303.

[131] Kim RY, Soni SR. Experimental and analytical studies on the onset of delamination in laminated composites. J Compos Mater 1984;18:70–80. https://doi.org/10.1177/002199838401800106.

[132] Soni SR, Kim RY. Delamination of composite laminates stimulated by interlaminar shear. Compos Mater ASTM STP 1986;893:286.

[133] Kim RY, Soni SR. Failure of composite laminates due to combined interlaminar normal and shear stresses. Composites 1986;86:341–50.

[134] Brewer JC, Lagace PA. Quadratic stress criterion for initiation of delamination. J Compos Mater 1988;22:1141–55. https://doi.org/10.1177/002199838802201205.

[135] Lu H, Guo L, Liu G, Zhong S, Zhang L, Pan S. Progressive damage investigation of 2.5 D woven composites under quasi-static tension. Acta Mech 2019;230:1323–36. https://doi.org/10.1007/s00707-017-2024-z.

[136] Muñoz-Reja M, Távara L, Mantič V, Cornetti P. Crack onset and propagation at fibre-matrix elastic interfaces under biaxial loading using finite fracture mechanics. Compos Part A Appl Sci Manuf 2016;82:267–78. https://doi.org/10.1016/j.compositesa.2015.09.023.

[137] Lorriot T, Marion G, Harry R, Wargnier H. Onset of free-edge delamination in composite laminates under tensile loading. Compos Part B Eng 2003;34:459–71. https://doi.org/10.1016/S1359-8368(03)00016-7.

[138] Kruger R, Konig M, Schneiderf T. Computation of local energy release rates along straight and curved delamination fronts of unidirectionally laminated DCM-and ENF-specimens. 34th Struct. Struct. Dyn. Mater. Conf., 1993, p. 1457. https://doi.org/10.2514/6.1993-1457.

[139] Hellen TK. On the method of virtual crack extensions. Int J Numer Methods Eng 1975;9:187–207. https://doi.org/10.1002/nme.1620090114.

[140] Delorenzi HG. Energy release rate calculations by the finite element method. Eng Fract Mech 1985;21:129–43. https://doi.org/10.1016/0013-7944(85)90060-8.

[141] Hwang CG, Wawrzynek PA, Tayebi AK, Ingraffea AR. On the virtual crack extension method for calculation of the rates of energy release rate. Eng Fract Mech 1998;59:521–42. https://doi.org/10.1016/s0013-7944(97)00103-3.

[142] Ishikawa H. A finite element analysis of stress intensity factors for combined tensile and shear loading by only a virtual crack extension. Int J Fract 1980;16:R243–6. https://doi.org/10.1007/BF00016590.

[143] George TS. On the virtual crack extension technique for stress intensity factors and energy release rate calculations for mixed fracture mode. Int J Fract 1984;25:R33-42. https://doi.org/10.1007/BF01141558.

[144] Nikishkov GP, Atluri SN. An equivalent domain integral method for computing crack-tip integral parameters in non-elastic, thermo-mechanical fracture. Eng Fract Mech 1987;26:851–67. https://doi.org/10.1016/0013-7944(87)90034-8.

[145] Raju IS, Shivakumar KN. An equivalent domain integral method in the two-dimensional analysis of mixed mode crack problems. Eng Fract Mech 1990;37:707–25. https://doi.org/10.1016/0013-7944(90)90070-W.

[146] Shivakumar KN, Raju IS. An equivalent domain integral method for three-dimensional mixed-mode fracture problems. Eng Fract Mech 1992;42:935–59. https://doi.org/10.1016/0013-7944(92)90134-Z.

[147] Rybicki EF, Schmueser DW, Fox J. An energy release rate approach for stable crack growth in the free-edge delamination problem. J Compos Mater 1977;11:470–87. https://doi.org/10.1177/002199837701100409.

[148] Raju IS. Calculation of strain-energy release rates with higher order and singular finite elements. Eng Fract Mech 1987;28:251–74. https://doi.org/10.1016/0013-7944(87)90220-7.

[149] Krueger R. Virtual crack closure technique: History, approach, and applications. Appl Mech Rev 2004;57:109–43. https://doi.org/10.1115/1.1595677.

[150] ANSYS R. Academic research release 15.0. Help system. ANSYS Mech Elem Ref 2013.

[151] Johannesson T, Sjöblom P, Seldén R. The detailed structure of delamination fracture surfaces in graphite/epoxy laminates. J Mater Sci 1984;19:1171–7. https://doi.org/10.1007/BF01120026.

[152] O'brien TK. Characterization of delamination onset and growth in a composite. Dam Compos Mater, ASTM STP 775 1982:140–67.

[153] Affdl JCH, Kardos JL. The Halpin-Tsai equations: a review. Polym Eng & Sci 1976;16:344–52. https://doi.org/10.1002/pen.760160512.

[154] Anderson T L. Fracture mechanics: fundamentals and applications. Fourth edition. Taylor & Francis Group. CRC Press 2017: ISBN-13:978-1-4987-2813-3.

[155] Meguid SA, Sun Y. On the tensile and shear strength of nano-reinforced composite interfaces. Mater Des 2004;25:289–96. https://doi.org/10.1016/j.matdes.2003.10.018.

[156] Atchuta Rao C, Krishna Murthy KSR, Chakraborty D. Influence of CNTs on interface delamination resistance in broken ply carbon/CNT-epoxy composites. Mech Based Des Struct Mach 2023;51:1189–200. https://doi.org/10.1080/15397734.2020.1864641.

[157] Chai H, Babcock CD. Two-dimensional modelling of compressive failure in delaminated laminates. J Compos Mater 1985;19:67–98. https://doi.org/10.1177/002199838501900105.

[158] Wang SS. Fracture mechanics for delamination problems in composite materials. J Compos Mater 1983;17:210–23. https://doi.org/10.1177/002199838301700302.

[159] Shen F, Lee KH, Tay TE. Modeling delamination growth in laminated composites. Compos Sci Technol 2001;61:1239–51. https://doi.org/10.1016/S0266-3538(01)00023-9.

[160] Tao J, Sun CT. Influence of ply orientation on delamination in composite laminates. J Compos Mater 1998;32:1933–47. https://doi.org/10.1177/002199839803202103.

# List of Publications

## Journal Publications

[1] Atchuta Rao C, Krishna Murthy KSR, Chakraborty D. Influence of CNTs on interface delamination resistance in broken ply carbon/CNT-epoxy composites. Mech Based Des Struct Mach 2023;51:1189–200. https://doi.org/10.1080/15397734.2020.1864641.

[2] Atchuta Rao C, Krishna Murthy KSR, Chakraborty D, 2023. Enhancement of resistance to interfacial delamination in carbon/epoxy laminates with part-through-the-width ply break by adding CNTs to adhesive. J Adh Sci Tech 2023;37:1–19. https://doi.org/10.1080/01694243.2022.2039439.

[3] Rao CA, Murthy K, Chakraborty D. Role of CNTs on the Resistance to Delamination Growth in Three-Phase FRP Laminates with Embedded Delamination: Finite Element Analysis. J Inst Eng Ser C 2023:1–12. https://doi.org/10.1007/s40032-023-01014-y.

[4] Rao CA, Murthy K, Chakraborty D. Improving resistance to embedded delaminations by adding CNTs to epoxy in carbon/(epoxy+ CNT) composites. Proc Inst Mech Eng Part L J Mater Des Appl 2024. https://doi.org/10.1177/14644207241230234.

## Conferences

[1] Rao CA, Murthy KSRK, Chakraborty D. Numerical study to investigate the influence of CNTs on delamination resistance in broken ply carbon/epoxy composites. IOP Conf. Ser. Mater. Sci. Eng., vol. 1248, 2022, p. 12066. https://doi.org/10.1088/1757-899X/1248/1/012066.


भारतीय प्रौद्योगिकी संस्थान गुवाहाटी
Indian Institute of Technology Guwahati